A NUMERICAL INVESTIGATION OF A TOKAMAK DISCHARGE WITH PARTICULAR ATTENTION TO THE INITIAL STAGES

Stephen John Webb

This thesis is submitted in fulfilment of the requirements for the Degree of Doctor of Philosophy in the University of London

Plasma Group,
Department of Physics,
Imperial College,
London.

November 1979.

ABSTRACT

The observed current rise phase of a tokamak discharge cannot be accounted for by either classical or neoclassical theory. Experimentally there is a remarkable absence of any evidence for a current skin effect lasting a significant proportion of the current rise time. In large devices the skin effect should be even more pronounced than in the smaller, older machines, but no such effect is reported.

One dimensional simulations model the current rise by increasing anomalously the transport coefficients. This would imply a high level of plasma turbulence and possibly an intolerable thermal loading on the limiter.

A two dimensional, one fluid and Lagrangian code, TICTOK, is used to study the early time behaviour of a tokamak discharge. The model includes inertial effects but removes the fast compressional Alfven waves associated with the large toroidal magnetic field, by assuming a small plasma beta. The code has been developed to include the effect of tensor thermal conductivity, and auxillary heating from a neutral beam source which requires also that anisotropic pressure be included.

It is found that azimuthal variations in the driving toroidal electric field lead to asymmetric plasma heating. The resulting increase of current density is found to produce plasma flow which has a subsequent effect on the magnetic surface structure, leading to an enhanced penetration of the current.

A neutral beam source was modelled by introducing a source of anisotropic pressure parallel to the magnetic field and following the resulting change in the hot plasma equilibrium. It is possible that a neutral beam may affect the delicate balance between flow and equilibrium, where the flow produces the electric field necessary to convert the applied toroidal electric field to that required for equilibrium. It is found that the source of parallel pressure, produces plasma flow that affects equilibrium and gives rise to a complex convective cell pattern.

TABLE OF CONTENTS

LIST OF ILLUSTRATIONS

LIST OF TABLES

ACKNOWLEDGEMENTS

The research for this thesis was carried out in the Plasma Group of the Physics Department at Imperial College, London. During this time I was in receipt of a bursary from Culham Laboratory under contract CUL 900. I would like to thank my supervisors Dr. D.E. Potter and Professor M.G. Haines for many a useful discussion throughout the course of this work. Also I am grateful to the students of the Plasma Group, especially those of the Theory section, for numerous informal, enlightening discussions.

I am indebted to my parents for their support not only during the course of this work, but throughout my education.

Finally, the continual help and encouragement of Sarah Cowen has aided the completion of this thesis, and her neat, accurate typing has eased the task of preparing the manuscript.

CHAPTER 1

INTRODUCTION

1.1 HISTORY

Over the past decade there has been a continual growth in the level of interest in tokamak devices. In this period there has been a number of notable achievements both experimental and theoretical. Two of these experimental achievements are cited here; the first because of its general importance to tokamak research, the second because of its bearing on this work.

Widespread interest in the tokamak device was first generated when Artsimovich, the originator of the tokamak configuration, reported[1],[2],[3] that the tokamak T-3 had attained an $n\tau$ value (product of number density and energy confinement time) of approximately 10^{18} m^{-3} s and an electron temperature of about 1 keV. This represented a considerable advance over existing measurements and a significant step towards the Lawson criterion[4] for thermonuclear breakeven ($n\tau \simeq 10^{20}$ m^{-3} s and ion temperature $\simeq$ 10 keV). These results, confirmed by Thompson scattering measurements[5], were sufficient to direct a large proportion of the controlled fusion effort into the development of the tokamak device, in order to contain a sufficiently hot, dense plasma long enough for breakeven to occur.

It has, however, long been recognised that ohmic heating of a tokamak plasma would alone be insufficient to raise the ion temperature to that required for scientific breakeven. Some form of auxillary heating is necessary, and the most promising method may be direct heating of the ions, by charge exchange collisions, using a beam of energetic neutrals. Whilst initial neutral beam heating experiments in Cleo[6], ATC[7], and ORMAK[8] reported ion temperature rises of about 50% with

modest amounts of neutral beam energy, the ion temperature was still far short of thermonuclear burn temperatures. However, soon after the commissioning of one of the first large tokamaks, the Princeton Large Torus (PLT), ion temperatures of approximately 5.5 keV were reported[9], achieved by injecting tangentially four neutral beams giving a total injected power of about 2 MW. Although their $n\tau$ value 10^{18} m^{-3} s is no nearer the Lawson criterion than the T-3 figure, this result demonstrated that neutral beam injection is a viable method of heating a tokamak plasma beyond its ohmic heating limit.

It remains now to be seen, as still larger machines, e.g. Joint European Torus (JET), Toroidal Fusion Test Reactor (TFTR), now under construction, become operational whether $n\tau$ and T_i scale as well as hoped.

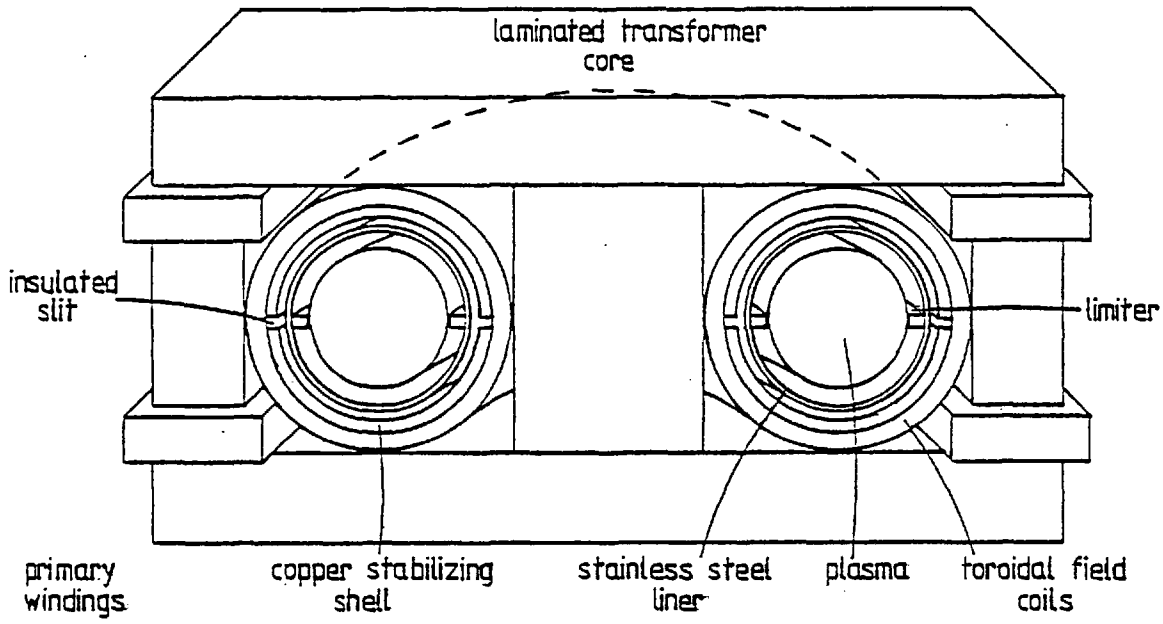

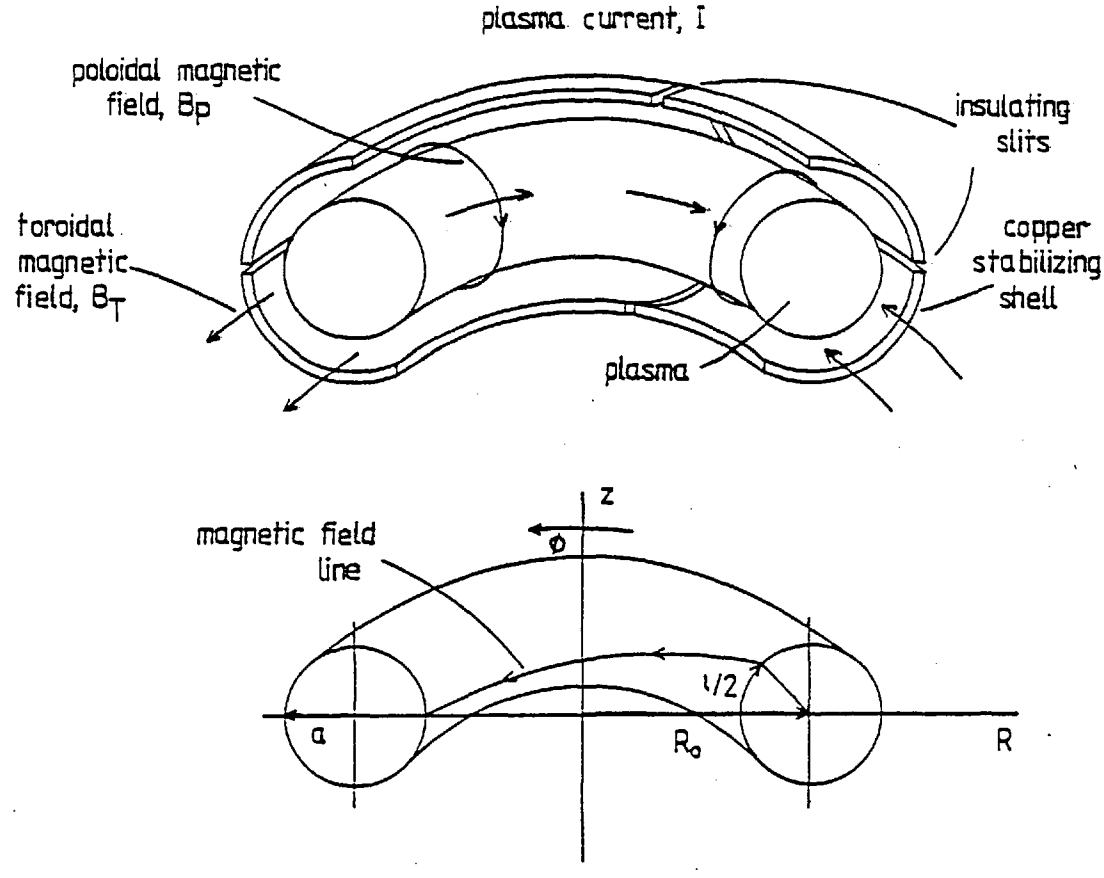

Fig. 1.1 Typical tokamak geometry

1.2 GEOMETRY

The basic tokamak configuration is illustrated in Fig. 1.1. The electrons and ions of the plasma are confined by nested magnetic surfaces comprised of helical magnetic field lines. The toroidal component of the magnetic field, B_T, produced by external coils around the torus, is much larger than the poloidal components of the magnetic field, B_p, produced by the plasma current, I. The plasma current is induced by changes of flux in an iron transformer core, the primary circuit of which is connected to the external power source (usually a capacitor bank) and the secondary circuit is the plasma itself.

The magnitude of B_p is limited by the minimum allowable safety factor, q, for magnetohydrodynamic (MHD) stability;

$$q = \frac{2\pi}{\iota} = \frac{aB_T}{RB_p} \qquad (1.1)$$

where ι is the rotational transform, and a and R are the minor and major radii of the plasma.

Without additional fields, the plasma ring would expand because of the force that exists on an element of plasma whose current interacts with the magnetic field produced by a similar element on the other side of the plasma loop. An additional vertical magnetic field is required and may be produced either by eddy currents induced in a toroidal copper shell surrounding the plasma or by electronically controlled currents in external coils. The latter is more prevalent in the present generation of tokamaks as the resistance of a copper shell must be sufficiently high to allow the penetration of the toroidal field yet still low enough to allow eddy currents to control the plasma position. In the older machines, e.g. T-3, penetration of the toroidal field was achieved by cutting an insulating slit in the copper shell that encircled the major axis.

1.3 EQUILIBRIUM AND STABILITY

The equations describing ideal MHD equilibria are given below.

$$\nabla p = \underline{J} \times \underline{B}$$

$$\nabla \times \underline{B} = \mu_0 \underline{J} \qquad (1.2)$$

$$\nabla . \underline{B} = 0$$

To obtain completely general equilibria these equations must be solved in three dimensions, which is an extremely complex problem[10], and only may be tackled computationally[11]. Equilibria are sought by allowing displacements of the plasma that only produce a negative definite change in the total energy.

A useful and usual approximation to make for a tokamak is to assume the plasma is axisymmetric. This, however, excludes helically symmetric equilibria. Assuming axisymmetry the equations (1.2) combine to give a second order partial differential equation[12] (Appendix C)

$$\Delta^* \psi = -\mu_0 RJ_\phi = -\mu_0 R^2 \dot{p} - F\dot{F} \qquad (1.3)$$

for the distribution of poloidal flux, ψ. The two functions p and F correspond to the plasma pressure and the flux function of the poloidal currents, respectively, and are functions of ψ only. For a tokamak with a circular cross section and a large aspect ratio, i.e. $R/a = 1/\varepsilon \gg 1$, equation (1.3) may be solved analytically by expanding in the small parameter ε and linearizing. For a particular value of the poloidal beta ($\bar{p}$ is the average plasma pressure),

$$\beta_p = \frac{\bar{p}}{B_p^2/2\mu_0} \qquad (1.4)$$

which describes the ratio of energy density in the plasma to that in the poloidal magnetic field, B_p, at the plasma surface, a particular

distribution of the flux surfaces is obtained. As β_p is increased, the magnetic surfaces shift outward in major radius, altering the current distribution to balance the plasma pressure. For $\beta_p > 1$ the poloidal magnetic field cannot alone balance the plasma pressure so poloidal currents flow that oppose the plasma pressure, and also reduce the toroidal field. The plasma, for $\beta_p > 1$ is therefore diamagnetic. For $\beta_p \sim R/a$ the magnetic surface becomes extremely non-circular and the toroidal current can reverse. Shafranov[13] suggests this is the limiting value for β_p before increased energy losses occur.

The toroidal magnetic field is now chosen by defining the safety factor, q, Eq. (1.1) so that the plasma equilibrium is stable, and the total beta,

$$\beta = \bar{P}/B^2/2\mu_o \simeq (a/qR)^2 \beta_p \qquad (1.5)$$

is maximised for economic viability. We seek therefore the smallest q to ensure stability. The subject of MHD stability, reviewed by Wesson[14], is complex and shall not be dealt with in detail here. By listing the choices of safety factor, we summarize the methods of stabilizing the most important modes in a circular, large aspect ratio tokamak.

Helical perturbations of the form

$$\xi \propto e^{i(m\theta - n\phi)}$$

where θ and ϕ are the poloidal toroidal angles respectively, occuring in an infinitely conducting plasma are stabilized if $q(a) > m/n$[15]. Since for kink modes the minimum value of n is unity stability for a given m is obtained for $q(a) > m$. Another important stabilizing effect is shear of the magnetic field, and for $q(a) > 1$ peaking of the current distribution alone can ensure that complete stability against kink modes is obtained[16]. Peaking of the current distribution is measured by the ratio $q(a)/q(o)$. The minimum amount of peaking to ensure complete stability is $q(a)/q(o) > 2$.

A requirement on the value of q(o) is given firstly by the stability of ideal internal modes. These are stabilized by shear, as determined by Suydam's criterion in cylindrical geometry, or the less restrictive Mercier criterion in a tokamak. For pressure decreasing towards the wall, localised modes are stable provided $q(o) > 1$. Thus for an infinitely conducting plasma we can ensure stability and maximise β by choosing $q(o) \gtrsim 1$ and $q(a) \gtrsim 2$.

When resistivity is introduced the choice of q is restricted still further. In a narrow layer around resonant surfaces, where $m = nq$, the magnetic field lines may break and rejoin. These tearing modes[17],[18] may be stabilized for high m numbers with a sufficiently peaked current profile[19], although the $m = 2$ and $m = 3$ modes remain unstable. To stabilize these modes it is necessary to exclude the appropriate resonant surface from the plasma by requiring $q(o) > m$. Therefore in principle this limits the minimum q on axis to $q(o) > 3$.

Thus equation (1.5) gives the maximum total beta as $\beta \sim 2 - 4\%$. As this is on the lower edge of economic attractiveness, the limit of $\beta_p < R/a$ has been questioned. Dory and Peng[20] suggest that this value of β_p limits the use of the cylindrical approximation, rather than the existance of equilibria. They show that shaping the cross section (small aspect ratio, D shaped) and rapid heating (from an unspecified source) can lead to equilibria with a total β of 20% and realistic q values ($q(o) \sim 1, q(a) \sim 5$). Apart from the economic advantages, small aspect ratio, high beta tokamaks have enhanced stability to tearing modes. In a tight torus with $\beta_p \sim 1$ and $R/a \sim 2 - 3$ the $m = 2$ tearing mode may become insignificant, therefore relaxing the restriction on q(o). One disadvantage is that with a shaped cross section axisymmetric modes are now possible.

At this time, the new generation of tokamaks, e.g. JET, are being built around the above criteria. They have $\frac{1}{\epsilon} \sim 2 - 4$, $\beta_p \sim 1 - 2$, can

therefore choose $q(o) \gtrsim 1$, $q(a) \sim 2 - 4$ which results in $\beta \sim 2 - 4\%$.

1.4 ATTAINMENT OF EQUILIBRIA

A question seldom asked is how the equilibria, described in the last section, are reached from the initial conditions of a tokamak discharge. Most one and two dimensional calculations start at or near an equilibrium state although it has been suggested[21] that a reason for lack of confinement may be the absence of an appropriate equilibrium state rather than instability. In general two dimensional calculations are used to examine the properties, e.g. β, q, of various equilibria[20] whilst one dimensional codes, e.g. Ref. (22), are mostly concerned with transport from a plasma near equilibrium. Only in a few cases are one dimensional calculations applied to the study of the relaxation of a tokamak plasma from initial discharge conditions to an equilibrium.

Abramov et al.[23] study the effect of ionisation process on the evolution of the early stages of a cylindrical tokamak. They conclude, however, that some anomalous process is necessary to permit the penetration of the current on a timescale comparable with that observed experimentally. Duchs et al.[24] use a one dimensional transport code to study the evolution of temperature and current profiles from an initially cool fully ionised plasma. They find that a large enhancement in the thermal conductivity is required to suppress a skin effect.

In Chapter 4 we present solutions obtained from a two dimensional, one fluid computer code, described in Chapter 2 and developed in Chapter 3. These solutions, of the initial stages of both a large and small tokamak, are distinctly two dimensional[25]. In the large tokamak, the solutions can show the coupling of plasma flow and magnetic field diffusion. These solutions indicate that the current penetration will occur in a time comparable to that observed experimentally without introducing any ad hoc anomaly factors.

1.5 AUXILLARY HEATING

Although the intrinsic ohmic heating process of the tokamak has proved most convenient in creating moderate sized plasmas with $T_e \sim 1 - 2$ keV and $\beta_p \sim 0.1 - 1.0$ it is not a promising method for attaining reactor temperatures in large experiments. We have seen in section 1.3 that it is desirable to raise the poloidal beta to near, or in excess of the MHD constraint, $\beta_p < R/a$, but even assuming that the only heat loss mechanisms are bremsstrahlung and pseudoclassical transport[26], ohmic heating can only produce a poloidal beta of

$$\beta_p \simeq \tfrac{1}{2} \{ 1 + (I/1.6\ \mathrm{MA})^2 \}^{-\frac{1}{2}}$$

Powerful auxillary heating methods are clearly necessary for the optimal levels of β_p, required for tokamak reactor experimentation, to be reached.

Since toroidal geometry permits many Coulomb collision times during one plasma confinement time it is possible to heat the plasma using a beam of neutral particles with energies that are many times greater than the desired plasma temperature. The injected neutrals undergo charge exchange interactions with cool plasma ions, and the resultant trapped energetic ions then slow down gradually losing energy in collisions with plasma ions and electrons. The production processes and spatial distribution of fast ions resulting from tangential injection have been investigated[27] and show that while maximum absorption occurs for injection approximately halfway between the magnetic axis and the wall of the torus, the fast ion distribution peaks strongly at the magnetic axis because of the geometry. These hot ions affect the distribution function of the plasma ions and also produce toroidal momentum[28]. This latter effect may be avoided if coinjected and counterinjected beams (parallel and antiparallel to the plasma current) are used.

In Chapter 6 a neutral beam is considered as a source of parallel pressure. At high temperatures collisions are sufficiently infrequent to isotropise the pressure on inertial timescales. Using the model of Chapter 2, additional theory is presented in Chapter 5, that allows an anisotropic pressure distribution to be included. Modifications to the momentum equation show that gradients of parallel pressure produce flow in the poloidal plane. This source of momentum is, however, not removed by employing a counterinjected beam.

Finally, in Chapter 7, the results and numerical techniques are discussed.

CHAPTER 2

A TOROIDALLY INCOMPRESSIBLE MODEL FOR A TOKAMAK

A large toroidal magnetic field is an essential feature of all tokamak devices. This implies a certain degree of axisymmetry in the system and is reflected in the type of models usually employed to simulate the tokamak. It also, however, implies that the timescale for torsional and compressional changes of this field is much smaller than the timescales associated with any other magnetohydrodynamic process. For instance the toroidal Alfven speed is much larger than the Alfven speed associated with the poloidal field, which in turn is much larger than the diffusive velocity of plasma relative to magnetic field lines. A model for the behaviour of such a plasma must remove these fast oscillations so that the plasma may be observed on a longer more interesting timescale.

For example, in hydrodynamics, in order to follow phenomena such as flow on a long timescale, the short timescales associated with sound waves may be removed from the model by considering the flow to be incompressible, assuming the pressure is large compared to the flow energy. In much the same way compressional Alfven waves associated with the large toroidal field are removed by assuming the plasma to be 'toroidally incompressible'.

In this chapter the toroidally incompressible model is reviewed and described for an infinitely conducting low beta plasma. Some ideas on the choice of coordinate systems are presented and corrections for finite resistivity, and finite plasma pressure are then added. An interpretation of the model is given, and finally a summary of the stages of the calculation.

Throughout the chapter attention is paid to ensuring that the equations are derived in general vector notation before being applied to a specific coordinate system.

2.1 THE MODEL

2.1.1 Qualitative description

In a model proposed by Potter and developed by Tuttle[29],[30] the normal tokamak geometry is considered (Fig. 1.1) in which the toroidal magnetic field, B_T, is much greater than the poloidal magnetic field, B_p. The toroidal field is produced externally by coils and the poloidal field by plasma currents. Defining the total beta to be the ratio of the average plasma internal energy to magnetic energy,

$$\beta = \frac{\bar{p}}{B^2/2\mu_o} \simeq \frac{\bar{p}}{B_T^2/2\mu_o} \tag{2.1}$$

and the poloidal beta the ratio of the plasma pressure compared to the poloidal field at the plasma edge

$$\beta_p = \frac{\bar{p}}{B_p^2/2\mu_o} \tag{2.2}$$

it follows that:

$$\beta_p >> \beta.$$

As we have seen in Chapter 1, stability considerations limit the size of the poloidal beta to the order of unity, so:

$$\beta << 1$$

The energy of the total magnetic field is therefore much greater than that of the plasma and consequently any motion of the plasma is unable to alter significantly the total magnetic field. The toroidal magnetic field therefore appears incompressible, or changes connected with the

toroidal field propagate at an infinite speed.

This is illustrated by considering the interactions of the various fields and currents present in the tokamak. The poloidal magnetic field is produced by the toroidal current induced in the plasma from the external circuit. This self magnetic field interacts with the current to give a compression of the plasma, which takes place on a timescale associated with the Alfven velocity of the poloidal magnetic field:

$$v_p = \left(\frac{B_p^2}{\mu_0 \rho}\right)^{\frac{1}{2}} \qquad (2.3)$$

The compression, however, results in a compression of the toroidal field which is produced by currents flowing in external coils. As a result poloidal currents are induced in the plasma which tend to oppose the changes in the toroidal field. These poloidal currents couple with the toroidal field to produce a force that opposes the compression. These effects take place on a timescale associated with the toroidal Alfven speed, v_T, which from (2.3) is:

$$v_T = v_p \frac{B_T}{B_p}$$

and is much larger than the poloidal Alfven speed, v_p. Thus the forces opposing the compression are set up on a timescale much shorter than the time taken to establish the compression itself. Thus at any instant the compression is balanced by a reactive force.

The development of the plasma is therefore considered to progress via a series of quasi equilibria. Changes in the poloidal field cause an instantaneous transition to another equilibrium state that is established on a timescale short compared to the timescale for changes in the poloidal field.

2.1.2 Ordering

Before we start to analyse this model quantitatively it is instructive to order the various physical processes present in this model. The Alfven velocity associated with the poloidal magnetic field is given by (2.3) and a similar expression gives the toroidal Alfven speed. The ratio of the timescales associated with changes in each of these fields is therefore:

$$\frac{\tau_T}{\tau_p} = \frac{v_p}{v_T} = \frac{B_p}{B_T}$$

Stability considerations limit, β_p to order unity, giving:

$$\bar{p} \sim \frac{B_p^2}{2\mu_o}$$

Using this in the above equation gives:

$$\frac{B_p}{B_T} \sim \frac{\tau_T}{\tau_p} \sim \beta^{\frac{1}{2}} \qquad (2.4)$$

A similar expression may be obtained for the change in magnetic field by considering the expression for energy balance in equilibrium:

$$\bar{p} + \frac{B^2}{2\mu_o} = \text{constant}$$

which yields:

$$\delta B \sim \beta B \qquad (2.5)$$

For the toroidal field as $\beta \ll 1$, changes are small compared to the total magnetic field, but for the poloidal magnetic field where $\beta_p \sim 1$ changes may be of the same order as the poloidal magnetic field.

This is a reiteration of the basis of the model. The plasma has sufficient energy to alter the poloidal field, but not the toroidal field.

2.1.3 Quantitative description

An expression for the variation of the total magnetic field may be obtained from Faraday's law:

$$\nabla \times \underline{E} = -\frac{\partial \underline{B}}{\partial t} \tag{2.6}$$

$$\nabla . \underline{B} = 0 \tag{2.7}$$

and a simple Ohms law:

$$\eta \underline{J} = \underline{E} + \underline{v} \times \underline{B} \tag{2.8}$$

where η is the scalar resistivity, and $\underline{v}$ the centre of mass velocity. Equation (2.8) neglects the Hall effect, a contribution from the electron pressure gradient, and one arising from $\partial \underline{J}/\partial t$. The omission of these terms is usual and may be justified by considering the timescales associated with these processes compared to those of interest.

Defining R as the distance from the major axis equations (2.6) to (2.8) yield:

$$\frac{1}{R^2} \frac{d}{dt} (R\underline{B}) = \frac{1}{R} (\underline{B}.\nabla)\underline{v} - R\underline{B} \nabla . (\frac{\underline{v}}{R^2}) - \frac{\underline{B}}{R^2} \underline{v}.\nabla R - \frac{1}{R} \nabla \times \eta \underline{J} \tag{2.9}$$

where

$$\frac{d}{dt} = \frac{\partial}{\partial t} + \underline{v} . \nabla$$

and is the Lagrangian derivative, or derivative in the fluid frame. As variations in the total magnetic field are small, of order β, we use this small quantity to perform an expansion of equation (2.9). This expansion (Appendix A) gives to zeroth order

$$\nabla \cdot \frac{\underline{V}}{\overline{\overline{R^2}}} = 0 \qquad (2.10)$$

The quantity $\frac{\underline{V}}{\overline{\overline{R^2}}}$ is solenoidal to this order and therefore may be described completely by two scalar functions. One such representation (which can be shown to be generally possible at least locally) is

$$\frac{\underline{V}}{\overline{\overline{R^2}}} = \nabla\phi \times \nabla\zeta \qquad (2.11)$$

The scalars ζ and ϕ are termed Euler potentials and were first used by Leonhard Euler to describe incompressible fluid flow in terms of "stream functions". Since then they have been used in axisymmetric flow, solar magnetohydrodynamics, and most recently plasma physics[31].

If a field is represented by Euler potentials in some region of space which possesses symmetry, then one potential may be derived from considerations of that symmetry. In this work we assume that the tokamak is axisymmetric, which allows us to equate the potential ϕ in equation (2.11) with the azimuthal coordinate, leaving only the stream function ζ to be determined.

It has been shown by Taylor[32] that toroidal discharges relax to a quiescent state independent of initial state and previous history. By assuming axisymmetry we are restricting our solutions to a two dimensional form rather than making a statement about the form of the tokamak. Our analysis will, therefore, not admit of helically symmetric or three dimensional solutions which may occur.

If $\underline{e}_\phi$ is the unit vector in the direction $\nabla\phi$ Eq. (2.11) becomes:

$$\underline{v} = R^2 \frac{\underline{e}_\phi}{R} \times \nabla\zeta$$

which leads to the expressions for the flow velocity and its components in (R, ϕ, z) coordinates derived by Tuttle[30]:

$$v_R = R \frac{\partial\zeta}{\partial z} \quad ; \quad v_z = - R \frac{\partial\zeta}{\partial R} \tag{2.12}$$

$$\underline{v} = - R^2 \nabla \times (\frac{\zeta \underline{e}_\phi}{R})$$

Vorticity, by definition, is associated with incompressible flow. The flow cannot compress the fluid, so it must be circulatory. It follows that there must be a vorticity associated with toroidally incompressible flow. Given this vorticity, Ξ, at some time, the relationship between the vorticity and the velocity vector, and remembering that we have from equation (2.10) an expression for the divergence of the flow velocity, we have sufficient information to determine the flow velocity, $\underline{v}$, everywhere.

In order to define the vorticity at each instant in time we must refer to an equation of motion for the plasma. By assuming a local thermodynamic equilibrium in the plasma we may describe the evolution of the system in terms of changes in temperature, density and a centre of mass velocity. This leads directly to a description of the plasma in terms of fluid equations.

A more detailed discussion is presented in Chapter 5, but essentially the fluid equations result from assuming that the collision time is far shorter than any macroscopic timescale associated with the fluid motion. The rapid randomising effects of these collisions then ensure that the velocity distribution remains isotropic. Likewise, the two species present, ions and electrons, have the same temperature if the interparticle collisions are sufficiently frequent. The plasma may then be described by one fluid equations[33] of continuity:

$$\frac{\partial \rho}{\partial t} + \nabla.(\rho \underline{v}) = 0 \tag{2.13}$$

momentum:

$$\rho \frac{d\underline{v}}{dt} = -\nabla p + \underline{J} \times \underline{B} \tag{2.14}$$

energy:

$$\frac{d}{dt}(p\rho^{-\gamma}) = \frac{(\gamma - 1)}{\rho^{\gamma}} \quad (\eta J^2 - \nabla.\underline{q}) \tag{2.15}$$

where ρ is the density, p the pressure, $\underline{q}$ the heat flux vector and γ the ratio of specific heats.

In the light of the toroidal incompressibility condition (2.11) the continuity equation (2.13) may be more usefully written:

$$\frac{d}{dt}(R^2\rho) = -R^4\rho \, \nabla.\left(\frac{\underline{v}}{R^2}\right) \tag{2.16}$$

For convenience the energy equation is rewritten using the specific internal energy density, ε:

$$\frac{d}{dt}(\rho^{-(\gamma-1)}\varepsilon) = \rho^{-(\gamma-1)}\left(\frac{\eta J^2}{\rho} - \frac{\nabla.\underline{q}}{\rho}\right) \tag{2.17}$$

where $\varepsilon = \frac{nkT}{(\gamma-1)\rho}$ where n is the number density, k Boltzmann's constant and T the temperature in ^{o}K.

We are now in a position to define the vorticity and derive an expression for its time dependence. We choose an expression for the vorticity

$$\underline{\Xi} = R\nabla \times R^2\rho \, \underline{v} \tag{2.18}$$

and obtain its time dependence by taking the curl of R^2 times the

momentum equation (2.14), which is detailed in Appendix B,

$$\frac{1}{R}\frac{d\Xi}{dt} - \frac{1}{2}|\nabla R^2\rho \times \nabla v^2| = 2R|\nabla p \times \nabla R| + R(\underline{B} \cdot \nabla)RJ_\phi \qquad (2.19)$$

We do this in order to remove terms depending on gradients of the total magnetic field. It is analogous to defining a vorticity in incompressible hydrodynamics where the pressure gradient term is removed when the curl of the momentum equation is taken in order to remove the sound waves from the problem. Likewise in this case removing the magnetic field gradient terms removes the Alfven waves associated with the toroidal field, but the pressure gradient term, (the first on the right hand side of equation (2.19)) remains. Sound waves are thus still present in this model, but as we shall see later, in a modified form. The second term on the right hand side of equation (2.19) is a source of vorticity caused by Alfven waves propagating in the poloidal plane.

Finally to complete the definition of the vorticity, (2.19), the poloidal magnetic field, $\underline{B}_p$, and toroidal current, $J\phi$, must be defined. We have seen that a solenoidal vector may be expressed in terms of two scalar functions. The magnetic field may therefore be expressed in this way as:

$$\nabla.\underline{B} = 0 \qquad (2.20)$$

Hence we may write:

$$\underline{B} = \nabla\psi \times \nabla\phi \qquad (2.21)$$

If we choose to write only the poloidal magnetic field, $\underline{B}_p$, in this form then the potential ϕ is just the azimuthal coordinate. The total magnetic field may then be written

$$\underline{B} = F\nabla\phi + \nabla\psi \times \nabla\phi \tag{2.22}$$

where the first term is the toroidal and the second the poloidal magnetic field. The requirement (2.20) demands that ∇F is perpendicular to $\nabla\phi$ i.e. F is the flux function of the total current in the poloidal plane, including currents in external coils, that produce the toroidal field. The potential ψ, together with the azimuth ϕ, determine the poloidal field, and ψ is therefore known as the poloidal flux. In an identical manner to (2.12) ψ may be related to the vector potential, $\underline{A}$:

$$\underline{A} = \frac{\psi}{R}\underline{e}\phi \tag{2.23}$$

Appendix C shows that using Amperes law:

$$\mu_0\underline{J} = \nabla \times \underline{B} \tag{2.24}$$

the toroidal current density $J\phi$ may be expressed:

$$\mu_0 R\, J\phi = -\Delta^*\psi \tag{2.25}$$

where Δ^* is the Grad-Shafranov operator, and:

$$\Delta^*\psi = R^2\left(\nabla.\frac{\nabla\psi}{R}\right) \tag{2.26}$$

which is the toroidal form of curl curl $\underline{A}$.

Hence the poloidal magnetic field and toroidal current density may be written totally in terms of the poloidal flux, ψ.

The evolution of ψ may be deduced from Faraday's and Ohms Laws, (2.6) and (2.8)

$$\frac{\partial\underline{B}}{\partial t} = \nabla \times \underline{v} \times \underline{B} - \nabla \times (\eta\underline{J})$$

Using (2.23) we arrive at

$$\frac{d\psi}{dt} = -\eta R J_\phi \qquad (2.27)$$

2.1.4 Summary

The model is thus complete. Summarizing, we initially find a vorticity (2.19) which by solving an elliptic equation (formed from (2.18) and (2.12)) defines a stream function ζ and a flow velocity. Density (2.16), temperature (2.17) and poloidal flux (2.27) are then altered by this flow velocity. Poloidal magnetic field (2.21) and toroidal current density (2.25) are then redefined and a new value of the vorticity is found. This is represented diagramatically in Fig. 2.1.

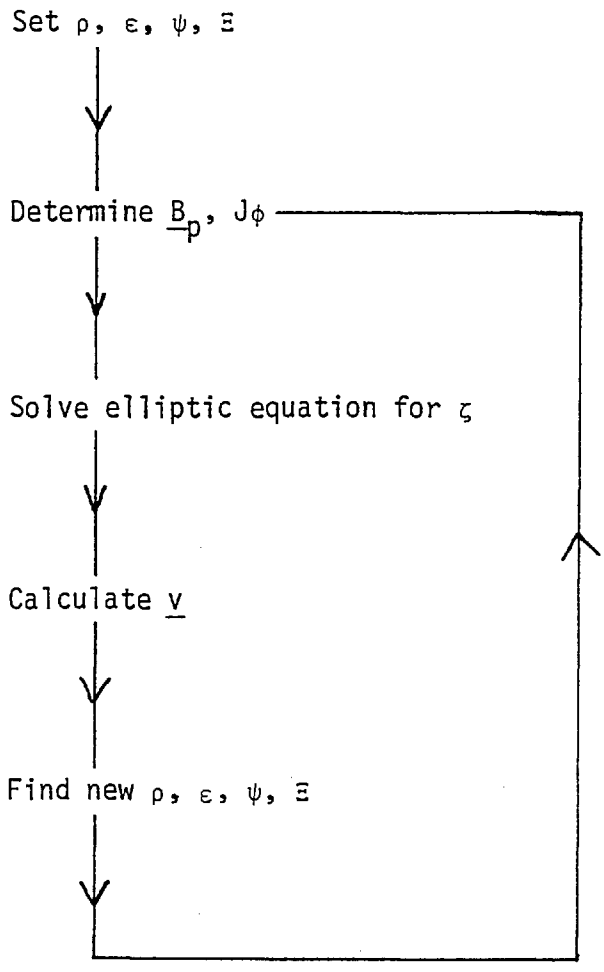

Fig. 2.1 Diagrammatic representation of the ideal model.

2.2 PERFECT CONDUCTIVITY

In the limit of low beta and infinite conductivity, the equations that form the model of the last section reduce to a considerably simpler form which leads to an obvious choice for a coordinate system in which to solve these equations.

Low beta, zero resistivity and heat flux allow equations (2.16) and (2.27) to be written:

$$\frac{d}{dt}\ (R^2\rho) \ = \ 0 \qquad (2.28)$$

$$\frac{d\psi}{dt} \ = \ 0 \qquad (2.29)$$

and from (2.28) it follows that (2.17) becomes:

$$\frac{d}{dt}\ (\varepsilon\ R^{2(\gamma-1)}) \ = \ 0 \qquad (2.30)$$

The full set of simplified equations are thus the three above, and equations (2.10), (2.18), (2.19) and (2.25) that define the vorticity, flow velocity and current density.

Equation (2.29) states that for zero resistivity surfaces of constant ψ move with the fluid. From (2.22) the poloidal magnetic field, $\underline{B}_p$, is always perpendicular to $\nabla\psi$ and $\nabla\phi$ so therefore lies in surfaces of constant ψ known as a magnetic surface. Thus (2.29) just states that for a perfectly conducting plasma the magnetic field lines are frozen into the plasma. This points to an alternative, natural, coordinate system in which to express the model.

2.3 CHOICE OF COORDINATE SYSTEM

2.3.1 Basic requirements

A basic requirement of any coordinate system is that there exists a one to one mapping between all the points in a region and the triad of values (f_1, g_1, h_1) where f, g and h are three families of parameters that define the coordinate system. There must exist therefore three one parameter families of surfaces, f, g, h for a coordinate system to exist.

We now choose f, so that it varies along some vector field $\underline{t}(\underline{r})$:

$$\underline{t} = b\nabla f$$

where b is a constant. Thus $\underline{t}(\underline{r})$ is everywhere parallel to ∇f and normal to the level surfaces f = constant. However, for such a vector field $\underline{t}(\underline{r})$ to exist we require that $\underline{t}$ be complex-lamellar:

$$\underline{t} \cdot \text{curl } \underline{t} = 0 \qquad (2.31)$$

This is easily seen by substituting for $\underline{t}$ to give:

$$b\nabla f . \nabla b \times \nabla f = 0$$

The determination of the scalars b and f is known as Pfaff's problem[34].

The condition (2.31) on $\underline{t}$ is of considerable interest in the restriction it places on the nature of $\underline{t}$. If we try to construct a coordinate such that one coordinate lies along the magnetic field $\underline{B}$ we see immediately that (2.31) becomes:

$$\underline{B} \cdot \text{curl } \underline{B} = 0$$

or

$$\underline{B} \cdot \underline{J} = 0$$

which is not generally true. Thus only in very special circumstances

may we construct a coordinate system in which one direction is always parallel to the magnetic field.

The quantity (2.31) is known as the abnormality and is a widely used term in hydrodynamics[35] where much theoretical work has analysed vector fields with varying degrees of abnormality.

2.3.2 Compatibility with boundary conditions

Boundary conditions are another important consideration when choosing a coordinate system. In a tokamak the boundary is defined by the limiter or conducting casing that is usually circular, or can be elliptical or D-shaped. Fitting boundary conditions on a coordinate system such as the (R, ϕ, z) system used so far would be extremely difficult. In fact the only simple solution is to allow one coordinate surface to coincide with the boundary. If the casing is assumed to be perfectly conducting then it will coincide with a magnetic surface.

2.3.3 Mesh interaction with solutions

It is well established that equations of the advective type, for example the simplified set, (2.28) to (2.30) can have solutions that are strongly anisotropic. In these cases the mesh can seriously affect the solution obtained. This is caused by the presence of terms of the form

$$\underline{K} \cdot \nabla w$$

where $\underline{K}$ is the magnetic field or flow velocity and w some physical variable. The problem is caused by symmetries in the mesh interacting in the solution with symmetries of the problem. If, however, $\underline{K}$ is aligned along one coordinate direction this problem does not occur[36]. The poloidal magnetic field lies naturally in the magnetic surface, and the flow velocity, as we shall see later, lies predominantly along the field lines.

2.3.4 Resolution

Finally the spacing of the mesh must be sufficiently small to resolve the detail of localised phenomena. If the mesh spacing is constant then to give the correct resolution at one place requires that there are other regions where the resolution is needlessly high. A coordinate system based on a physical variable that changes as the system evolves will give a denser mesh where the variable is changing more quickly.

2.3.5 Natural coordinates

These four main requirements point towards using a natural coordinate system, in the sense that surfaces on which one physical variable remains constant is used as one of the coordinates.

The first requirement restrains us from using the total magnetic field as one coordinate direction, but we can use the surfaces of constant ψ, magnetic surfaces, and axisymmetry to construct two of the three coordinates.

The use of magnetic surfaces as one coordinate ensures that the boundary is treated easily, interaction of advective terms with the mesh is minimised, and as these surfaces move with the fluid (Eq. (2.30)) resolution is provided where needed for the other physical variables (Eqs. (2.28), (2.29)) frozen into the fluid. The choice of a natural coordinate such as ψ which moves with the fluid means that we are no longer describing the system in an Eulerian manner but in a Lagrangian one. (Normally an Eulerian frame is refered to as the stationary laboratory frame, and a Lagrangian frame as that moving with the fluid. These terms are however, not historically correct[35] as the Lagrangian description was due initially to Euler. However, following conventions we shall leave the definitions as they stand). Any problems associated

with coordinate lines crossing as a result of the motion are avoided by choosing a physical variable as one coordinate. In this "waterbag"[37] description, no two waterbags can cross and therefore topology is preserved.

Finally we must construct the third coordinate. Already we have the magnetic surfaces ψ and the azimuth ϕ, so in principle any third family of one parameter surfaces, χ, would do. In general an element of length in the poloidal plane, ds is given by:

$$(ds)^2 = g_{\chi\chi}\, d\chi^2 + 2g_{\chi\psi}\, d\chi d\psi + g_{\psi\psi}\, d\psi^2$$

where g_{ij} is the metric tensor. In order to simplify, for example gradients, we choose χ to be orthogonal to ψ, in which case the off diagonal terms of the metric tensor vanish and the length element may be written:

$$(ds)^2 = (h_\chi\, d\chi)^2 + (h_\psi\, d\psi)^2 \qquad (2.32)$$

The mesh (χ,ψ) moves with the fluid and will become non-orthogonal so (2.32) will cease to apply. However, after the mesh has been moved we reconstruct the χ lines so that it is once again orthogonal. This is facilitated by the orthogonalising package ORTHO[38].

Thus from an Eulerian (R, ϕ, z) mesh, we proceed to a Lagrangian (χ, ψ, ϕ) mesh, Fig. 2.2. Considering the simplified set of equations, (2.28) to (2.30) $R^2\rho$ and $\varepsilon R^{2(\gamma-1)}$ remain constant on the ψ surfaces. The vorticity Ξ determines the velocity of the ψ surfaces and only now is an advective equation solved, for the advection of the ψ surfaces relative to laboratory space. A new metric is therefore defined, and the new vorticity found.

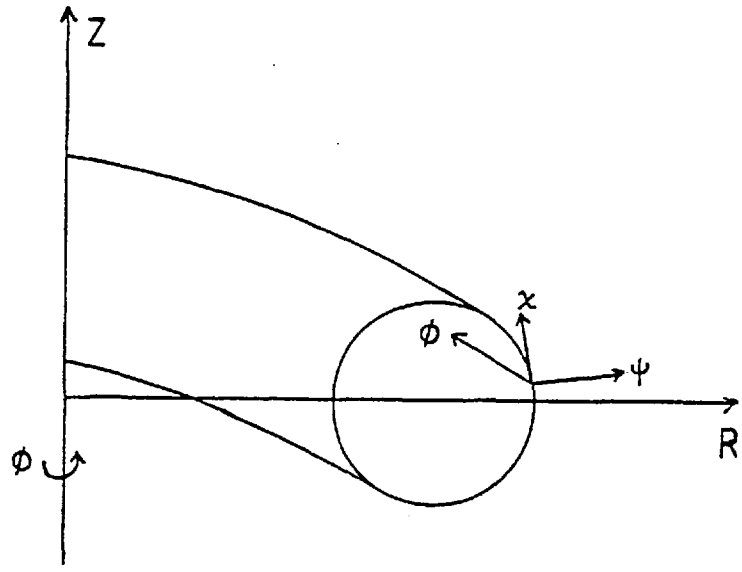

Fig. 2.2 Cylindrical (R,ϕ,z) and natural (χ,ψ,ϕ) coordinate systems.

2.4 HIGHER ORDER BETA AND FINITE RESISTIVITY CORRECTIONS

We have already seen that to the lowest order in beta the equation (2.9) for the variations in total magnetic field yields the condition (2.10). To the next order in $\beta^{\frac{1}{2}}$ and in the presence of resistivity (Appendix A) Eq. (2.10) is replaced by:

$$\nabla.\left(\frac{\nu}{R^2}\right) = \frac{1}{RB\phi}\ \underline{B}.\nabla v\phi - \frac{\eta}{\mu_o}\frac{1}{R^3B\phi}\ \Delta^*RB\phi + \frac{1}{R^2B\phi}\frac{\nabla\eta}{\mu_o}.\nabla B\phi \tag{2.33}$$

Consequently (2.12) becomes:

$$v_R = R\frac{\partial\zeta}{\partial z} + \frac{v\phi B_R}{B\phi} + \frac{\eta}{\mu_o}\frac{1}{RB\phi}\frac{\partial}{\partial R}\ RB\phi \tag{2.34}$$

$$v_z = -R\frac{\partial\zeta}{\partial R} + \frac{v\phi B_z}{B\phi} + \frac{\eta}{\mu_o}\frac{1}{RB\phi}\frac{\partial}{\partial z}\ RB\phi$$

which with Ampere's Law (2.24) and the momentum equation (2.14) give

$$v_R = R\frac{\partial\zeta}{\partial z} + \frac{v\phi B_R}{B\phi} - \frac{\eta}{B\phi^2}\left[\frac{\partial p}{\partial R} - J_\phi B_z + \rho\left(\frac{\partial}{\partial R}\left(\frac{v_R^2 + v_z^2}{2}\right) - \frac{v\phi^2}{R} + v_z\,\xi + \frac{\partial v_R}{\partial t}\right)\right]$$

$$v_z = -R\frac{\partial\zeta}{\partial R} + \frac{v\phi B_z}{B\phi} - \frac{\eta}{B\phi^2}\left[\frac{\partial p}{\partial z} + J_\phi B_R + \rho\left(\frac{\partial}{\partial z}\left(\frac{v_R^2 + v_z^2}{2}\right) - v_R\,\xi + \frac{\partial v_z}{\partial t}\right)\right] \tag{2.35}$$

where $\xi = \frac{\partial v_R}{\partial z} - \frac{\partial v_z}{\partial R}$

For v_R, v_ϕ and v_z on the right hand side of (2.35) we use the zero order

approximations (2.12), and (Appendix A (A8)):

$$\frac{dv_\phi}{dt} = \frac{-\underline{B}.\nabla p}{\rho B_\phi} - \beta^{\frac{1}{2}} \frac{d}{dt} (v_R^2 + v_Z^2)^{\frac{1}{2}} \tag{2.36}$$

The full set of equations to order β may therefore be compiled:

$$\nabla.\frac{\underline{v}}{R^2} = \frac{1}{RB_\phi}\left[\frac{\partial}{\partial R}\left(v_\phi B_R + \frac{\eta}{\mu_0 R}\frac{\partial}{\partial R} RB_\phi\right) + \frac{\partial}{\partial z}\left(v_\phi B_Z + \frac{\eta}{\mu_0 R}\frac{\partial}{\partial z} RB_\phi\right)\right] \tag{2.37}$$

$$v_R = R\frac{\partial \zeta}{\partial z} + v_\phi \frac{B_R}{B\phi} - \frac{\eta}{B\phi^2}\left[\frac{\partial p}{\partial R} - J_\phi B_Z + \rho\left(\frac{\partial}{\partial R}\left(\frac{v_R^2 + v_Z^2}{2}\right) - \frac{v_\phi^2}{R} + v_Z \xi + \frac{\partial v_R}{\partial t}\right)\right] \tag{2.38}$$

$$v_Z = -R\frac{\partial \zeta}{\partial R} + v_\phi \frac{B_Z}{B\phi} - \frac{\eta}{B\phi^2}\left[\frac{\partial p}{\partial z} + J\phi B_R + \rho\left(\frac{\partial}{\partial z}\left(\frac{v_R^2 + v_Z^2}{2}\right) - v_R \xi + \frac{\partial v_Z}{\partial t}\right)\right] \tag{2.39}$$

$$\Xi = |R \nabla \times R^2\rho \underline{v}| \tag{2.40}$$

$$\frac{d\Xi}{dt} = \frac{R}{2}|\nabla R^2\rho \times \nabla v^2| + 2R^2\frac{\partial p}{\partial z} + R^2(\underline{B}.\nabla) RJ_\phi - (R^2\nabla.\frac{\underline{v}}{R^2})\Xi \tag{2.41}$$

$$\frac{d}{dt}(R^2\rho) = -R^2 \nabla.(\frac{\underline{v}}{R^2}) \quad R^2\rho \tag{2.42}$$

$$\frac{d}{dt}(R^{2(\gamma-1)}\varepsilon) = -(R^2 \nabla.\frac{\underline{v}}{R^2}) R^{2(\gamma-1)}\varepsilon + \rho^{-(\gamma-1)}\left(\frac{\eta J^2}{\rho} - \frac{\nabla.\underline{q}}{\rho}\right) \tag{2.43}$$

$$\frac{d\psi}{dt} = -\eta RJ_\phi \tag{2.44}$$

$$\mu_0 RJ_\phi = -\Delta^*\psi \tag{2.45}$$

2.5 INTERPRETATION

It is instructive initially to look at the simplified set of equations, (2.28) to (2.30) and analyse their behaviour in the absence of resistivity and finite beta effects. These equations state that certain dependent variables are frozen into the fluid. In the fluid frame, ψ, $R^2\rho$ and $R^{2(\gamma-1)}\varepsilon$ are all conserved. We have looked at the implications of ψ being constant in the fluid frame already. The implications of the other conserved quantities are quite interesting. Conservation of mass and energy imply that:

$$\rho \propto {}^{1}/_{R^2}$$

and

$$\varepsilon \propto {}^{1}/_{R^{2(\gamma-1)}}$$

It follows that if the position of the plasma is altered with respect to the major radius the plasma is compressed and compressional heating takes place. This occurs in the ATC tokamak experiment[39]. For $\gamma = {}^{5}/_{3}$ the above compression ratios agree with those found in the ATC experiment.

It was mentioned earlier that the terms contributing to the generation of vorticity (2.19) were sound waves, and poloidal Alfven waves. This is seen more clearly if Fourier components are considered.

We use the simplified equations and (2.30) rewritten in terms of the pressure:

$$\frac{dp}{dt} = -p\gamma\nabla.\underline{v}$$

in cylindrical components (R,ϕ,z):

$$\frac{\partial v_R}{\partial R} + \frac{\partial v_z}{\partial z} - \frac{v_R}{R} = 0$$

$$\Xi = R^3\left(\frac{\partial}{\partial z}\rho v_R - \frac{\partial}{\partial R}\rho v_z - \frac{2\rho v_z}{R}\right)$$

$$\frac{d\Xi}{dt} = 2R^2 \frac{\partial p}{\partial z} + R^2 B_R \frac{\partial}{\partial R} RJ_\phi + R^2 B_Z \frac{\partial}{\partial z} RJ_\phi$$

$$- \frac{R}{2} \frac{\partial v^2}{\partial z} \frac{\partial}{\partial R} R^2\rho + \frac{R}{2} \frac{\partial v^2}{\partial R} \frac{\partial R^2\rho}{\partial z}$$

$$B_R = -\frac{1}{R} \frac{\partial \psi}{\partial z} \; ; \; B_Z = \frac{1}{R} \frac{\partial \psi}{\partial R} \; ; \; \frac{\partial \psi}{\partial t} = v_R \frac{\partial \psi}{\partial R} + v_Z \frac{\partial \psi}{\partial z}$$

$$\mu_o RJ_\phi = \frac{2}{R} \frac{\partial \psi}{\partial R} - \frac{1}{R} \frac{\partial}{\partial R} \left(R \frac{\partial \psi}{\partial R} \right) - \frac{\partial^2 \psi}{\partial z^2}$$

$$\frac{dp}{dt} = -\gamma p \left(\frac{\partial v_R}{\partial R} + \frac{\partial v_z}{\partial z} + \frac{v_R}{R} \right)$$

To include sound waves we consider perturbations in the z direction of the form $e^{i(kz + \omega t)}$ and obtain, neglecting the Alfven terms

$$ikv_z - \frac{v_R}{R} = 0$$

$$\Xi = 2R^3 \rho v_R \, ik - 2\rho R^2 v_z$$

$$i\omega \Xi = 2R^2 ikp - R^2 \rho ikv^2$$

$$i\omega p = -\gamma p \left(ikv_z + \frac{v_R}{R} \right)$$

These rearrange to give a dispersion relation:

$$\omega^2 \left[\left(1 - \frac{1}{4\gamma} \right) + \left(1 + \frac{1}{4\gamma} \right) k^2 R^2 \right] = 2 \frac{\gamma p}{\rho} k^2$$

Hence we find:

$$\omega = \pm k \sqrt{2C_s^2 / f}$$

where:

$$f = \left(\left(1 - {}^{1}/_{4\gamma} \right) + \left(1 + {}^{1}/_{4\gamma} \right) k^2 R^2 \right)$$

and the sound speed:

$$C_s = \sqrt{\gamma p/\rho}$$

Equation (2.19) therefore gives rise to sound waves with a phase velocity:

$$C_s^1 = \frac{\omega}{k} = \sqrt{2C_s^2/f} \qquad (2.46)$$

These sound waves arise from the terms $2R\frac{\partial p}{\partial z}$ and $\frac{1}{2}|\nabla R^2\rho \times \nabla v^2|$ in (2.19). The first comes from the pressure gradient in the momentum equation, and the second arises because the operators $\frac{d}{dt}$ and curl do not commute. These sound waves are dispersive as f is a function of k. For k approximately equal to $\frac{1}{a}$ where a is the minor radius, we note that

$$C_s^1 \simeq C_s/\sqrt{1 + R^2/a^2}$$

This is the longest wavelength that can be accommodated in the poloidal plane. For shorter wavelengths, k is larger so C_s^1 decreases and as k becomes very large:

$$C_s^1 \to 0$$

The modified sound speed, C_s^1, is therefore always less than the normal sound speed. As the major radius of the torus, R is increased, C_s^1 decreases until in the limit as $R \to \infty$, $C_s^1 \to 0$. This is to be expected because in this limit the torus is a cylinder and normal incompressible hydrodynamics apply where sound waves are removed from the equations.

If now the sound waves are omitted from (2.19) and once again Fourier components are considered, proceeding in a similar manner to before a dispersion relation is obtained for the poloidal Alfven waves, defining a modified Alfven speed:

$$C_A^1 = \frac{\omega}{k} = \frac{C_A}{\sqrt{2g}} \tag{2.47}$$

where

$$g = 1 + k^2R^2$$

and

$$C_A^2 = B_R^2/\mu_o\rho$$

This describes the speed of Alfven waves propagating in the poloidal plane. The longest wavelength accommodated will define the largest value of g and therefore the fastest poloidal Alfven speed. This wavelength will be of the order of the minor radius, a. Thus

$$g = 1 + (\frac{R}{a})^2$$

and the modified Alfven speed will always be less than the normal Alfven speed. As R is varied the modified Alfven speed behaves in the same way as the modified sound speed.

The introduction of terms to the next order in $\beta^{\frac{1}{2}}$ into this Fourier analysis indicates the nature of these terms and their effects on the plasma.

The toroidal velocity modifies the toroidal incompressibility condition:

$$\nabla.\frac{\underline{v}}{R^2} = \frac{1}{RB_\phi}\ \underline{B}.\nabla v_\phi$$

This introduces a term into the sound wave dispersion equation of order $\beta^{\frac{1}{2}}\ C_s$ and into the Alfven wave dispersion equation of order $\beta^{\frac{1}{2}}\ C_A$. As explained in Appendix A, the importance of these two effects depends upon the sound mach number. In a supersonic regime the modification to the Alfven wave dispersion relation is the more important, and models the effect of modifications of the toroidal magnetic field on the toroidal

flow.

In a subsonic regime the modification to the sound wave dispersion equation is the most dominant. This term therefore models the propagation of sound waves around the torus in the toroidal direction. These small compressive corrections may be included with those arising from the inclusion of finite resistivity.

Consider now the full equations containing finite resistivity, (2.37) to (2.45). We note now that the incompressibility condition (2.37) is no longer true but contains small compressive corrections. The conservation equations for density and specific internal energy are hence modified, (2.42) and (2.43), and resistivity allows the field to slip through the fluid, as now the frozen in condition no longer holds, (2.44), as well as adding a Joule heating term to the energy equation, (2.43). Thermal conductivity is included, but this will be dealt with later in greater detail.

The compressive corrections occur because in the presence of resistivity the plasma is no longer completely toroidally incompressible. The poloidal currents that balance the force of the induced toroidal current and its self field decay with resistivity present which leads to an imbalance in the equilibrium, and hence allows a slight compressive flow.

2.6 SUMMARY

In essence the model may be described as follows. Equations for the time dependence of density, internal energy and vorticity (2.41), (2.42) and (2.43) are solved in the fluid frame. The vorticity arises because to zeroth order in $\sqrt{\beta}$ the plasma is toroidally incompressible, (2.37). This leads to a velocity stream function, from which a flow velocity may be derived, (2.38), (2.39) and (2.40). The fluid frame is then moved with respect to the laboratory frame with this flow velocity.

When the resistivity is small the magnetic surfaces remain fixed in the fluid frame (2.44). This results in these surfaces being chosen as one of the fluid coordinates.

If, however, the resistivity and plasma beta is finite, the magnetic surfaces move with respect to the fluid, and the plasma is no longer toroidally incompressible, which results in a compressive flow, and hence corrections to density, energy and vorticity.

The current density and magnetic field are found self consistently from the metric of the magnetic surface coordinate system.

The above is best pictured in the form of a flow diagram by extending Fig. 2.1:

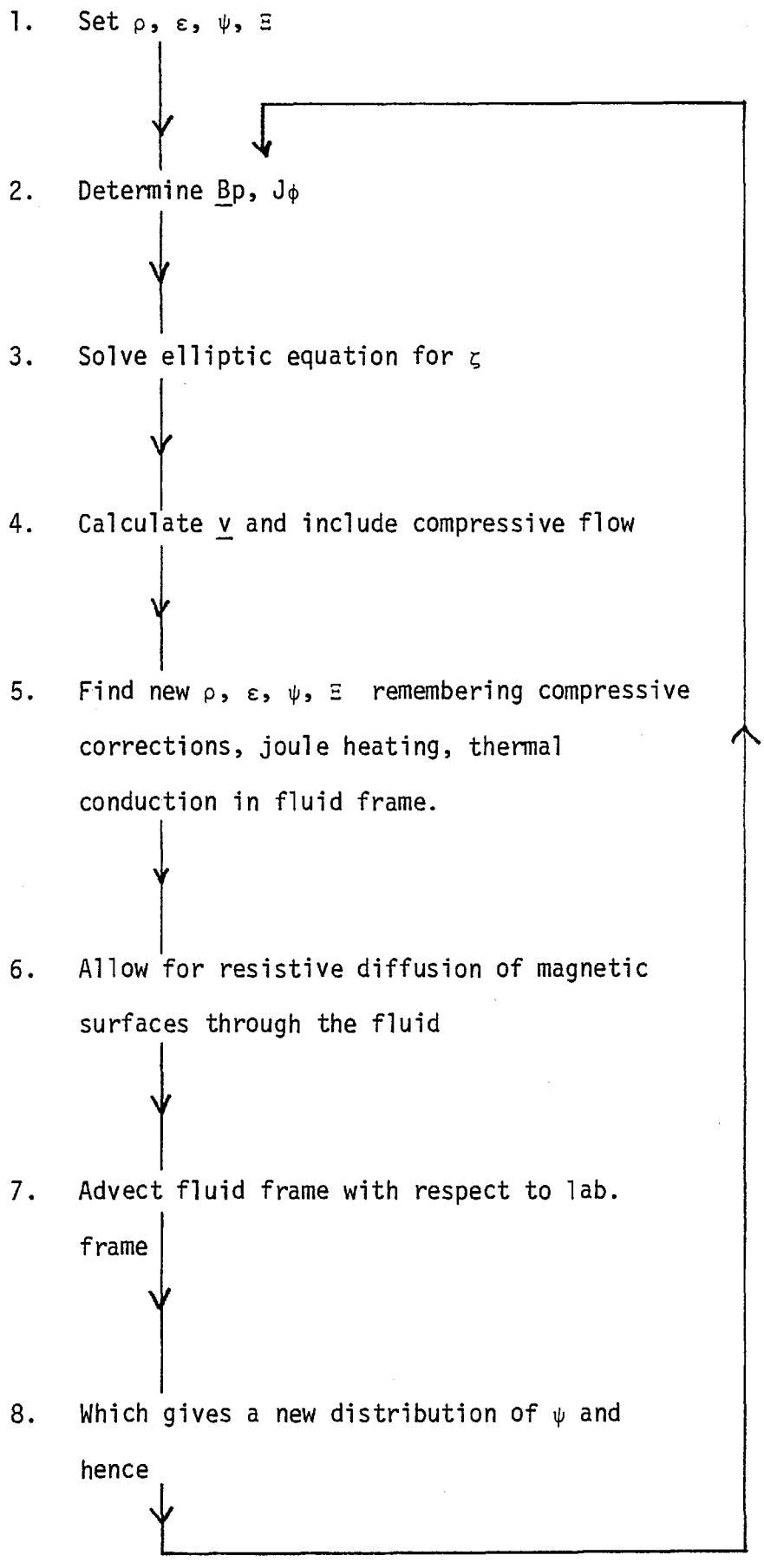

Fig. 2.3 Summary of the full model.

CHAPTER 3

THE NUMERICAL MODEL

In this chapter we describe the initiation and main evolutionary cycle of the computer code, TICTOK, based on the physical model described in the last chapter. A new method which sums the mesh area and volume accurately, and that leads to good energy conservation is described. Finally the orthogonalization method, ORTHO, is reviewed and discussed.

3.1 INITIATION

At all times in the simulation it is assumed that the plasma is fully ionised. This can be effected initially by some ionising pre-pulse brought about by a rf or microwave generator. Initial conditions, therefore, assume a uniform temperature plasma at rest with a prescribed density distribution. In low temperature runs a flat density profile is prescribed, whereas, at high initial temperatures the density profile is calculated so that the pressure gradient approximately balances the $\underline{J} \times \underline{B}$ force.

In the low temperature cases the initial current density distribution is assumed to take the form of the toroidal electric field that produces the toroidal current. This is discussed in detail in the next section. This initial condition ensures that the current density is matched to the boundary condition, which demands that the outer surface is a contour of poloidal flux. This arises if we assume that the wall coincides with a perfectly conducting copper casing.

At high initial temperatures the initial current density distribution is calculated by prescribing approximately the poloidal beta, temperature and loop voltage of the plasma. This will be dealt with more fully in a later chapter.

3.1.1 Toroidal current density distribution

The toroidal current in tokamaks, which produces the poloidal field, is induced in the plasma by a transformer network. An iron core surrounds the plasma and vacuum vessel (Fig. 1.1). The primary of the transformer is connected to capacitor banks; the secondary winding is the plasma itself.

Current in the primary causes a changing magnetic field that is confined to the iron core. This produces an electric field whose curl

is virtually zero everywhere except inside the iron core. Thus outside the iron core a toroidal electric field is produced that varies inversely as the major radius.

Initially it is assumed that the plasma is fully ionised, and if the initial temperature is chosen as uniform, the current density distribution will have the same form as the electric field. In order to define our initial coordinate system which is based on the magnetic surfaces, we must find surfaces that correspond to such a current distribution.

Now:

$$\Delta^*\psi = -\mu_0 RJ\phi$$

where Δ^* is the Grad-Shafranov operator. If this is written in toroidal coordinates, Fig. 3.1, the result is:

$$\frac{1}{r}\frac{\partial}{\partial r}\left(r\frac{\partial\psi}{\partial r}\right) + \frac{1}{r^2}\frac{\partial^2\psi}{\partial\theta^2} - \frac{1}{R}\left(\cos\theta\frac{\partial\psi}{\partial r} - \frac{\sin\theta}{r}\frac{\partial\psi}{\partial\theta}\right) = -\mu_0 RJ\phi$$

If

$$\varepsilon = r/R_0$$

where R_0 is the radius of the minor axis and

$$J_c = \mu_0 RJ\phi$$

which, because $J_\phi \propto 1/R$, is a constant. The final rearrangement is:

$$\frac{\partial}{\partial r}\left(r\frac{\partial\psi}{\partial r}\right) + \frac{1}{r}\frac{\partial^2\psi}{\partial\theta^2} - \frac{\varepsilon}{1+\varepsilon\cos\theta}\left(\cos\theta\frac{\partial\psi}{\partial r} - \frac{\sin\theta}{r}\frac{\partial\psi}{\partial\theta}\right)$$

$$= -J_c r \qquad (3.1)$$

This may now be solved by employing an expansion in the inverse aspect

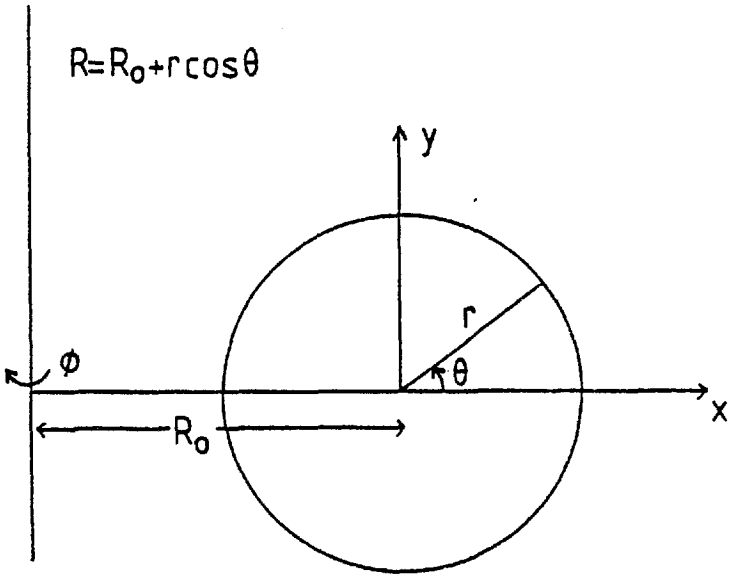

Fig. 3.1 Toroidal coordinate system.

ratio ε. By writing

$$\psi = \psi_0(r) + \psi_1(r,\theta) \tag{3.2}$$

where $\psi_1 \sim \varepsilon \psi_0$, the lowest order of Eq. (3.1) yields:

$$\psi_0 = -\tfrac{1}{4} J_c r^2 + C$$

Now we choose

$$\psi_1(r,\theta) = f(r) \cos\theta$$

which when substituted in Eq. (3.1) gives:

$$\psi_1 = -\left(\frac{J_c r^3}{16R_0} + Dr\right) \cos\theta$$

where C and D are constants. D is chosen such that ψ on the outer

surface, at the wall (where r = a) has a circular cross section and therefore no θ dependence. The absolute value of ψ is given by C, which as the vector potential is only even defined up to an arbitrary constant, may be chosen so that ψ(a) = 0. Thus

$$D = \frac{J_c\, a^2}{16R_o}, \qquad C = \frac{J_c\, a^2}{4}$$

and

$$\psi = \frac{J_c\, a^2}{4}\left(1 - \frac{r^2}{a^2}\right)\left(1 + \frac{r}{4R_o}\cos\theta\right) \tag{3.3}$$

to first order in the inverse aspect ratio.

In order to obtain the equation of a surface of constant ψ this solution must be inverted to give r in terms of ψ and θ. The result is a cubic equation that is rather tedious to solve analytically:

$$\frac{\cos\theta\; r^3}{4R_o} + r^2 - a^2\,\frac{\cos\theta}{4R_o}\, r + \frac{4\psi}{J_c} - a^2 = 0 \tag{3.4}$$

Instead the solution is found numerically using Newton's method. This is well known but may be sumarized as follows: if r_n is a guess for f(r) = 0 then

$$r_{n+1} = r_n - \frac{f(r_n)}{f'(r_n)}$$

is a better guess.

The numerical solution, however, is not completely straightforward as may be seen from Eq. (3.3). The maximum value of ψ does not occur at the origin of the (r,θ) coordinate system, but at a point on θ = 0 given by

$$\delta = \frac{4R_o}{3}\left[\left(\frac{3\, a^2}{16R_o^2} + 1\right)^{\frac{1}{2}} - 1\right] \tag{3.5}$$

Therefore if Eq. (3.4) is solved for r in this region, for a particular value of θ, r is multivalued. This may be overcome by writing Eq. (3.4) in a coordinate system centred at $r = \delta$, which shall be called (r',θ'). These two systems are related by

$$x = r\cos\theta = r'\cos\theta' + \delta$$
$$y = r\sin\theta = r'\sin\theta'$$

where x and y are shown in Fig. 3.1. This leads to

$$r = (r'^2 + 2r'\,\delta\cos\theta' + \delta^2)^{\frac{1}{2}}$$
$$\theta = \tan^{-1}\left(\frac{r'\sin\theta'}{r'\cos\theta' + \delta}\right)$$

Thus Newtons method solves, for a constant specified value of θ':

$$f(r(r',\theta'),\ \theta(r',\theta')) = 0$$

where $f'(r,\theta)$ is given by:

$$\left.\frac{df}{dr'}\right|_{\theta'} = \left.\frac{\partial f}{\partial r}\right|_{\theta}\left.\frac{dr}{dr'}\right|_{\theta} + \left.\frac{\partial f}{\partial \theta}\right|_{r}\left.\frac{d\theta}{dr'}\right|_{\theta'}$$

A first guess for r' is obtained using

$$r' = \left(a^2 - \frac{4\psi}{J_c}\right)^{\frac{1}{2}}$$

for

$$\frac{4\psi}{J_c} < a^2$$

or:

$$r' = \left(\frac{4\psi}{J_c} - a^2\right)\frac{4R_o}{a^2}$$

when

$$\frac{4\psi}{J_c} > a^2$$

Solutions may be obtained in two ways. Firstly, by choosing values of ψ equally spaced between zero and ψ_{max} (where ψ_{max} is obtained by inserting Eq. (3.5) into Eq. (3.3)) surfaces are obtained that are spaced equally in ψ. Secondly, solutions that are equally spaced in r (in one direction, usually $\theta = 0$) may be obtained by calculating the necessary value of $\frac{4\psi}{J_c a^2}$ from

$$\frac{4\psi}{J_c a^2} = (1 - \frac{r^2}{a^2})(1 + \frac{r}{4R_o})$$

and then using this value to obtain a first guess for r'. It must, however, be noted that as the surfaces are now no longer equally spaced in ψ this may not be used as the coordinate perpendicular to the surfaces, i.e. in the direction of $\nabla\psi$. The coordinate is denoted now by Ψ where

$$\nabla\psi = \frac{\partial\psi}{\partial\Psi} \nabla\Psi$$

where the increment of Ψ is equal between the magnetic surfaces.

The exact form of $\mu_o RJ_\phi$ due to a first order expansion in ε may be calculated analytically. The first order solution for ψ, Eq. (3.3) is substituted into Eq. (3.1) and an expression for $\mu_o RJ_\phi$ in terms of r, θ and the initial specified value of J_c is readily obtained.

$$\mu_o RJ_\phi = J_c (1 + \frac{a^2}{16R_o R} (1 - \frac{r^2}{a^2}) + \frac{3r^2 \cos^2\theta}{8R_o R}) \qquad (3.6)$$

This agrees very well with that found numerically. Fig. 3.2 shows the initial ψ surfaces and the distribution of $\mu_o RJ_\phi$ to which they correspond. Notice there are peaks of $\mu_o RJ_\phi$ on the axis of symmetry at $\theta = 0$ and $\theta = \pi$. These arise from the $\cos^2\theta$ term in Eq. (3.6). The peak at $\theta = \pi$ is slightly larger as R is smaller there. The amount by which $\mu_o RJ_\phi$ deviates from a constant corresponds to an error of order ε^2,

which is consistent with the first order scheme.

The general shape of the ψ distribution depends entirely on the sign of J_c. If J_c is positive then ψ peaks on the magnetic axis, and if J_c is negative then ψ is a minimum there. This is only a reflection of the sign of the vector potential A_ϕ relative to the toroidal current density J_ϕ. Simple vector considerations require them both to be of the same sense.

Computationally the procedure for finding the initial current distribution is as follows: the positions of the magnetic surfaces that correspond to a flat distribution of $\mu_0 RJ_\phi$ are found using a first order expansion in ε. The distribution of $\mu_0 RJ_\phi$ is then calculated, as it is at later times in the simulation using the Grad-Shafranov operator.

The quantity $\mu_0 RJ_\phi$ is therefore well defined over the whole mesh except at the outer surface where Eq. (C8) may not be differenced exactly. At later times in the simulation the current density at this outer surface is calculated from the toroidal electric field. Initially, however, the electric field

$$\frac{\partial \psi}{\partial t} = RE_\phi$$

is not known on the outer surface so we have to resort to another method of calculating the initial current density there.

Fig. 3.2 Initial distribution of the magnetic surfaces ψ and toroidal current density $\mu_0 RJ_\phi$ for magnetic surfaces spaced equally in r at $\theta = 0$. The major axis is to the left.

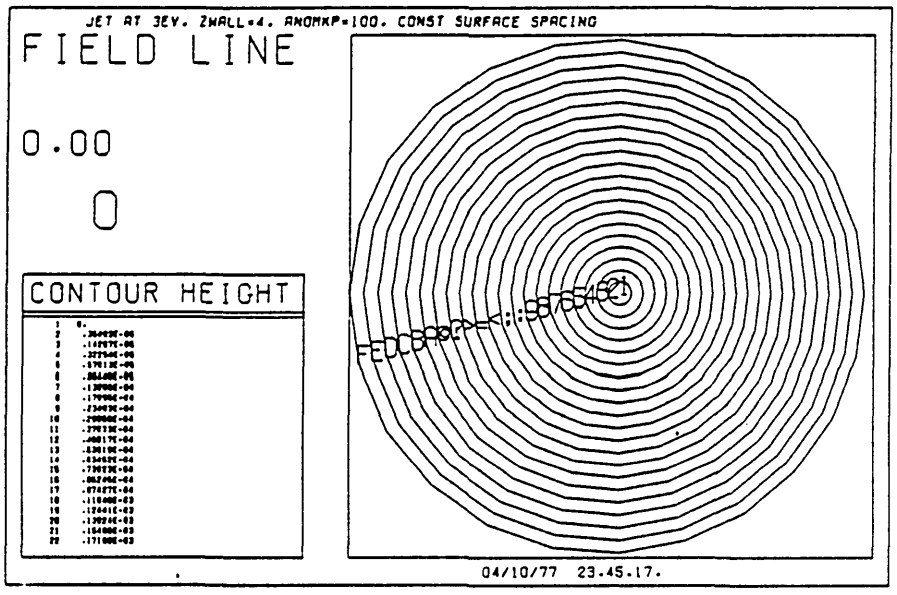
JET AT 3EV. ZWALL=4. ANOMKP=100. CONST SURFACE SPACING
FIELD LINE
0.00
0
CONTOUR HEIGHT
04/10/77 23.45.17.

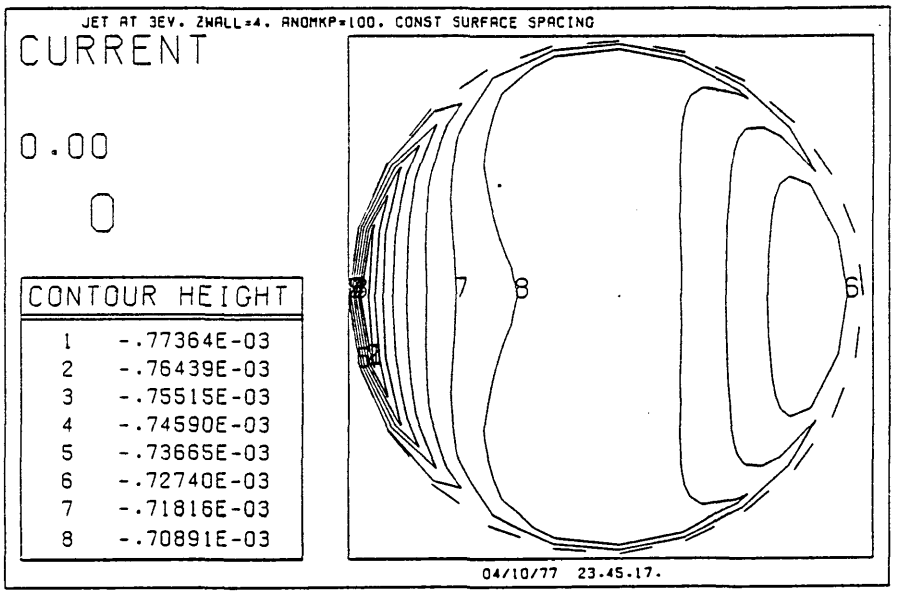
JET AT 3EV. ZWALL=4. ANOMKP=100. CONST SURFACE SPACING
CURRENT
0.00
0
CONTOUR HEIGHT
1 -.77364E-03
2 -.76439E-03
3 -.75515E-03
4 -.74590E-03
5 -.73665E-03
6 -.72740E-03
7 -.71816E-03
8 -.70891E-03
04/10/77 23.45.17.

Changes with time of the total current always affect the current density distribution at the surface of a conductor[40]. Using Maxwells equations and Ohms Law at the outer surface where $\underline{v} \times \underline{B} = 0$ we arrive at

$$\mu_o \frac{\partial J_\phi}{\partial t} = \frac{1}{h_\chi h_\psi} \frac{\partial}{\partial \Psi} \left(\frac{h_\chi}{R h_\psi} \frac{\partial}{\partial \Psi} (R\eta J_\phi) \right)$$

The total current flowing in the plasma is

$$\int_S \underline{J} \cdot \underline{ds} = \int J_\phi \, h_\chi h_\psi \, d\chi d_\psi$$

Therefore

$$\mu_o \frac{dI}{dt} = \oint \frac{h_\chi}{R h_\psi} \frac{\partial}{\partial \Psi} (R\eta J_\phi)\Big|_{wall} d\chi \qquad (3.7)$$

as the gradient of the current density will be zero on the inner surface. The rate of change of total current with time is prescribed, so Eq. (3.7) may be used to find the current density at the outer surface.

3.2 MAIN EVOLUTIONARY CYCLE

3.2.1 Choice of timestep

The rate at which a time dependent simulation may step forward in time is in general governed by two factors; firstly the physical processes that are modelled by the system of equations, and secondly, the schemes used to solve these equations.

We have described in section 2.1 of Chapter 2 how the fastest physical process, that of compressional toroidal Alfven waves, has been removed from this model by assuming toroidal incompressibility. The next fastest processes, in approximate order of increasing timescales are; poloidal Alfven waves, thermal diffusion, sound waves, plasma flow and resistive diffusion. This list applies to a large tokamak at a temperature of one kilovolt. At lower temperatures the order may change slightly, but is in general true. We must therefore integrate our equation with schemes that will allow a timestep to be taken long enough for us to see the physical process desired, i.e. the plasma flow. We therefore use implicit schemes for the two fastest processes, the poloidal Alfven waves, and the thermal diffusion so that the timestep may be longer than the characteristic times for these two effects. The sound waves are treated explicitly, and these impose a restriction on the timestep. However, the analysis of section 2.5 of Chapter 2 shows that these sound waves are modified by the geometry and are dispersive. They have a modified sound speed which is always less than the normal sound speed (Eq. 2.44)

$$C_s' = C_s\sqrt{2/f}$$

where

$$f \simeq 1 + k^2R^2$$

C_s' is smallest at the largest wavelength which is approximately equal to

the minor radius. The timestep is therefore only restricted to

$$\Delta t_{sound} < \frac{a}{C_s\sqrt{2}} (1 + R^2/a^2)^{\frac{1}{2}} \qquad (3.8)$$

and does not depend upon the mesh spacing.

If fast enough, resistive diffusion can limit the timestep. The motion of the surfaces, because of resistivity, limits the timestep to the resistive diffusion time, (where Δx is the mesh spacing)

$$\Delta t_{\eta} < \frac{\mu_o \Delta x^2}{\eta} \qquad (3.9)$$

because the motion of the surfaces is treated explicitly. Once, however, the surfaces have been moved, the value of the poloidal flux is found implicitly.

If a timestep is chosen, subject to these restrictions, solutions may be found that are numerically stable.

3.2.2 Stream function and flow velocity

The first step in the evolutionary cycle is to obtain the flow velocity. Equations (2.12) and (2.18) give an elliptic equation for the stream function, ζ. In natural coordinates, we obtain:

$$\Xi = \frac{R}{h_\chi h_\psi}\left(\frac{\partial}{\partial\chi}\frac{h_\psi}{h_\chi}R^3\rho\frac{\partial\zeta}{\partial\chi} + \frac{\partial}{\partial\Psi}\frac{h_\chi}{h_\psi}R^3\rho\frac{\partial\zeta}{\partial\Psi}\right) \tag{3.10}$$

and from the stream function, the flow velocity may be found:

$$\begin{aligned} v_\chi &= -\frac{R}{h_\psi}\frac{\partial\zeta}{\partial\Psi} \\ v_\psi &= \frac{R}{h_\chi}\frac{\partial\zeta}{\partial\chi} \end{aligned} \tag{3.11}$$

The compressive corrections, and those arising from finite resistivity given in Eqs. (2.38) and (2.39) are added in at this point.

Equation (3.10) is differenced using a five point scheme, Fig. 3.3:

$$\begin{aligned} \left(\frac{h_\chi h_\psi}{R}\Xi\right)_c &= A_{N/2}\,\zeta_N - (A_{N/2}+A_{S/2})\,\zeta_c + A_{S/2}\,\zeta_S \\ &+ B_{E/2}\,\zeta_E - (B_{E/2}+B_{W/2})\,\zeta_c + B_{W/2}\,\zeta_W \end{aligned} \tag{3.12}$$

where

$$A = \frac{h_\psi}{h_\chi}R^3\rho$$

and

$$B = \frac{h_\chi}{h_\psi}R^3\rho$$

Equation (3.12) is rearranged into block Jacobi form by normalising the terms to the coefficient of ζ_c. This quin-diagonal system of linear equations may now be solved using a suitable procedure.

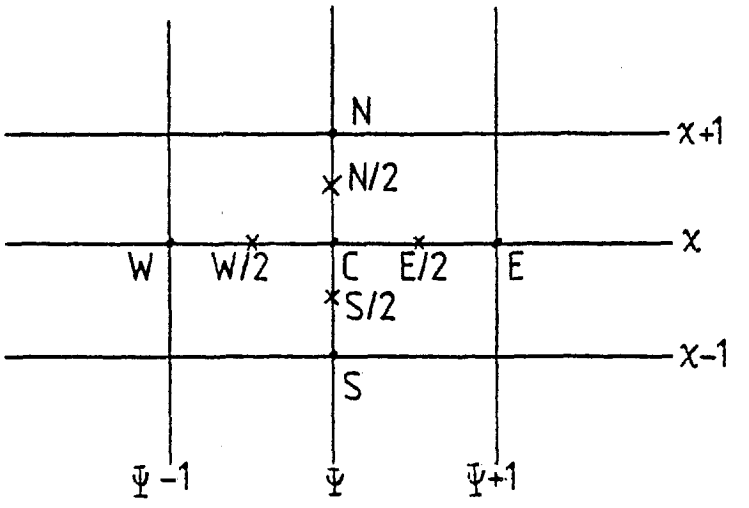

Fig. 3.3 Five point difference notation.

There are a number of methods by which a quin-diagonal matrix may be inverted. Those which consider the non-zero elements only are iterative and have differing convergence rates. The one chosen in this work is the Alternating Direction Implicit (ADI)[41] method, which because of its simplicity and rapidity, has gained popularity recently. No account of this, or other methods is given in this work as a detailed discussion may be found elsewhere[42].

In order to obtain a unique solution for this elliptic equation (3.10) boundary conditions must be applied. If solutions were to be obtained analytically it would be sufficient to specify boundary conditions on the outer boundary and just require that the solutions remain finite at the magnetic axis. Computationally the region has two boundaries; the usual outer boundary, and an inner boundary at the magnetic axis. It is therefore necessary in the code to specify conditions

on both these boundaries.

At the outer boundary it is assumed in this model that the limiter and conducting copper casing coincide. It is assumed that plasma extends right up to the limiter and there is no vacuum region. The outer boundary therefore, does not allow mass flow across it, but energy may flow to the limiter as this is, in effect, at a constant temperature, because the energy content of a plasma is insufficient to heat the limiter to any significant degree.

The boundary condition at the outer surface on the flow therefore requires that flow perpendicular to the boundary is zero. Thus from Eq. (3.11):

$$v_{\psi \text{ boundary}} = \frac{R}{h_\chi} \frac{\partial \zeta}{\partial \chi} = 0$$

which implies that ζ is a constant around the outer boundary.

This type of boundary condition on the flow can lead to the accumulation of plasma at the limiter, as the density, temperature and vorticity are all conserved at the boundary, except in allowing for compressive flow from the mesh that arises because

$$\nabla . \frac{\underline{v}}{R^2} \neq 0$$

To avoid this, a free flux boundary condition could be employed, by allowing ζ to vary around the boundary so that flow from the system was unrestricted. Conversely, this would allow unrestricted flow into the system. A method by which information can enter the mesh from outside is intuitively wrong and could be numerically unstable. This could be overcome by allowing flow out of the mesh but not into it, which would lead to a depletion of matter from regions near the wall. This is complicated to implement because careful accounting of mass and energy is necessary to ensure that total mass and energy is conserved.

Boundary conditions on the inner boundary, at the magnetic axis are a little more elusive, as it is only the discrete nature of the computational mesh that makes them necessary. Taken to the limit this inner surface shrinks to a point, which is the analytic situation. Therefore, in this limit we would expect the value of the dependent variable to be the same at all points on this surface. Thus we require the interior derivative of the dependent variable to be zero on the inner boundary.

Previously[30] it was necessary to assume the flow was symmetric about the mid-plane ($z = 0$) and omit the Hall term in Ohms Law, Eq. (2.7), that would lead to asymmetric flow. Now, although the Hall term is not included owing to extreme limitations on the timestep, asymmetric flow is allowable. Indeed, if there is no initial flow and density, temperature and current density distributions are symmetric about the mid-plane then the vorticity and stream function should be antisymmetric in order to conserve angular momentum. This therefore presents a check on the code for if asymmetric flow is produced, then it must have occurred numerically.

As flow in both the R and z directions can occur at the inner boundary, motion of the magnetic axis must be considered. This is best achieved by creating a local cartesian mesh at the magnetic axis and differencing the stream function on this mesh. The R and z components of a fluid element at the magnetic axis are given by Eq. (2.12). The inner boundary is therefore moved with this velocity, and given the timestep, its new position may be found.

3.2.3 Energy

The energy equation (2.43) describes the change of internal energy of a fluid element arising from motion of the fluid, finite β compressive

corrections, Ohmic heating and thermal diffusion. Its solution is split into three parts; firstly, source terms corresponding to finite β corrections and Ohmic heating are included explicitly, then the thermal diffusion is treated implicitly to avoid limitation of the timestep, and lastly, we account for changes of energy arising from advection of the fluid, when the mesh is advected.

This fractional timestep method produces an intermediate temperature which is then diffused by an amount determined by the coefficients of thermal conduction which are evaluated at the old timestep. If ε^* represents this intermediate temperature, then:

$$\varepsilon^* - \varepsilon^n = \Delta t\left(\frac{\eta J^2}{\rho} - R^2\nabla.\left(\frac{\underline{v}}{R^2}\right)\varepsilon^n\right) \qquad (3.13)$$

which is followed by the thermal diffusion:

$$\varepsilon^{n+1} - \varepsilon^* = -\Delta t\rho^{-(\gamma-1)}\frac{\nabla.\underline{q}}{\rho} \qquad (3.14)$$

Lastly, to account for energy changes that accompany advection of the fluid, we ensure that we obey the conservation relation:

$$\frac{d}{dt}\left(R^{2(\gamma-1)}\varepsilon\right) = 0$$

as the fluid is moved.

Equation (3.13) may be solved analytically because the resistivity is a function of temperature (Table 3.1). Neglecting the finite β corrections, if we define θ as:

$$\theta = \frac{kT}{e(\gamma-1)} \qquad (3.15)$$

and use for the resistivity:

$$\eta = \eta_c\,\theta^{-3/2}$$

we obtain:

$$\theta^* = \left(\theta^{n\ 5/2} + \frac{5}{2}\frac{(\gamma-1)\ M\ n_c\ J^2}{\rho e}\Delta t\right)^{2/5}$$

where M is the ion mass.

The thermal diffusion portion, Eq. (3.14) is derived in section 3.3 and reproduced here:

$$\frac{d}{dt}\left(R^{2(\gamma-1)}\theta\right) = -\frac{(\gamma-1)M}{R^2\rho\ k}\frac{R}{h_\chi h_\psi}\left[\frac{\partial}{\partial\chi}\left(C\frac{\partial\theta}{\partial\chi}\right) + \frac{\partial}{\partial\Psi}\left(D\frac{\partial\theta}{\partial\Psi}\right)\right] \quad (3.16)$$

where

$$C = \frac{\kappa_o e}{2R^2\ B_\phi^2}\frac{R}{h_\chi h_\psi}\left(\frac{\partial\psi}{\partial\Psi}\right)^2$$

and

$$D = \lambda\frac{R}{2}\frac{h_\chi}{h_\psi}\left(\frac{h_\kappa e}{h_\kappa I}\right)^2\frac{g_\kappa I}{g_\kappa e}\left(\frac{M}{m}\right)^{\frac{1}{2}}\frac{\kappa_o e}{\omega_e z}$$

Equation (3.16) is differenced using the Crank-Nicholson scheme which ensures second order accuracy. Although this differencing scheme is unconditionally stable[43] oscillations in the solution can occur when the timestep is much larger than the physical diffusion time. This will occur in our problem only when the temperature is in excess of a kilovolt.

Using the notation of the last sub-section, the difference equation is:

$$-C_{N/2}\,\theta_N^{n+1} + \left(C_{N/2} + C_{S/2} + \frac{1}{2F_c}\right)\theta_c^{n+1} - C_{S/2}\,\theta_S^{n+1}$$

$$-D_{E/2}\,\theta_E^{n+1} + \left(D_{E/2} + D_{W/2} + \frac{1}{2F_c}\right)\theta_c^{n+1} - D_{W/2}\,\theta_W^{n+1}$$

$$= \frac{\theta_c^*}{F_c} + C_{N/2}\,\theta_N^n + C_{S/2}\,\theta_S^n + D_{E/2}\,\theta_E^n + D_{W/2}\,\theta_W^n$$

$$- (C_{N/2} + C_{S/2} + D_{E/2} + D_{W/2})\,\theta_c^n \qquad (3.17)$$

where:

$$F = \Delta t\ \frac{M}{k}\ \frac{(\gamma-1)}{R^2\rho}\ \frac{R}{h_\chi h_\psi}$$

Once again, if Eq. (3.17) is arranged in block Jacobi form, it may be inverted using the ADI method.

3.2.4 Vorticity

The time dependence of the vorticity given by Eq. (2.41) contains terms that describe the production of sound waves and poloidal Alfven waves. The generation of sound waves is treated explicitly along with finite β compressive corrections. The poloidal Alfven wave production term is treated implicitly in order to remove the restriction that an explicit treatment would impose upon the timestep. These Alfven waves propagate only around the magnetic surfaces thus rendering the problem one dimensional. The implicit treatment[30] which uses a time centred differencing scheme requires for its solution the inversion of a tridiagonal matrix alone.

3.2.5 Density

The evolution of density given by Eq. (2.42) is particularly simple as in the fluid frame it is modified only by small compressive corrections. These corrections, of the order of $\beta^{\frac{1}{2}}$ are treated explicitly, as are the compressive corrections to the other advected quantities of energy and vorticity.

3.2.6 Resistive Diffusion

The distributions of toroidal current density and poloidal magnetic field are given entirely by the distribution of poloidal flux, ψ. An equation for its change in time will describe fully the evolution of the field and current density. Using Faraday's and Ohm's Laws, we arrive at:

$$\frac{d\psi}{dt} = -\eta R J_\phi \tag{3.18}$$

The rate at which the poloidal flux changes in the fluid frame is dependent upon the resistive part of the voltage. An expression for the toroidal current density (Appendix C) yields a diffusion equation for ψ:

$$\frac{d\psi}{dt} = \frac{\eta}{\mu_o} \Delta^* \psi \tag{3.19}$$

It is clear that the poloidal flux can only change in the fluid frame by resistive diffusion. If the resistivity is zero the poloidal flux, and therefore the magnetic field, is 'frozen' into the fluid. However, when the resistivity is finite, the poloidal flux may diffuse through the fluid, so that the magnetic surfaces can move with respect to the fluid. Therefore, as the computational mesh is based on the magnetic surfaces, the presence of resistivity allows the mesh to move relative to the fluid. In essence, when resistivity is finite, the mesh is not strictly Lagrangian as it is no longer tied to the fluid, but it is Lagrangian, in a sense, because it still moves but now with the magnetic surfaces.

We have, therefore, three frames of reference; the laboratory, the fluid and the mesh. The fluid moves with respect to the laboratory and then the mesh moves relative to the fluid. From the definition of the Lagrangian derivative, we obtain:

$$\left.\frac{d\psi}{dt}\right|_{fluid} = \left.\frac{\partial\psi}{\partial t}\right|_{lab} + \underline{v}_{fl}.\nabla\psi$$

where $\underline{v}_{fl}$ is the velocity of fluid with respect to the laboratory. Similarly:

$$\left.\frac{d\psi}{dt}\right|_{fluid} = \left.\frac{\partial\psi}{\partial t}\right|_{mesh} + \underline{v}_{fm}.\nabla\psi$$

where $\underline{v}_{fm}$ is the velocity of fluid with respect to the mesh. These relative velocities, $\underline{v}_{fl}$, $\underline{v}_{fm}$ and the velocity of the mesh relative to the laboratory, $\underline{v}_{ml}$, are shown in Fig. 3.4

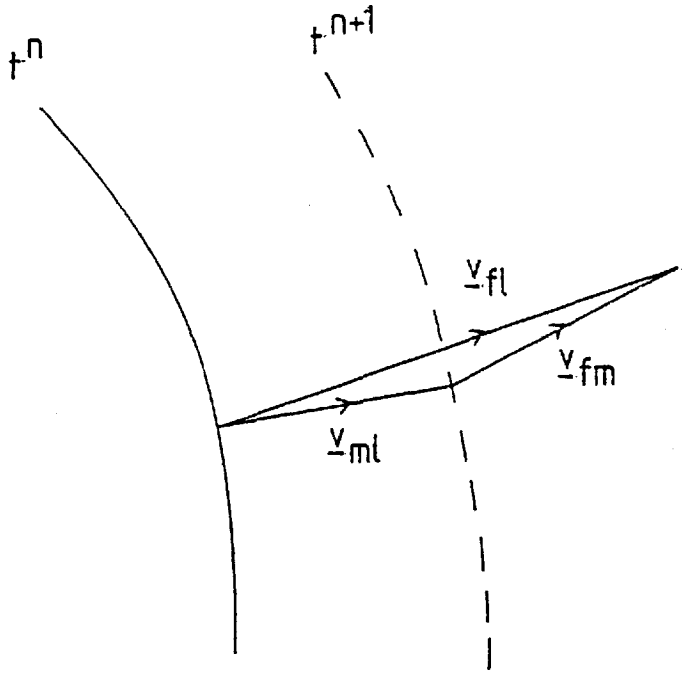

Fig. 3.4 Relative motion of fluid, mesh and laboratory, between timesteps n and n+1.

Thus from Eq. (3.18)

$$\underline{v}_{fm}.\nabla\psi = -\eta RJ_{\phi} \left.\frac{-\partial\psi}{\partial t}\right|_{mesh} \qquad (3.20)$$

To describe the evolution of the poloidal flux, the simplest procedure is to fix the value of ψ on the mesh, so that the diffusion of the surfaces is represented completely by a movement of the mesh relative to the fluid. However, the equations of the model Eqs. (2.35) - (2.43) are written in the fluid frame and some additional advection of dependent variables would be necessary to correct for the diffusive motion of the mesh. When the temperature is low the resistivity is relatively large and this auxillary advection can be larger than the main advection of fluid relative to the laboratory. A better procedure is to allow the value of ψ to alter on the mesh, in such a way that the diffusive velocity of the mesh relative to the fluid $\underline{v}_{fm}$ is minimised.

A surface average of equation (3.18) yields

$$\left\langle \frac{v_\psi}{h_\psi} \right\rangle = - \frac{\partial \psi}{\partial t} \Big/ \frac{\partial \psi}{\partial \Psi} - \left\langle \frac{\eta R J_\phi}{\partial \psi / \partial \Psi} \right\rangle$$

where

$$V = 2\pi \oint dl/B_p$$

and

$$V\langle x \rangle = 2\pi \oint x \, dl/B_p$$

B_p is as usual, the poloidal field, and dl is taken along the intersection of surfaces of constant ψ and ϕ. To minimise the relative velocity of mesh and fluid, we choose:

$$\left\langle \frac{v_\psi}{h_\psi} \right\rangle = 0$$

Therefore, the change of poloidal flux on each surface must alter by:

$$\frac{\partial \psi}{\partial t} = - \langle \eta R J_\phi \rangle \qquad (3.21)$$

which results in a diffusive velocity given by Eq. (3.20).

Essentially the average diffusive motion of the surfaces is replaced by a change in ψ on the surface. The only diffusive motion that occurs now is if the diffusion is differential around the surface, owing to variations of resistivity or current density on a surface. Large movement of the mesh is therefore avoided when the resistivity is high and the mesh remains more closely coupled to the fluid although of course, the magnetic surfaces still move through the fluid.

Differential motion of the surfaces may be calculated, once $\partial\psi/\partial t$ has been found from Eq. (3.21), by using the non-surface averaged equation (3.20)

$$\frac{v_\psi}{h_\psi}\frac{\partial\psi}{\partial\Psi} = -\eta RJ\phi - \frac{\partial\psi}{\partial t}$$

The diffusive motion of each point on the surface may thus be calculated. To obtain the total velocity of the surfaces the diffusive motion must be added to the motion of the fluid (as given by the flow velocity including finite beta corrections, Eq. (2.38) and Eq. (2.39)). This is the velocity used for the main advection of the surfaces described in the next section.

Whilst the dependent variables are defined on the surfaces they should be advected only with the fluid velocity, as can be seen from Eq. (2.41) to Eq. (2.43). An auxillary advection must be performed that corrects the main advection where the dependent variables are advected with the fluid, plus the diffusive surface velocity. This auxillary advection velocity is therefore equal and opposite to the surface diffusion velocity.

Having moved the surfaces and calculated a new metric, the new magnetic field and current distributions must be found. It must first be noted that when in difference form Eq. (3.21) is not time centred,

as the new current density is obviously unknown prior to the advection of the surfaces. The new ψ on each surface may therefore be inaccurate. To avoid this, Eq. (3.21) is solved twice, firstly in an auxillary manner to obtain the diffusive surface motion, and then having used this velocity, plus the fluid velocity, to move the surfaces and create a new metric, it is solved to second order accuracy using the implicit Crank-Nicholson scheme, to obtain ψ on each surface at the new time level.

Equation (3.21) is a one dimensional diffusion equation, and is therefore, far easier to solve than the two dimensional diffusion equation, described in section 3.2.3, for the temperature. The boundary conditions are more complicated as they involve the coupling to the external circuit.

Using the Crank-Nicholson scheme Eq. (3.21) becomes:

$$\psi_\Psi^{n+1} + \frac{\Delta t}{2} <\eta R J\phi>_\Psi^{n+1} = \psi_\Psi^{n} - \frac{\Delta t}{2} <\eta R J\phi>_\Psi^{n}$$

substituting for the current density, $J\phi$, we obtain:

$$\psi_\Psi^{n+1} - \frac{\Delta t}{2} <\frac{\eta R}{\mu_o h_\chi h_\Psi} \frac{\partial}{\partial \Psi} \frac{h_\chi}{R h_\Psi} \frac{\partial \psi}{\partial \Psi}>_\Psi^{n+1} = \psi_\Psi^{n} - \frac{\Delta t}{2} <\eta R J\phi>_\Psi^{n} \qquad (3.22)$$

If the term containing the second derivative of ψ is now differenced

$$-\psi_{\Psi+1}^{n+1} \frac{\Delta t}{2} <\frac{\eta_\Psi}{\mu_o} R_\Psi^2 \left(\frac{h_\chi}{R h_\Psi}\right)_{\Psi+\frac{1}{2}}>^{n+1}$$

$$+ \psi_\Psi^{n+1} \{1 + \frac{\Delta t}{2} <\frac{\eta_\Psi}{\mu_o} R_\Psi^2 \left[\left(\frac{h_\chi}{R h_\Psi}\right)_{\Psi+\frac{1}{2}} + \left(\frac{h_\chi}{R h_\Psi}\right)_{\Psi-\frac{1}{2}}\right]>\}^{n+1}$$

$$- \psi_{\Psi-1}^{n+1} \frac{\Delta t}{2} <\frac{\eta_\Psi}{\mu_o} R_\Psi^2 \left(\frac{h_\chi}{R h_\Psi}\right)_{\Psi-\frac{1}{2}}>^{n+1}$$

$$= \psi_\Psi^{n} - \frac{\Delta t}{2} <\eta R J\phi>_\Psi^{n} \qquad (3.23)$$

is produced, which is of the form

$$A_\Psi \psi_{\Psi+1} + B_\Psi \psi_\Psi + C_\Psi \psi_{\Psi-1} = S_\Psi$$

and may be recognised as the standard tridiagonal matrix form[44], which is easily inverted. Still in standard notation, at the boundaries Eq. (3.23) has the form:

$$\begin{aligned} A_1 \psi_2 + B_1 \psi_1 &= S_1 \\ B_J \psi_J + C_J \psi_{J-1} &= S_J \end{aligned} \qquad (3.24)$$

where 1 labels the inner boundary and J the outer.

At the inner boundary the value of ψ is determined by the auxillary value of ψ at the new time level. The boundary condition at the magnetic axis is therefore Dirichlet and

$$A_1 = 0; \quad B_1 = 1; \quad S_1 = \psi_{\text{auxillary}}.$$

The outer boundary is assumed to be coincident with the perfectly conducting copper casing and must therefore be a magnetic surface. On this surface ψ may be specified directly by giving the loop voltage, or $\nabla\psi$ is determined when the total current is known.

In most tokamak experiments, the total plasma current rises linearly with time at first, and then flattens off to a plateau value for the major part of the discharge duration. The voltage, however, does not exhibit such simple behaviour and is a more sensitive measure of the plasma development, Fig. 3.5. We choose to specify the current as a linearly increasing function of time in the low temperature simulations, and as a constant independent of time in the higher temperature runs.

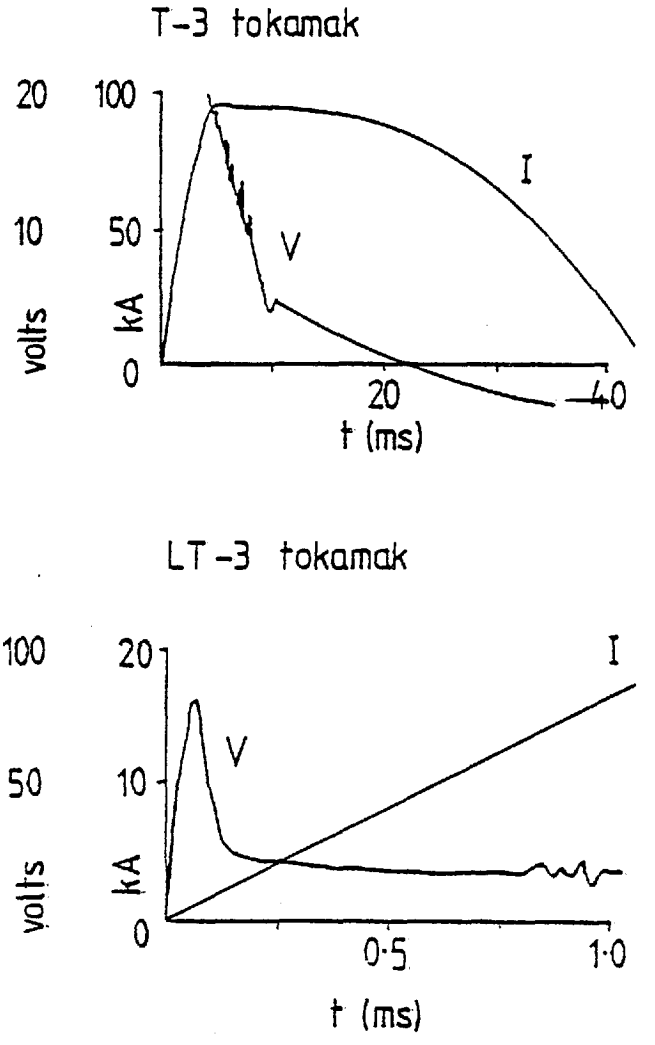

Fig. 3.5 Experimental current and voltage traces for the T-3 and LT-3 tokamaks.

We may obtain an expression for the total current by considering it in two parts; that within the surface $\Psi = J-\frac{1}{2}$ and that outside this surface but within the wall, Fig. 3.6. Current within the surface $\Psi = J-\frac{1}{2}$ may be found using:

$$\mu_o I_{inner} = \oint \underline{B}.\underline{dl} = \int B_X h_X dx$$

However, outside this surface the current flowing must be found by

referring to the current density:

$$I_{outer} = \oint \underline{J}.\underline{ds} = \int J_\phi h_\chi h_\psi d\chi d\psi$$

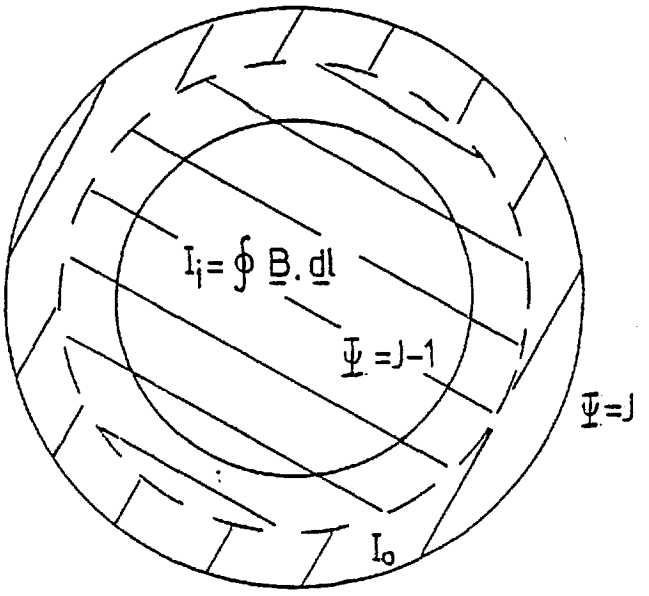

Fig. 3.6 Calculation of the total toroidal current in two parts; I_i up to the surface $\Psi = J-\frac{1}{2}$ and I_o between $\Psi = J-\frac{1}{2}$ and $\Psi = J$.

The total current is therefore:

$$I_t = -\tfrac{1}{2} \int \frac{h_\chi h_\psi}{\eta R} d\chi \left.\frac{\partial \psi}{\partial t}\right|_J + \frac{1}{\mu_o} \int \frac{h_\chi}{R h_\psi} d\chi \left.\frac{\partial \psi}{\partial \Psi}\right|_{J-\frac{1}{2}} \qquad (3.25)$$

This may be differenced implicitly to second order accuracy to obtain an expression for ψ at the boundary, in the form of Eq. (3.24):

$$\left[\left(\int \frac{\mu_o}{\eta} \frac{h_\chi h_\psi}{R} d\chi\right)_J^{n+1} + \Delta t\left(\int \frac{h_\chi}{R h_\Psi} d\chi\right)_{J-\frac{1}{2}}^{n+1}\right] \psi_J^{n+1}$$

$$- \Delta t\left(\int \frac{h_\chi}{R h_\psi} d\chi\right)_{J-\frac{1}{2}}^{n+1} \psi_{J-1}^{n+1}$$

$$= 2\Delta t\, \mu_o I_t - \Delta t \frac{\partial \psi}{\partial \Psi}\Big|_{J-\frac{1}{2}}^{n} \left(\int \frac{h_\chi}{R h_\psi} d\chi\right)_{J-\frac{1}{2}}^{n} + \psi_J^n \left(\int \frac{h_\chi h_\psi}{R} \frac{\mu_o}{\eta} d\chi\right)_J^n \tag{3.26}$$

3.2.7 Advection of the mesh relative to real space

The final step in the evolutionary cycle is to advect our natural coordinate relative to real space. This is the only point in the whole calculation where the advective equation must be solved. As described in the last section, the mesh is advected with the fluid velocity plus a component that accounts for the differential diffusion of the surfaces. This total motion is expressed as the advection of real space past the natural coordinates. The change of the position vector $\underline{R}$ in natural coordinates is:

$$\frac{d\underline{R}}{dt} = \underline{v} . \nabla \underline{R}$$

For example, in cylindrical coordinates (R, ϕ, z) the change of radius R is:

$$\frac{dR}{dt} = \frac{v_\chi}{h_\chi} \frac{\partial R}{\partial \chi} + \frac{v_\psi}{h_\psi} \frac{\partial R}{\partial \Psi} \tag{3.27}$$

After differencing, equation (3.27) may be expressed as a quindiagonal matrix operating on a vector $\underline{R}$. Using the notation of Fig. 3.3, equation (3.27) becomes:

$$-\left(\frac{\Delta t v_\chi}{2h_\chi}\right)_c (R_N^{n+1} - R_S^{n+1}) + R_c^{n+1} - \left(\frac{\Delta t v_\psi}{2h_\psi}\right)_c (R_E^{n+1} - R_W^{n+1})$$

$$= \left(\frac{\Delta t v_\chi}{2h_\chi}\right)_c (R_N^n - R_S^n) + R_c^n + \left(\frac{\Delta t v_\psi}{2h_\psi}\right)_c (R_E^n - R_W^n) \qquad (3.28)$$

which is in a form ready for solution by the ADI method.

The ADI method is therefore used three times in each evolutionary cycle; first to solve an elliptic equation (section 3.2.2), secondly to solve a parabolic equation (section 3.2.3) and lastly, in this section, to solve a first order equation. In each case, after differencing, the partial differential equation may be expressed as a system of linear equations:

$$Ax = b \qquad (3.29)$$

where $A = (a_{ij})$ is a (NXN) matrix; N is the number of mesh points.

The following conditions[49] are sufficient to prove the existence of a unique solution to equation (3.29):

(i) $|a_{ii}| \neq 0 \quad i = 1, 2.....N$

(ii) $|a_{ii}| \geq \sum_{\substack{j=1 \\ j\neq i}}^{N} |a_{ij}|$ and for some i strict inequality holds.

(iii) A is irreducible.

If matrix A satisfies these conditions it is non-singular, and is termed irreducibly diagonally dominant.

It is interesting to note that for the elliptic problem, the inequality requirement of (ii) may only be satisfied at a boundary point as at all interior points condition (ii) produce equality. This, however, is sufficient and only reflects the normal requirement that in an elliptic problem a Dirichlet condition need by applied at only one point on the boundary for a unique solution to be obtained.

The conditions under which the ADI iterations converge are, however, more restrictive than conditions (i) - (iii). Varga[42] shows that if A is a Stieljes matrix the convergence of the ADI method is assured. A Stieljes matrix is a real symmetric positive definite matrix with non-positive off diagonal elements; a positive definite matrix has positive real eigenvalues (i.e. is an Hermitian irreducible diagonally dominant matrix with positive real diagonal elements).

It is clear that the ADI method will converge for both the elliptic and parabolic cases as Stieljes matrices are obtained because the operators are self-adjoint. When used to solve the first order equation (3.27) it has been shown[30] that the ADI iterations are convergent for the special case of advection in an incompressible fluid when equation (3.27) may be written in conservative form:

$$\frac{\partial R}{\partial t} + \nabla.(R\underline{v}) = 0$$

We must, however, note that the sufficient conditions (i) - (iii) for the existence of solutions to equation (3.29) require in particular that the sum of the moduli of the off diagonal elements is less than the modulus of the diagonal element. From equation (3.28) it is easily seen that a sufficient condition for a unique solution is approximately

$$\Delta t < \frac{h}{2v} \qquad (3.30)$$

where h and v are some averages of the Ψ and χ components. The restriction, Eq. (3.30), on the timestep, is just the Courant-Friedricks-Lewy condition[43] which is normally applicable to explicit schemes. We must note that conditions (i) - (iii) are only sufficient, but not necessary for a unique solution to exist. Whilst solutions may exist for a timestep larger than the CFL conditon would allow, we choose to

restrict the timestep by Eq. (3.30) to ensure a solution is obtained, which will be accurate to second order in both the time and space dimensions.

3.3 TRANSPORT COEFFICIENTS

The transport coefficients of resistivity and thermal conductivity are included in the code. Resistivity appears in both the equation for the diffusion of poloidal flux, Eq. (2.44), and energy equation, Eq. (2.43). Thermal conductivity appears in the latter alone.

The resistivity is assumed scalar and takes the value derived by Spitzer[45] for electrical conduction parallel to a magnetic field. The thermal conductivity, however, must have tensor form. In the presence of a large magnetic field, thermal transport perpendicular to the field is much smaller than conduction parallel to the lines of force. In natural coordinates the divergence of the heat flux takes the form:

$$\nabla.\underline{q} = \frac{1}{Rh_\chi h_\Psi}\left[-\frac{\partial}{\partial\chi}\left(R\,\frac{h_\Psi}{h_\chi}\left(\gamma^2\kappa_\perp+\alpha^2\kappa_0\right)\frac{\partial T}{\partial\chi}\right)\right.$$

$$+\frac{\partial}{\partial\chi}\left(\gamma R\kappa_R\,\frac{\partial T}{\partial\Psi}\right)-\frac{\partial}{\partial\Psi}\left(\gamma R\kappa_R\,\frac{\partial T}{\partial\chi}\right) \qquad (3.31)$$

$$\left.-\frac{\partial}{\partial\Psi}\left(R\,\frac{h_\chi}{h_\Psi}\,\kappa_\perp\,\frac{\partial T}{\partial\Psi}\right)\right]$$

where

$$\alpha = \frac{B_\chi}{B}$$

$$\gamma = \frac{B_\phi}{B}$$

and the components of the thermal conductivity tensor are given in Table 3.1, together with the resistivity.

The dependence of the transport coefficients on the atomic number, Z, is detailed in Table 3.1 because a profile of effective atomic numbers may be defined for a simulation. This is because most tokamak

experiments, e.g. TFR[47] quote a Z in excess of unity, which is usually accredited to the presence of impurities in the discharge. The impurity concentration is usually found to rise near the wall, so for a typical simulation a Z of unity is defined on the magnetic axis, rising linearly to a value of between two and four at the wall.

Table 3.2 illustrates some properties of the transport coefficients. Heat flux parallel to the magnetic field is dominated by the electrons; perpendicular, the ions transport the major part of the energy, while the Righi-Leduc heat flow, perpendicular to both magnetic field and temperature gradient, appears to vanish.

Consider the Righi-Leduc terms in equation (3.31). For equal electron and ion temperatures a total thermal conductivity may be constructed from the sum of the electron and ion components. Thus using Table 3.1 a total Righi-Leduc thermal conductivity may be written in the limit where $\omega_I^2 >> 1$, for Z = 1:

$$\kappa_R = \kappa_R^e + \kappa_R^I = \frac{\kappa_o^e}{\omega_e}\left(1 - \frac{h_\kappa^e}{h_\kappa^I}\right) \qquad (3.32)$$

Conduction around the magnetic surfaces is given by the first term on the right hand side of Eq. (3.31). Adding electron and ion thermal conductivities, the conduction coefficient is:

$$(\kappa_\perp^e + \kappa_\perp^I)(1 - \alpha^2) + (\kappa_o^e + \kappa_o^I)\,\alpha^2$$

For $\omega_I^2 >> 1$ this becomes

$$\frac{\kappa_o^e}{\omega_e^2}\left[1 + \left(\frac{M}{m}\right)^{\frac{1}{2}} \frac{g_\kappa^I}{g_\kappa^e}\left(\frac{h_\kappa^e}{h_\kappa^I}\right)^2 + \alpha^2\,\omega_e^2\left(1 + \left(\frac{m}{M}\right)^{\frac{1}{2}} \frac{g_\kappa^e}{g_\kappa^I}\right)\right] \qquad (3.33)$$

Across the surfaces the conduction is given by those terms in $\partial^2 T/\partial\psi^2$ in Eq. (3.31). $\kappa_\perp^e + \kappa_\perp^I$ reduces for $\omega_I^2 >> 1$ to

TABLE 3.1

Thermal Conductivity (watt(m ^{o}K)$^{-1}$)

Electron

Perpendicular $$\kappa_{\perp}^{e} = \kappa_{o}^{e} \cdot \frac{1}{1 + \omega_e^2}$$

Righi-Leduc $$\kappa_{R}^{e} = \kappa_{o}^{e} \cdot \frac{\omega_e}{1 + \omega_e^2}$$

Parallel $$\kappa_{o}^{e} = \frac{5n\ k^2T}{m} \cdot \frac{Z}{g_{\kappa}^{e}\ \nu_{ei}}$$

Ion

Perpendicular $$\kappa_{\perp}^{I} = \kappa_{o}^{I} \cdot \frac{1}{1 + \omega_I^2}$$

Righi-Leduc $$\kappa_{R}^{I} = -\kappa_{o}^{I} \cdot \frac{\omega_I}{1 + \omega_I^2}$$

Parallel $$\kappa_{o}^{I} = \frac{5n\ k^2T}{M} \cdot \frac{1}{g_{\kappa}^{I}\ \nu_{ii}} = \frac{\kappa_{o}^{e}}{Z^3} \left(\frac{m}{M}\right)^{\frac{1}{2}} \frac{g_{\kappa}^{e}}{g_{\kappa}^{I}}$$

Hall Parameter

Electron $$\omega_e = \frac{h_{\kappa}^{e}}{g_{\kappa}^{e}}\ \omega_b\ \tau_{ei}$$

Ion $$\omega_I = \frac{h_{\kappa}^{I}}{g_{\kappa}^{I}}\ \Omega_b\ \tau_{ii} = \frac{h_{\kappa}^{I}\ g_{\kappa}^{e}}{g_{\kappa}^{I}\ h_{\kappa}^{e}} \left(\frac{m}{M}\right)^{\frac{1}{2}} \frac{\omega_e}{Z}$$

Electron-ion collision frequency (sec^{-1})

$$\nu_{ei} = \frac{4(2\pi)^{\frac{1}{2}}}{3}\ n\left(\frac{Ze^2}{4\pi\varepsilon_0 kT}\right)^2 \left(\frac{kT}{m}\right)^{\frac{1}{2}} \ln\Lambda$$

Ion-ion collision frequency (sec^{-1})

$$\nu_{ii} = Z^2 \left(\frac{m}{M}\right)^{\frac{1}{2}}\ \nu_{ei}$$

Coulomb logarithmn $$\Lambda = \frac{3(4\pi\varepsilon_0 kT)^{3/2}}{2Z^{3/2}\ e^3 (\pi n)^{\frac{1}{2}}}$$

Parallel electrical resistivity (ohm-m)

$$\eta = \frac{0.5064\ m\ \nu_{ei}}{Z\ ne^2}$$

where n = ion number density ($=n_i = Zn_e$)
e = ionic charge or magnitude of electronic charge
T = electron or ion temperature (i.e. equal) ^{o}K
Z = atomic number
m = electron mass
M = ion mass
k = Boltzmanns constant

$$\omega_b = \left|\frac{eB}{m}\right| \qquad \Omega_b = \left|\frac{eZB}{M}\right| = \frac{Zm}{M}\ \omega_b \qquad \tau_{ei} = \frac{1}{\nu_{ei}}$$

g_{κ}^{e}, g_{κ}^{I}, h_{κ}^{e}, h_{κ}^{I} are all numerical factors that depend to some extent on the corresponding Hall parameter. Their detailed behaviour is given in references (46) and (33). For Z = 1:

	Temperature (eV)		
	3	10^2	10^3
g_{κ}^{e}	.7321	.7312	.7312
h_{κ}^{e}	2.0005	2.0000	2.0000
g_{κ}^{I}	1.1260	1.1310	1.1312
h_{κ}^{I}	2.0026	1.9996	1.9999

TABLE 3.2

		Temperature (eV) 3	10^2	10^3
Thermal Conductivity (Watt/m-deg K)	$\kappa_\perp^e$	$2.69.10^{-6}$	$4.63.10^{-7}$	$1.46.10^{-7}$
	$\kappa_\perp^I$	$1.76.10^{-4}$	$3.06.10^{-5}$	$9.67.10^{-6}$
$\kappa_\perp = \kappa_\perp^e + \kappa_\perp^I$		$1.78.10^{-4}$	$3.10.10^{-5}$	$9.72.10^{-6}$
	κ_R^e	$3.47.10^{-3}$	$1.15.10^{-1}$	1.15
	κ_R^I	$-3.46.10^{-3}$	$-1.15.10^{-1}$	-1.15
$\kappa_R = \kappa_R^e + \kappa_R^I$		$0.01.10^{-3}$	0	0
	κ_o^e	4.47	$2.87.10^4$	$9.06.10^6$
	κ_o^I	$6.78.10^{-2}$	$4.33.10^2$	$1.37.10^5$
$\kappa_o = \kappa_o^e + \kappa_o^I$		4.54	$2.91.10^4$	$9.20.10^6$
Hall parameter				
	ω_e	$1.29.10^3$	$2.49.10^5$	$7.88.10^6$
	ω_I	$1.96.10^1$	$3.76.10^3$	$1.19.10^5$
Electron-ion collision frequency (sec^{-1})	ν_{ei}	$1.13.10^9$	$5.85.10^6$	$1.85.10^5$
Electrical conductivity ($(ohm\text{-}m)^{-1}$)	σ	$5.06.10^3$	$9.73.10^5$	$3.08.10^7$
Coulomb logarithmn				
	$\ln\Lambda$*	7	14	17

Note these values are for $n = 10^{20}$ m^{-3}, B = 3T, and Z = 1.

* Approximate values from Spitzer[45].

$$\left(\frac{h_\kappa^e}{h_\kappa^I}\right)^2 \quad \frac{g_\kappa^I}{g_\kappa^e} \quad \left(\frac{M}{m}\right)^{\frac{1}{2}} \frac{\kappa_0^e}{\omega_e^2} \tag{3.34}$$

Owing to the large magnetic field, ω_e^2 will always be much greater than unity. If we neglect these terms for the moment, the Righi-Leduc heat flow and the poloidal projection of the toroidal heat flow are all that remain. To neglect the Righi-Leduc heat flux, the following inequality must be satisfied:

$$\omega_e >> \left| \frac{1}{\alpha^2} \left(1 - \frac{h_\kappa^e}{h_\kappa^I}\right) \right| \tag{3.35}$$

Now α is related to the Kruskal-Shafranov safety factor, q_{KS}, by

$$q_{KS} = \frac{rB_T}{RB_p} \simeq \frac{r}{\alpha R}$$

where r is the minor radius. Therefore Eq. (3.35) becomes:

$$\omega_e >> \left| q_{KS}^2 \left(1 - \frac{h_\kappa^e}{h_\kappa^I}\right) \right|$$

At low temperatures and low currents, before the poloidal field has become very large, this is only marginally satisfied, as q_{KS} can be large, but as the temperature increases, q_{KS} decreases and so Eq. (3.35) is more readily satisfied.

Thus the Righi-Leduc heat flow is neglected because as the temperature and current both increase, this term becomes small compared to other heat conduction terms. Qualitatively this is because the Righi-Leduc heat flow arises from a term $\underline{\Omega} \times \nabla T$ where $\underline{\Omega}$ is the cyclotron motion vector. For ions and electrons this is in opposite directions, and so if the electron and ion temperatures are equal, the heat flow owing to the ions balances that of the electrons.

Returning to Eq. (3.31), by neglecting the Righi-Leduc heat flow, the energy equation with tensor thermal conductivity becomes:

$$\rho^{(\gamma-1)} \frac{d}{dt} \left(R^{2(\gamma-1)}\varepsilon\right) = \frac{\eta J^2}{\rho} - \frac{1}{\rho R h_\chi h_\psi} \left[\frac{\partial}{\partial \chi} \left(R \frac{h_\psi}{h_\chi} \kappa_o{}^e \alpha^2 \frac{\partial T}{\partial \chi}\right)\right.$$

$$\left. + \frac{\partial}{\partial \Psi} \left(R \frac{h_\chi}{h_\psi} \left(\frac{h_\kappa{}^e}{h_\kappa{}^I}\right)^2 \frac{g_\kappa{}^I}{g_\kappa{}^e} \left(\frac{M}{m}\right)^{\frac{1}{2}} \frac{\lambda \kappa_o{}^e}{\omega_e{}^2} \frac{\partial T}{\partial \Psi}\right)\right] \qquad (3.36)$$

There is a coefficient, λ, introduced in Eq. (3.36) to increase transport across the surfaces; it could be linked with an anomalous process such as microturbulence or drift waves. In much the same spirit, B_p is used in the Hall parameter, ω_e, rather than B_T in the "pseudoclassical" model of Duchs et al.[24] in order to achieve a reasonable agreement with T-3 and ST tokamak data.

3.4 ENERGY CONSERVATION

It is most desirable at all times to ensure that energy on the computational mesh is conserved. Firstly, this is a useful diagnostic as one can quickly see into which channel the energy is moving, and from this draw a conclusion about the physical processes occurring. Of greater importance, however, is its function as a check upon the numerical calculation. If energy is being lost or produced, then the numerical scheme is at fault and the results of dubious worth. A tally of the total energy can show this at a glance and may also indicate where the error is to be found.

The energy is accumulated as four separate totals; internal energy, magnetic energy, flow energy and energy gained by or lost from the mesh.

The first three totals take their conventional form,

internal energy:

$$E_I = \int_\tau \frac{nkT}{\gamma-1} \, d\tau \tag{3.37}$$

magnetic energy:

$$E_M = \int_\tau \frac{B^2}{2\mu_o} \, d\tau \tag{3.38}$$

flow energy:

$$E_F = \int_\tau \tfrac{1}{2}\rho v^2 \, d\tau \tag{3.39}$$

where τ is the total volume of the plasma. The fourth term consists of two parts; the energy gained by the plasma from the external circuit, and the energy lost to the limiter from the outer region of the plasma. The energy flow into the plasma for a timestep, Δt, is the Poynting vector

integrated over the surface area

$$E_{EXT} = \Delta t \int_A \underline{S}.\underline{dA} \tag{3.40}$$

The energy lost to the limiter is calculated in two parts. Firstly, the compressive terms discussed in section 2.4 of Chapter 2, result in a change of total energy when evaluated at the plasma surface, if the plasma volume is assumed constant. However, as these corrections are of order $\beta^{\frac{1}{2}}$ and β is always small, this source or sink of energy is very small. Secondly, and more importantly, is the loss associated with the plasma touching the limiter. The limiter acts as a constant temperature sink because, although the plasma is very hot, its energy content is small and does not heat the limiter to any great extent. Thus current flowing in the very outer region of the plasma will not increase the energy content of the plasma, but slightly increases the temperature of the limiter. In effect, this energy is lost from the plasma and must be included as a loss term.

Another check made on the numerical scheme is the conservation of mass. Obviously this must be conserved if no mass flow into or out of the plasma is allowed. The only source or sink of mass is the compressive correction mentioned earlier in this section. The total mass is:

$$M_T = \int_\tau \rho d\tau \tag{3.41}$$

Equations (3.37) to (3.41) are easily converted to difference form so that they appear in terms of variables defined on the computational mesh.

$$E_I = 2\pi \frac{e}{M} \sum_{\chi,\Psi} R^2 \rho \theta \frac{h_\chi h_\psi}{R}$$

$$E_M = \pi \sum_{\Psi} I_\Psi \frac{\partial \psi}{\partial \Psi}$$

$$E_F = \pi \sum_{\chi,\Psi} R^2 \rho v^2 \frac{h_\chi h_\psi}{R} \qquad (3.42)$$

$$E_{EXT} = 2\pi \mu_o I \frac{\partial \psi}{\partial t} \Delta t$$

$$M_T = 2\pi \sum_{\chi,\Psi} R^2 \rho \frac{h_\chi h_\psi}{R}$$

where θ is defined by Eq. (3.15). The scale factors h_χ and h_ψ are stored on the computer in terms of the reciprocal of a weighted mesh area $\frac{R}{h_\chi h_\psi}$ and a mesh aspect ratio $\frac{h_\chi}{h_\psi}$. It is for this reason that the energy and mass totals appear in the above form, Eqs. (3.42). I is the total current, and I_Ψ is the current flowing within a magnetic surface, Ψ.

3.4.1 Mesh area and volume summation

We have seen in the preceding section the importance of good energy conservation. Our efforts are futile, however, if the area and volume of the mesh are calculated incorrectly and these two quantities vary. This problem is trivial on an Eulerian mesh where the scale factors are time independent. However, on a mesh that changes shape at every timestep, we must be careful to calculate both area and volume exactly before we can expect the mass and energy to be conserved.

The outer boundary of the mesh is the limiter. As the position of this device remains the same throughout the experiment, it follows that the total volume and area of the mesh should behave likewise.

The method first employed to calculate the area of the mesh is illustrated in Fig. 3.7. The area assigned to the mesh point χ, Ψ is

half the area of the dotted quadrilateral. It is easy to see that the dotted boxes nest exactly to twice the total area of the mesh. The area of the quadrilateral is $\frac{1}{2}\,\underline{a} \times \underline{b}$. If the position vector of the point χ, Ψ in (R,z) coordinates is $\underline{r}$ (R,z) then:

$$\tfrac{1}{2}\,\underline{a} \times \underline{b} \;=\; 2\,\frac{\partial \underline{r}}{\partial \chi} \times \frac{\partial \underline{r}}{\partial \Psi} \;=\; 2\,\frac{\partial (R,z)}{\partial (\chi,\Psi)} \qquad (3.43)$$

The total area of the mesh is therefore, a quarter of the sum of the Jacobians, and is exact. An error is introduced, however, when the area at each point is related to the product of the scale factors $h_\chi h_\Psi$.

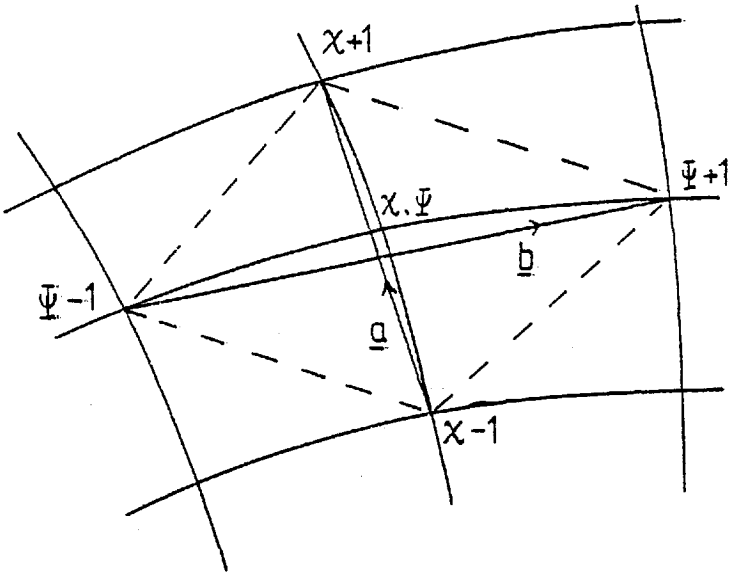

Fig. 3.7 Original mesh area calculation at the point χ,Ψ.

Consider an infinitesimal area dA in a region defined by two base vectors $\underline{e}_1$ and $\underline{e}_2$ that are not necessarily perpendicular. Now the area may be expressed in terms of the metric tensor g_{ij};

$$dA \;=\; \sqrt{g}\;\; dx^1\, dx^2$$

where

$$g = |g_{ij}|$$

and

$$g_{ij} = \frac{\partial \underline{X}}{\partial x^i} \cdot \frac{\partial \underline{X}}{\partial x^j}$$

Thus

$$|g_{ij}| = \begin{vmatrix} h_1^2 & g_{12} \\ g_{12} & h_2^2 \end{vmatrix}$$

where

$$h_i = \sqrt{g_{ii}}$$

Therefore

$$dA = (h_1^2 h_2^2 - g_{12}^2)^{\frac{1}{2}} \, dx^1 \, dx^2 \qquad (3.44)$$

$$= h_1 h_2 \left(1 - \frac{g_{12}^2}{2h_1^2 h_2^2}\right) dx^1 \, dx^2$$

for g_{12}, the off diagonal elements of the metric tensor, small. If $\underline{e}_1$ is perpendicular to $\underline{e}_2$ then g_{12} is zero and $dA = h_1 h_2 \, dx^1 \, dx^2$. If the two vectors are not orthogonal then there is a contribution to dA that depends upon the angle between the two base vectors. Now

$$g_{12} = \frac{\partial \underline{X}}{\partial x^1} \cdot \frac{\partial \underline{X}}{\partial x^2}$$

which from the definition of g_{11} and g_{12} gives

$$\cos\theta = \frac{g_{12}}{\sqrt{g_{11} \, g_{22}}} \qquad (3.45)$$

where θ is the angle between $\underline{e}_1$ and $\underline{e}_2$. So Eq. (3.44) becomes:

$$dA = h_1 h_2 \sin\theta \, dx^1 \, dx^2 \qquad (3.46)$$

Thus the error in representing dA by the product of h_1 and h_2 is

$$\varepsilon = 1 - \sin\theta$$

If $\delta = \pi/2 - \theta$ then the error becomes to second order

$$\varepsilon \simeq \delta^2 \tag{3.47}$$

Thus the error in approximating the area to the product of the scale factors, $h_1 h_2$ is proportional to the square of the deviation of the base vectors from orthogonality. The error will be greatest therefore, where the mesh is changing direction quickly and will depend upon the number of mesh points placed in that region.

If we now consider, instead, a finite area dA^1 of a mesh, much of the above analysis may be carried through. For instance, between mesh points the metric tensor is no longer a variable, but remains constant

$$\sqrt{g_{11}} = \frac{\partial X}{\partial x^1} \rightarrow \frac{\Delta X}{\Delta x^1} \tag{3.48}$$

From Eq. (3.44) the area element dA^1

$$dA^1 = \sqrt{g_{11}\, g_{22}}\,\left(1 - \frac{g_{12}^2}{g_{11}\, g_{22}}\right)^{\frac{1}{2}}$$

which using Eqs. (3.45) and (3.48) becomes

$$dA^1 = \frac{\Delta X}{\Delta x^1}\,\frac{\Delta X}{\Delta x^2}\,\sin\theta \tag{3.49}$$

This is, of course, what we should expect as the infinitesimal area dA may equally well be written

$$dA = J\, dx^1\, dx^2$$

where J is the Jacobian. Rewriting Eq. (3.49)

$$dA^1 = \frac{\Delta X}{\Delta x^1} \times \frac{\Delta X}{\Delta x^2}$$

we obtain the Jacobian and reproduce Eq. (3.43) used to calculate the mesh area.

Having found the mesh area, in principle the mesh volume is easy to find:

$$V = 2\pi \int R\, h_\chi h_\psi \, d\chi d\psi \qquad (3.50)$$

where $h_\chi h_\psi$ is found using Eq. (3.43) and R is the distance of the mesh point, at which $h_\chi h_\psi$ is centred, from the major axis. However, using this method of evaluating the volume it was found that the mesh volume was not independent of time if the magnetic surfaces were not concentric. This variation was improved by using a finer mesh, but the variation was completely removed if the magnetic surfaces were concentric. The variation of volume was not associated with a corresponding variation of the area. This indicated that the incorrect value of R was being used.

A more successful method of calculating the mesh volume was conceived which involved splitting the mesh into triangles and finding their area and volume. This leads to a time independent volume and therefore good energy conservation.

Equation (3.50) for the mesh volume is exact in the continuous case, but on a discrete mesh error will arise because R varies across the area element. When the magnetic surfaces are concentric, errors on one side of the magnetic axis will cancel with those on the other. When the surfaces are not concentric, this cancellation does not occur. Moreover, the area elements on the inside of the magnetic axis (towards the major axis) become larger and the approximation of constant R across an area element, becomes worse.

We assume a linear variation of R across a mesh element in order to calculate the volume. As the mesh has been divided into a number of triangular regions, this amounts to finding the centre of position of

each triangle, and using this volume of R to calculate the volume

$$R = \frac{1}{3}(R_a + R_b + R_c)$$

where R_a, R_b and R_c denote the positions of the three vertices.

The calculation of the mesh area and volume is made easier by using the periodicity of the mesh. At each mesh point, the area and volume of a "leading" and "following" triangle is calculated, Fig. 3.8. Only at the centre and the wall does the algorithm have to be modified to produce a set of triangles that nest exactly.

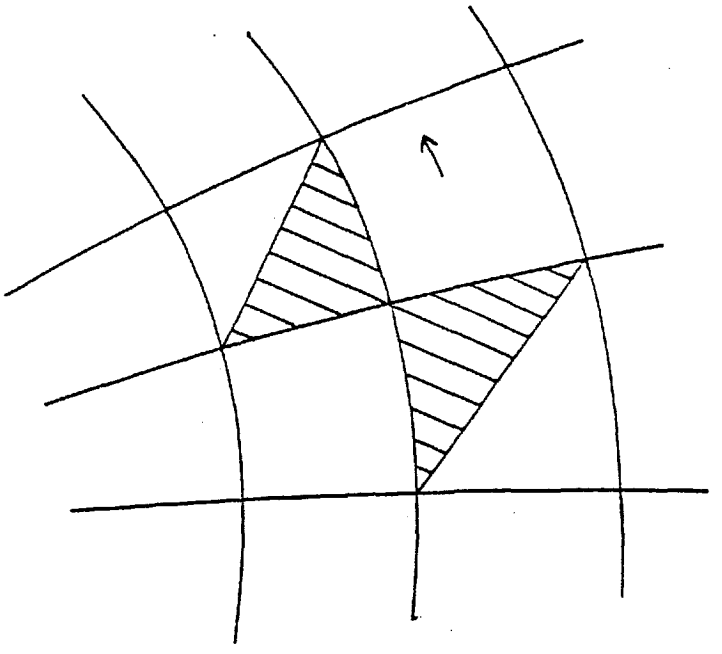

Fig. 3.8 New method of mesh area and volume calculation. The two triangles are scanned around the mesh.

By associating the area of these two triangles with the centre mesh point, we have taken the average of the areas of two quadrilaterals on either side of the mesh point rather than calculate an area totally enclosing the mesh point. Whilst this makes no difference to the calculation of

the area, the volume is more accurate because firstly, it is constructed from the triangles which are smaller basic units, and secondly, the variation of R across these basic units is treated.

3.5 MESH ORTHOGONALISATION : ORTHO

A detailed description of this method for orthogonalising a two dimensional mesh may be found elsewhere[37][38]; this section serves only to outline the techniques used and to comment upon the effectiveness of the package when contained in a large magnetohydrodynamic code.

The basis of the method may be described in the following way. If there exists two families of one parameter surfaces, a third family of surfaces may be constructed orthogonal to the other two families of surfaces as long as the abnormality of a vector perpendicular to these new surfaces is zero (see section 2.3.1 of Chapter 2). Consider for example, the magnetic surfaces, ψ, as one family of surfaces. A second family of surfaces, z, is constructed orthogonal to the magnetic surfaces, Fig. 3.9, leading to:

$$\nabla\psi.\nabla z = 0 \qquad (3.51)$$

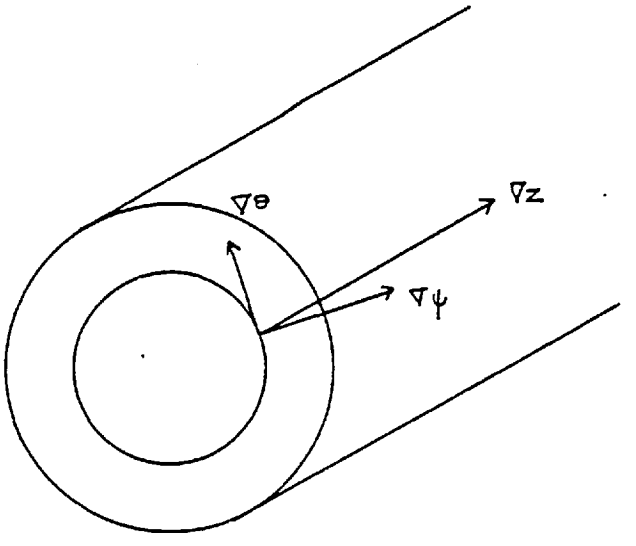

Fig. 3.9 Three mutually orthogonal directions (θ,ψ,z).

A vector perpendicular to both these families of surfaces may be constructed:

$$\underline{c} = g\nabla\psi \times \nabla z \tag{3.52}$$

where g is some arbitrary function. Supposing the third family of surfaces is denoted θ then $\underline{c}$ may be expressed:

$$\underline{c} = \nabla f(\theta) = \frac{df}{d\theta} \nabla\theta \tag{3.53}$$

Combining Eq. (3.52) and Eq. (3.53) and incorporating $\frac{df}{d\theta}$ in g, results in:

$$\nabla\theta = G\nabla\psi \times \nabla z \tag{3.54}$$

We require that the identity

$$\nabla \times \nabla\theta = 0$$

holds, thus taking the curl of Eq. (3.54), some rearrangement produces:

$$G\nabla^2\psi + \nabla\psi.\nabla G = 0$$

giving:

$$\nabla.(G\nabla\psi) = 0 \tag{3.55}$$

The vector product of Eq. (3.54) with ∇z yields:

$$\nabla\psi = \frac{-1}{G} \nabla\theta \times \nabla z$$

and an expression similar to Eq. (3.55) may be obtained. We note that:

$$\nabla\psi = \frac{e\psi}{h\psi}$$

and using this and a similar expression for $\nabla\theta$, we obtain:

$$G = G(\theta,\psi) = \frac{h_\psi}{h_\theta}$$

G is therefore, the ratio of the scale factors for θ and ψ.

If we now assume that the ratio of the scale factors is a separable function of θ and ψ such that G may be written:

$$G(\theta,\psi) = \frac{dP(\theta)}{d\theta} \frac{dQ(\psi)}{d\psi} \tag{3.56}$$

the result of Potter and Tuttle[36] is obtained:

$$\begin{aligned} \nabla^2 P &= 0 \\ \nabla^2 Q &= 0 \end{aligned} \tag{3.57}$$

where $P = P(\theta)$ and $Q = Q(\psi)$. As the ratio of the scale factors must always be positive, P is either a monotonically increasing or decreasing function of θ and therefore may be used to describe an orthogonal coordinate in the θ direction.

Greens theorem may now be applied to Laplaces Eq. (3.57), to find P, if an appropriately placed branch cut is made. This is of a particularly simple form as $\frac{\partial P}{\partial \psi} = 0$ and thus the integral containing the normal derivative vanishes, leaving:

$$P(\underline{r}) = -\frac{1}{\pi} \oint P(r^1) \frac{\partial}{\partial n} \left(\log \frac{1}{|\underline{r} - \underline{r}^1|}\right) d\underline{r}^1 \tag{3.58}$$

Having found P the orthogonal coordinate to the ψ surfaces may be constructed, for example, from the outside surface inward. Points are equally spaced around the outer surface, and Eq. (3.58) for P is solved on both surfaces. The position of the orthogonal coordinate on the inner surface is then found by interpolation. The procedure is repeated for this newly orthogonalised surface and the next inner until the whole mesh has been treated.

The results of this method have been compared[38] with coordinate systems that may be calculated easily by analytic methods and have been found to be very accurate. However, as this method relies on the ratio of the scale factors, Eq. (3.58), being a separable function of the two coordinates, which is, in general, true for coordinate systems that are readily calculated analytically, the accuracy must be expected.

The development of a continuous Lagrangian coordinate system that arises from the complex flow structure of the tokamak will not, in general, be analytically calculable, and there seems no reason why the scale factors of this coordinate system should be a separable function of the coordinates. This is more easily seen by rearranging Eq. (3.55):

$$G\,\nabla^2\psi + \nabla G.\nabla\psi = 0$$

or

$$G\,\nabla^2\psi + \frac{\partial G}{\partial \psi}\,(\nabla\psi)^2 = 0$$

giving:

$$\frac{1}{G}\,\frac{\partial G}{\partial \psi} = -\frac{\nabla^2\psi}{(\nabla\psi)^2} \qquad (3.59)$$

If G is a separable function of θ and ψ then it is clear from Eq. (3.59) that:

$$\frac{\nabla^2\psi}{(\nabla\psi)^2} = F(\psi) \qquad (3.60)$$

where $F(\psi)$ is some function of ψ only. This is a complicated function involving the derivative of the scale factors with respect to ψ and not in general a function of ψ alone.

There is, therefore, an approximation involved in using this scheme to orthogonalise general continuous coordinate systems. We must remember

however, that "discrete" rather than "continuous" coordinate systems are being dealt with, that is a coordinate system which joins mesh points with straight lines, rather a continuously varying curve. By making the approximation Eq. (3.56) and then using Green's theorem to solve Laplace's equation (3.57), we are discarding information between the ψ surfaces and using information on the ψ surfaces only. This is in fact all the information we have due to the discrete nature of the coordinate system, but in making the approximation, Eq. (3.56), and then using Eq. (3.58) to solve for P, we neglect the term involving the normal derivative of P, $\frac{\partial P}{\partial \psi}$, which may exist, if Eq. (3.60) is inappropriate for the continuous coordinate system.

An advantage of this procedure, is that because Green's theorem is used to solve for P, information from the whole surface is used to construct P, and therefore, the orthogonal coordinate. This enables ORTHO to cope with a coordinate system that is highly sheared.

We conclude this section with a discussion of two problems concerning the mesh. The first is directly related to the orthogonalisation; the second concerns all meshes of a similar topology to ours.

An important quantity in the code is the ratio of scale factors, h_θ/h_ψ. This quantity integrated around the outside of the mesh is used to derive the total current and hence the energy in the poloidal magnetic field. To ensure accurate energy accounting, it is necessary to determine h_θ/h_ψ accurately.

We note that h_θ/h_ψ is closely related to the function P used to construct the orthogonal coordinate and defined in Eq. (3.56). If we redefine:

$$\frac{1}{G} = \frac{dP^1(\theta)}{d\theta} \frac{dQ^1(\psi)}{d\psi}$$

integrating h_θ/h_ψ around a ψ surface, we obtain:

$$\oint \frac{h_\theta}{h_\psi} \, d\theta = \frac{dQ^1}{d\psi} \Delta P^1$$

where ΔP^1 is related to the change of P over one period of θ. The scale factors h_θ/h_ψ may therefore be found at each point on a ψ surface directly from the gradient of P^1 at that point:

$$\frac{h_\theta}{h_\psi}(\theta,\psi) = \left(\frac{1}{\Delta P^1} \oint \frac{h_\theta}{h_\psi} \, d\theta\right) \frac{dP^1}{d\theta} \qquad (3.61)$$

$\oint h_\theta/h_\psi \, d\theta$ is calculated directly from the mesh by summing the quantity $h_\theta h_\psi/h_\psi{}^2$ (which may be easily determined from a unit cell of the mesh) around a ψ line.

In order to gauge the effect of using different schemes to calculate h_θ/h_ψ (θ,ψ) on the magnetic energy, Eq. (3.61) is integrated around the outer ψ surface. Table 3.3 shows values of this integral quantity using three point Lagrangian interpolation, five point interpolation, and a direct method of finding h_θ/h_ψ (θ,ψ) respectively. In all cases the difference is slight, and less than ½%.

The fourth value, however, shows what happens if the orthogonalisation procedure is not repeated five times before the scale factors are examined. The difference in this case is over 1%, indicating that the shape of the mesh changes even though there has been no advection of the mesh. It is clear, therefore, that we cannot expect to conserve total energy to an accuracy of better than 1% as the orthogonalisation procedure introduces errors of this order.

The second problem is concerned not with the orthogonalisation procedure itself, but is a problem potentially inherent in all meshes with a similar topology to ours. The orthogonal mesh is formed by choosing points on the outer surface, and then moving the points on the next inner surface so that orthogonal trajectories are constructed. This works well

until we reach the centre of the mesh where the origin is represented by a point, or in our case a very small circle. Unless the mesh is coincident with an orthogonal curvilinear coordinate system, it cannot be orthogonal here because the degree of freedom of movement of points on the origin is seriously restricted, owing to its small size. The mesh constructed is not orthogonal at the centre and therefore errors result when one assumes it is.

TABLE 3.3

	No. of ORTHO repeats	$\oint h_\theta/h_\psi \, d\theta$	% difference
3 point interpolation	5	109.352	-
5 point interpolation	5	109.503	.138
direct method for h_θ/h_ψ	5	108.906	.408
3 point interpolation	1	108.086	1.158

Let us consider the operation $\nabla.\nabla F$, where $F = x^2/2$ and $x = R - R_0$. The operator div grad is a reasonably severe test of the mesh and is related to the operator Δ^* which revealed the error through the calculation of the current density. Additionally F is rapidly varying function on the mesh. In Figure 3.10 the orthogonal mesh is shown together with plots of F and $\nabla.\nabla F$[48]. The direction I lables the χ line anticlockwise from the midplane to the right of the origin, J labels the ψ lines from second surface outwards from the origin. We see that $\nabla.\nabla F$ takes its correct value of unity (with a very small variation in the I direction) on all ψ lines except J = 1. On this surface the error is large with values of $\nabla.\nabla F$ ranging from about 0.8 to 1.2, an error of $\pm$ 20%.

This error is not confined to our problem alone, but will occur whenever a coordinate system is constructed to be orthogonal in this kind of topology, but is not coincident with a curvilinear orthogonal coordinate system. To avoid these considerable errors propagating to dependent variables, the origin must receive special treatment. Because ψ is an Euler potential, an area averaged quantity for $\Delta^*\psi$ may be found

$$\overline{\Delta^*\psi} = \oint |\underline{\nabla\psi}| \, dl \; / \int ds$$
$$\quad\; R$$

This may equally well be applied to any other Euler potential such as the velocity stream function. In doing this, however, it is assumed that within the second ψ surface from the centre, the plasma is uniform, so detail is sacrificed. To avoid this, one would have to take into account the non-orthogonality of the mesh at the origin, and include off-diagonal terms in the metric tensor.

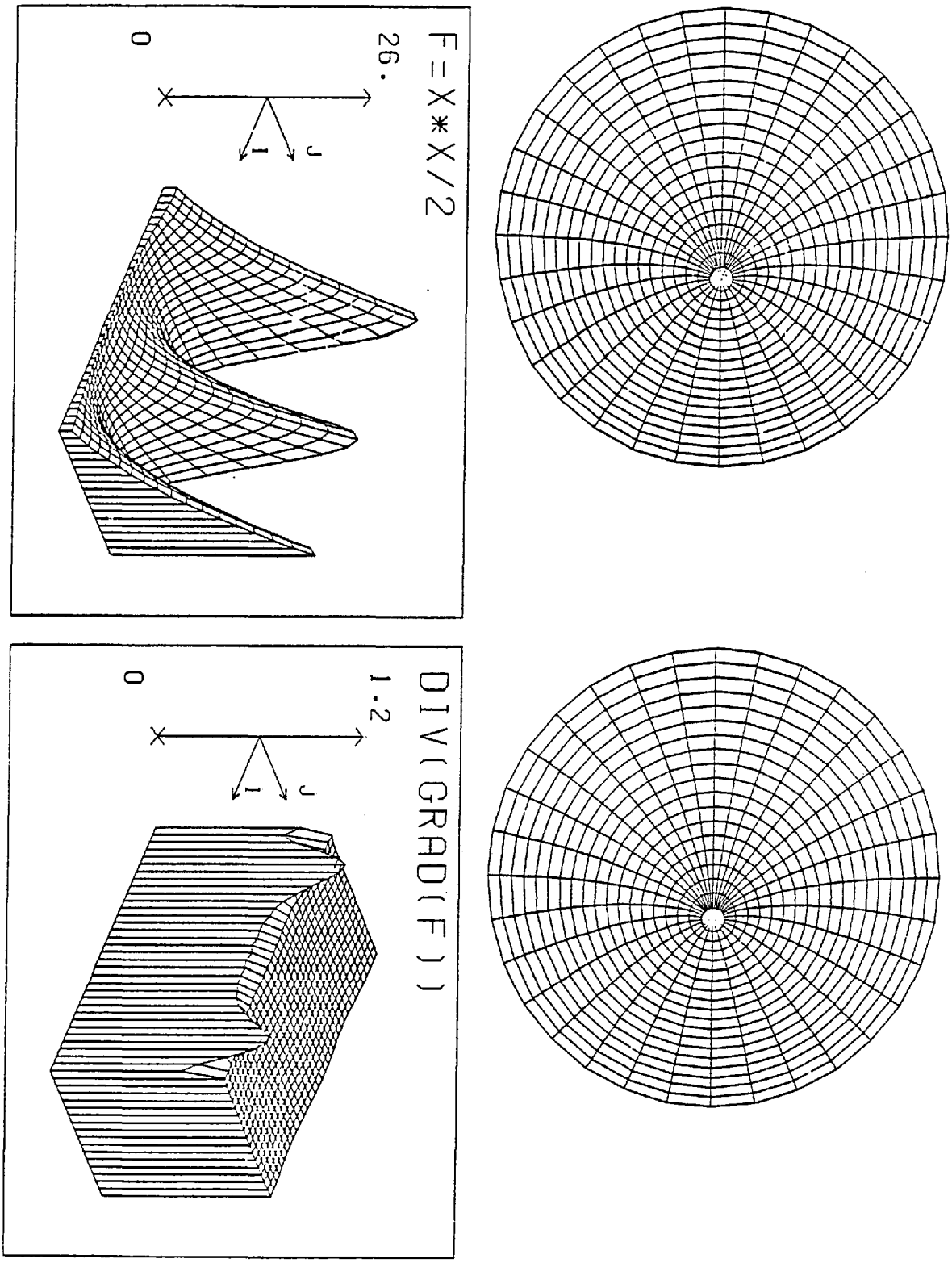

Fig. 3.10 Variation of $\frac{1}{2}x^2$ and $\nabla.\nabla(\frac{x^2}{2})$ on an orthogonalised mesh with a surface structure similar to that obtained in a Shafranov (shifted circle) equilibrium.

3.6 EXECUTION STATISTICS OF THE CODE.

Production runs of the TICTOK code use a 24 x 22 mesh; 22 Ψ surfaces each with 24 χ points around them. The χ points are spaced at equal angles around the outer Ψ surface. The orthogonalisation routine ORTHO then defines the position of the χ points on the other Ψ surfaces.

The TICTOK code runs on the CDC 6500/Cyber 174 at Imperial College or, for production runs, on the CDC 7600 at the University of London Computer Centre (ULCC). Each timestep for a 24 x 22 mesh takes approximately 2 seconds of CP time on the CDC 7600 of which about half is spent in orthogonalising the mesh. The code occupies about 25,000 words of central (small core) memory. A normal production run executes for 500 timesteps, therefore, using just over 15 minutes of CP time.

Graphical output, used extensively in chapters 4 and 6, is produced by a post-processing program MICRO, which relies upon both the MICROFILM and DIMFILM user libraries at ULCC. This program reads the information generated by a production run from a magnetic tape which may also be used to restart the simulation.

CHAPTER 4

INITIAL STAGES OF A TOKAMAK DISCHARGE

In both the first generation tokamaks (for example T-3 and ST tokamaks, hereafter referred to as "small") and the second generation, "large" tokamaks e.g. PLT and T-10 there is, in general, a complete absence of any evidence to suggest that there is a current skin effect which lasts for any significant period of the current rise phase. This is in contrast to numerical simulations[24] which show that assuming neoclassical transport coefficients should imply a pronounced and prolonged skin effect in large tokamaks. In this chapter, we present simulations of both small and large tokamaks in this low temperature current rise regime. For different values of the magnetic Reynolds number, R_m, we observe the effects of diffusion and of flow. When R_m is approximately equal to unity, a steady flow pattern arises that results in the advection of the magnetic surfaces, and enhanced penetration of the current into the discharge. The non-linear development of this flow indicates the breakup of the magnetic surface structure. This would also assist the relaxation of the current profile from a skin current to a centre peaked profile.

4.1 SKIN EFFECT IN TOKAMAKS

The distribution of current density in a solid cylindrical conductor when the total current is a sharply rising function of time, is well known[40]. For an overdamped pulse, the solutions are illustrated in Fig. 4.1. During the initial stages, the current is confined to the surface of the conductor, but after a time

$$\tau_\eta \sim \frac{\mu a^2}{15\eta} \text{ sec.} \qquad (4.1)$$

where a is the radius of the conductor in metres, the current diffuses into the conductor.

For a plasma the situation is not so clear. Firstly, the electric field, in the presence of a perpendicular magnetic field, can induce motion, and secondly, the resistivity of a plasma is a non-linear function of the local temperature. If we consider a typical large tokamak with major radius 3m, minor radius 1m, and an initial temperature of 10eV, assuming constant resistivity the skin time $\tau_\eta \simeq 2.5$ms. However, the one dimensional code[24] shows that for this size of tokamak, the skin effect is still extremely pronounced after half a second even when the electron thermal conductivity is enhanced. The hollow current profile persists because a type of thermal instability[50] occurs. The current causes ohmic heating which leads to a local temperature rise. The consequential drop in resistivity then ensures more current flows in this region.

Duchs et al.[24] restrict the persistance of the skin effect by anomalously increasing the resistivity and thermal conductivity. In our typical tokamak, the anomally factors for resistivity γ^* and thermal conductivity κ^* affect the skin time thus:

$$\tau_\eta \sim 8.10^4/(\gamma^*\kappa^{*3})^{\frac{1}{4}} \quad \text{ms}$$

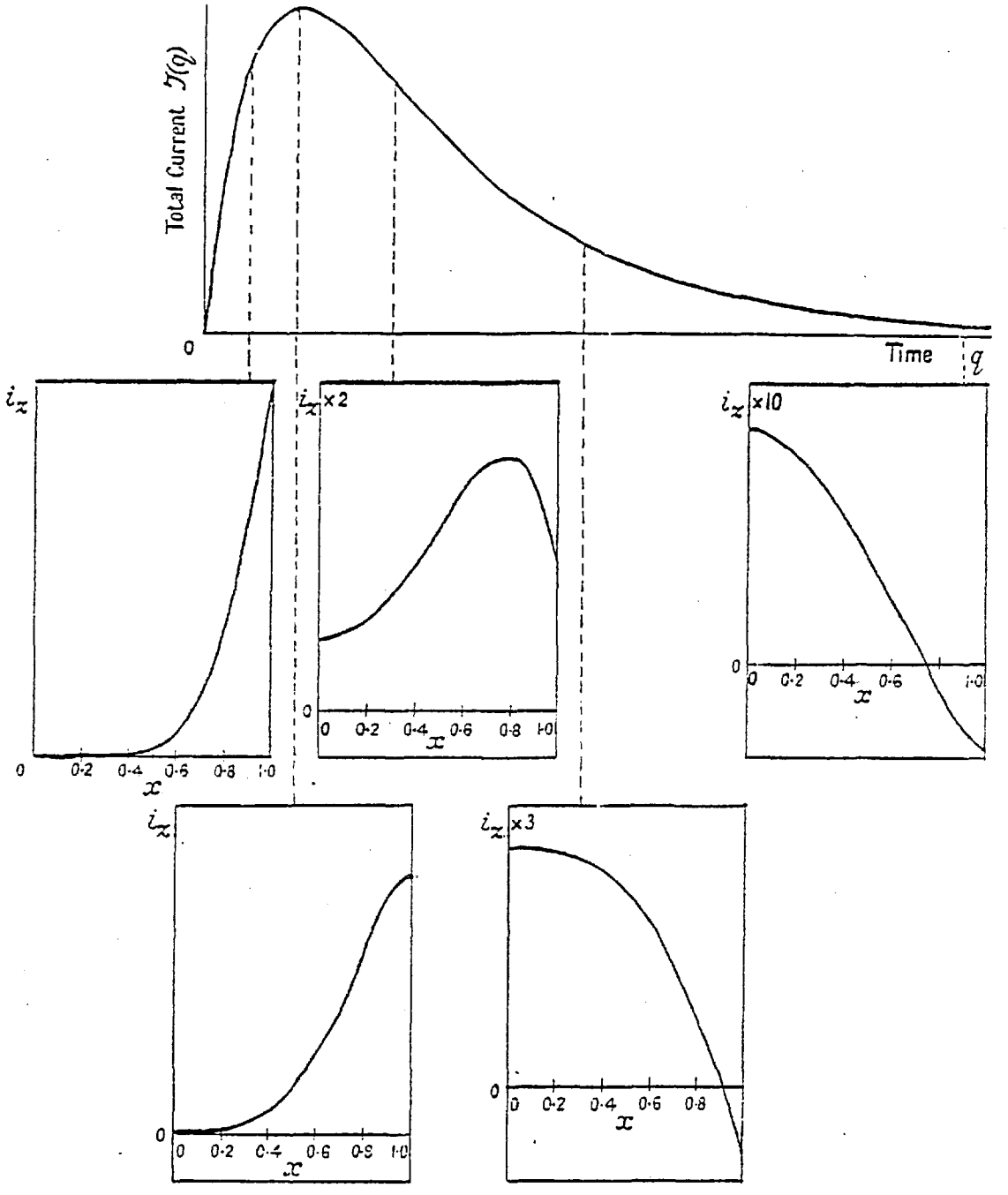

Fig. 4.1 Current density distribution in a solid conductor for a sharply rising overdamped current pulse[40].

Enhancing the resistivity is relatively ineffective, so an enhancement to the thermal conductivity of 10^4 beyond the classical value is required. This, however, leads to excessive energy dissipation and loss of volt-seconds. The energy is lost by the plasma to the limiter and the magnitude of the heat pulse is such that no existing limiter could cope with this without excessive wear.

An alternative approach by which the skin effect may be prevented, is to use a moving limiter. This was suggested initially by Kadomtsev[51] and is modelled in the Duchs code. It requires the limiter radius to behave

$$r_{limiter}(t) \propto (I(t))^{\frac{1}{2}}$$

The plasma radius is allowed to expand as the current increases and fills the aperture without forming a skin. They now find heat loading on the limiter is minimal and the limiter speed is not so great as to present any technical problems. It is assumed, however, that as the limiter aperture expands, the plasma density at the moving limiter edge materialises as required to give the required radial density profile. In practice, this may need to be provided by neutral gas injection and preionisation.

Experimentally, this is unnecessary. Moving limiters are not employed in large tokamaks and neither does excessive damage to the limiter occur. Data from T-3[52] and ST[53] tokamaks do not suggest the existence of a current skin. In large tokamaks, such as PLT[54] and T-10[55] there is no reported difficulty connected with penetration of the current. In fact, the only reported observation of a skin effect in a tokamak is in the LT-3 tokamak[56]. Using magnetic probe measurements during the early stages of the discharge, the toroidal current density profile was derived. This has a distinctly hollow profile for the first 0.5 ms of the

discharge, Fig. 4.2, but then relaxes to a substantially flat profile at about 0.7 ms. The safety factor, q, is measured throughout the discharge and during the period when the toroidal current density is hollow, q is about 8 on the magnetic axis and falls to a minimum of below 4 within the plasma. After 0.7 ms the q profile is approximately flat at about 4.

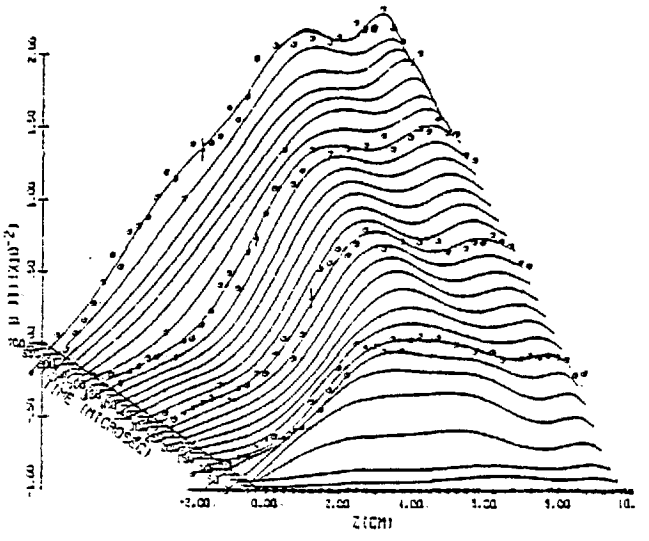

EVOLUTION OF POLOIDAL MAGNETIC FIELD

(a)

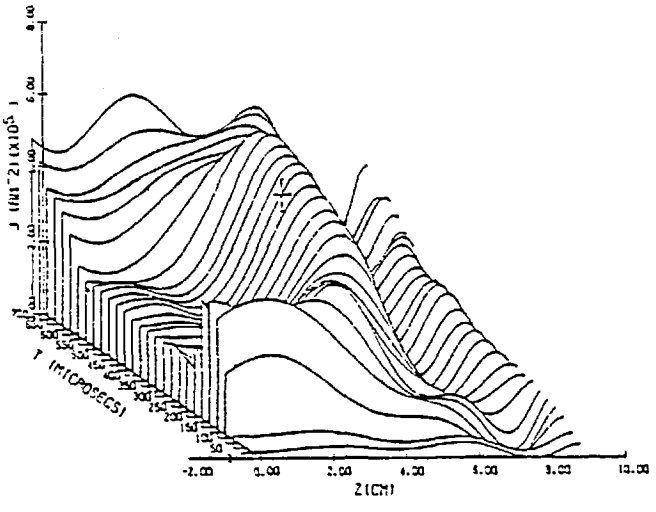

EVOLUTION OF CURRENT DENSITY

(b)

Fig. 4.2 The evolution of (a) poloidal magnetic field and (b) current density in the LT-3 tokamak[56].

When a minimum of the q profile occurs within a discharge, one expects the discharge to be unstable to all resistive MHD (tearing-mode) perturbations[19]. The non-linear growth of two tearing-mode perturbations has been postulated to cause disruption of the magnetic surfaces and hence rapid levelling of the current profile. In the LT-3 tokamak, magnetic perturbations indicate the presence of a slowly growing m = 4 mode. This is followed by a substantial increase in diffusion of runaway electrons at about the time the current distribution relaxes to a flat profile. This is indicative of the overall disruption of the magnetic surfaces. Observations of MHD mode structure in T-3 also show the presence of m = 4 - 6 perturbations[57] while the current is rising.

The overall picture is then of the non-linear temperature dependence of the resistivity being responsible for the occurence of a pronounced skin effect. This, however, modifies the q profile making the skin area unstable to tearing-mode perturbations. This instability causes the subsequent relaxation of the hollow current distribution to a centrally peaked profile by enhanced transport caused by the reorganisation of the magnetic surface structure.

4.2 MECHANICS OF THE SIMULATION

4.2.1 1 - D or 2 - D?

While the current is rising, at least, the tokamak is most definitely a two dimensional problem. The current in the primary of the transformer induces a varying magnetic flux in the iron core that in turn produces an electric field, varying inversely with major radius, R. The electric field is therefore greater on the inner side of the torus than on the outer, an effect that will be more pronounced in the new second generation (large) tokamaks, which have small aspect ratios. In a uniformly preionised plasma, this electric field will induce a larger current on the inner side, which will cause the temperature to rise differentially. The resistivity will decrease and more current will flow. Thermal conductivity parallel to the magnetic field is a very sensitive function of temperature. This will tend to conduct the heat around the magnetic surfaces but the extent to which this happens will depend very critically on the temperature, and is also limited initially by high values of q. Local maxima of current and temperature will both lead to flow and this flow may alter the magnetic surface structure.

It is clear, therefore, that averaging around magnetic surfaces in order to form a one dimensional model is not a good approximation and that a two dimensional treatment is necessary. The model described in chapters 2 and 3 is ideally suited to this problem as it is two dimensional and contains both resistivity and thermal conductivity. That it is Lagrangian is advantageous because the modification of the magnetic surfaces is easily followed and provides resolution where it is needed.

4.2.2 Timescales

The type of behaviour we expect will depend upon the relative magnitude of four timescales in particular; the modified sound and Alfven times (Chapter 2, section 5):

$$\tau_s = \frac{a}{c_s}\sqrt{\frac{1 + R^2/a^2}{2}} \quad \text{sec} \tag{4.2}$$

$$\tau_A = \frac{a}{c_A}\sqrt{2(1 + R^2/a^2)} \quad \text{sec} \tag{4.3}$$

the resistive diffusion time, Eq. (4.1):

$$\tau_\eta = \frac{\mu_o a^2}{15\eta} \quad \text{sec}$$

and the thermal diffusion time (Chapter 3, section 3):

$$\tau_\kappa = (\gamma - 1)\frac{k}{M}\frac{\rho L^2}{\kappa} \quad \text{sec.} \tag{4.4}$$

where $L = \frac{T}{\nabla T}$.

Consider firstly the relative importance of the inertial and diffusion processes

$$\frac{\tau_n}{\tau_s} = \frac{R_m}{M_s} \sim 4\frac{a^2\theta^2}{R} \tag{4.5}$$

where R_m is the magnetic Reynolds number, M_s the sound Mach number, θ the temperature in eV, and a the radius in metres. Likewise

$$\frac{\tau_n}{\tau_A} = \frac{R_m}{M_A} \sim \frac{10^{-4} I a \theta^{3/2}}{4R} \tag{4.6}$$

where M_A is the Alfven mach number. When expressions (4.5) and (4.6) are large sound waves and Alfven waves will be the fastest processes (which one is quickest depends on $\frac{M_A}{M_s} \sim \beta_p$) and the effects of diffusion small.

Conversely, when Eqs. (4.5) and (4.6) are much less than unity, then resistive diffusion will dominate. When however, Eqs. (4.5) and (4.6) are approximately unity, then we may expect some coupling between the two processes which can lead to enhanced current penetration[58].

Consider now the timescales associated with thermal diffusion. If the Peclet number becomes greater than unity

$$P_C = \frac{v\tau_\kappa}{L} \tag{4.7}$$

where v is the characteristic flow velocity, we may expect convection to play an important role in heat transfer. Consider also the rate at which an element of fluid is heated by the current compared to the rate at which heat is dissipated by thermal conduction. If we associate a time τ_{OH} with ohmic heating, then if the ratio

$$\frac{\tau_{OH}}{\tau_\kappa} < 1$$

we may expect the fluid element to be heated faster than thermal transport can remove heat from that element. Under these conditions, preferential heating will occur in regions of the plasma where the current is largest, and the thermal conduction will not be sufficient to conduct the heat away from these hotter areas. Quantitatively, the power density supplied by ohmic heating is

$$P_{OH} = \eta J^2 \simeq \frac{\theta^{3/2}\, E^2}{10^{-3}}$$

The power density, dissipated by the thermal conductivity in a strong magnetic field is

$$P_\kappa = \nabla.(\kappa\nabla T) \simeq \frac{0.6\ \theta^{7/2}}{L^2}$$

The safety factor q relates the scale length, L, parallel to the magnetic field to a scale length, L_p, in the poloidal plane

$$P_\kappa \simeq \frac{0.6\ \theta^{7/2}}{q^2\ L_p^{\ 2}}$$

which is a much simplified version of Eq. (3.36). The ratio P_{OH}/P_κ determines the relative importance of dissipation and heating

$$\frac{P_{OH}}{P_\kappa} = 1.6\ 10^3\ \theta^{-2}\ q^2\ L_p^{\ 2}\ E^2 \qquad (4.8)$$

4.2.3 Inductance

The inductance of a conductor simply represents the distribution of current density within a conductor, without depending upon the actual magnitude of the current. For this reason it is an ideal indicator of the current distribution within a plasma and is often used as an experimental diagnostic, for example in z-pinch plasmas.

Inductance is normally defined as

$$L = \frac{\psi}{I} \qquad (4.9)$$

where ψ is a flux per unit length. Expressing both the flux and current as integral quantities, and using the geometry defined in Fig. 4.3

$$L = \mu_o \frac{\int \underline{B_p}.\underline{ds}}{\oint \underline{B_p}.\underline{dx}}$$

Now $\underline{B_p} = \nabla\psi \times \nabla\phi$ and if ds is an area element per radian in the ϕ direction then the inductance is

$$L = \frac{\mu_o}{K} \qquad (4.10)$$

where

$$K = \oint \frac{h_x}{R h_\psi}\ dx$$

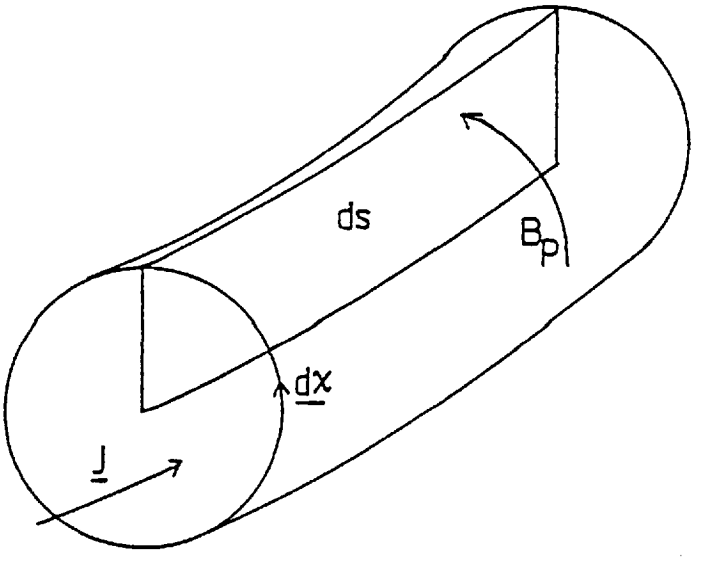

Fig. 4.3 Geometry used for inductance calculations

We see therefore, that the inductance is a purely geometrical relationship depending only upon the scale factors of the flux surface coordinate system. The inductance may therefore be altered, not only by the resistive diffusion of the current into the plasma, but also by the motion of the plasma itself which will move the flux surfaces.

The inductance will therefore, indicate the extent to which the current distribution has penetrated the plasma. Consider, for example, a cylindrical conductor with the current flowing in an annular region, Fig. 4.4

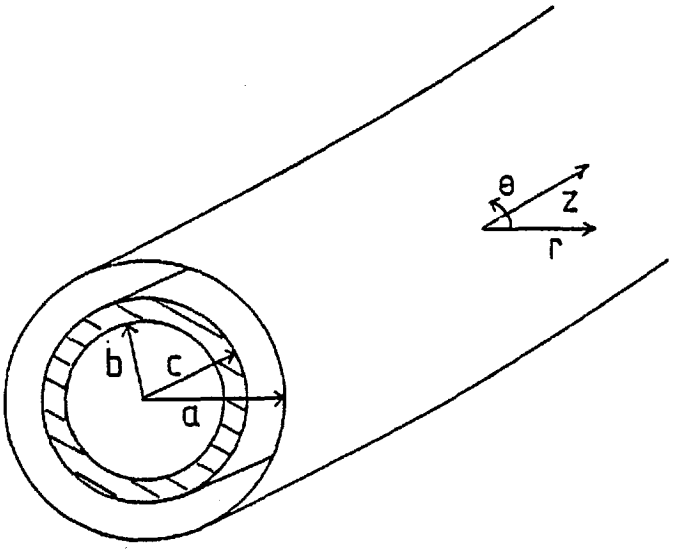

Fig. 4.4 A cylindrical conductor with the current flowing in the annular region bc.

The current density in the z direction

$$\begin{aligned} J_z(r) &= 0 \quad && r < b \\ &= J \quad && b < r < c \\ &= 0 \quad && c < r < a \end{aligned}$$

Now

$$\psi = \int \underline{B} \cdot \underline{ds}$$
$$I = \int \underline{J} \cdot \underline{dA} \quad = \quad \pi J(c^2 - b^2)$$

(where dA is in the $r - \theta$ plane and ds in the $r - z$ plane) and

$$\begin{aligned} B_\theta(r) &= 0 && && r < b \\ &= \frac{\mu_0}{2} J && \left(r - \frac{b^2}{r}\right) && b < r < c \\ &= \frac{\mu_0 I}{2\pi r} && && r > c \end{aligned}$$

Therefore after a little manipulation we find the inductance per unit length

$$L = \frac{\mu_0}{4\pi}\left[1 + 2\ln\frac{a}{c} - 2\frac{b^2}{c^2 - b^2}\ln\frac{c}{b}\right] \qquad (4.11)$$

As we take various limits, Eq. (4.11) becomes more familiar. For the constant current case, $b \to o$, $c \to a$ we have

$$L_{cc} = \frac{\mu_0}{4\pi}$$

and for a skin current where $b \to c \to a$

$$L_{sk} = O$$

and finally for a delta function current distribution on the axis at $r = o$, where $b \to o$ and $c \to o$

$$L_{\delta} = \frac{\mu_0}{2\pi}\ln\frac{a}{c}$$

which approaches infinity logarithmically.

We note therefore that the inductance per unit length of a cylindrical conductor with a uniform current profile is

$$L_{cc} = 10^{-7} \text{ henries}$$

and for a skin current is

$$L_{sk} = O \text{ henries}$$

4.3 NUMERICAL SOLUTIONS OF THE CURRENT RISE PHASE

The current rise phase was simulated in two contrasting machines. One simulation of a small tokamak, was based on the LT-3 experiment[59] which is a fairly large aspect ratio device. The other simulation, of a large tokamak, was derived from the proposed Joint European Torus (JET)[60] and has a small aspect ratio. In each case, a number of simulations were performed to investigate the effect of varying certain parameters. A selection of those runs is presented here.

4.3.1 Small tokamak

The first series of simulations are of the current rise in a small tokamak with the parameters of LT-3 (see Table 4.1). The initial electron density is assumed to be 5.10^{19} m^{-3} and the discharge gas deuterium. At all times it is assumed that this gas is fully ionised at all chosen initial temperatures, i.e. in the range 1 to 10 eV. Efficient pre-ionisation at these temperatures can impose severe limitations on the range of filling pressures and driving electric fields[61], but this may be avoided by using a strong HF pre-ionisation.

At an initial temperature of 1 eV resistive diffusion is the fastest process with a classical diffusion time of $\tau_\eta \sim 0.5$ μs (Eq.(4.1)) compared to a sound time of $\tau_s \sim 22$ μs (Eq.(4.2)) and an Alfven time of $\tau_A \sim 120$ μs (Eq. (4.3)). Figure 4.5 shows contour plots in the poloidal plane of (a) the vorticity Ξ, (b) stream function ζ, (c) the product of the toroidal current density and major radius R in units of $\mu_0 R J_\phi$, and (d) energy in eV at approximately one classical diffusion time. As with all these diagrams of the poloidal plane, the major axis lies to the left. It is clear that even after only one diffusion time, a current distribution that is peaked at the centre is already well established.

TABLE 4.1

	LT-3	JET
Minor radius, a (m)	0.1	1.28
Major radius, R_o (m)	0.4	2.93
Toroidal magnetic field, B_ϕ (T)	0.5	3.0
Initial toroidal current, I_o (kA)	1	10
Maximum toroidal current, I_m (kA)	15	1000
Current rise time, τ_I (ms)	1	10
Effective Z (axis)	1	1
Effective Z (wall)	2	2
Initial q(a)	60	900

The flow is very small and arises from vorticity generated almost entirely from gradients of pressure, Fig. 4.6, parallel to the major axis, near the wall (Eq. 2.19). Preferential heating on the inner side (the side nearest the major axis) is evident. This is caused by more Ohmic heating to this area because the current density is larger there, although the effects of the current penetration is obvious as the heated region is extending across the whole left hand side of the torus. This is not an effect of the thermal conductivity because if we look at the heating to dissipation ratio, Eq. (4.8)

$$\frac{P_{OH}}{P_\kappa} \sim 1.6\ 10^3\ \theta^{-2}\ q^2\ L_p^{\ 2}\ E^2$$

when $\theta = 1$ eV, $q = \frac{a\ B\phi}{R\ B_p} \sim 60$, $L_p \sim$ a metres and $E \sim 10$ V/m we obtain

$$\frac{P_{OH}}{P_\kappa} \sim 10^7$$

confirming that thermal conductivity is unimportant in this case.

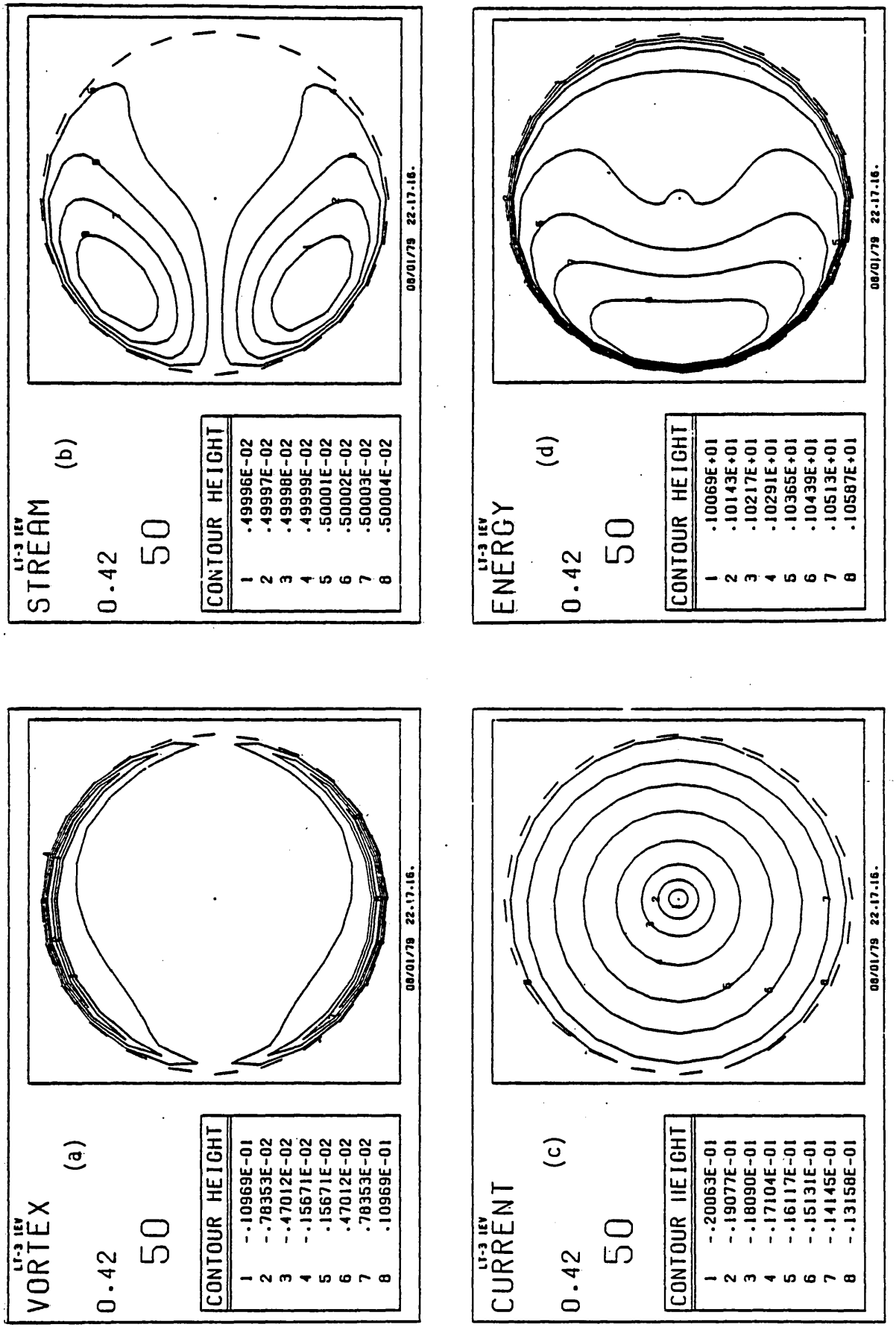

Fig. 4.5 Contour plots shown after one classical diffusion time, (a) the vorticity, (b) stream function, (c) the current in units of $\mu_0 R J_\phi$ and (d) the temperature in eV. The contour heights are equally spaced from the lowest value (contour 1) to the highest (contour 8). Simulation time in μs and time-step number are shown above contour heights. The major axis is to the left.

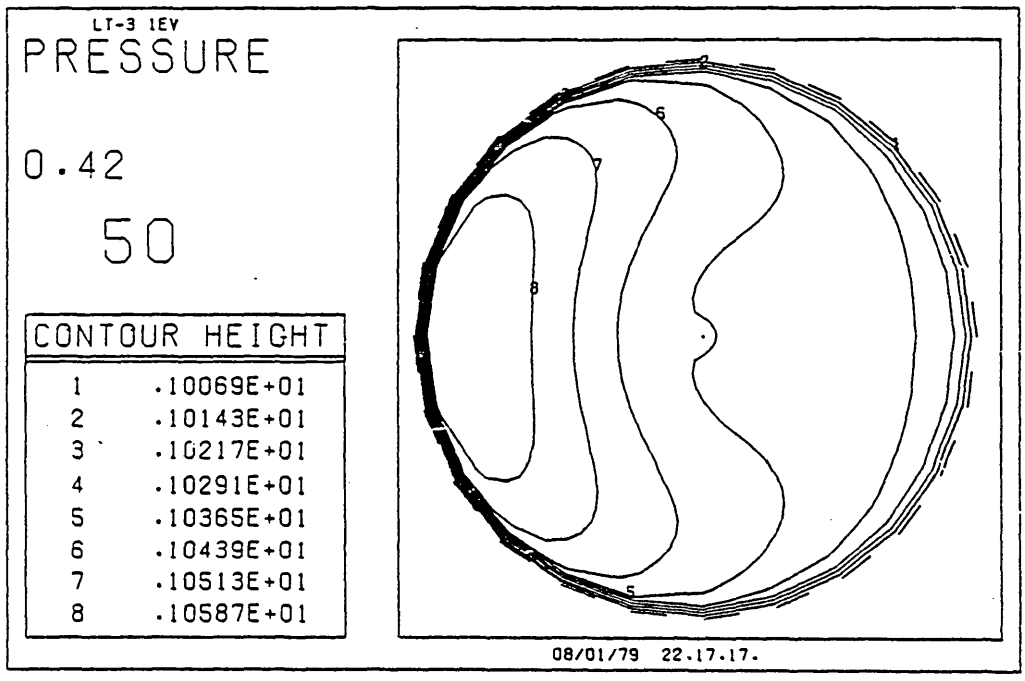

Fig. 4.6 Pressure gradients parallel to the major axis are responsible for the flow pattern seen in the last figure.

As a confirmation of our conclusions, we look to the time history of the total current, voltage and inductance, Fig. 4.7. The current is a prescribed function of time and the voltage is that normally measured in tokamaks as the loop voltage

$$V = \oint \underline{E}.d\underline{\ell} \qquad (4.12)$$

where $d\underline{\ell}$ is parallel to $\nabla\phi$ i.e. in the toroidal direction. The electric field is calculated from the rate of change of poloidal flux at the plasma edge minus that at the magnetic axis.

$$V = -2\pi R \left(\frac{\partial\psi}{\partial t}\bigg|_{r=a} - \frac{\partial\psi}{\partial t}\bigg|_{r=o}\right)$$

As the plasma vacuum boundary is held fixed, this voltage is just a measure of the difference of electric field between the magnetic axis

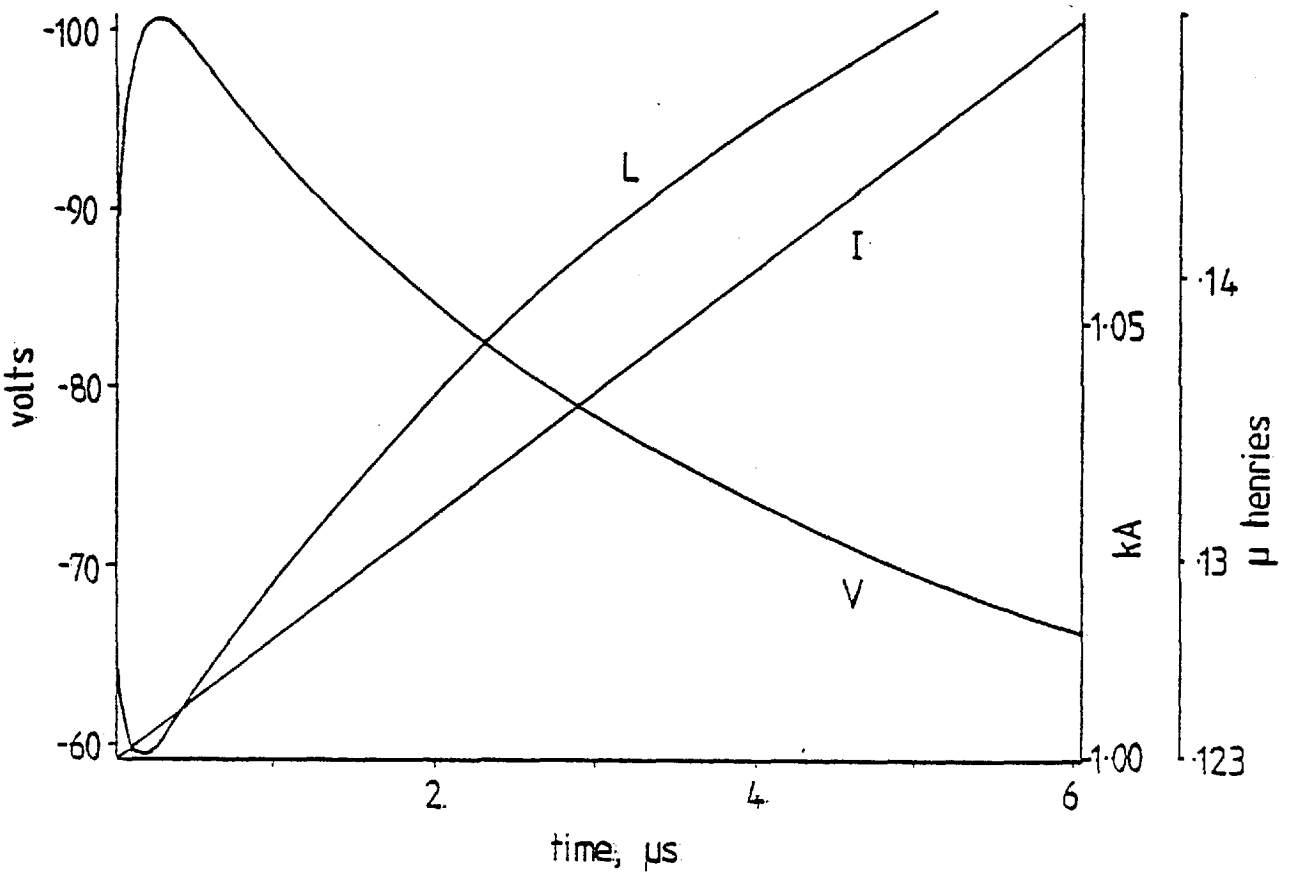

Fig. 4.7 Traces of voltage, current and inductance against time for 1eV initial temperature in LT-3.

and plasma boundary. ψ is changed on the plasma edge so that a prescribed current flows, while ψ on the axis is determined by resistive diffusion. The inductance is trivially derived from the total magnetic energy

$$L = \frac{2\ Um}{I^2} \qquad (4.13)$$

We note that although I is a linearly increasing function of time, the loop voltage, V, after an initial sharp increase, decreases steadily. This indicates that initially the electric field increases sharply on the

edge, signalling the formation of a skin current. After less than 0.5 μs the voltage has started to decrease showing that the electric field, and therefore, the current is starting to penetrate the interior of the plasma. This is confirmed by the inductance which, after an initial decrease, increases past its initial value.

When the initial temperature is raised to 5eV, the sound and diffusion times are much closer than in the previous simulation; τ_s ~ 10 μs and τ_η ~ 6 μs. After one classical diffusion time, a centre peaked distribution has begun to form, but there is still appreciable current flowing near the plasma edge.

Finally, at an initial temperature of 10eV, when the sound time is τ_s ~ 7 μs and less than the diffusion time of τ_η ~ 16 μs, a skin current is still well developed even after nearly one classical diffusion time, Fig. 4.8.

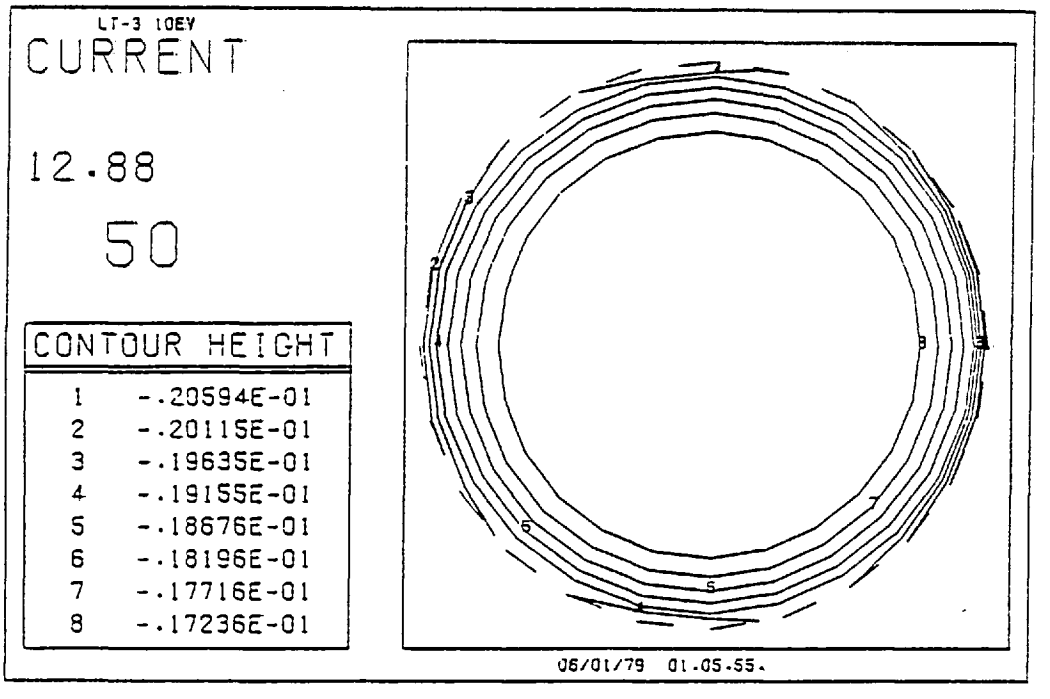

Fig. 4.8 The current, after nearly one diffusion time in LT-3 with an initial temperature of 10eV.

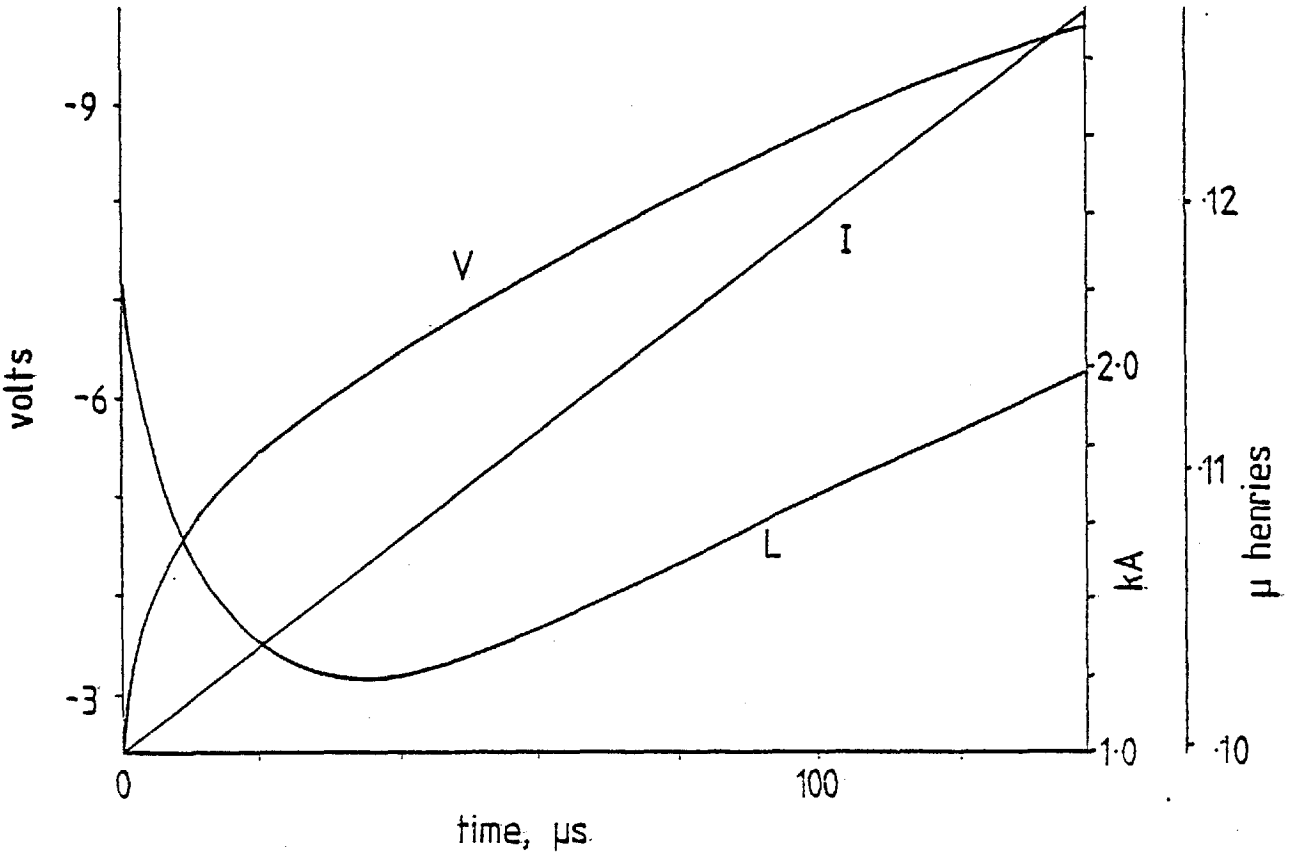

Fig. 4.9 Traces of voltage, inductance and current for the same parameters as Fig. 4.8.

At 16 μs Fig. 4.9 shows that not only is the loop voltage increasing, which indicates that the electric field is not penetrating and current is accumulating at the plasma edge but also the inductance is decreasing, confirming the formation of a current skin.

These three simulations have covered ratios of τ_η/τ_s of approximately .02 to 2. As this ratio has increased we have seen a deviation from classical current penetration. In the first run, the plasma behaved as would a solid conductor and the current has penetrated during a classical diffusion time. As the ratio τ_η/τ_s is increased, less

current penetration occurs within a classical diffusion time. As the sound time becomes comparable to the diffusion time, the plasma flow becomes increasingly important. With an initial temperature of 1eV after $t = \tau_\eta$, the plasma velocity in units of minor radius per microsecond (Fig. 4.5(b)) is $v \sim 1.5.10^{-5}$ (~ 1.5 m/s). At $t = \tau_\eta$ in the 10eV run, the maximum flow speed is $v \sim 7.2.10^{-4}$ (~ 72 m/s), Fig. 4.10. As the flow contributes to the electric field in the plasma, it will obviously affect the current distribution.

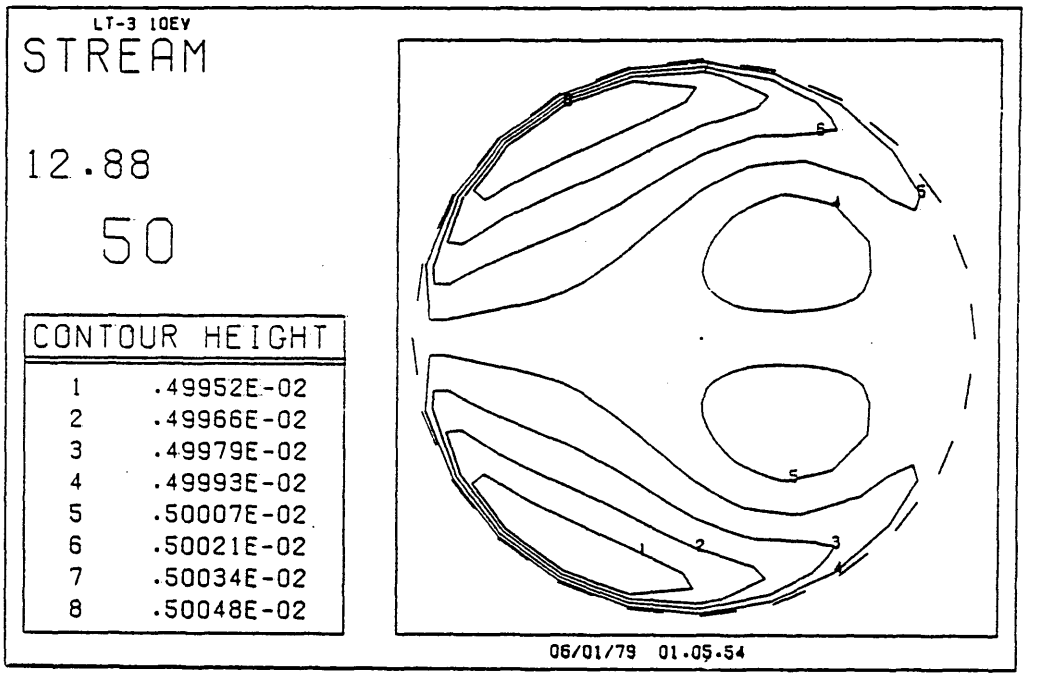

Fig. 4.10 Stream function after nearly one classical diffusion time in LT-3 with the same parameters as Fig. 4.8.

Consider in turn a solid conductor and a highly conductive plasma, given Ohms Law

$$\eta \underline{J} = \underline{E} + \underline{v} \times \underline{B}$$

In the conductor there is no flow, so $\eta \underline{J} = \underline{E}$ together with Faradays Law

gives a diffusion equation for the magnetic field into the conductor. Conversely, in a perfectly conducting plasma, flow will occur so that

$$\underline{E} + \underline{v} \times \underline{B} = 0$$

In a perfectly conducting plasma, this will prevent the magnetic field in the moving fluid frame from changing and therefore affect the penetration of current. Between these two limits, it is clear that flow in a resistive plasma can affect the current distribution.

If we now continue the simulation with an initial temperature of 10eV past 16 μs we see the effect of this plasma flow. First, Fig. 4.9, the inductance reaches a minimum value and then increases indicating that current penetration has begun. Secondly, dV/dt becomes negative indicating that the electric field on the magnetic axis is increasing, and less current is accumulating in the skin.

The plasma flow is at first generated by a pressure gradient parallel to the major axis. Reproducing Eq. (2.19):

$$\frac{1}{R}\frac{d\Xi}{dt} + \left|\nabla v^2 \times \nabla R^2 \rho\right| = \left|\nabla p \times \nabla R^2\right| + R\,\underline{B}.\nabla\, RJ_\phi$$

we see that this pressure gradient leads to the generation of vorticity, Fig. 4.11. Flow results which attempts to reduce the pressure gradient by increasing the density in the low pressure region, near the edge of the plasma. In this it is largely successful, for after a number (~ 15) sound times, these sound waves are dissipated and $\nabla p \times \nabla R^2 \sim 0$, Fig. 4.12(a).

The flow, however, persists because RJ_ϕ now varies around a magnetic surface, Fig. 4.12(b). This occurs because diffusion of the magnetic surfaces through the plasma is reduced where the plasma is hottest, Fig. 4.12(c), which is near the inner edge. This impedes current penetration, but where the temperature is lower, the magnetic surfaces diffuse inwards more easily. The variable "etachi" gives a quantitative

description of this phenomenom.

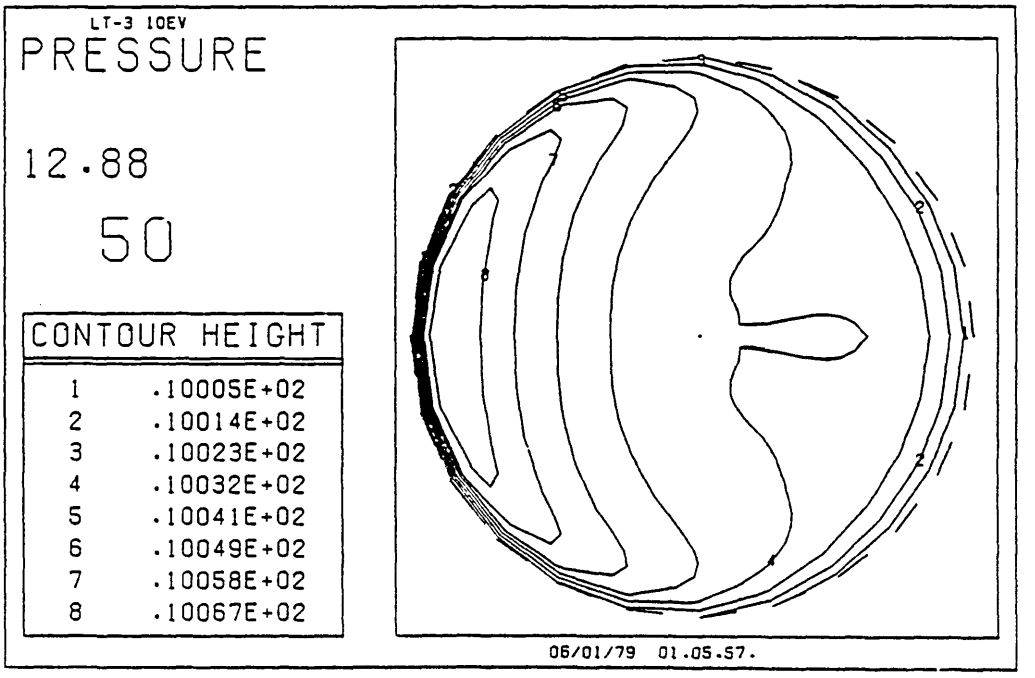

Fig. 4.11 Pressure after nearly one classical diffusion time in LT-3 with the same parameters as Fig. 4.8.

"Etachi" is given by Eqs. (3.18) and (3.20) and is:

$$-\underline{v}_{fm}\cdot\nabla\psi = \eta RJ_\phi - \langle\eta RJ_\phi\rangle$$

and is a measure of the velocity of the fluid relative to the mesh that arises because of differential resistive diffusion. The average motion of each surface is treated by changing the value of ψ on that surface, but the surface must then be moved differentially to account for the variation of resistive diffusion around the surface.

Figure 4.12(d) indicates that the largest outward motion of the surfaces relative to the fluid to correct for the average resistive diffusion is on the inner edge of the plasma. Around the edge, this relative motion decreases rapidly until on the outer edge the surfaces

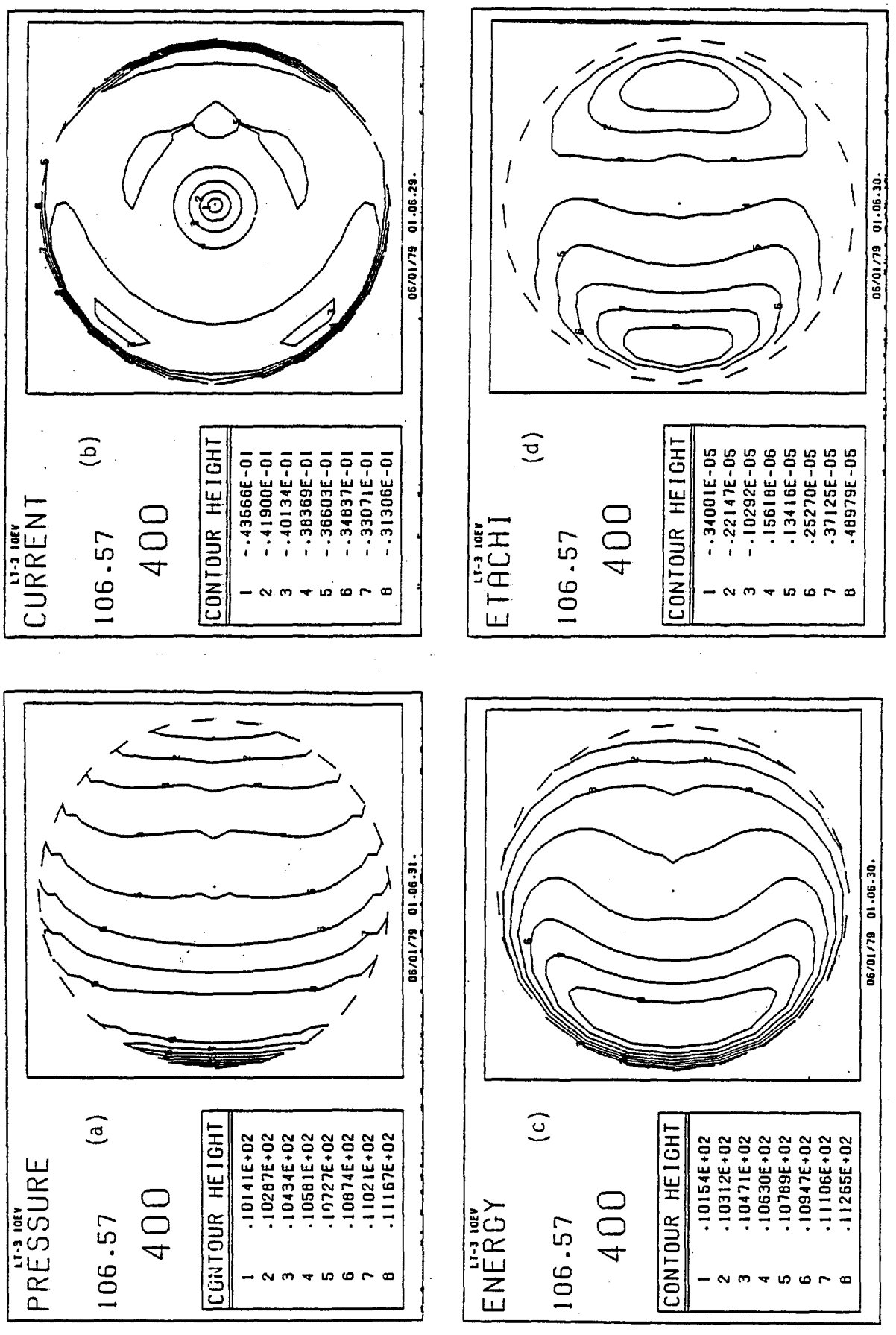

Fig. 4.12 Contour plots of (a) pressure, (b) current, (c) temperature, and (d) etachi for LT-3, with the same parameters as Fig. 4.8, after approximately 15 sound times, or 7 diffusion times.

must move inwards relative to the fluid. Current is therefore able to diffuse into the plasma more quickly in regions other than the inside edge, and causes vorticity, Fig. 4.13(a) because the gradient of RJ_ϕ in the magnetic surfaces is no longer zero. The flow, Fig. 4.13(b), is similar to that produced by the pressure gradient, but will persist as long as there is a gradient of RJ_ϕ in the magnetic surfaces. This is driven by preferential heating on the inner side of the torus which will persist until the thermal conductivity is large enough for dissipation to occur. From Eq. (4.8) we see that the temperature must rise to about 1 keV before thermal conductivity can overcome the ohmic heating source. The flow will therefore persist, and after about 107 μs the maximum velocity has reached 290 ms^{-1}, Fig. 4.13(c).

The flow speed outwards along the midplane from the inner edge is smaller, about 65 ms^{-1}. Even if we assume this speed does not increase, a fluid element originating at the edge will reach the centre of the torus after about 1 ms. A fluid element above or below the midplane will not travel as fast so surfaces advected with the fluid will exhibit a shape shown in Fig. 4.14. This will be aided by the higher temperatures in the region near the inner edge, because although the magnetic surfaces will tend to diffuse through the fluid and may be left behind, this diffusion will be smaller where the temperature is higher. The advection does not help the penetration of the temperature to the interior of the plasma to any great extent. The heating rate by convection is only about 10eV per sec. in the hottest region of the plasma near the inner wall. This is because conservation of energy demands that fluid elements moving away from the major axis should cool. Whilst they may displace colder elements, the heating effect will be reduced.

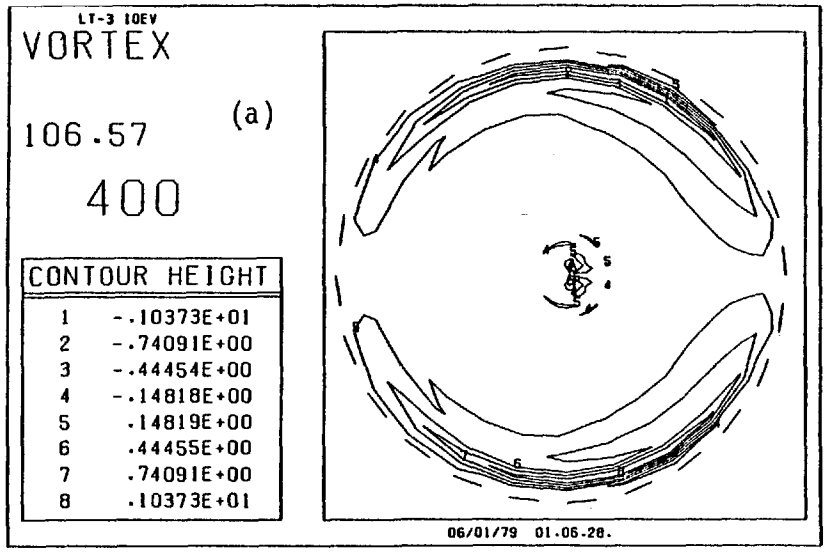

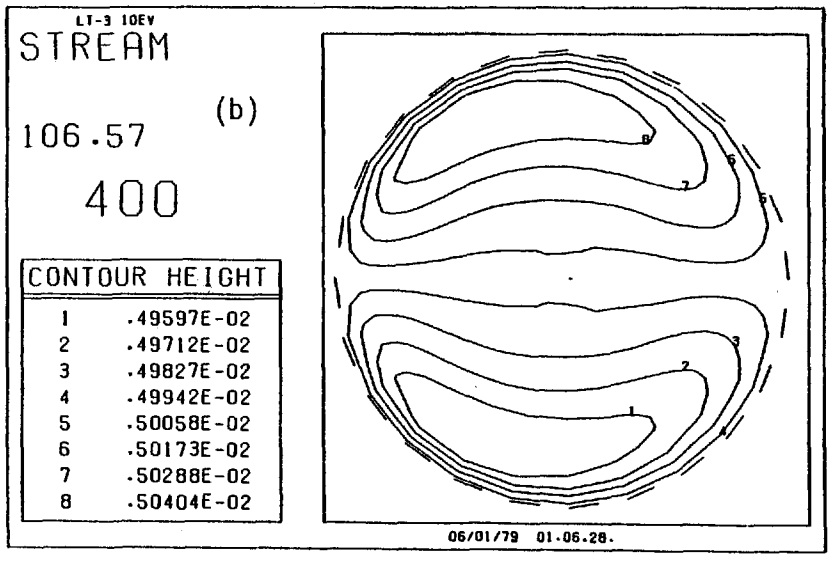

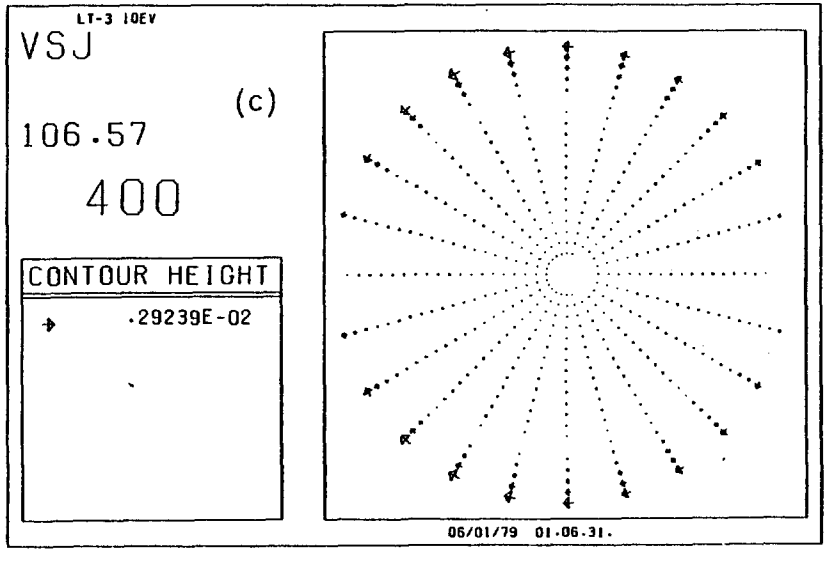

Fig. 4.13 (a) Vorticity
(b) Stream function and
(c) Flow velocity at the same instant as Fig. 4.12.

Advection could therefore lead to a disruption of the magnetic surfaces in an m = 2, n = 0 instability. This would occur on a times scale comparable with the instability and relaxation of the skin current seen experimentally in LT-3.

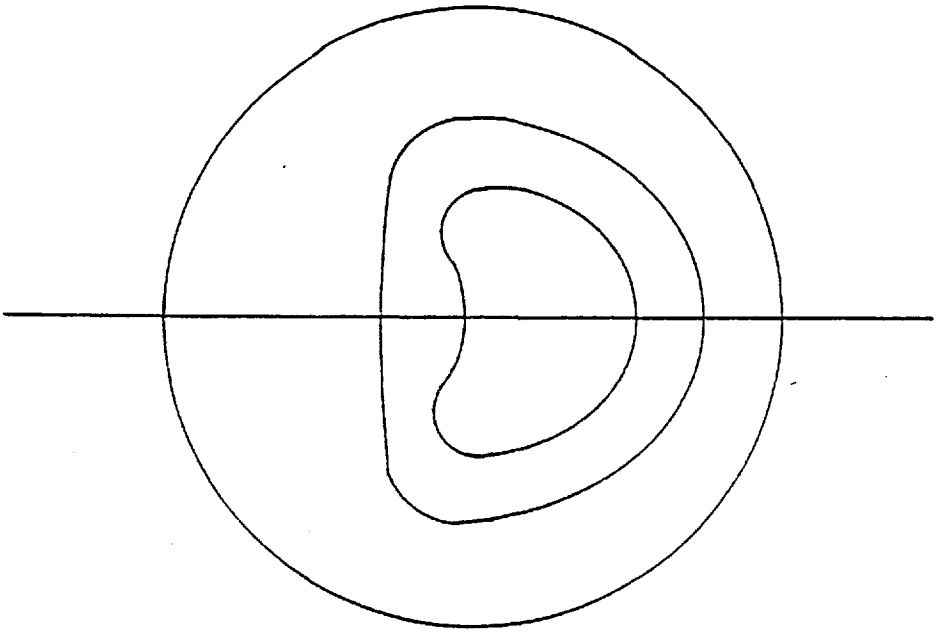

Fig. 4.14 Predicted shape of the magnetic surfaces as a result of steady flow arising from gradients of RJ_ϕ in the magnetic surfaces.

4.3.2 Large tokamak

The second series of simulations are of the current rise phase in a large tokamak based on JET (for parameters see Table 4.1). Again the initial electron density is 5.10^{19} m^{-3} and the discharge gas is deuterium which is always assumed fully ionised. The JET tokamak differs from the LT-3 tokamak discussed in the previous section in two

essential features. Firstly, it has a much larger minor radius, 1.28 m compared to 0.1 m in LT-3, and secondly, the aspect ratio is much smaller, 2.3 compared to 4 in LT-3. It is because of these two differences that we obtain markedly different numerical solutions at similar initial temperatures.

For an initial temperature of 3eV, the classical diffusion time in a large tokamak is much greater than the sound time. For JET, the ratio is 4.75 with $\tau_\eta \sim 475\mu s$ and $\tau_s \sim 100\mu s$. This is even larger than the ratio of τ_η/τ_s for the highest initial temperature in LT-3 where we saw that the plasma flow had a marked effect on the current penetration.

After approximately one diffusion time, Fig. 4.15(a), two opposing vortices have been generated in the upper half of the torus. Again, refering to Eq. (2.19), the negative vortex is produced by the second term, i.e. the gradient of RJ_ϕ parallel to B_p, Fig. 4.15(b), and is reinforced by the negative vertical pressure gradient at the edge, Fig. 4.15(c). The small positive vortex is produced by the positive pressure gradient just inwards from the edge. The current density and pressure distributions are quite different from those seen in LT-3. This is largely because thermal conductivity has a much smaller effect, because the ratio P_{OH}/P_κ, Eq. (4.8) is much larger, not only is q much bigger, but as JET is a far larger machine, L_p is also. Thus for θ = 3eV

$$\frac{P_{OH}}{P_\kappa} \sim 2.2.10^9$$

This large ratio of thermal heating to dissipation, coupled with a larger ratio of τ_η/τ_s results in marked preferential heating on the inner side of the torus, Fig. 4.15(d).

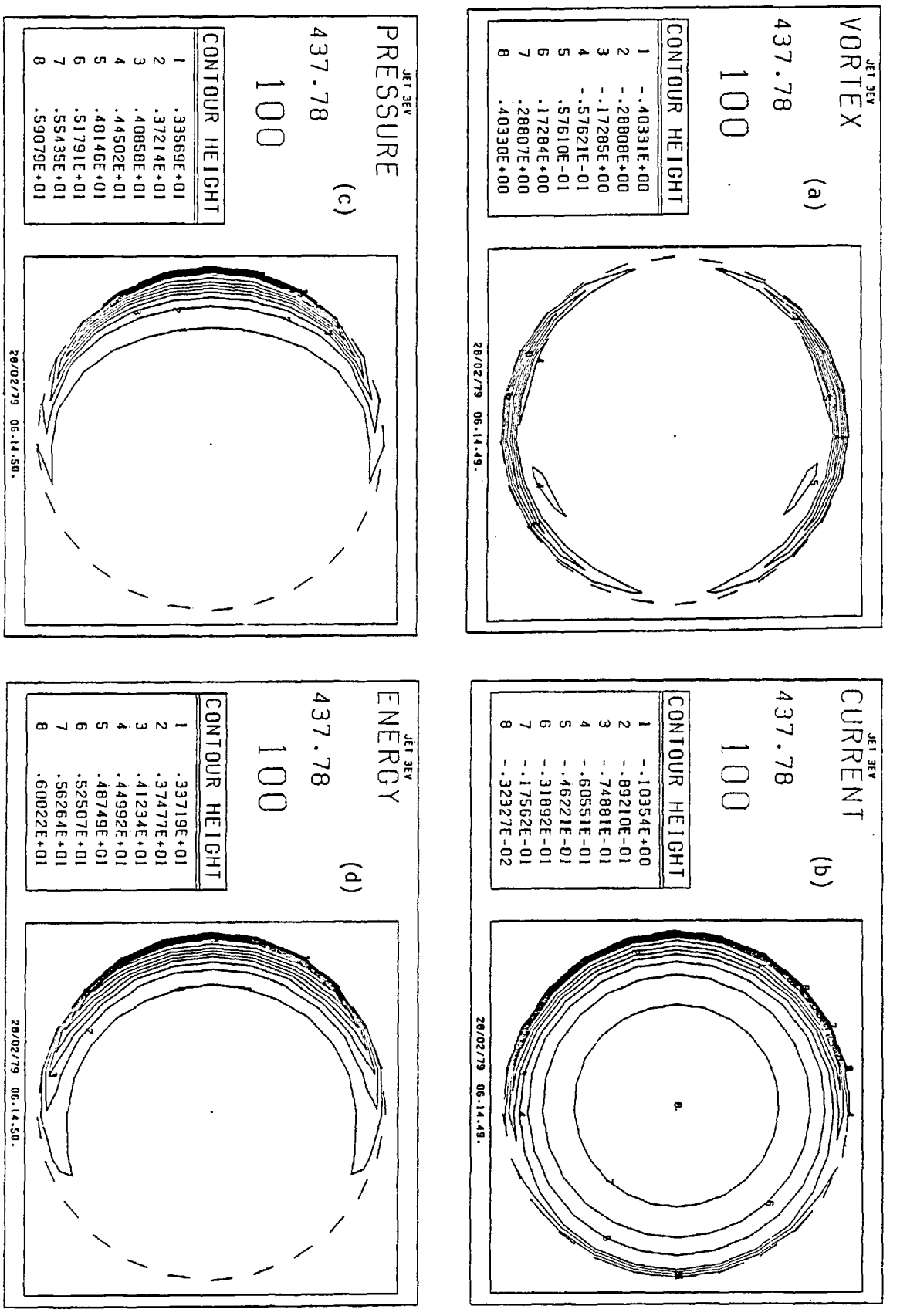

Fig. 4.15 Contour plots of (a) vorticity, (b) the current ($\mu_0 R J_\phi$) (c) the pressure, and (d) the temperature (eV) after one classical diffusion time for a tokamak with the parameters of JET with an initial temperature of 3 eV.

The vorticity pattern, Fig. 4.15(a), produces counter rotating cells shown in the stream function, Fig. 4.16(a), that correspond to flow in a direction shown diagramatically in Fig. 4.16(b), confirmed by the arrow plot of Fig. 4.17(a). The maximum flow velocity, which occurs parallel to the magnetic surfaces is $4.2.10^3$ ms^{-1}. This flow advects the plasma which is most clearly seen in the plot of density. As discussed in section 5 of Chapter 2, a consequence of assuming toroidal incompressibility is that a volume element is compressed as it moves towards the major axis. Conservation of mass implies therefore, that $\rho \propto {}^{1}/_{R^2}$. Thus in Fig. 4.17(b), where flow moves the plasma towards the major axis, the density is higher; where the flow is away from the major axis, the density is lower. The flow also advects the magnetic surfaces, moving the magnetic axis nearer the major axis.

In Fig. 4.17(c), the variable "etachi" is plotted. Broadly speaking, as the fluid velocity perpendicular to the magnetic surfaces is small, "etachi" shows that the mesh is moving outwards on the left of the magnetic axis, and inwards on the right, the top and the bottom. Thus, superimposed on the general inward diffusion of the poloidal flux, accounted for by a $\partial\psi/\partial t$ on each surface, the surfaces are diffusing into the plasma at a greater rate on the right, top and bottom of the magnetic axis.

Finally, it is interesting to note that the flow away from the heated region is resisted by poloidal currents, Fig. 4.17(d), generated as the flow tries to move the mesh. The cross product of these currents with the toroidal field (parallel to the toroidal current) leads to a force towards the major axis in the hot region.

Thus after one diffusion time, the situation is by no means as clear as it was for a similar temperature in a small tokamak. Pressure variations in the vertical direction caused by ohmic heating cause a flow that moves the magnetic axis towards the major axis.

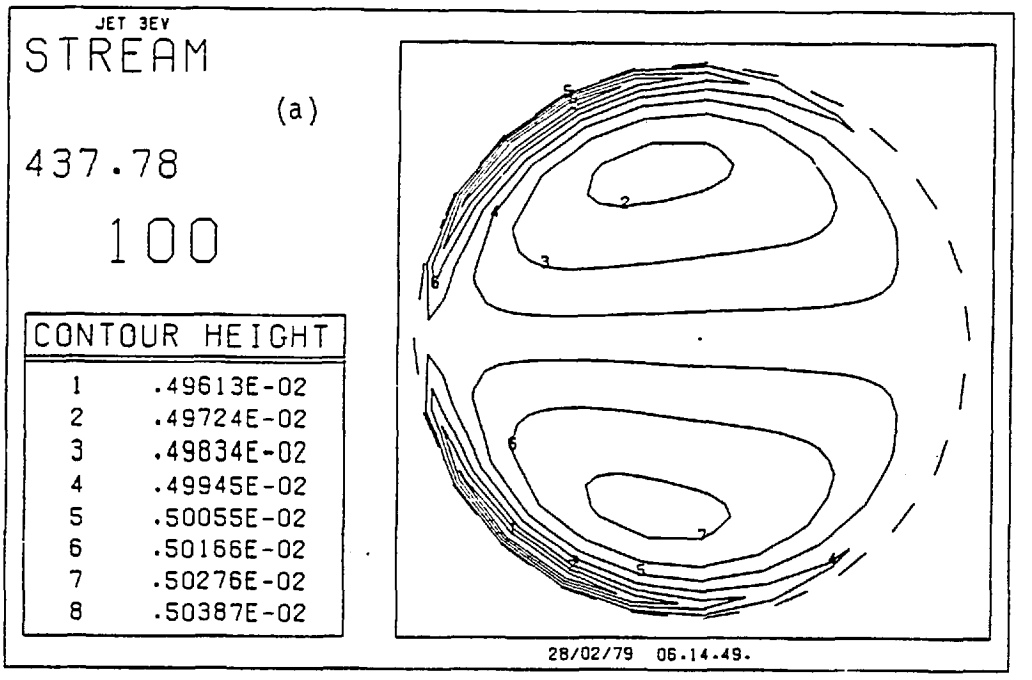

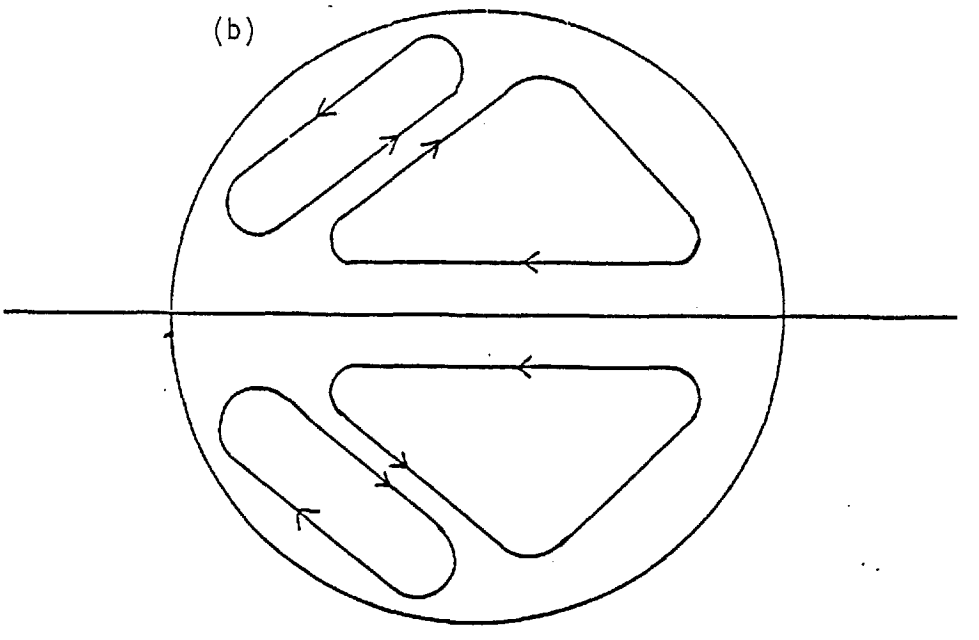

Fig. 4.16 The stream function (a) shows a counter rotating cell structure illustrated diagrammatically (b) which arises from the vorticity shown in Fig. 4.15(a).

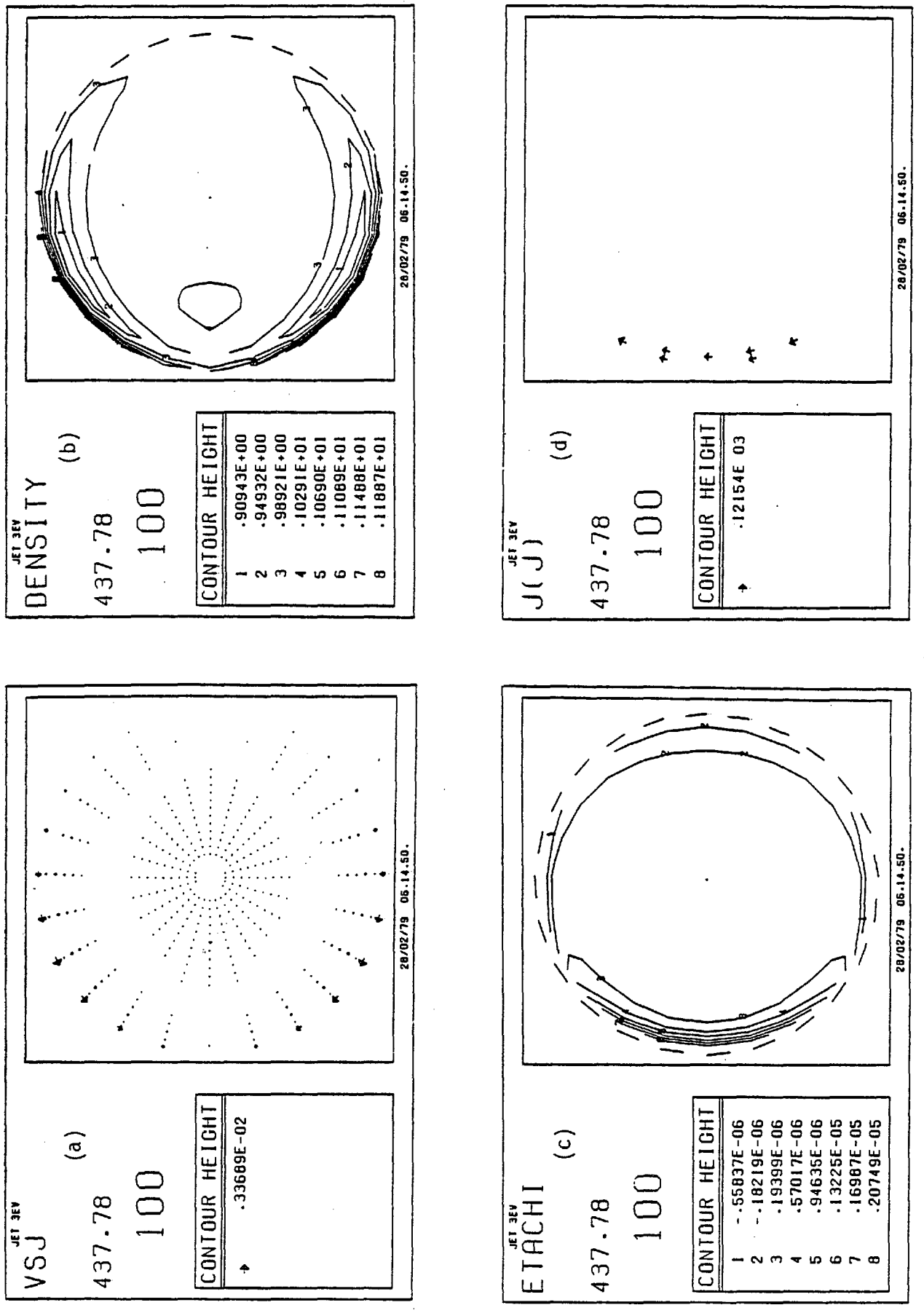

Fig. 4.17 For the parameters of Fig. 4.15 vector plots of (a) the flow velocity and (d) the poloidal current, and contour plots of (b) the density and (c) etachi are given.

On the other hand, increased current flow at the left hand edge arises because the applied electric field is larger and, due to Ohmic heating, the resistivity is smaller. This generates counter rotating cells near the left hand edge which gives rise to the flow pattern shown in Fig. 4.16. The flow pattern advects the magnetic surfaces from the left and right hand edges into the discharge, helped in places by differential resistive diffusion. So, although the temperature dependence of the resistivity tries to prolong the skin time, it creates flow that assists the penetration of the poloidal flux, and therefore, the current.

For confirmation of this, we look at the time development of voltage and inductance, Fig. 4.18. After about 600μs the loop voltage starts to decrease indicating that poloidal flux is being removed from the edge of the plasma. The inductance, however, continues to increase indicating that current penetration is occuring. This behaviour is similar to the small tokamak LT-3 at an initial temperature of 10eV, although in this case a voltage maximum has been reached.

If we continue the run, the current continues to grow at the left hand edge, Fig. 4.19(a), driven by the larger electric field and lower resistivity in this hotter region, Fig. 4.19(b). The gradient of RJ_ϕ parallel to B_p now dominates any pressure variation, leading to vortices, Fig. 4.19(c), that produce a flow pattern which advects plasma outwards, away from the major axis, Fig. 4.19(d). After ~0.9 ms this steady flow has reached a maximum speed, Fig. 4.20, of $7.3.10^3$ ms^{-1} and in the mid-plane the speed is 2.10^2 ms^{-1}. This flow will advect magnetic surfaces towards the magnetic axis, helped by the higher temperatures near the left hand edge, which reduces the resistive diffusion of the field through the fluid, resulting in the magnetic surfaces following the fluid flow more closely. This advection, however, will not result in much heating of the central region.

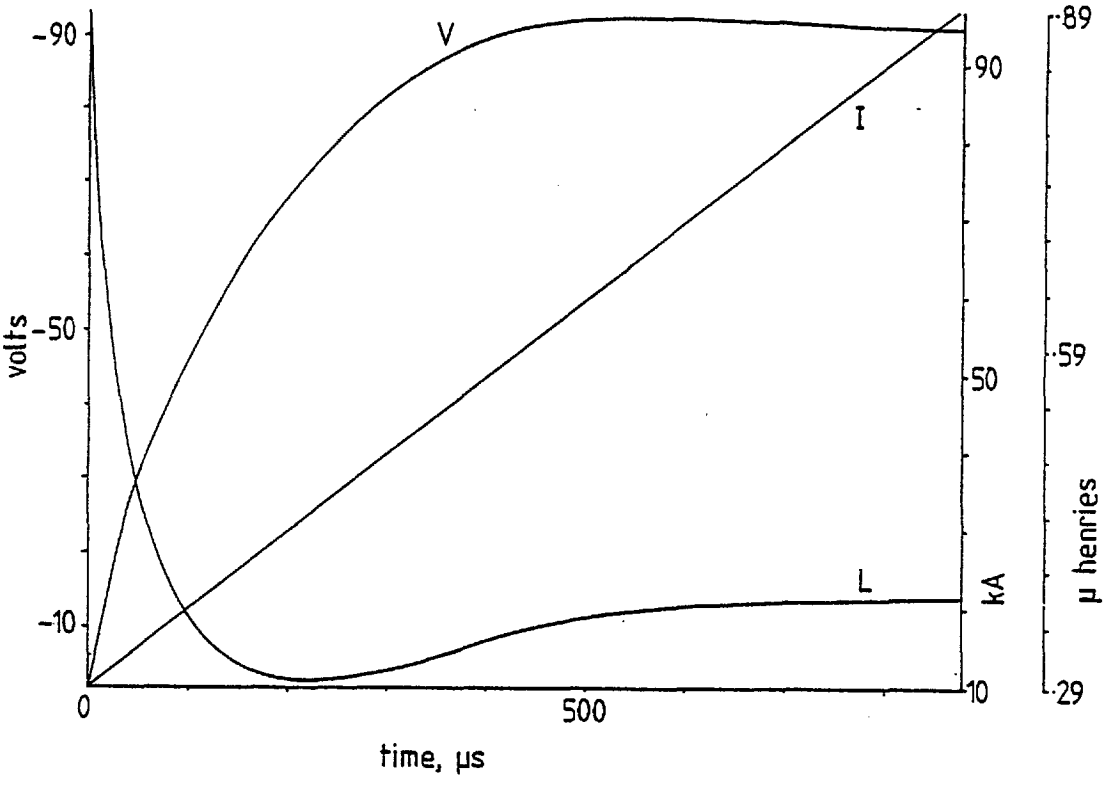

Fig. 4.18 Time dependence of voltage, inductance and current for a simulation with the parameters of Fig. 4.15.

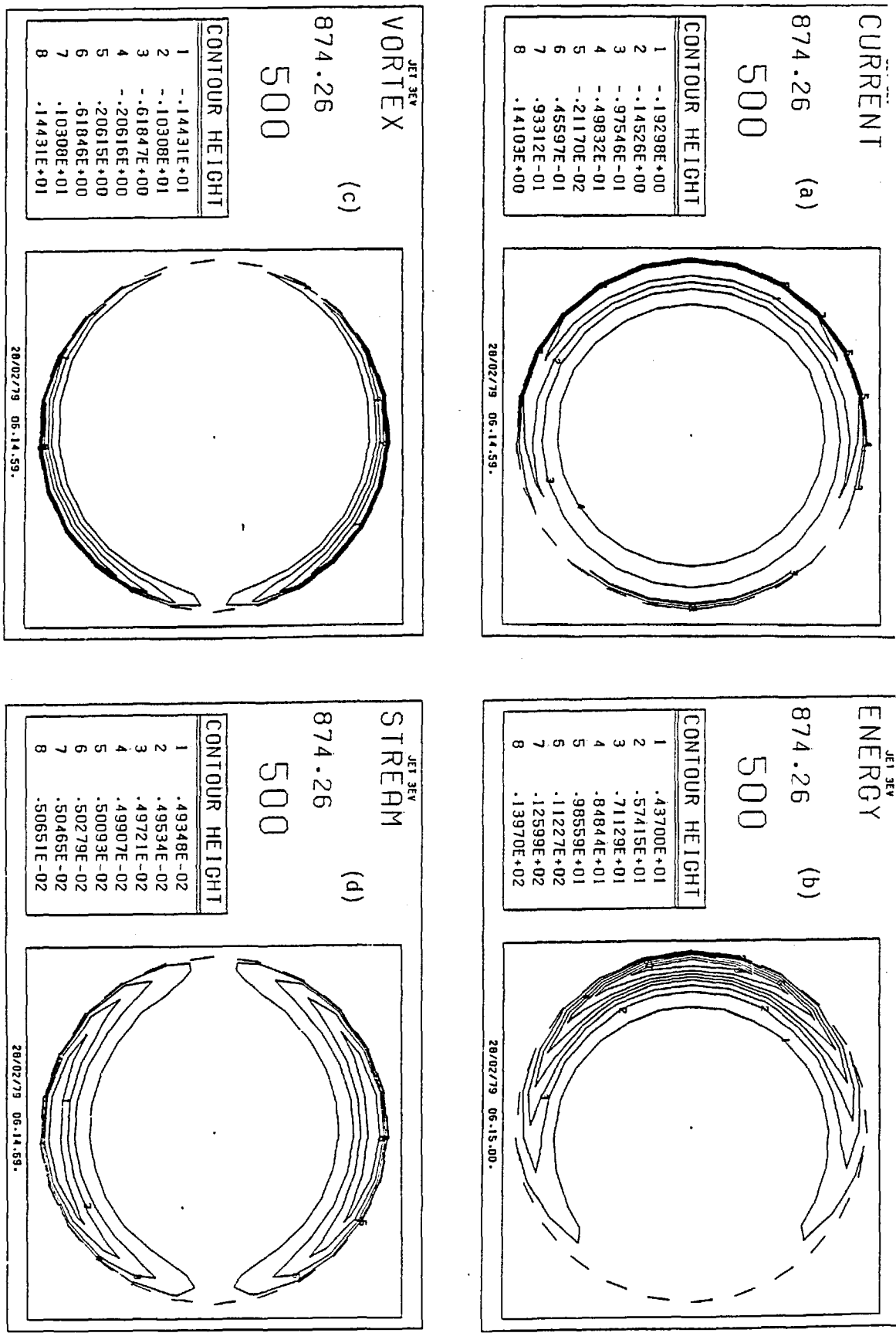

Fig. 4.19 After about two classical diffusion times a run with the parameters of Fig. 4.15 shows (a) the current and (b) the temperature localised near the inner wall, which gives rise to (c) the vorticity and (d) the stream function shown.

In a manner analogous to the density, toroidal incompressibility implies that when a fluid element moves; its energy must alter by an amount proportional to $R^{-2(\gamma-1)}$ in order to conserve energy. A flow away from the magnetic axis will therefore cool the fluid element although this may displace a cooler fluid element. The penetration of the current to the central region of the plasma therefore, seems unlikely to occur because the centre is heated by convection. A more likely mechanism is the disruption of the magnetic surfaces caused by advection of the surfaces from the inner edge towards the magnetic axis. From the flow speed in Fig. 4.20, a fluid element from the inner edge will reach the centre of the torus after ~ 15 ms, which is short compared to the total expected lifetime of JET and is indeed comparable to the current rise time.

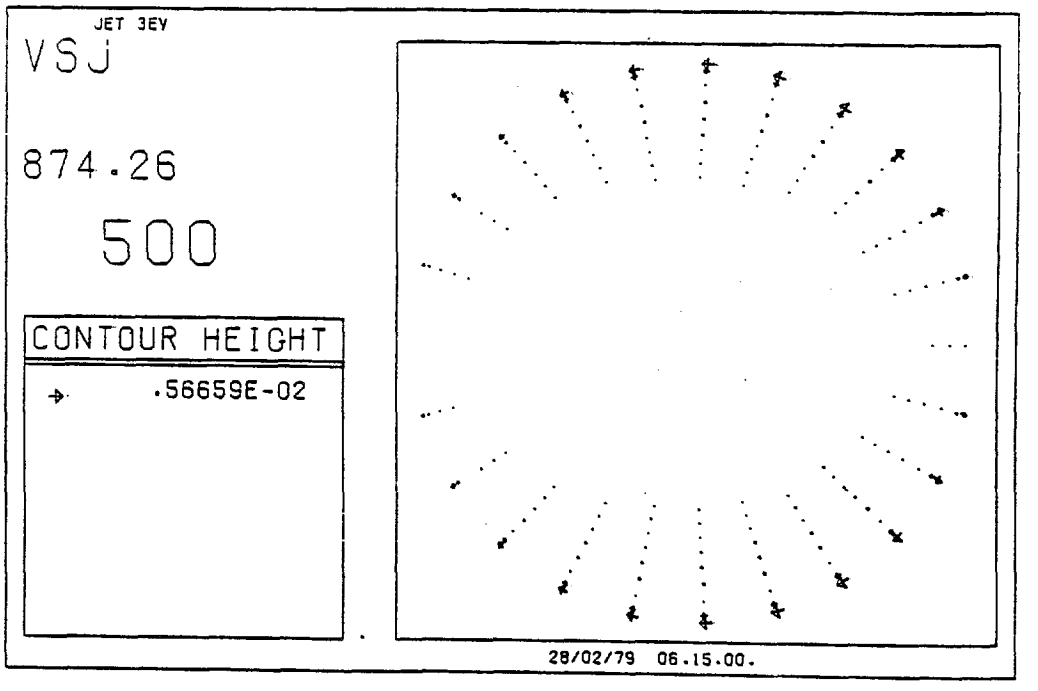

Fig. 4.20 Flow velocity corresponding to the stream function shown in Fig. 4.19(d)

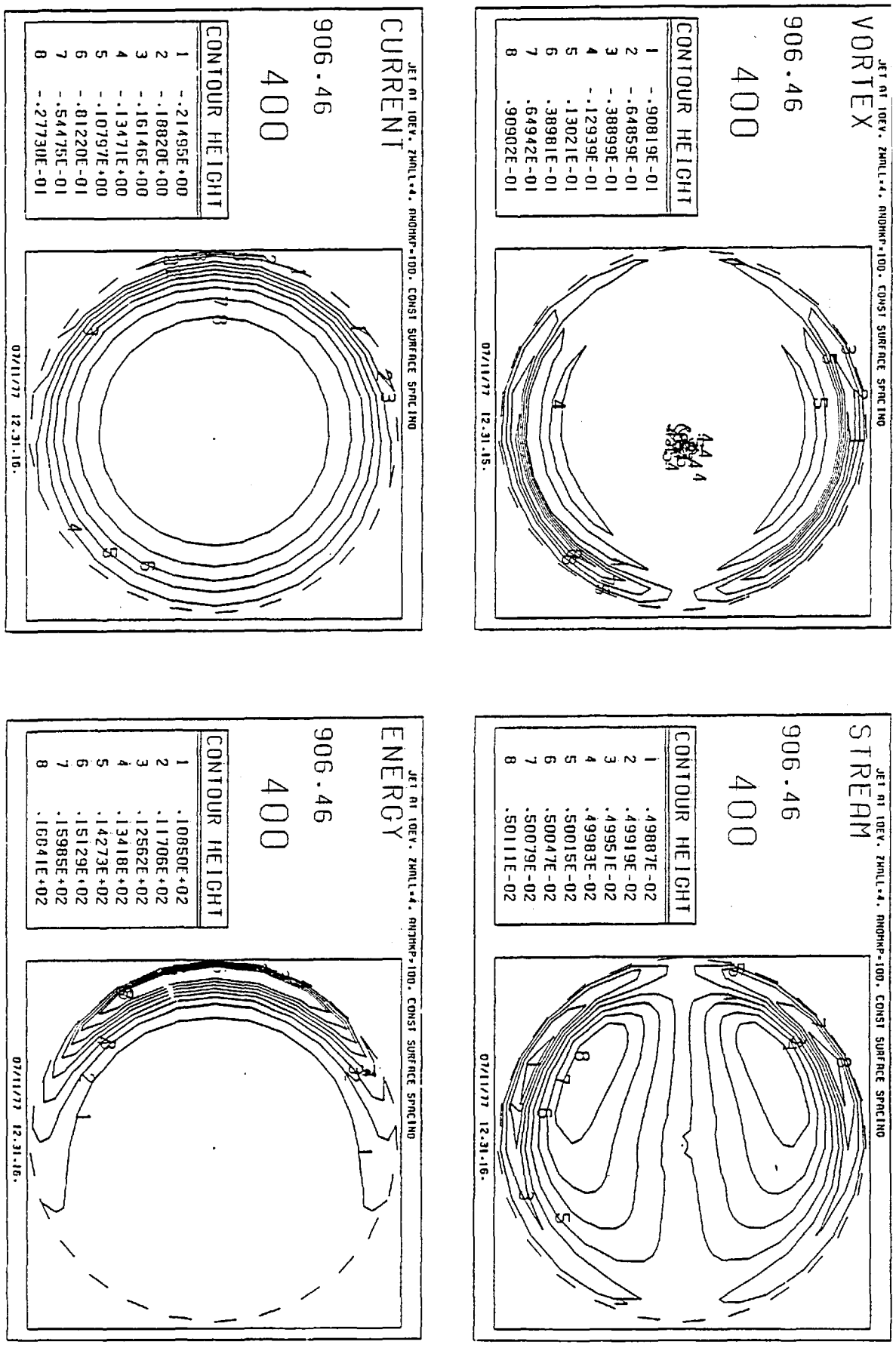

Fig. 4.21 A simulation of JET with an initial temperature of 10 eV after about $\frac{1}{4}$ of a classical diffusion time. The behaviour is very similar to that of the 3 eV case (Fig. 4.15) but the flow develops more quickly

At the higher initial temperature of 10eV we see similar behaviour, Fig. 4.21, but the steady flow driven by the gradient of RJ_ϕ parallel to B_p appears much sooner in relation to the classical diffusion time, which is τ_η ~ 3 ms. This is because the sound time τ_s ~ 52μs is much smaller, and pressure gradients which give rise to competing vortices are smoothed out more quickly.

4.3.3 Energy conservation

In the runs described in the last two sections, the total energy conservation was in line with the limit imposed by the orthogonalisation procedure. The simulation of LT-3 with an initial temperature of 1eV conserved energy to better than 3% in a run that lasted for 500 time-steps. For similar length runs, the simulations of LT-3 at 10eV and JET at 3eV and 10eV returned energy conservation figures of 6%, 7.4% and 9%.

4.4 SUMMARY

In this series of simulations, we have seen that the numerical solutions are dependent basically on three parameters, the initial temperature, aspect ratio and minor radius. These three parameters affect three relevant timescales, the sound time, diffusion time and thermal conduction time, and it is the relative magnitude of these that determines the type of solution obtained.

Flow may occur when there is a vertical pressure gradient, or when there is a gradient of RJ_ϕ parallel to the poloidal magnetic field (Eq. 2.19). If the thermal conduction time is small compared to the diffusion time, the ohmic heat supplied at the inner edge will quickly diffuse around the magnetic surfaces, so RJ_ϕ will remain uniform on a magnetic surface. Flow will therefore arise only from the term $\nabla p \times \nabla R^2$ and this flow will quickly dampen if the sound time is also small. If the aspect ratio is large, then J_ϕ will be uniform around a magnetic surface and once again flow will only arise from a vertical pressure gradient.

When the minor radius is small, the diffusion time can become less than the sound time. In these circumstances, current penetration occurs on a timescale short compared to the sound time, and therefore, J_ϕ is approximately uniform on a magnetic surface. Flow due to a vertical pressure gradient can occur, but does not grow with sufficient speed (because the sound time is large) for the flow to affect the current penetration.

In these limits the flow and current diffusion decouple. However, if the thermal conduction time is chosen large, and the diffusion time a few times the sound time we may see the effects of plasma flow and magnetic field diffusion coupling. By choosing a small aspect ratio and large minor radius as in the JET simulations, we find that at

experimentally realistic initial temperatures, plasma flow does modify the magnetic field diffusion. This is also seen in the LT-3 simulations although a slightly higher initial temperature is required. The time for penetration of the current indicated in this case is of the same order observed experimentally, and far less than the penetration time given by the one dimensional codes described in the first section of this chapter.

CHAPTER 5

HIGH TEMPERATURE PLASMAS AND PRESSURE ANISOTROPY

A plasma may be described by macroscopic variables such as temperature, density and a centre of mass velocity if the collision frequency of its constituent particles is sufficiently large to ensure that at all times a local thermodynamic equilibrium exists. Additionally if these macroscopic variables vary over characteristic lengths large compared to the mean free path, and vary sufficiently slowly compared to the collision frequency, collisional transport theory may be applied to the plasma and its evolution described by fluid or magnetohydrodynamic (MHD) equations. This represents a considerable simplification of the Liouville equation, which describes the plasma by referring to the coordinates and velocity components of all its constituent particles.

In high temperature plasmas, however, it does not immediately follow that MHD equation may be used automatically, because collisions become less frequent as the temperature of the plasma increases. For instance, in Table 3.2 we see that a typical kilovolt tokamak plasma has an electron-ion collision frequency, ν_{ei} comparable to the Alfven or sound wave frequencies. Furthermore, a local thermodynamic equilibrium may not be established in a time-scale which is short compared to those of interest. On the other hand, for any contained plasma of interest, the collision time is very small compared to the containment time which suggests that in some sense there must exist a near thermodynamic equilibrium. In this event a fluid theory might be possible.

In this chapter, this idea is developed into a fluid model appropriate for high temperature plasmas in a strong closed magnetic field, in which the plasma pressure must be represented as a tensor quantity.

5.1 CONCERNING BANANAS

The geometry of the magnetic field in the tokamak, and most other toroidal devices ensures that inhomogeneities exist along the magnetic field lines. As the helical field lines in a tokamak spiral around the torus the strength of the magnetic field increases as the field line moves closer to the major axis. An adiabatic trap therefore occurs between the weak field region on the outer side of the torus and strong field region on the inner side. These adiabatic traps were first noted by Morozov and Solev'ev[62] who realised that particles could be trapped in these regions in a manner similar to that of a magnetic bottle. This idea was extended by Galeev and Sagdeev[63] who calculated the effect of these trapped particles on the transport coefficients. The "neoclassical" diffusion coefficients they obtained were considerably larger than classical values, but still did not account for experimentally observed losses. Neoclassical transport theory, which still forms the backbone of most one dimensional diffusion codes[64] fails to describe electron energy transport, although it is somewhat modified by trapped ion and electron contributions to the diffusion.

A particle is trapped in a magnetic bottle if its kinetic energy parallel to the magnetic field is insufficient to overcome the potential barrier at the magnetic mirror. We may write the conservation of energy for a particle as:

$$\frac{mv_{\parallel}^2}{2} + \mu B + e\Phi = \text{constant}$$

where

$$\mu = \frac{mv_{\perp}^2}{2B}$$

Guiding centre motion theory demonstrates that μ is an adiabatic invariant if the magnetic field varies over distances large compared to

the Larmor radius and on a timescale long compared to the cyclotron orbit time. If the electrostatic potential, Φ, is constant, then a certain class of particle will be reflected at the magnetic mirror. If $v_{\parallel}$ is large the particle will escape from the magnetic trap and is termed a "passing" particle. For $v_{\parallel}$ small the particle is reflected at the magnetic mirror and is hence called "trapped". Fig 5.1 shows the trajectories of both passing and trapped particles from which the origin of the term banana, to describe the trapped particles, is obvious.

The concept of passing and trapped particles is dependent upon the time between collisions. If the collisions time is shorter than the transit or bounce time of a particle in the magnetic trap then it will be scattered out of the trap before it can execute one bounce. Therefore in order that we may talk about passing or trapped particles, we require:

$$\tau_c > \tau_t \tag{5.1}$$

Having established that passing and trapped particles can exist, we must consider the length of time particles can remain in these traps. The guiding centres of particles in a magnetic field drift onto adjacent field lines if inhomogeneities in the field, such as curvature or gradient, exist. In the magnetostatic case, with a source free magnetic field with small gradients, the gradient and curvature drifts may be written:

$$v_d = \frac{m}{eB}\left(\frac{v_{\parallel}^2}{L} + \frac{v_{\perp}^2}{2L}\right)$$

where L is the radius of curvature. Approximately:

$$v_d \sim \frac{v_{th}^2}{\Omega L} \tag{5.2}$$

where v_{th} is the thermal velocity and Ω the cyclotron frequency. The transit time of a particle in a magnetic trap is:

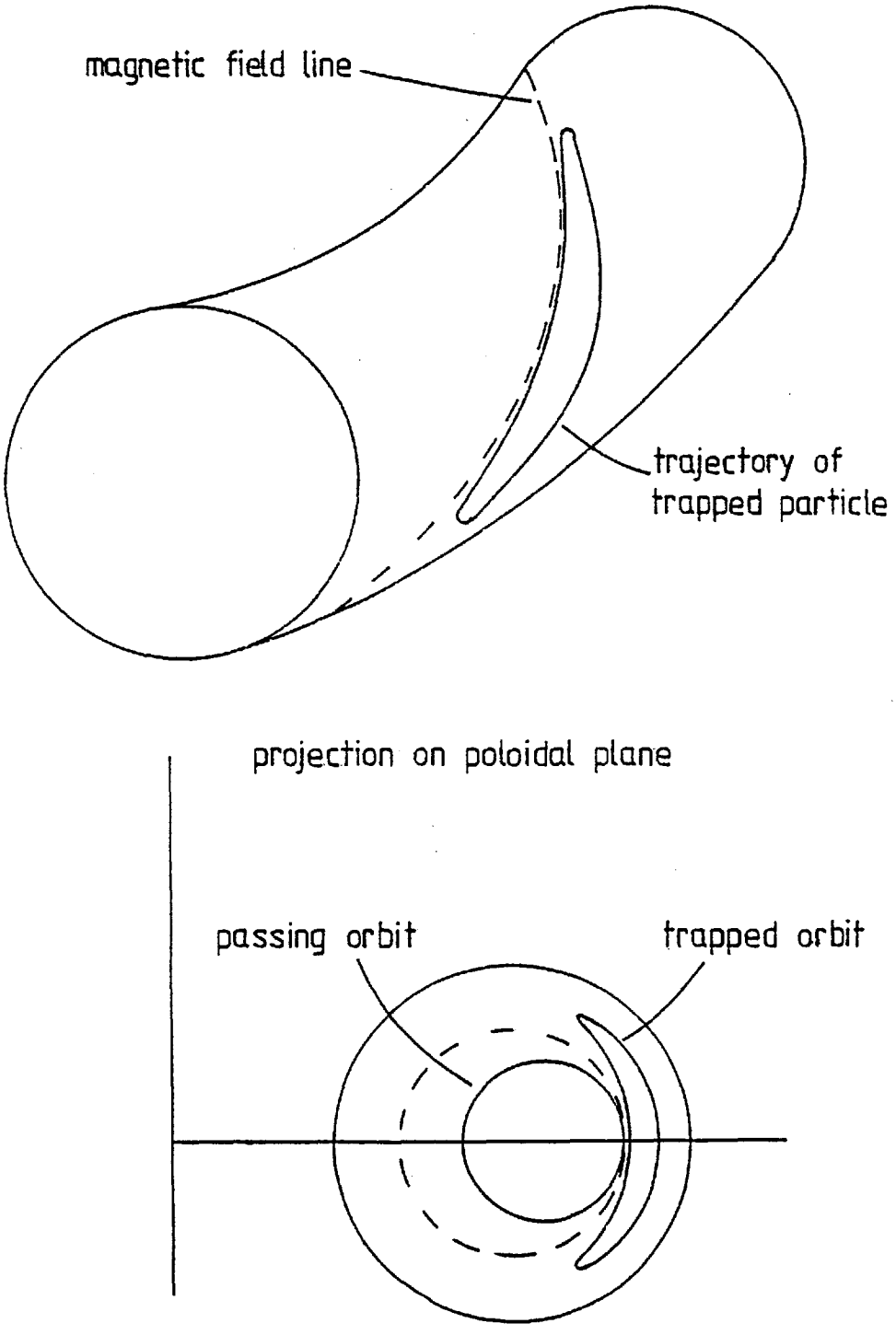

Fig. 5.1 Trapped and passing particles

$$\tau_t = L_\parallel / v_\parallel \qquad (5.3)$$

where $L_\parallel$ is the distance between the mirror points. Comparing the drift time and transit time we find:

$$\tau_d = \frac{\Omega L_\perp}{v_{th}} \tau_t \qquad (5.4)$$

which essentially implies that if the Larmor radius is small compared to scale lengths perpendicular to the field, the drift time is large compared to the transit time.

In any conceivable fusion plasma which is magnetically contained, the collision time is much longer than times associated with particle motion, and Eq. (5.1) is satisfied. Furthermore, Eq. (5.4) implies the drift time substantially exceeds the transit time. On the other hand, for any confined plasma of interest, the collision time is very small compared to the containment time, which implies:

$$\tau_d > \tau_c \qquad (5.5)$$

We have therefore, a plasma in which there must exist, in some sense, a thermodynamic equilibrium. We now proceed to develop a fluid theory which is applicable in these circumstances.

5.2 THERMODYNAMIC EQUILIBRIUM WITH RARE COLLISIONS

We have described above the conditions in a typical tokamak plasma. Hence, in the development of this theory we shall assume that the Larmor radii are small;

$$a \ll L_\perp$$

which is equivalent to

$$v_{th} \ll \Omega L_\perp \tag{5.6}$$

where $L_\perp$ is a characteristic scale length, Ω the cyclotron frequency and v_{th} the thermal velocity. We define a small parameter, ε, such that:

$$\varepsilon = \frac{v_{th}}{\Omega L_\perp}$$

We shall also assume that the plasma is nearly stationary

$$v_d \ll v_{th}$$

or

$$v_d = \varepsilon v_{th} \tag{5.7}$$

The opposite situation exists in the Chew-Goldberger-Low[67] regime. In addition we assume that the magnetic field lines are closed.

We now develop this idea by considering the transit time for the particles. The time for a particle to return to an equivalent point on a magnetic surface, if $L_\parallel$ and $v_{th_\parallel}$ are a scale length and a thermal velocity parallel to the field, is:

$$\tau_t \sim L_\parallel / v_{th_\parallel}$$

We consider the field lines closed in the sense that the transit time for

the particle is less than the drift time.

$$\tau_t < L_{\parallel}/v_d \tag{5.8}$$

These conditions are fulfilled by the plasma discussed in the last section.

Under these conditions, a thermodynamic equilibrium, in some sense is to be expected. Perpendicular to the magnetic field, although collisions are rare and will not localise the particles in space, the Larmor radius of the particles is small and the cyclotron orbit has the effect of localising particles perpendicular to the magnetic field. Therefore, even though the collisions are rare, because the particles are localised for a long time a thermodynamic equilibrium may be set up with which a perpendicular temperature, $T_{\perp}$, may be associated.

Parallel to the magnetic field particles are not localised as the collision time is comparable to or longer than the transit time. Conversely, because a magnetic surface is closed, a particle may orbit many times around the surface before drifting away. Again, in this circumstance, the rare collisions can imply that an entire field line is in thermodynamic equilibrium described by a parallel temperature, $T_{\parallel}$. In the limit when $\tau_c >> \tau_t$ we would expect $T_{\parallel}$ to be constant along an entire field line whilst as $\tau_c \lesssim \tau_t$ the particles become localised by collisions and we return to local thermodynamic equilibrium where $\underline{T_{\perp}} \sim T_{\parallel}$. There is, however, no a priori reason why $T_{\parallel}$ should equal $\underline{T_{\perp}}$ when $\tau_c > \tau_t$.

These ideas are central to the theory and we do indeed find that $T_{\parallel}$ becomes constant along a field line. In order to develop the theory further we describe an expansion of the Fokker-Planck equation, and apply these ideas to obtain fluid-like equations.

5.3 MOMENTS OF THE FOKKER-PLANCK EQUATION

The most fundamental description of a collection of particles is the Liouville equation which describes the state of the system of particles by referring to the coordinates and velocity components of all its constituent particles. In a magnetically confined plasma, the number of particles in a Debye sphere is large, $n_D \sim 10^6$, and the state of the plasma may be represented by a continuous distribution function, $f(\underline{x}, \underline{w}, t)$. Small collisional effects may be described as a diffusion in velocity space and it is therefore appropriate to begin with the Fokker-Planck equation for the distribution function of each species:

$$\frac{\partial f}{\partial t} + \underline{w} \cdot \nabla f + \frac{e}{m} (\underline{E} + \underline{w} \times \underline{B}) \cdot \nabla_w f = Cf \qquad (5.9)$$

where C is the Fokker-Planck collision operator. The collisions are generally a small effect and we shall assume a simple linearised form for the collision operator:

$$C = \langle \nu \rangle \frac{\partial^2}{\partial \lambda^2} \qquad (5.10)$$

where ν is the velocity averaged collision frequency and λ the pitch angle in velocity space. For electron-ion collisions, this form is correct to order $(m_e/m_i)^{\frac{1}{2}}$ but is not correct for like-particle collisions. Electron-ion collisions are however, predominately important.

In order to analyse the Fokker-Planck equation under the conditions of interest (section 5.2) we expand the distribution function by an infinite set of moments, and obtain from Eq. (5.9) an infinite set of coupled moment equations for each species. The first five moments which occur are:

density: $$\rho = \int m f \, d^3\underline{w} \qquad (5.11)$$

momentum: $$\rho \underline{v} = \int m f \, \underline{w} \, d^3\underline{w} \qquad (5.12)$$

momentum transfer: $$\rho \underline{vv} + \underline{\underline{P}} = \int m\, f\, \underline{w}\, \underline{w}\, d^3\underline{w} \tag{5.13}$$

energy transfer: $$\rho \underline{vvv} + \{\underline{\underline{P}}\, \underline{v}\} + \underline{\underline{\underline{Q}}} = \int m\, f\, \underline{w}\, \underline{w}\, \underline{w}\, d^3\underline{w} \tag{5.14}$$

energy pressure: $$\rho \underline{vvvv} + \{\underline{\underline{P}}\underline{vv}\} + \{\underline{\underline{\underline{Q}}}\underline{v}\} + \underline{\underline{\underline{\underline{R}}}} = \int m\, f\, \underline{w}\, \underline{w}\, \underline{w}\, \underline{w}\, d^3\underline{w} \tag{5.15}$$

Higher moments may similarly be defined. The terms such as $\{\underline{\underline{P}}\, \underline{v}\}$ refer to the creation of a symmetric tensor by the cyclic permutation of the free tensor indices, and is the same as the notation used by Macmahon[65]. For example

$$\{\underline{\underline{P}}\, \underline{v}\} = P^{ij}v^k + P^{ki}v^j + P^{jk}v^i$$

Therefore, from the Fokker-Planck equation, and in its place we obtain an infinite set of coupled moment equations, of which we give the first four:

density: $$\frac{\partial \rho}{\partial t} + \nabla.\rho\underline{v} = 0 \tag{5.16}$$

momentum: $$\frac{\partial}{\partial t}(\rho\underline{v}) + \nabla.(\rho\underline{vv} + \underline{\underline{P}}) - \frac{e}{m}\rho(\underline{E}+\underline{v}\times\underline{B}) = \frac{\delta}{\delta t}(\rho\underline{v}) \tag{5.17}$$

momentum transfer: $$\frac{\partial}{\partial t}(\underline{\underline{P}} + \rho\underline{vv}) + \nabla.(\rho\underline{vvv} + \{\underline{\underline{P}}\, \underline{v}\} + \underline{\underline{\underline{Q}}})$$

$$- \frac{e}{m}\rho\{\underline{v}(\underline{E} + \underline{v} \times \underline{B})\} - \frac{e}{m}\{\underline{\underline{P}} \times \underline{B}\} = \frac{\delta}{\delta t}(\underline{\underline{P}} + \rho\underline{vv}) \tag{5.18}$$

energy transfer: $$\frac{\partial}{\partial t}(\underline{\underline{\underline{Q}}} + \{\underline{\underline{P}}\, \underline{v}\} + \rho\underline{vvv}) + \nabla.(\rho\underline{vvvv} + \{\underline{\underline{P}}\, \underline{vv}\} + \{\underline{\underline{\underline{Q}}}\, \underline{v}\} + \underline{\underline{\underline{\underline{R}}}})$$

$$- \rho\frac{e}{m}\{(\underline{E} + \underline{v} \times \underline{B})\underline{vv}\} - \frac{e}{m}\{(\underline{E} + \underline{v} \times \underline{B})\underline{\underline{P}}\} - \frac{e}{m}\{\underline{v}(\underline{\underline{P}} \times \underline{B})\}$$

$$- \frac{e}{m}\{\underline{\underline{\underline{Q}}} \times B\} = \frac{\delta}{\delta t}(\underline{\underline{\underline{Q}}} + \{\underline{\underline{P}}\, \underline{v}\} + \rho\underline{vvv}) \tag{5.19}$$

This infinite set of moment equations is simply an alternative representation of the Fokker-Planck equation; there is no approximation involved in this procedure.

Using the ideas and conditions discussed in section 5.2 we proceed to simplify and then truncate the equations (5.16) - (5.19).

The conditions (5.6) - (5.8) imply

$$v_{th} << \Omega L$$

and

$$\langle \nu \rangle << \Omega$$

so from the zero moment, Eq. (5.16) we find

$$\frac{\partial}{\partial t} \sim \frac{v}{L} \tag{5.20}$$

We may infer from the first moment, Eq. (5.17) that the electric field

$$E \sim P/neL \tag{5.21}$$

and observe that the condition, Eq. (5.7) is consistent with the first moment. From the second and third moments, Eqs. (5.18) and (5.19), and indeed the fourth and higher moment equations, we obtain to the lowest order:

$$\begin{aligned} &\text{2nd moment:} && \{\underline{\underline{P}} \times \underline{B}\} = 0 \\ &\text{3rd moment:} && \{\underline{\underline{\underline{Q}}} \times \underline{B}\} = 0 \\ &\text{4th moment:} && \{\underline{\underline{\underline{\underline{R}}}} \times \underline{B}\} = 0 \end{aligned} \tag{5.22}$$

If we now choose a frame of reference such that the magnetic field is always parallel to one coordinate direction such that

$$\underline{B} = B\, \underline{e}_3$$

and rewrite Eqs. (5.22) in the tensor notation of Appendix D giving:

$$\{\varepsilon^{jmn} P^{k}_{\ m} B_n\} = 0 \tag{5.23}$$

$$\{\varepsilon^{jmn} Q^{kl}_{\ \ m} B_n\} = 0 \tag{5.24}$$

$$\{\varepsilon^{jnp} R^{klm}{}_{n} B_p\} = 0 \tag{5.25}$$

we find that there are only a few non-zero terms of $\underline{\underline{P}}$, $\underline{\underline{\underline{Q}}}$ and $\underline{\underline{\underline{R}}}$ to the lowest order. For instance, from Eq. (5.23) we obtain for the lowest order $\underline{\underline{P}}$:

$$\underline{\underline{P}}^{(o)} = \begin{bmatrix} p_\perp & 0 & 0 \\ 0 & p_\perp & 0 \\ 0 & 0 & p_\parallel \end{bmatrix} \tag{5.26}$$

from which it must be noted that there is no a priori reason why $p_\perp^{(o)}$ should equal $p_\parallel^{(o)}$. From Eq. (5.24) the non-zero elements of $\underline{\underline{\underline{Q}}}^{(o)}$ are

$$\begin{aligned} Q^{11}{}_3 &= Q^{22}{}_3 = Q_{\perp\parallel}^{\perp} \\ Q^{33}{}_3 &= Q_\parallel^{\parallel} \end{aligned} \tag{5.27}$$

which refers to thermal transport of perpendicular and parallel energy along the magnetic field. The non-zero elements of the zero order fourth rank tensor $\underline{\underline{\underline{R}}}^{(o)}$ are:

$$\begin{aligned} R^{111}{}_1 &= R^{222}{}_2 = 3R^{112}{}_2 = R_\perp^\perp \\ R^{113}{}_3 &= R^{223}{}_3 = R_\parallel^\perp \\ R^{333}{}_3 &= R_\parallel^\parallel \end{aligned} \tag{5.28}$$

In the work of Chew, Goldberger and Low the system of equations was truncated at the second moment by assuming that the heat flux moment (the third) was zero because the flow velocity was assumed large compared to the thermal velocity. This is not the case here as $v_{th} >> v$, hence $\underline{\underline{\underline{Q}}}$ may be large. We therefore proceed to the fourth moment and truncate the system by assuming an "equation of state"

which specifies $\underline{\underline{R}}^{(o)}$ in terms of the pressure. This is suggested by the nature of the pressure tensor, Eq. (5.26) and the conditions on $\underline{\underline{R}}^{(o)}$, Eq. (5.28). We assume

$$R^{111}{}_1 = R^{222}{}_2 = 3R^{112}{}_2 = \frac{3p_\perp{}^2}{\rho} \tag{5.28}$$

$$R^{113}{}_3 = R^{223}{}_3 = \frac{p_\parallel\, p_\perp}{\rho} \tag{5.29}$$

$$R^{333}{}_3 = \frac{p_\parallel{}^2}{\rho} \tag{5.30}$$

which is consistent with an ellipsoidal distribution function in phase space to lowest order

$$f^{(0)}(\underline{r}, \underline{w}, \underline{t}) = \left(\frac{m}{2\pi k}\right)^{3/2} \frac{n}{T_\perp\, T_\parallel{}^{\frac{1}{2}}}\, e^{-\frac{mw_\perp{}^2}{kT_\perp}}\, e^{-\frac{mw_\parallel{}^2}{2kT_\parallel}} \tag{5.31}$$

where $T_\perp$, $w_\perp$ and $T_\parallel$, $w_\parallel$ refer to the temperature and velocity perpendicular and parallel respectively to the magnetic field.

From these results we may now proceed to evaluate the moment equations expressed to a higher order.

5.3.1 Conservation Equations

We obtain conservation equations for particles and for the energy of each species. Assuming quasi-neutrality

$$n = n_e = n_i$$

the density moment, Eq. (5.16), gives:

$$\frac{\partial n}{\partial t} + \nabla.(n\,\underline{v}) = 0 \tag{5.32}$$

and defining the internal energy of each species as

$$\varepsilon_a = \frac{1}{\rho}\,(2p_\perp + p_\parallel)_a$$

the trace of the momentum transfer equation, Eq. (5.18) yields:

$$\frac{\partial}{\partial t}\rho\varepsilon_e + \nabla.(\rho\varepsilon_e \underline{v} + \underline{q}_e) = \rho\nu_{eq}(\varepsilon_i - \varepsilon_e) \qquad (5.33)$$

$$\frac{\partial}{\partial t}\rho\varepsilon_i + \nabla.(\rho\varepsilon_i \underline{v} + \underline{q}_i) = \rho\nu_{eq}(\varepsilon_e - \varepsilon_i) \qquad (5.33)$$

In Eq. (5.32) $n\,\underline{v}$ is the particle flux and $\rho\,\varepsilon\underline{v} + \underline{q}$ in Eq. (5.33) the energy flux. The heat flux $\underline{q}$ is defined below.

5.3.2 Fluxes

We may use the momentum equation, Eq. (5.17) to obtain an expression for the particle flux for each species "a"

$$-n\,\underline{v}_a \times \underline{B} + \nu_{aa'}\frac{\rho}{e}(\underline{v}_{a'} - \underline{v}_a) = \frac{1}{e}\nabla.\underline{\underline{P}}_a + n\,\nabla\Phi \qquad (5.34)$$

where Φ is the electrostatic potential. The energy flux may be obtained by taking the trace of the energy transfer equation, Eq. (5.19), $\underline{v}$ multiplied by the momentum transfer equation, Eq. (5.18) and defining a total heat flux vector for each species, whose kth component is:

$$(\underline{q})_k = Q^{11}{}_k + Q^{22}{}_k + Q^{33}{}_k$$

we obtain (Appendix E):

$$\frac{e}{m}\underline{q}_a \times \underline{B} + \nu_{aa'}(\underline{q}_{a'} - \underline{q}_a) = \underline{\underline{P}}_a.\nabla\varepsilon_a + 2\underline{\underline{P}}_a:\nabla(\underline{\underline{P}}_a/\rho) \qquad (5.35)$$

Given both Φ and $\underline{\underline{P}}$ both these equations may be solved for the particle and energy fluxes.

5.3.3 Pressure Tensor

Direct collisional effects are apparent in Eqs. (5.34) and

(5.35). However, the off-diagonal elements of the pressure tensor $\underline{\underline{P}}$ also give rise to particle and energy diffusion. These "viscous" elements are determined by evaluating the momentum transfer equation, Eq. (5.18), to the next order. The lowest order pressure tensor, Eq. (5.26) is given by Eq. (5.23). To the next order this equation becomes:

$$\nabla.\underline{\underline{Q}}^{(o)} - \frac{e}{m}\{\underline{\underline{P}}^{(1)} \times \underline{B}\} = \frac{\delta \underline{\underline{P}}^{(o)}}{\delta t} \tag{5.36}$$

However, the only non-zero elements of $\underline{\underline{Q}}$ are (Eq. 5.27) $Q^{11}{}_3 = Q^{22}{}_3 = Q_{\perp\!\!\!\perp}$ and $Q^{33}{}_3 = Q_{\parallel}$. Defining

$$\sigma = Q_{\perp\!\!\!\perp} \tag{5.37}$$

we obtain:

$$\underline{\underline{P}}^{(1)} = \begin{bmatrix} p_\perp & 0 & -\frac{1}{\Omega}\frac{\partial \sigma}{\partial x^2} \\ 0 & p_\perp & \frac{1}{\Omega}\frac{\partial \sigma}{\partial x^1} \\ -\frac{1}{\Omega}\frac{\partial \sigma}{\partial x^2} & \frac{1}{\Omega}\frac{\partial \sigma}{\partial x^1} & p_\parallel \end{bmatrix} \tag{5.38}$$

The form of the viscous pressure tensor is a consequence of the large thermal velocity compared to the centre of mass velocity. It no longer depends upon gradients of velocity, but on energy fluxes.

We must now determine $p_\parallel$, $p_\perp$, σ and Φ for each species along the magnetic field. These variables are found from the zero order equations in which the cyclotron frequency does not enter.

5.3.4 Parallel Equations

Components of the moment equations along the magnetic field direction,

$$\underline{B} = B\underline{e}_3$$

define $p_{\parallel}$, $p_{\perp}$, σ and Φ. To the lowest order the first, second and third moment equations yield:

1st moment:
$$\underline{e}_3 \cdot \left[\nabla.\underline{\underline{P}} - n\, e\, \underline{E}\right] = 0 \tag{5.39}$$

2nd moment:
$$\underline{\underline{I}}_{\alpha} : \left[\nabla.\underline{\underline{\underline{Q}}} - \frac{\delta \underline{\underline{P}}}{\delta t}\right] = 0 \tag{5.40}$$

$$\underline{e}_3\underline{e}_3 : \left[\nabla.\underline{\underline{\underline{Q}}} - \frac{\delta \underline{\underline{P}}}{\delta t}\right] = 0 \tag{5.41}$$

3rd moment:
$$\underline{e}_3\, \underline{\underline{I}}_{\alpha} \vdots \left[\nabla.\underline{\underline{\underline{R}}} - \frac{e}{m}\{\underline{\underline{P}}\, \underline{E}\} - \frac{\delta \underline{\underline{\underline{Q}}}}{\delta t}\right] = 0 \tag{5.42}$$

$$\underline{e}_3\underline{e}_3\underline{e}_3 \vdots \left[\nabla.\underline{\underline{\underline{R}}} - \frac{e}{m}\{\underline{\underline{P}}\, \underline{E}\} - \frac{\delta \underline{\underline{\underline{Q}}}}{\delta t}\right] = 0 \tag{5.43}$$

where

$$\underline{\underline{I}}_{\alpha} = \underline{\underline{I}}_2 - \underline{e}_3\underline{e}_3$$

and $\underline{\underline{I}}_2$ is the unit second rank tensor. The divergence of these tensors may be evaluated by covariant differentiation (Appendix D) in the local coordinate frame parallel to the magnetic field. We have assumed a quasi-equilibrium situation in which the electric field is static and may be expressed:

$$\underline{E} = -\nabla\Phi$$

and also we have used the condition:

$$\nabla.\underline{B} = 0$$

to obtain for Eqs. (5.39) to (5.43):

$$\frac{\partial p_{\parallel}}{\partial x^3} + (p_{\perp} - p_{\parallel})\, \frac{1}{B}\, \frac{\partial B}{\partial x^3} + ne\, \frac{\partial \Phi}{\partial x^3} = 0 \tag{5.44}$$

$$\frac{\partial Q_{\perp}^{\perp}}{\partial x^3} - 2\frac{Q_{\perp}^{\perp}}{B}\frac{\partial B}{\partial x^3} = \frac{\delta p_{\perp}}{\delta t} \tag{5.45}$$

$$\frac{\partial Q_{\parallel}^{\parallel}}{\partial x^3} + (2Q_{\parallel}^{\perp} - Q_{\parallel}^{\parallel})\frac{1}{B}\frac{\partial B}{\partial x^3} = \frac{\delta p_{\parallel}}{\delta t} \tag{5.46}$$

$$\frac{\partial}{\partial x^3}\left(\frac{p_{\perp} p_{\parallel}}{\rho}\right) + \frac{2p_{\perp}}{\rho}(p_{\perp} - p_{\parallel})\frac{1}{B}\frac{\partial B}{\partial x^3} + \frac{e}{m} p_{\perp}\frac{\partial \Phi}{\partial x^3} = \frac{\delta Q_{\parallel}^{\perp}}{\delta t} \tag{5.47}$$

$$\frac{\partial}{\partial x^3}\left(\frac{p_{\parallel}^2}{\rho}\right) + \frac{p_{\parallel}}{\rho}(p_{\perp} - p_{\parallel})\frac{1}{B}\frac{\partial B}{\partial x^3} + \frac{e}{m} p_{\parallel}\frac{\partial \Phi}{\partial x^3} = \frac{1}{3}\frac{\delta Q_{\parallel}^{\parallel}}{\delta t} \tag{5.48}$$

If we now evaluate the collision terms we find that Eqs. (5.44) to (5.48) simplify considerably.

It may be shown[33] that the pressure tensor collision terms are, for electrons

$$\left(\frac{\delta p_{\perp}}{\delta t}\right)_{ee} = \frac{1}{5}(\sqrt{2}\,\nu_{ee} + 2\,\nu_{ei})(p_{\parallel} - p_{\perp})_e \tag{5.49}$$

$$\left(\frac{\delta p_{\parallel}}{\delta t}\right)_{ee} = \frac{2}{5}(\sqrt{2}\,\nu_{ee} + 2\,\nu_{ei})(p_{\perp} - p_{\parallel})_e \tag{5.50}$$

and for ions similar expressions are valid. The transfer of energy between species (when $T_{\perp} = T_{\parallel}$) is

$$\frac{\delta p_e}{\delta t} = (p_i - p_e)\,\nu_{eq} \tag{5.51}$$

where

$$\nu_{eq} \simeq {}^{2m}/_{M}\,\nu_{ei} \tag{5.52}$$

The equipartition of energy between species will in general be much smaller than the equipartition between parallel and perpendicular temperatures of the same species.

We may now combine Eqs. (5.45) and (5.46) using Eqs. (5.49) and

(5.50) to give:

$$\frac{\partial}{\partial x^3}\left(\frac{2Q_{\perp}^{\perp} + Q_{\parallel}^{\parallel}}{B}\right) = 0 \qquad (5.53)$$

Thus using the definition Eq. (5.37):

$$\sigma = Q_{\perp}^{\perp} = -\tfrac{1}{2} Q_{\parallel}^{\parallel} \qquad (5.54)$$

Equation (5.53) states that the divergence of the total heat flux is zero. Eq. (5.54) shows that if a particle gains parallel energy it does so at the expense of the perpendicular energy. The equation for σ is obtained from Eq. (5.45)

$$\frac{\partial \sigma}{\partial x^3} - \frac{2\sigma}{B}\frac{\partial B}{\partial x^3} = \nu(p_{\parallel} - p_{\perp}) \qquad (5.55)$$

where ν is the appropriate collision frequency.

In a similar manner to the above, we define the heat flux tensor collisions terms. Writing

$$\frac{\delta Q_{\perp}^{\perp}}{\delta t} \simeq \nu(Q_{\parallel}^{\parallel} - Q_{\perp}^{\perp}) = -3\nu\sigma \qquad (5.56)$$

we may define the collisional change of the parallel flux of parallel energy by assuming heat flux is conserved in collisions:

$$\frac{\delta}{\delta t}(2Q_{\perp}^{\perp} + Q_{\parallel}^{\parallel}) = 0 \qquad (5.57)$$

Thus using Eqs. (5.56) and (5.57) and pressure balance Eq. (5.44), Eqs. (5.48) and (5.47) become respectively:

$$n\frac{\partial T_{\parallel}}{\partial x^3} = 2\frac{m\nu\sigma}{T_{\parallel}} \qquad (5.58)$$

$$n \frac{\partial T_\perp}{\partial x^3} + \frac{T_\perp}{T_\parallel B}(p_\perp - p_\parallel) \frac{\partial B}{\partial x^3} = \frac{-3m\nu\sigma}{T_\parallel} \qquad (5.59)$$

These equations apply to each species and with the condition of quasi-neutrality specify n and Φ along a closed field line, and also $T_\perp$, $T_\parallel$ and σ for electrons and ions.

5.3.5 Discussion

We examine the properties of these equations (Eqs. (5.44), (5.55), (5.58) and (5.59)) in the limit when the collision frequency, ν, tends to zero. We integrate these equations to find constants on magnetic surfaces. As $\nu \to 0$:

$$\sigma = 0 \qquad (5.60)$$

$$T_\parallel = \text{constant} \qquad (5.61)$$

$$\frac{n}{T_\perp} e^{e\Phi/T_\parallel} = \text{constant} \qquad (5.62)$$

$$\frac{T_\parallel}{B} - \frac{T_\perp}{B} = \text{constant} \qquad (5.63)$$

for each species.

These equations describe the particle invariants of motion and include the description of trapped particles. Consider the general particle invariants given by:

$$\varepsilon = \tfrac{1}{2} m w_\parallel^2 + \tfrac{1}{2} m w_\perp^2$$

$$\mu = \frac{m w_\perp^2}{B}$$

when the electrostatic potential is zero. Along a field line from a point of minimum to maximum field strength, the perpendicular velocity increases. Therefore, for every particle transiting around a magnetic

surface:

$$w_{\parallel}^2 (B_{max}) < w_{\parallel}^2 (B_{min})$$

If we average over a number of transiting particles,

$$T_{\parallel} (B_{max}) < T_{\parallel} (B_{min})$$

which is, however, contradicted by Eq. (5.61). This can be satisfied only if particles with the largest parallel velocities transit around the magnetic surfaces, and all others are trapped.

The result of constant parallel temperature on a magnetic surface in the limit of zero collision frequency is what we expected and is consistent with the concept of thermodynamic equilibrium on an entire magnetic surface.

The flux parallel to the magnetic field of parallel and perpendicular energy is both an interesting and essential feature of these equations. In the collisionless limit the particle motion invariants cause separate temperatures parallel and perpendicular to the field according to the strength of the magnetic field, Eq. (5.63). This provides a potential of temperature for both $T_{\perp}$ and $T_{\parallel}$. Species collisions realise this potential.

As a particle moves into a region of stronger magnetic field, the perpendicular energy is increased at the expense of parallel energy. Collisions tend to transfer energy from perpendicular to parallel energy, Eqs. (5.58) and (5.59). Thus as a particle moves round a magnetic surface it transports this change of energy as a heat flow, Eq. (5.55). But the thermal flux of parallel energy is exactly equal and opposite to the thermal flux of perpendicular energy, Eq. (5.53). From Eq. (5.58) we see that this heat flow is a maximum when the collision frequency is approximately the bounce or transit time. At higher collision

frequencies the equipartition of parallel and perpendicular energies is achieved.

Finally, if we consider both electrons and ions, the condition of quasi-neutrality:

$$\nabla.\underline{J} = 0$$

requires that the ion loss must be equal to the electron loss; the diffusion must be ambipolar. Individually, the diffusion of electrons is found to be much greater than the ions, so in order to make the diffusion ambipolar an electric field is set up in the magnetic surface which reduces the magnetic trapping of the ions, and increases the trapping of electrons. This electrostatic potential is described by Eq. (5.62) in the collisionless limit.

5.4 ANISOTROPIC PRESSURE AND PLASMA FLOW

Anisotropic pressure affects the plasma flow via both Ohms Law and the momentum equation. The former, which is derived from the momentum equation for the electrons, Eq. (5.34), includes the divergence of the electron pressure tensor. This affects plasma flow by altering the toroidal incompressibility condition, Eq. (2.10), which is derived from an expansion of Faradays Law and Ohms Law.

The latter, the combined momentum equation for both species, likewise includes the divergence of the total pressure tensor, which affects the flow by contributing additional terms to the vorticity, Eq. (2.19).

We now discuss both these sources of plasma flow, but in the computational work that follows we include flow due only to the contribution from the total momentum equation.

5.4.1 Ohms Law

Ohms Law is derived from the electron momentum equation, Eq.(5.34) and assuming quasi-neutrality, may be written:

$$\frac{m\,\nu_{ei}}{ne^2}\,\underline{J} = \underline{E} + \underline{v} \times \underline{B} - \frac{\underline{J} \times \underline{B}}{ne} + \frac{\nabla.\underline{\underline{P}}_e}{ne} \qquad (5.64)$$

Thus when deriving the condition of toroidal incompressibility (Chapter 2 section 1.3) the Ohms Law Eq. (2.8) must be replaced by Eq. (5.64) when forming Eq. (2.9). The electron pressure tensor gives rise to an additional term in Eq. (2.9), neglecting as before the terms in $\underline{J} \times \underline{B}$:

$$\frac{1}{R^2}\frac{d}{dt}(R\underline{B}) = \frac{1}{R}(\underline{B}.\nabla)\,\underline{v} - R\underline{B}\,\nabla.\left(\frac{\underline{\underline{v}}}{R^2}\right) - \frac{\underline{B}}{R^2}\,\underline{v}.\nabla R$$

$$- \frac{1}{R}\nabla \times \eta\,\underline{J} + \frac{1}{neR}\nabla \times \nabla.\underline{\underline{P}}_e \qquad (5.65)$$

As in Appendix A, we take the toroidal component, and eliminate those forms which are not the lowest order in β.

$$\nabla.\left(\frac{\underline{v}}{R^2}\right) = -\frac{1}{R^2 n_e B_\phi}\left(\nabla R \times \nabla\left(p_{\perp e} - p_{\parallel e}\right)\right)_\phi \qquad (5.66)$$

In situations where the difference of parallel and perpendicular electron pressures vary around or across magnetic surfaces toroidal incompressibility itself is in doubt, affected by electric fields produced by the difference of parallel and perpendicular electron pressures.

5.4.2 Momentum Equation

The momentum equation for both species, electrons and ions may be derived from the single species momentum equation, Eq. (5.17) by defining a total density ρ, centre of mass velocity $\underline{v}$, total stress tensor $\underline{\underline{P}}$ and current density $\underline{J}$. Assuming quasi-neutrality:

$$\rho = \sum_a \rho_a$$

$$\rho\underline{v} = \sum_a \rho_a \underline{v}_a$$

$$\rho\underline{vv} + \underline{\underline{P}} = \sum_a \left(\rho_a \underline{v}_a \underline{v}_a + \underline{\underline{P}}_a\right)$$

$$\underline{J} = n\sum_a e_a \underline{v}_a$$

and Eq. (5.17) becomes:

$$\frac{\partial}{\partial t}(\rho\underline{v}) + \nabla.(\rho\underline{vv} + \underline{\underline{P}}) = \underline{J} \times \underline{B} \qquad (5.67)$$

In Chapter 2 we obtained the vorticity, Ξ using

$$\Xi = \nabla \times R^2 \rho\, \underline{v}$$

thus in our derivation of its rate of change with time (Appendix B) we must now calculate a term of the form

$$\underline{\Lambda} = -\nabla \times (R^2 \nabla . \underline{\underline{P}}) \tag{5.68}$$

This is easily achieved using the tensor notation of Appendix D.

$$\Lambda_k = -(R^2 p^{jl}{}_{|l})_{|m}\, g^{mi}\, \varepsilon^{ijk} \tag{5.69}$$

As before we require the toroidal component of Eq. (5.68) in order to form an equation, analogous to Eq. (2.19) for the evolution of the vorticity. We therefore require the component k = 3 of Eq. (5.69):

$$\Lambda_3 = -\frac{h_3}{h_1 h_2}\left((h_2{}^2 N^2)_{,1} - (h_1{}^2 N^1)_{,2}\right) \tag{5.70}$$

where

$$N^j = R^2 p^{jl}{}_{|l}$$

The pressure tensor, to the lowest order, in a frame parallel locally to the magnetic field is given by Eq. (5.26). However, in flux surface coordinates (χ,ψ,ϕ):

$$\underline{\underline{P}} = \begin{bmatrix} \gamma^2 p_\perp + \alpha^2 p_\parallel & 0 & \alpha\gamma(p_\parallel - p_\perp) \\ 0 & p_\perp & 0 \\ \alpha\gamma(p_\parallel - p_\perp) & 0 & \alpha^2 p_\perp + \gamma^2 p_\parallel \end{bmatrix} \tag{5.71}$$

where

$$\gamma = B_\phi / B$$

and

$$\alpha = B_\chi / B$$

Neglecting terms that include α^2 and approximating $\gamma^2 \simeq 1$ we find, after some algebra:

$$\Lambda_\phi = -(R\nabla R \times \nabla(p_\perp + p_\parallel))_\phi \qquad (5.72)$$

The parallel pressure therefore affects the vorticity in the same way as the perpendicular pressure.

Consider the simple case of a tokamak in which the plasma density is constant and the temperature high. We assume the magnetic surfaces are concentric circles. For each species, these magnetic surfaces will also be surfaces of constant parallel temperature. If $T_\parallel$ of a species is large compared to $T_\perp$, for instance if a neutral beam is used to heat the plasma and $T_\parallel$ varies across the poloidal plane, gradients of $p_\parallel$ will produce flow as indicated by Eq. (5.72). Fig. 5.2 shows a distribution of $T_\parallel$ that could arise if a neutral beam were to deposit its parallel energy about the dotted line. As we have assumed the density constant, the contribution $p_\parallel$ makes to the vorticity is shown in Fig. 5.3. This vorticity causes four circulatory cells; two above and two below the axis of symmetry. The flow pattern is indicated in Fig. 5.4.

If the neutral beam were sufficiently intense, this flow could dominate the normal flow arising from sound waves and Alfven waves. Also, at high plasma temperatures, the magnetic field is frozen into the plasma, so this too is convected with the flow. It is easy to see the sheared flow shown in Fig. 5.4 could lead to the disruption of magnetic surfaces. However, before that occurred, poloidal currents may play a rôle in limiting the process.

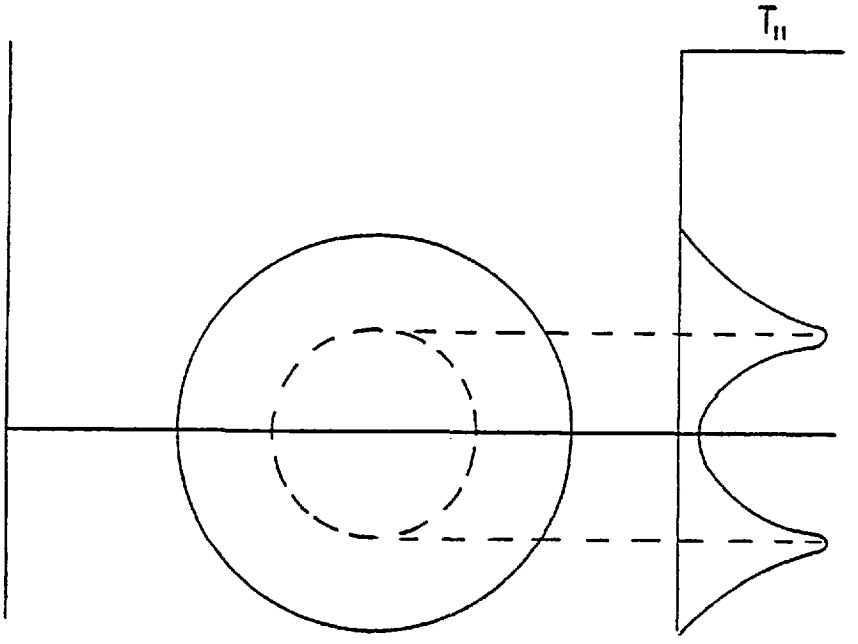

Fig. 5.2 Conceptual distribution of parallel temperature arising from neutral beam deposition in the region of the dotted line.

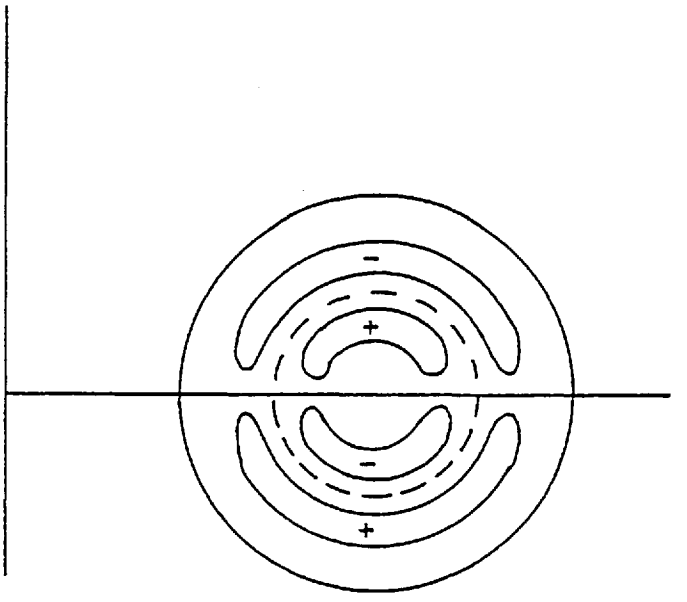

Fig. 5.3 Vorticity generated by the distribution of parallel pressure shown in Fig. 5.2.

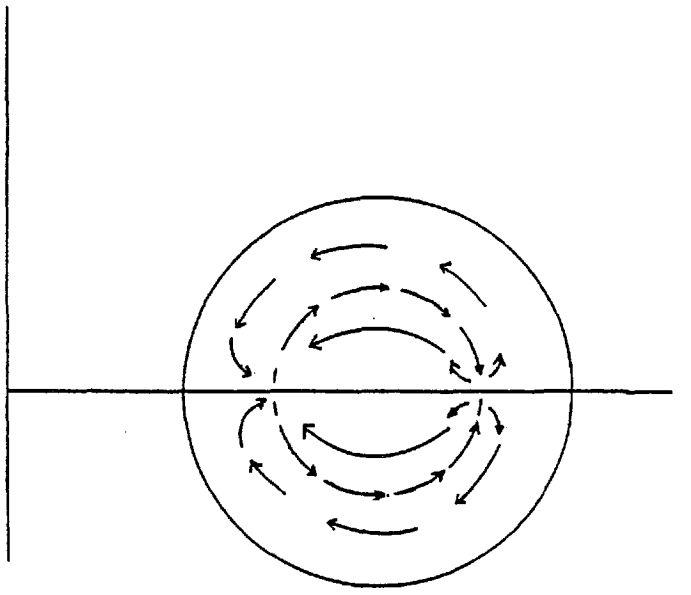

Fig. 5.4 Flow pattern arising from the distribution of parallel pressure shown in Fig. 5.2.

5.5 SUMMARY

The model described in this Chapter uses Eqs. (5.60) - (5.63) to define, in the limit of zero collision frequency, the perpendicular and parallel temperatures on a magnetic surface. These high temperature relations replace the classical energy equation described in Chapter 2 used in a cooler, more collisional regime. Anisotropic pressure affects Ohms Law and the momentum equation. In the first of these, (Eq. (5.66)) the electron pressure tensor puts toroidal incompressibility in doubt because of electric fields generated by the difference in perpendicular and parallel pressures. In the second, the total pressure tensor adds an extra contribution to the vorticity.

In the next Chapter we shall investigate the effects of this second source of flow on the plasma equilibrium.

CHAPTER 6

SIMULATION OF HIGH TEMPERATURE PLASMAS AND NEUTRAL BEAM INJECTION

6.1 INTRODUCTION

In contrast to the low temperature simulations described in an earlier chapter, this chapter describes simulations of high temperature plasmas, and in particular the effect of neutral beam injection on the plasma flow.

Neutral beams have been considered for some years now as the most promising form of auxillary heating to take tokamak plasmas from the maximum temperature attainable by Ohmic heating to temperatures required for alpha particle heating to become important. Recent results[9] show that substantial heating is possible using neutral beams, but the value of $n\tau$, the product of density and energy confinement time, is still no nearer the Lawson criterion for energy breakeven.

The simulations in this chapter are not concerned with mechanisms of neutral beam penetration and heating, which are in general well understood[27], but with the effect which a neutral beam has on the plasma flow. If the flow is enhanced, the increased level of turbulence could lead to larger transport and a reduction in the energy confinement time.

Firstly, the initialisation of these high temperature simulations is described, for which an approximate solution of the axisymmetric equilibrium equation is used to obtain the current density $\underline{J}$. Pressure balance then gives the pressure, p. Simulations without a neutral beam are then described with the initial condition close to equilibrium.

Finally, a neutral beam is introduced as a source of pressure parallel to the magnetic field, and a simulation presented to show its effect upon the plasma flow. This run is compared in detail with the run in which no neutral beam was present.

6.2 INITIALIZATION

To study the effects of a neutral beam on the plasma flow, it is beneficial to have the plasma close to equilibrium so that as the neutral beam is injected into the plasma, resultant flow may be associated with the beam and not with the general motion of the plasma towards an equilibrium.

6.2.1 Approximate solution of the equilibrium equation

For a particular poloidal beta and toroidal current, the surfaces of constant pressure may be found by solving the axisymmetric equilibrium equation (Appendix C),

$$\Delta^*\psi = -\mu_0 R^2 \dot{p} - F\dot{F} = -\mu_0 R J_\phi \qquad (6.1)$$

where the plasma pressure $p(\psi)$ and poloidal current function $F(\psi)$ are functions of ψ and

$$\dot{F} = dF/d\psi$$

Equation (6.1) has been solved[69] with $p(\psi)$ and $F\dot{F}(\psi)$ as given functions of ψ. Also equilibria have been found[20] when $\dot{p}(\psi)$ and $q(\psi)$ (the Kruskal-Shafranov Safety factor) are given functions. It is however, much more complex to obtain, in toroidal geometry, self-consistent solutions of the axisymmetric equilibrium equation using the poloidal component of Ohms Law and some requirement upon the flux of plasma across magnetic surfaces[70].

In our case it is sufficient to employ a first order inverse aspect ratio expansion to obtain the distribution of magnetic surfaces. This is analogous to the calculation of the magnetic surface distribution discussed in Chapter 3.1.1 from a required initial current density

distribution. From this approximate equilibrium the plasma will relax to the exact equilibrium solution of Eq. (6.1).

We consider the current density at a distance from the major axis equal to the major radius, and define

$$J_c = \mu_o R_o J_\phi \ (R_o) \tag{6.2}$$

As the poloidal beta relates the internal energy of the plasma to the magnetic energy of the poloidal field, we may write approximately

$$\beta_p = \frac{\mu_o R_o^2 \dot{p}}{J_c} \tag{6.3}$$

and therefore

$$F\dot{F} = (1 - \beta_p) J_c \tag{6.4}$$

Substituting Eqs. (6.3) and (6.4) into Eq. (6.1) we find

$$\Delta^* \psi = -J_c (1 + 2\beta_p \frac{r}{R_o} \cos\theta)$$

where r is the distance from the minor axis and θ is measured from the mid plane (Fig. 3.1). This is of the same form as Eq. (3.1) and may be solved in an entirely analogous manner, giving to the first order in the inverse aspect ratio:

$$\psi = \frac{J_c a^2}{4} (1 - \frac{r^2}{a^2}) (1 + \frac{r}{4R_o} (4\beta_p + 1) \cos\theta) \tag{6.5}$$

Equation (6.5) gives the distribution of surfaces of constant poloidal flux for a plasma with a given poloidal beta. The toroidal current distribution is then easily calculated using the Grad-Shafranov equation.

For $\beta_p = \frac{1}{4}$ contours of ψ and J_ϕ are shown in Fig. 6.1 where the arrow plots show the poloidal current. This current flows so that the

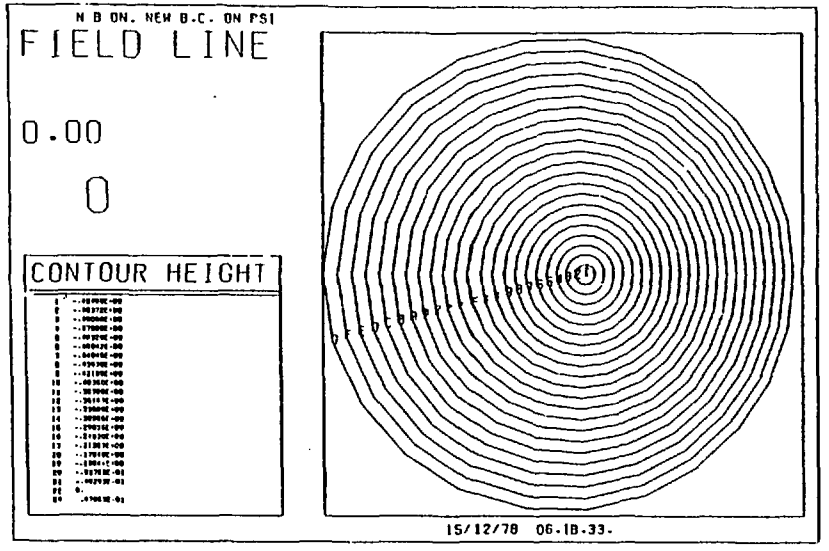

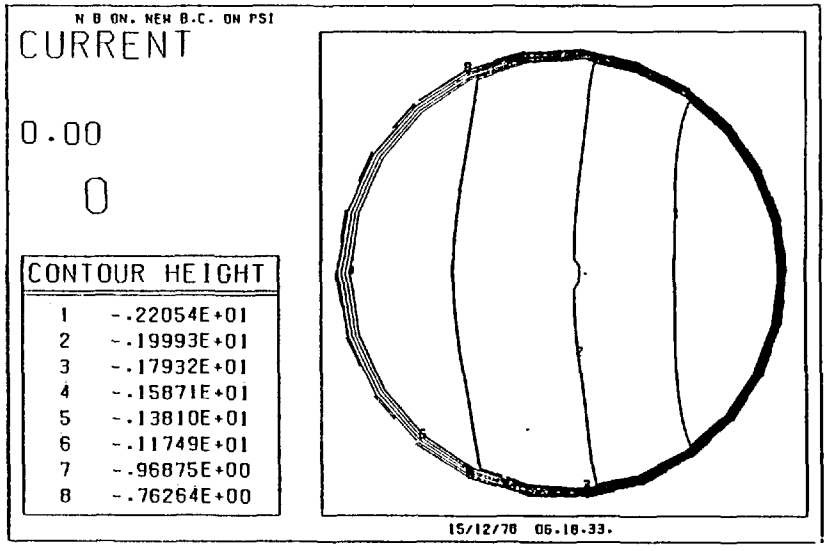

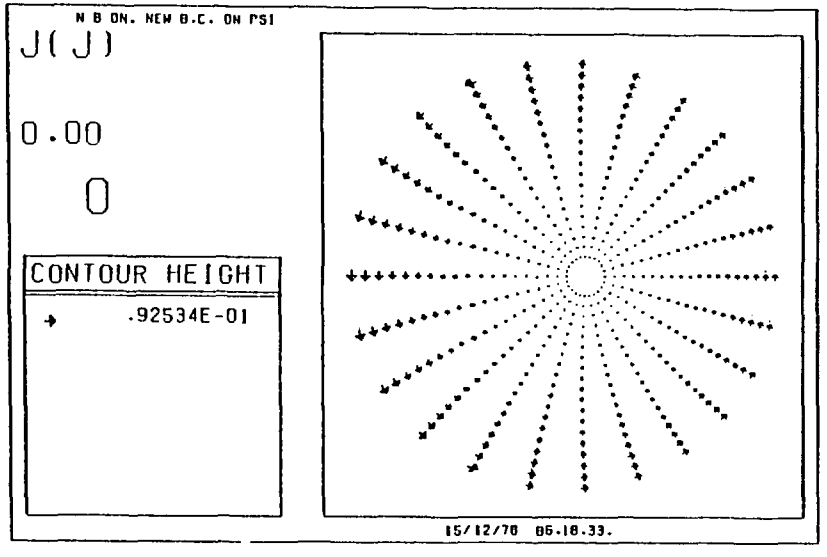

Fig. 6.1 Contours of ψ, J_ϕ and a plot of poloidal current for $\beta_p = \frac{1}{4}$

force $\underline{J}_p \times \underline{B}_\phi$ assists the pressure gradient in opposing the force $\underline{J}_\phi \times \underline{B}_p$. We note also that the magnetic axis is shifted towards the outside of the torus away from the major axis which is, as always, to the left. The shift of the magnetic axis is obtained by finding the extremum of Eq. (6.5). Again a similar expression is obtained to Eq. (3.5) modified only by β_p, for the shift δ along $\theta = 0$ from the minor axis.

$$\delta = \frac{4R_o}{3(4\beta_p + 1)} \left[\left(\frac{3a^2(4\beta_p + 1)^2}{16\ R_o^2} + 1 \right)^{\frac{1}{2}} - 1 \right] \qquad (6.6)$$

For $R_o = 2.93$m, $a = 1.28$m and $\beta_p = \frac{1}{4}$, Eq. (6.6) gives $\delta = .135$m.

Fig. 6.2 shows the same dependent variables as in Fig. 6.1, but with $\beta_p = 1$. We notice the shift of the magnetic axis is much greater in this case, $\delta = .294$m, and the magnetic surfaces are more bunched towards the outside of the torus. Correspondingly, this causes the toroidal current density to be more peaked in this region. The poloidal current, however, is much smaller in this case because the pressure gradient almost entirely balances $\underline{J}_\phi \times \underline{B}_p$. The balance is not exact because distribution of ψ is calculated only to first order in the inverse aspect ratio, and a small poloidal current flows that reinforces $\underline{J}_\phi \times \underline{B}_p$ in order to balance ∇p. Fig. 6.3 shows the difference in the profiles of J_ϕ for the above two cases.

6.2.2 Choice of initial equilibrium conditions

The preceding section has shown us how an equilibrium may be set up by choosing the parameters β_p, J_c and the aspect ratio. It is however, more useful to relate the equilibrium to the usually observed parameters of current, loop voltage and temperature. Now:

$$J_c = \frac{\mu_o R_o I}{\pi a^2} \qquad (6.7)$$

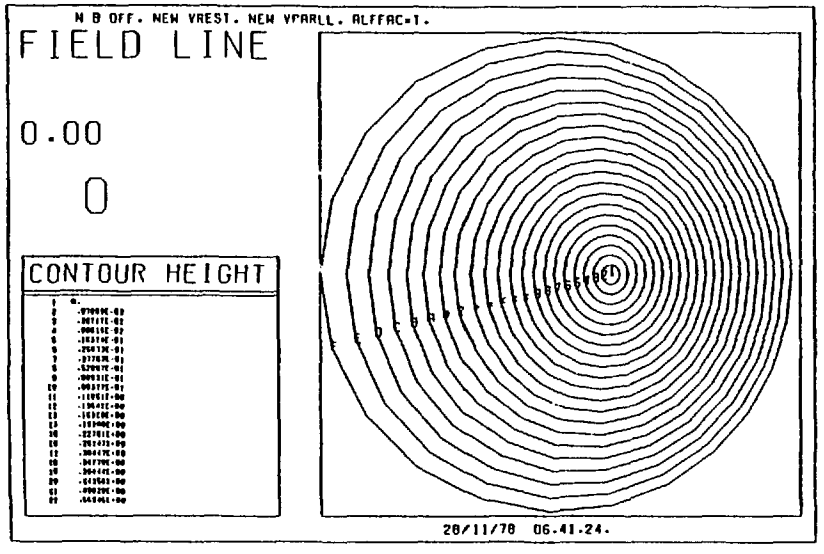

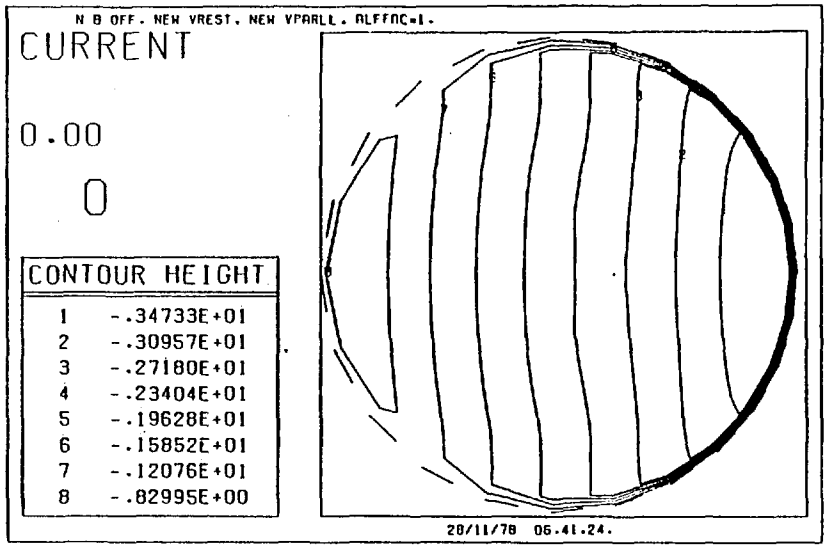

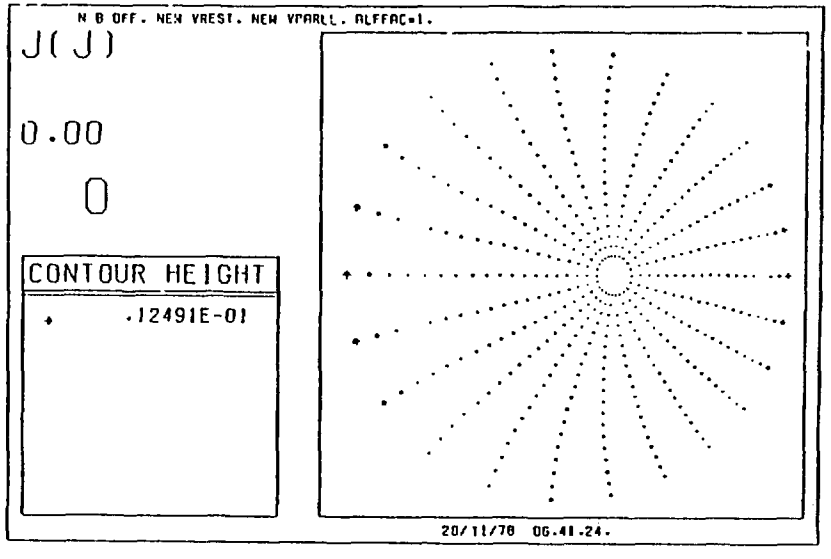

Fig. 6.2 ψ, J_ϕ and J_p for $\beta_p = 1$

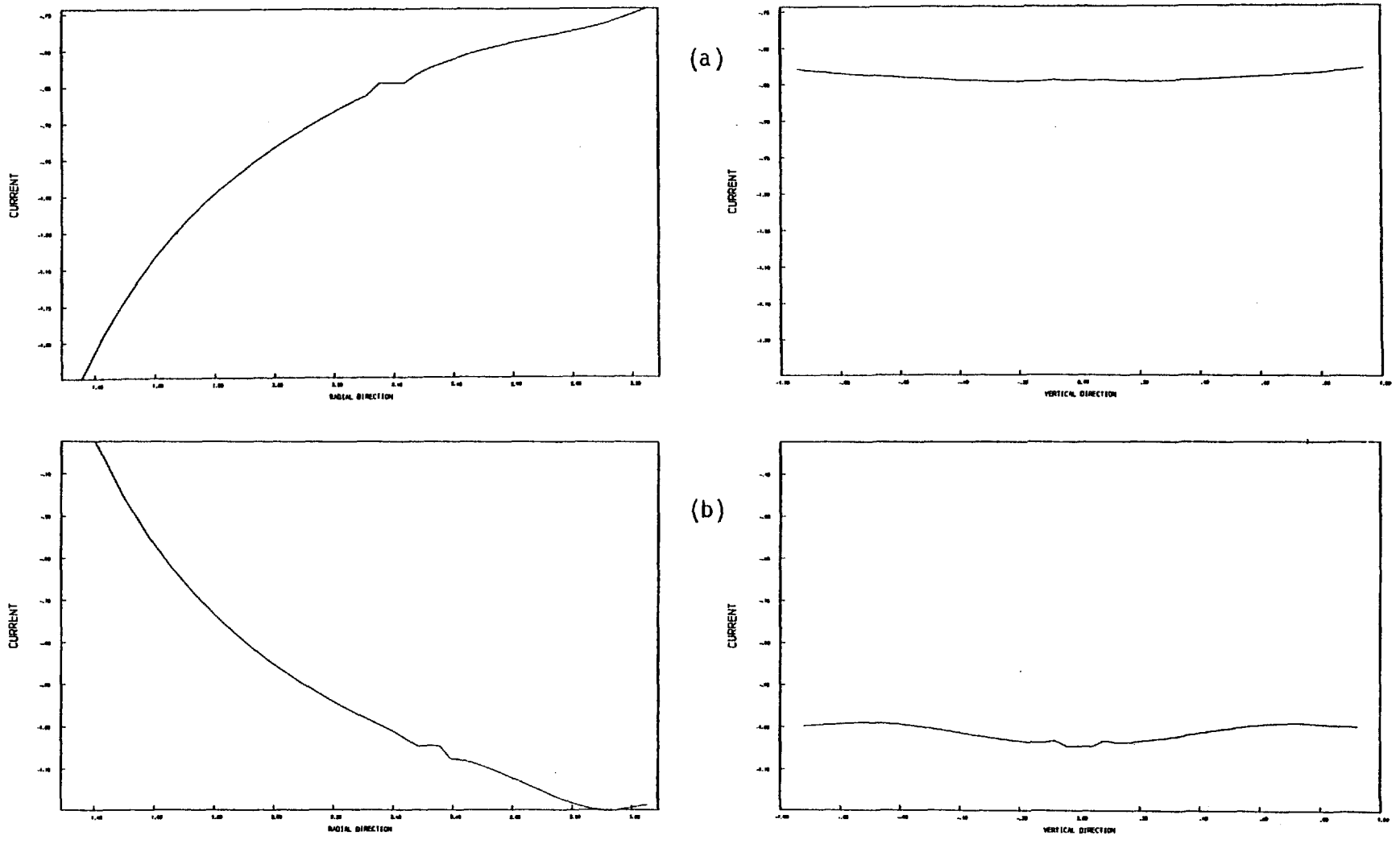

Fig. 6.3 Profiles of the toroidal current density for (a) $\beta_p = \frac{1}{4}$ and (b) $\beta_p = 1$

where I is the total plasma current; and the pressure gradient, from Eq. (6.3) is

$$\dot{p} = \beta_p \frac{I}{\pi a^2 R_o}$$

We must, however, choose initial temperature and density profiles that will give this pressure profile.

In order to choose initial conditions that are closest to an equilibrium we demand that the temperature is uniform and that the density profile follows the pressure profile[71]. If θ is the temperature temperature in electron volts then

$$\dot{n} = \frac{\beta_p I}{e\theta\pi a^2 R_o} \qquad (6.8)$$

A more realistic model would be one where the temperature follows the pressure profile and the density uniform, because experimentally the plasma has both a density and temperature profile, but the temperature profile is far more pronounced. Computationally, it is difficult to choose initial conditions close to an equilibrium that are of this kind. This is because the resistivity is temperature dependent and this affects the equilibrium current distribution, which modifies the pressure profile, which in turn feeds back to the resistivity. This would be a very interesting exercise, but as the intention is to produce a near equilibrium plasma, we do not pursue it.

Finally, the loop voltage, V, is related to the current and temperature.

$$V = \oint \underline{E} \cdot \underline{dl}$$

Very approximately $E_\phi = \eta J_\phi$ and $\eta = 10^{-3}/\theta^{3/2}$ ohm-m, so using Eq. (6.8) we find

$$\dot{n} \simeq \frac{10^{22}}{3.2\pi} \quad \frac{V\beta_p \, \theta^{\frac{1}{2}}}{R_o} \tag{6.9}$$

and Eq. (6.7) is:

$$J_c = 2.10^{-4} \, V \, \theta^{3/2} \tag{6.10}$$

Therefore, in principle by supplying the loop voltage, poloidal beta, average temperature and major radius, we define a unique equilibrium.

6.3 SIMULATION WITHOUT A NEUTRAL BEAM

All the numerical solutions presented in this chapter were obtained by using the parameters of the JET tokamak. The aspect ratio, major radius and toroidal magnetic field are given in Table 4.1. We assume in the simulations of this chapter that the initial temperature is 1.18 keV and the total plasma current (which given the temperature defines the loop voltage) is held constant at 2.8 MA. These chosen values correspond to the postulated values for the JET experiment, and give a safety factor $q(a) \simeq 3.5$.

In the run described we choose β_p of order unity. As we have already seen from Fig. 6.2 the plasma is not quite in equilibrium because of the expansion used to determine J_ϕ and p. Therefore, ∇p and $\underline{J} \times \underline{B}$ do not balance exactly and the plasma accelerates because of the net force on it. This appears in the simulation as a source of vorticity. Equation (2.19):

$$\frac{d\Xi}{dt} \simeq R^2 |\nabla p \times \nabla R^2| + R^2 \underline{B}_p . \nabla R J_\phi$$

shows that vorticity is generated either by a vertical (perpendicular to the midplane) gradient of pressure leading to sound waves, or by a gradient of RJ_ϕ parallel to the poloidal field, leading to Alfven waves. In equilibrium, these two sources would balance and no flow would result. However, the initial conditions are not an exact equilibrium.

At first the sound term dominates the vorticity, producing a negative vortex above the midplane, Fig. 6.4, and producing flow which pushes the magnetic surfaces outwards; i.e. away from the major axis. This flow, however, shifts the magnetic surfaces towards the outer wall and increases J_ϕ, Fig. 6.5. At the same time, this advection modifies the density and thus the temperature. The flow attempts to reduce the pressure gradient by cooling the centre of the plasma and heating the

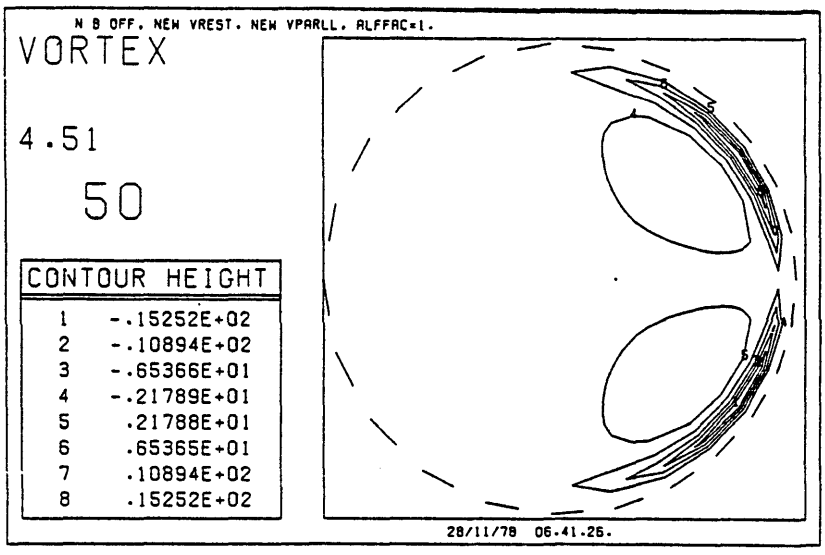

Fig. 6.4 Flow pushes the surfaces outwards

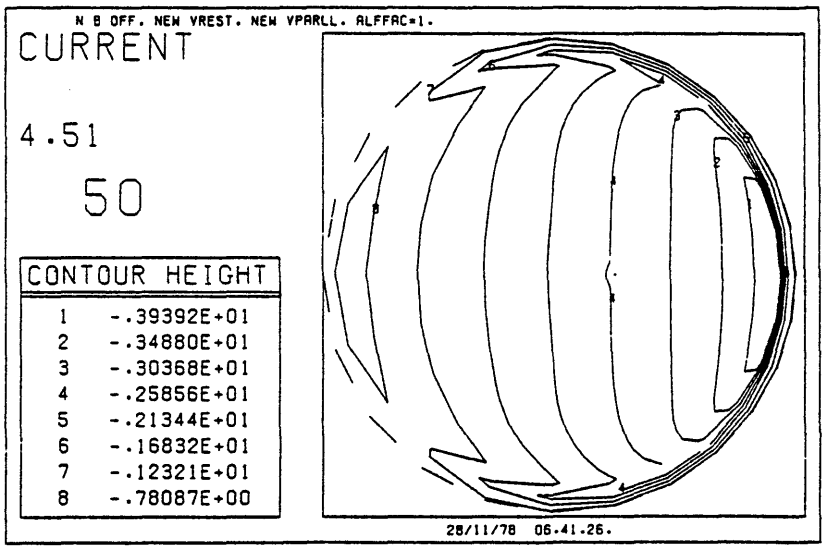

Fig. 6.5 Current density increases at the outer edge

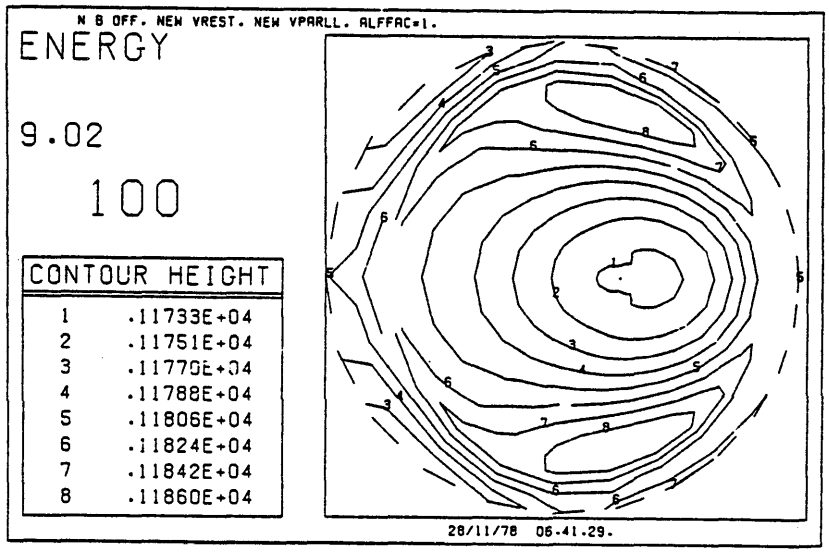

Fig. 6.6 The edges are heated and the centre is cooled

edges, Fig. 6.6. The steepening of ∇RJ_ϕ and reduction of $\nabla p \times \nabla R^2$, eventually results in the fluid moving back towards the major axis, until the Alfven term is reduced and the sound term increased again. This is shown in sequence by Fig. 6.7, which shows the stream function at intervals of 4.5 μs, from which the flow velocity may be derived using Eqs. (2.12)

$$v_R = R \frac{\partial \zeta}{\partial z} , \qquad v_z = -R \frac{\partial \zeta}{\partial R}$$

In Fig. 6.7(a) the flow is outwards, but in (b) the Alfven flow is approximately balancing the sound flow on the outer side of the torus, whilst on the inner side there is still a strong flow caused by the pressure gradient. In (c) the Alfven flow is dominant on the outer side and advects the surfaces inwards while the sound flow still dominates the inner region. These oscillations are slowly damped by resistivity.

In this high temperature simulation, the resistivity is very small and the oscillations continue throughout the simulation period. Also, because of the high temperature the diffusion rate of magnetic flux is very small. When the fluid moves, the magnetic surfaces do also; thus after 500 timesteps of the simulation the value of poloidal flux on the magnetic surfaces is virtually unchanged, (compare Figs. 6.8 and 6.2).

This oscillating behaviour of the plasma is more easily studied by following the total internal, magnetic and flow energies in time. These are calculated using the algorithms discussed in Chapter 3, section 4, and are plotted in Fig. 6.9. Although the total energy is a growing function of time, which occurs because of a slowly growing numerical instability associated with the boundary condition on ψ, the interaction of sound and Alfven waves is clear.

The sound and Alfven times (Chapter 2) are respectively:

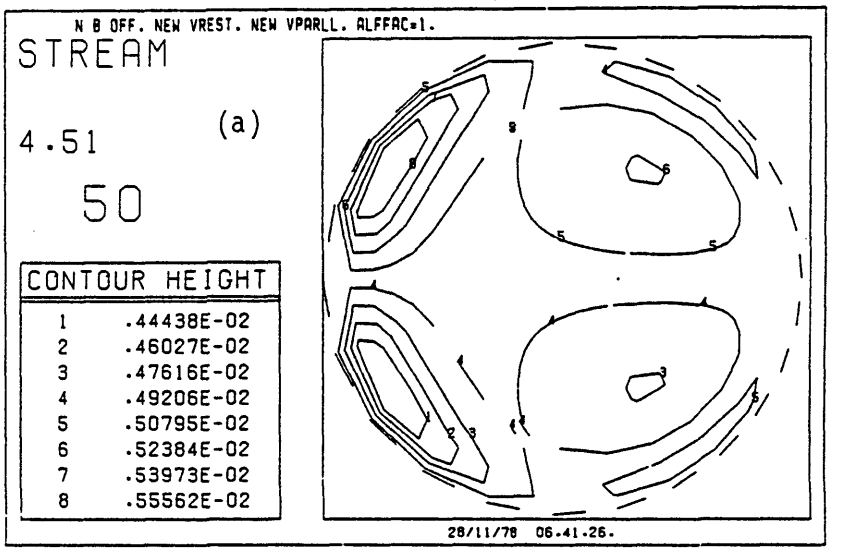

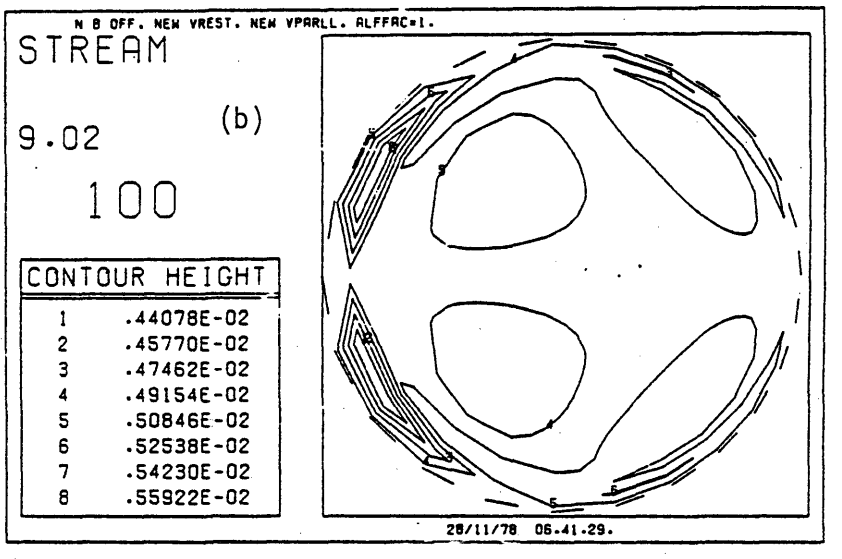

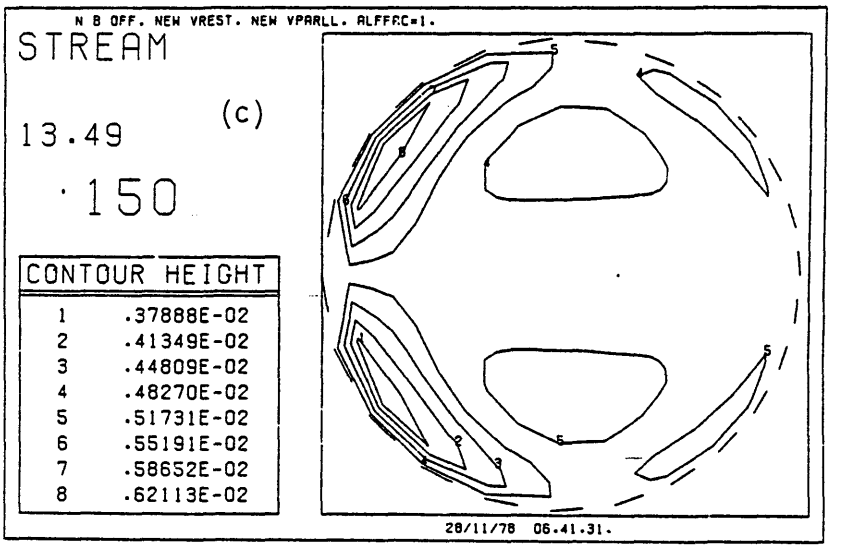

Fig. 6.7 Stream function at intervals of 4.5 μs.

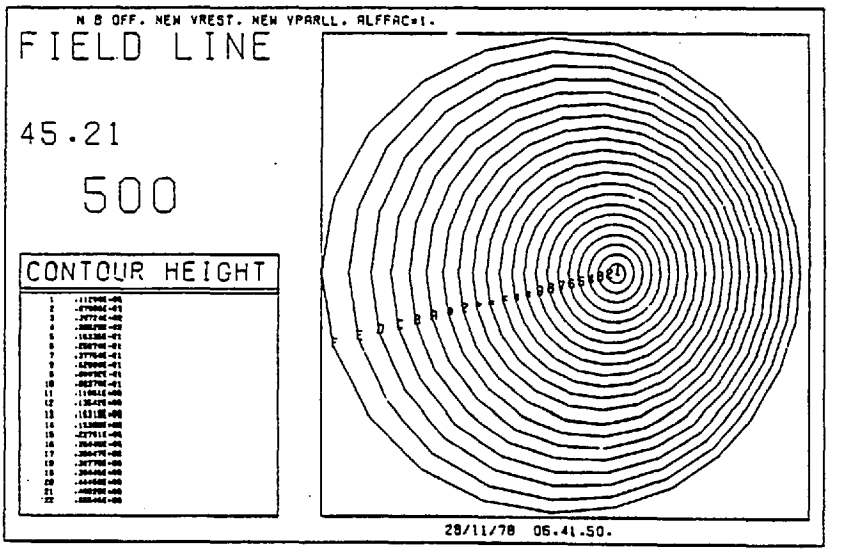

Fig. 6.8 The poloidal flux stays virtually constant throughout the simulation (cf. Fig. 6.2)

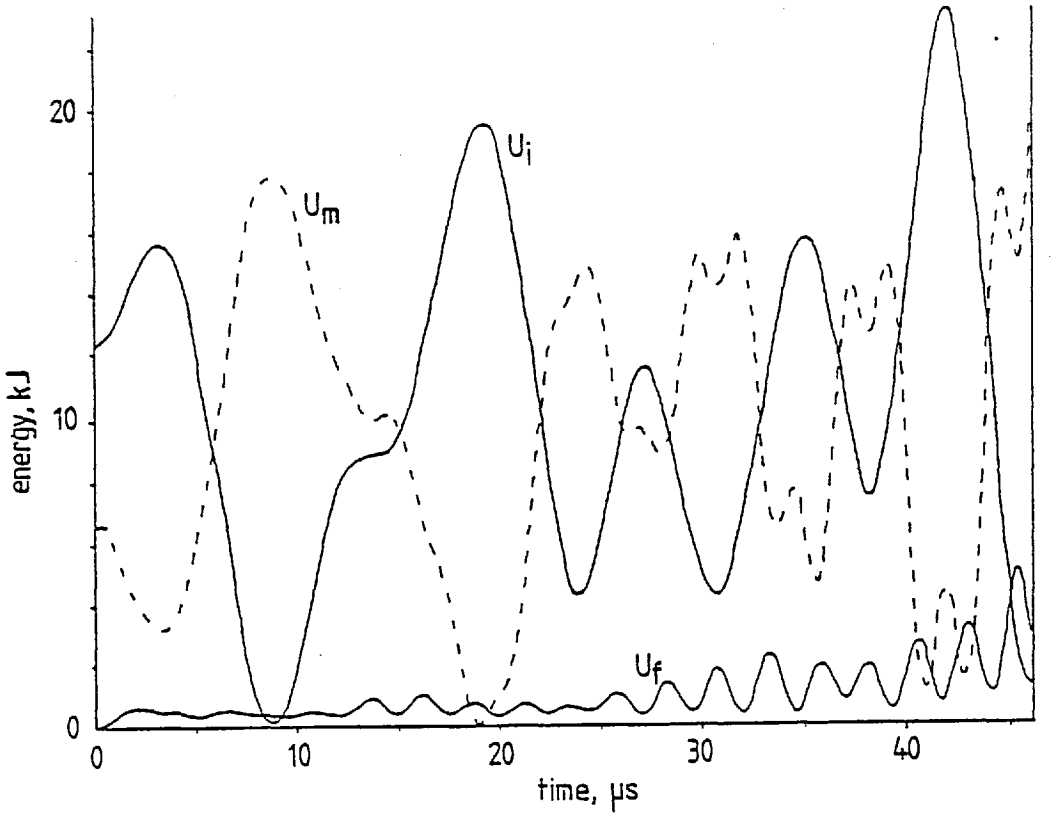

Fig. 6.9 Plasma internal, magnetic and flow energy change plotted against time

$$\tau_s = \frac{a}{c_s}\sqrt{\frac{1 + R^2/a^2}{2}}$$

$$\tau_A = \frac{a}{c_A}\sqrt{2\ (1 + R^2/a^2)}$$

where c_s and c_A are the normal sound and Alfven speeds. For the parameters of this simulation τ_s = 56 μs and τ_A = 8.8 μs. The two hyperbolic processes superimpose to give a frequency of combination

$$f_c = \frac{1}{\tau_A} + \frac{1}{\tau_s}$$

and a beat frequency

$$f_B = \frac{1}{\tau_s} - \frac{1}{\tau_A}$$

These give a combination time $\tau_c \simeq 3$ μs and a beat time $\tau_B \simeq 15$ μs. The flow energy exhibits this behaviour giving a beat time ~ 15 μs and a combination time ~ 2 μs, because the plasma will move according to the superposition of the Alfven and sound processes. Throughout the first well defined beat, energy conservation is reasonable. For the first 25 μs the total energy varies only by ~ 5%. However, after this a numerical instability causes the total energy to increase rapidly.

The inductance of the plasma is calculated from the magnetic energy, Eq. (4.13) and shown in Fig. 6.10. This varies in the same way as the total magnetic energy because the total current is conserved by adjusting the boundary condition on the poloidal flux, which is the same as altering the loop voltage. It is, of course, reasonable that the inductance should have a periodic time dependence. We see from Eq. (4.10) that inductance depends upon the geometry of the magnetic surfaces. If these are moved then the inductance will change. Equation (4.10),

$$L = \frac{\mu_0}{\oint h_\chi / R h_\psi \, dx}$$

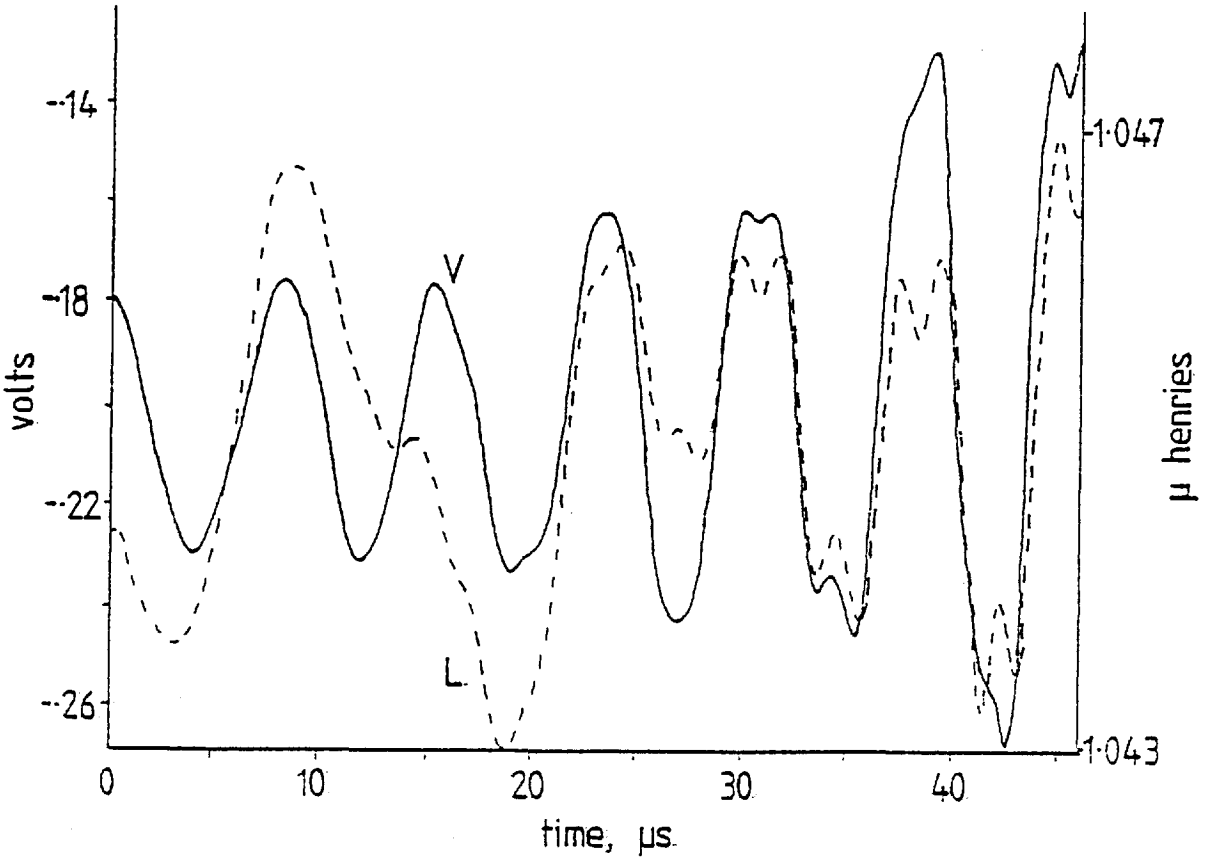

Fig. 6.10 Plasma inductance and loop voltage against time

indicates that if the surfaces are moved towards the major axis then the inductance will decrease. Fig. 6.10 shows that the initial motion is towards the major axis. Then at about the time of Figs. 6.4, 6.5 and 6.7(a), i.e. 4.5 μs, the inductance starts to increase indicating the plasma is moving away from the major axis. This motion continues until about 9 μs (the time of Figs. 6.6 and 6.7(b)) when the inductance decreases again indicating the plasma is moving inwards once again. The interpretation of Figs. 6.4 - 6.7 is therefore correct, except that there is a small amount of initial motion towards the major axis

(indicating an initial domination of Alfven flow) before the pressure gradient drives the plasma outwards.

The oscillations of the loop voltage arise because the inductance varies in the above manner. The boundary value of the poloidal flux is fixed so that the total current I is constant. If we consider the plasma loop as shorted, then:

$$L \frac{dI}{dt} = -I \frac{dL}{dt}$$

Changes in inductance would cause the current to change if ψ on the boundary were constant. However, this current change is balanced by a change of current at the plasma edge brought about by ψ on the boundary. Thus the total current remains constant. The rate of change of poloidal flux at the boundary gives the loop voltage. Equation (4.12) for the loop voltage

$$V = \oint \underline{E} \cdot \underline{dl}$$

may be rearranged

$$V = -2\pi R\left(\frac{\partial \psi}{\partial t}\bigg|_{r=a} - \frac{\partial \psi}{\partial t}\bigg|_{r=o}\right)$$

As $\partial\psi/\partial t$ at the magnetic axis is very small, because the field is frozen in, V is given entirely by $\partial\psi/\partial t$ at the plasma edge. In Fig. 6.10 we see that on average $\frac{\partial \psi}{\partial t}\Big|_{r=a}$ is increasing slowly and represent the change of flux required to balance the ohmic decay of current (for this current and temperature the loop voltage should be ~ .15 V which compares well). The variations in $\frac{\partial \psi}{\partial t}\Big|_{r=a}$ correspond well to the changes in magnetic energy. For a shorted discharge

$$\frac{dU_m}{dt} = \frac{1}{2} LI \frac{dI}{dt}$$

so as U_m decreases initially, Fig. 6.10, the shape of $\partial\psi/\partial t$ indicates that ψ increases steeply to counteract the impending drop in current. Then as U_m increases the rate of increase of ψ decreases, again so that the current will remain constant.

This boundary condition on ψ, whilst producing a current trace that is experimentally realistic, almost certainly results in a numerical instability. Because current is continually changing at the plasma edge, this affects the current distribution (in Fig. 6.5, the sharp rise in current density near the top and bottom edge occurs because of this) which drives Alfven waves that grow.

It is instructive to check the size of the inductive voltage given by I dL/dt against the electric field that arises because the flow is perpendicular to the poloidal magnetic field. Between 5 μs and 10 μs (Fig. 6.10) $\Delta L = 2.5.10^{-9}$ henries. The inductive voltage is $v_L \sim 1.5.10^3$V. From Fig. 6.7(a) the flow velocity away from the magnetic axis $v_\psi \sim 6.10^2$ ms^{-1}. As $B_p \lesssim \mu_o I/2\pi a \lesssim .2$ T we arrive at $\underline{v}_\psi \times \underline{B}_p \lesssim 120$ Vm^{-1}. However, evaluating the voltage $\oint \underline{v}_\psi \times \underline{B}_p . dl \lesssim 2.2.10^3$ V, we see that these two voltages are of the same order, which is what we would expect. This is because the inductive voltage is equivalent to the loop voltage formed by integrating the local $\underline{v}_\psi \times \underline{B}_p$ electric field.

Finally, we may integrate the density and internal energy within each surface in time in order to see whether this oscillatory behaviour has any effect on the diffusive losses. In a toroidal geometry we expect the normal Pfirsch-Schluter[72] enhancement of classical diffusion losses. In an equilibrium situation this exists because convective flow, set up to produce the equilibrium current distribution, results in a net outward force. This diffusive flow may be derived for a tokamak geometry

$$\langle v_\psi \rangle = \frac{n|\nabla p|}{B^2} (1 + 2q^2)$$

where $\langle v_\psi \rangle$ is the surface averaged diffusion velocity. Integrating the particle flux over the whole magnetic surface, we may obtain a mass loss rate. A surface near the wall gives a predicted loss rate of $\sim 2.10^{-6}$ kg/sec.

A loss rate from the code is obtained by integrating the mass loss from each surface over as many oscillation periods as the simulation will allow. In the simulation described this number was about 15 although mass and energy conservation were not good towards the end of the run. Table 6.1 gives the mass loss from magnetic surfaces integrated up to 45 μs. The integrated mass loss from the outer surface, the wall, should be zero because there is no particle production or loss mechanism in the code. Mesh errors lead to inaccuracies in volume calculation, and therefore to variations in total mass and energy so in fact the mass within the outer wall is not constant. To take this into account, it is assumed that this numerical loss is dependent upon the volume of the magnetic surface. Therefore, the loss from each surface is adjusted by an amount proportional to the loss from the outer surface times the ratio of the volume of the surface to the total volume. The integrated loss rate from each surface varies from about 4.10^{-6} kg s^{-1} near the magnetic axis to about 4.10^{-5} kg s^{-1} near the outer surface. The average mass loss rate is $\sim 10^{-5}$ kg s^{-1} which is about ten times the Pfirsch-Schluter value.

It seems, therefore, that flow resulting from the interaction of Alfven and sound waves can lead to diffusive losses in excess of ten times the value predicted by classical theory. This may arise because the flow speed in the simulation, at times, exceeds the steady flow necessary to produce an equilibrium. Our simulation will reach equilibrium when the oscillations have been damped by resistivity. Before that happens the plasma will oscillate about the equilibrium giving rise to large plasma flow. This would increase the diffusive loss rate.

TABLE 6.1

Change of mass within each Ψ surface for no source of P_n

Ψ surface	Mass change after 45 μs (kg)
4	$-1.27 \cdot 10^{-9}$
6	$-1.3 \cdot 10^{-9}$
8	$-2.7 \cdot 10^{-9}$
10	$-4.2 \cdot 10^{-9}$
12	$-3.9 \cdot 10^{-9}$
14	$-2.8 \cdot 10^{-9}$
16	$5.0 \cdot 10^{-9}$
18	$1.0 \cdot 10^{-9}$
20	$2.0 \cdot 10^{-9}$
22	$5.0 \cdot 10^{-9}$

6.4 MODEL OF A NEUTRAL BEAM

Neutral beams have long been proposed as a method of heating contained plasmas to thermonuclear fusion temperatures[68]. Essentially, in the case of a tokamak, an energetic beam of particles is injected (usually tangential to the plasma and in the plane of the torus) into the containment device. The particles are neutral so that their trajectories are unaffected by the magnetic field and may penetrate into the interior of the plasma. The beam particles are usually either hydrogen or deuterium which help refuel the plasma and offset diffusion losses, and their energies are chosen to ensure that they reach the interior of the plasma (the mean free path is proportional to the beam energy). These hot neutral beam particles exchange electrons with cold plasma ions to give fast ions and slow neutrals.

The classical deceleration of an energetic ion is described by Furth[26]. For typical tokamak parameters the injected ions are slow compared to the plasma electrons and fast compared to the plasma ions; hence the electrons are important in the slowing down process. If the fast ion energy is greater than some critical energy W_{crit} then the energy is given principally to the electrons while for the fast ion energy less than W_{crit} the energy goes to the plasma ions. For a typical tokamak reactor plasma the beam energy is greater than W_{crit}, and so the electrons receive the fast ion energy. This energy, however, is very directed, as both the fast ions and heated electrons have a very large velocity parallel to the direction of the neutral beam. If the neutral beam is injected tangentially to the magnetic surfaces then the fast electrons and ions have a large velocity and, thus temperature parallel to the magnetic surface. We therefore regard a neutral beam as a source of parallel pressure.

We consider a neutral beam delivering a total power of W watts tangential to a particular magnetic surface ψ, volume V. The rate of

change of total parallel pressure (assuming that all the neutral beam energy goes into parallel pressure) is:

$$\frac{d}{dt} p_{\parallel}(\psi) = \frac{W}{V} \qquad (6.11)$$

However, on other surfaces not all the beam energy will go into parallel pressure, as shown in Fig. 6.11, looking down on the torus.

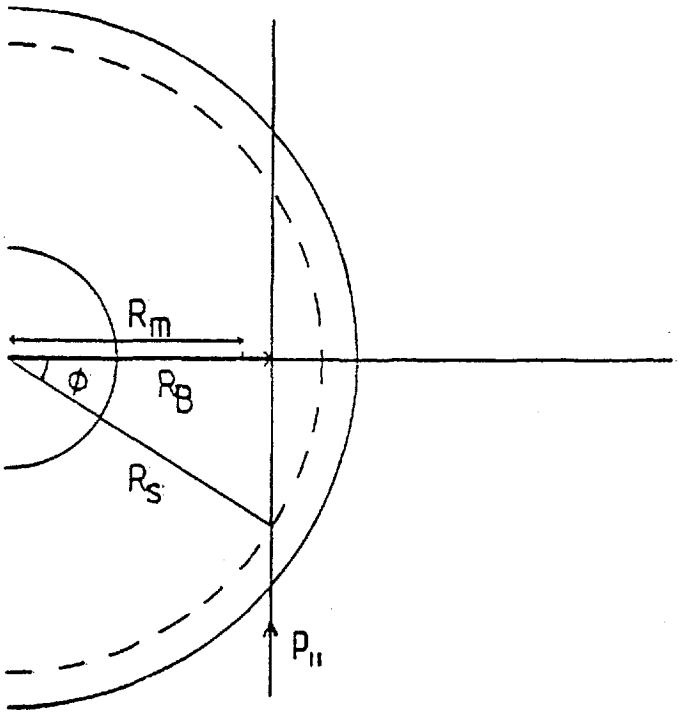

Fig. 6.11 Neutral beam injection geometry

For $R_B > R_M$ the corrected parallel pressure $\bar{p}_{\parallel}$ on a surface of radius R_S is:

$$\bar{p}_{\parallel} = p_{\parallel}(\psi) \frac{R_S}{R_B} + p_{\parallel\ \text{initial}} \qquad R_S > R_B$$

$$\bar{p}_{\parallel} = p_{\parallel\ \text{initial}} \qquad R_M < R_S < R_B$$

where $p_{\parallel}(\psi)$ is given by Eq. (6.11)

The model of chapter 5 allows us to define the parallel pressure throughout a magnetic surface given the parallel pressure at just one point on that surface. Finally, we do not separate the electron and ion pressures because the flow effects we consider in the next section, are generated by the gradient of total parallel pressure rather than either the electron or ion component.

6.5 EFFECT OF PARALLEL PRESSURE ON THE FLOW

The simulation described in section 3 of this chapter was repeated with a source of parallel pressure modelling the injection of a neutral beam.

In both these simulations the model described in Chapter 5 has been used to determine the parallel and perpendicular temperatures on a magnetic surface. We assume that the temperature is sufficiently high for collisions to be negligible. Also we described both species by total temperatures perpendicular and parallel to the magnetic field. Under these conditions, Eqs. (5.61) and (5.63) may be written:

$$\frac{\partial}{\partial X^3} T_{\parallel} = 0$$

$$\frac{\partial}{\partial X^3} \left(\frac{T_{\perp}}{\rho}\right) = 0$$

Thus the parallel and perpendicular temperatures may be uniquely determined on a magnetic surface.

The source of parallel pressure introduces energy of about 250 kJ during the timescale of the simulation, which is confirmed by energy balance. This amount of energy is far less than the amount that will be injected into JET i.e. 10 - 25 MW, for the order of a second[74]. We constrain the parallel pressure to rise linearly from the beginning of the simulation and assign it to each magnetic surface according to the angle at which the beam cuts each magnetic surface. In the run described below we assume the beam penetrates the plasma to a magnetic surface about half way between the wall and the magnetic axis. The parallel pressure increases on surfaces outside this but remains constant on surfaces within. The initial pressure distribution is assumed isotropic.

After 4.5 μs the plasma evolution is almost identical to the isotropic simulation. If Fig. 6.12(a), (b), are compared to Figs. 6.4

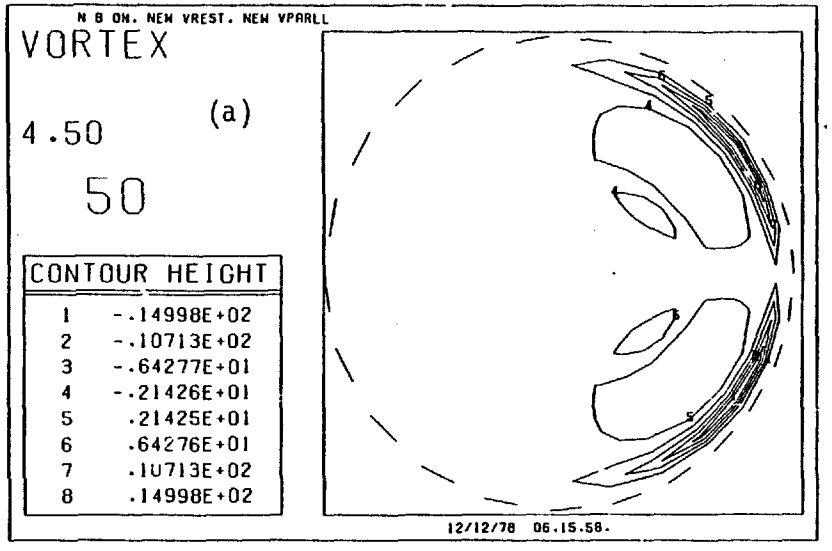

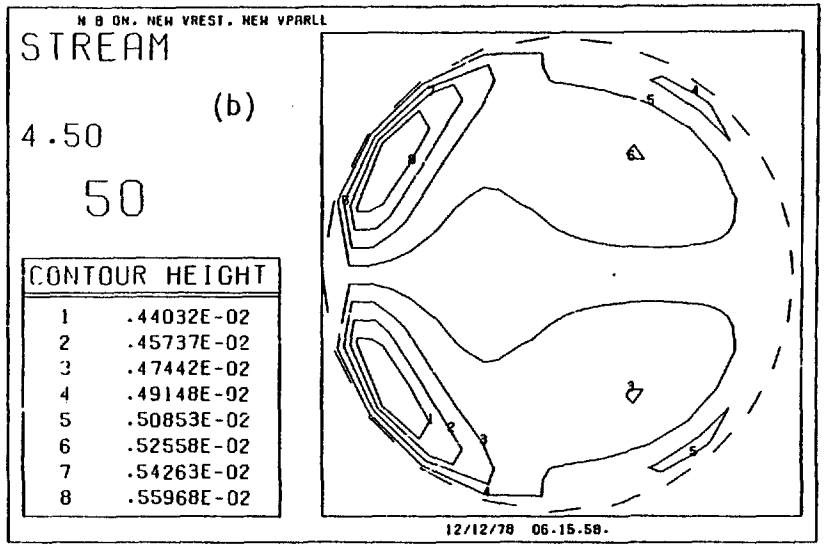

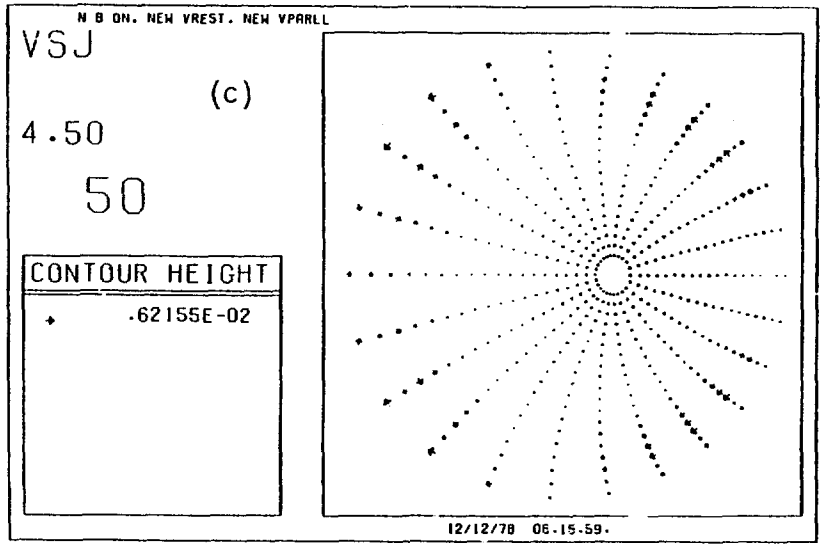

Fig. 6.12 Plasma evolution after 4.5 μs is very similar to the case without a source of parallel pressure

and 6.7, the similarity is clear. The positive vortex near the outer edge arises from $\underline{B}.\nabla RJ_\phi$ and the negative valued vortex nearer the magnetic axis is from the $\nabla p_\perp \times \nabla R^2$ term. These two vortices give rise to the counter rotating cell pattern characteristic of the interaction of sound and Alfven waves, Fig. 6.12(c). The remaining small vortex in Fig. 6.12(a) indicates that parallel pressure is beginning to affect the flow. As discussed in the last chapter, the parallel and perpendicular pressures both give rise to similar contributions, Eq. (5.72), for vorticity production:

$$\frac{1}{R}\frac{d\Xi}{dt} - \tfrac{1}{2}|\nabla R^2\rho \times \nabla v^2| = \tfrac{1}{2}|\nabla p_\perp \times \nabla R^2| + \tfrac{1}{2}|\nabla p_\parallel \times \nabla R^2| + R\underline{B}.\nabla RJ_\phi$$

The small vortex indicates that a vertical gradient of $p_\parallel$ is beginning to appear.

After 25 μs the picture is quite different. The vertical gradient of $p_\parallel$, whose form is indicated in Fig. 5.2, has become large and positive above the mid-plane about half way between the magnetic axis and wall. This gives rise to a positive vortex, Fig. 6.13(a). The slower decrease in $p_\parallel$ towards the wall leads to a smaller negative vortex. This agrees exactly with the flow predicted in Figs. 5.3 and 5.4. The vortices near the wall are identical to those seen in the previous run. These arise because of gradients of RJ_ϕ parallel to B_p and are interpreted as Alfven waves. This oscillatory flow is modified by the steady flow that arises from the gradients of $p_\parallel$, Fig. 6.13(b), (c), which alters by advection the magnetic surfaces, density and energy, Fig. 6.14. However, because the ψ distribution is altered the current distribution changes, Fig. 6.15. The increased spacing of the ψ surfaces reduces the magnetic field to the right of the magnetic axis, but closer surface spacing to the left means that the magnetic field is increased. This leads to increased current to the left, but a region of current reversal

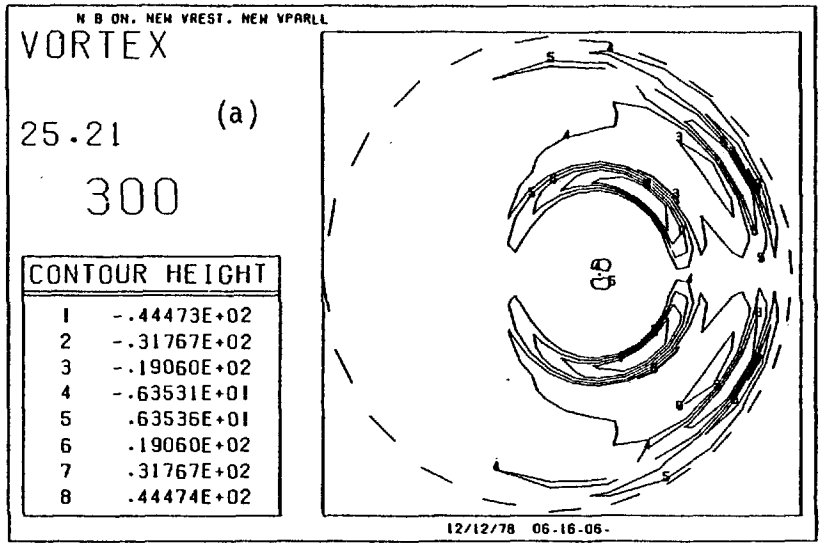

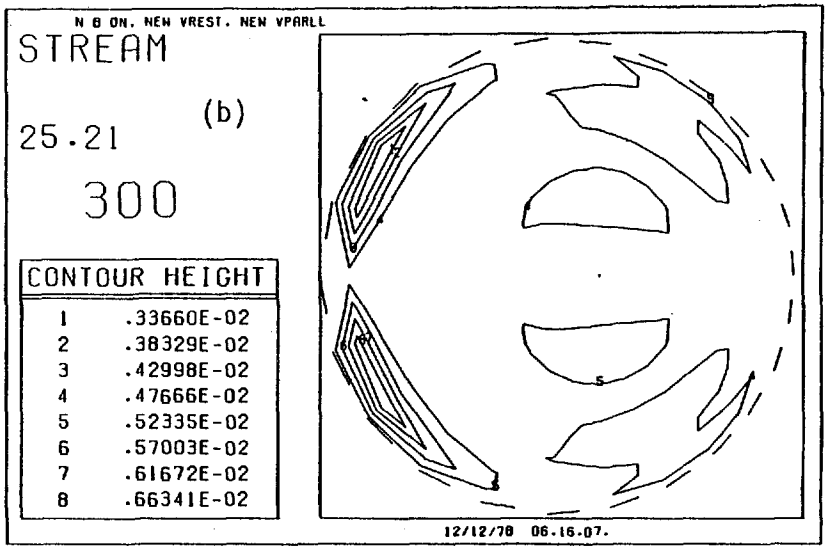

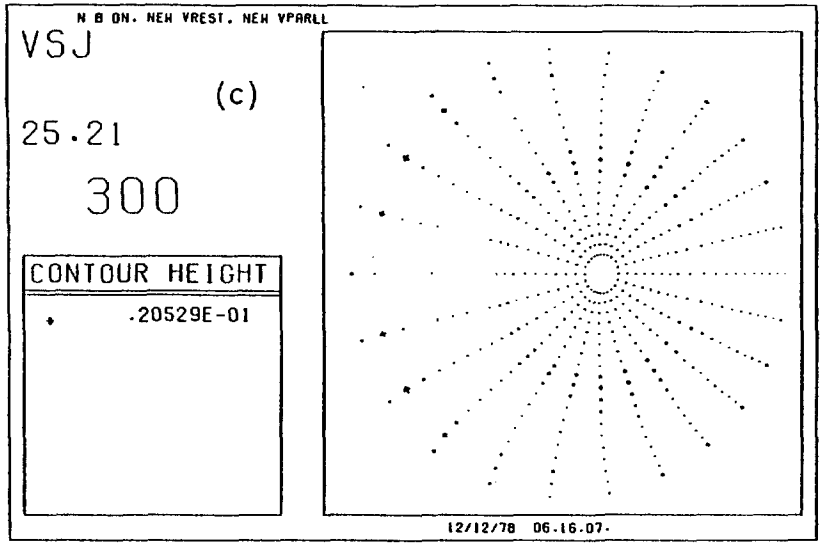

Fig. 6.13 After 25 μs the effect of the source of $p_{\parallel}$ may be seen.

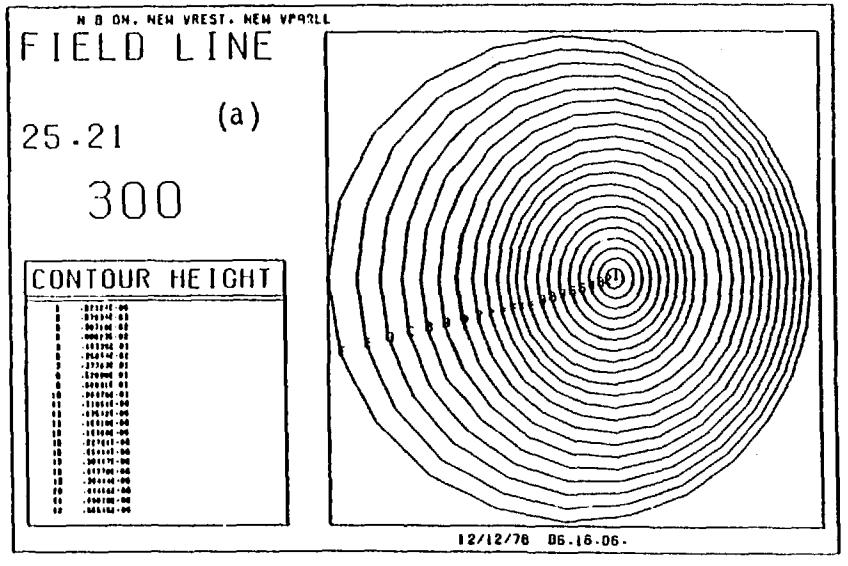

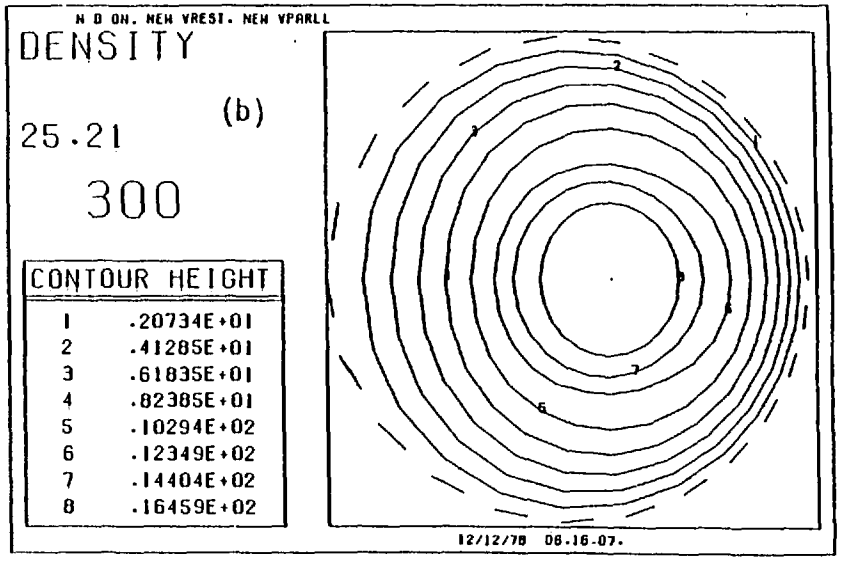

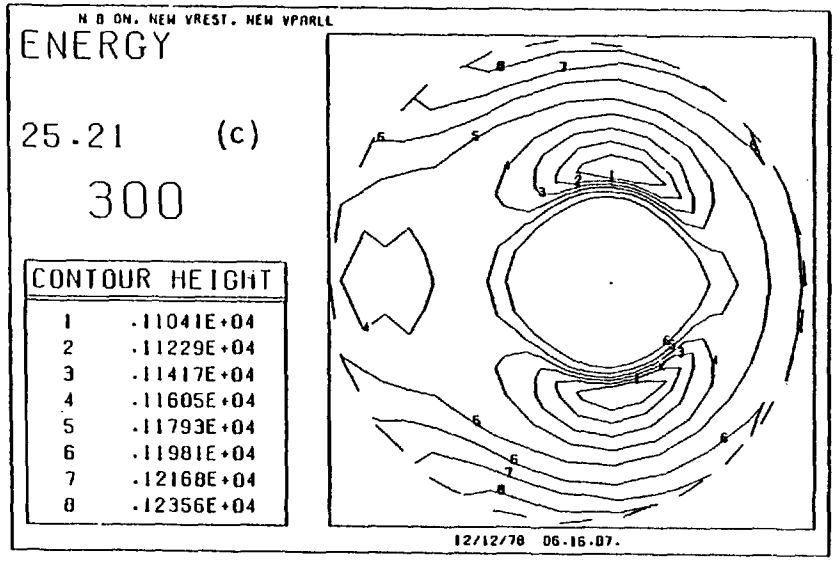

Fig. 6.14 The source of $p_{\parallel}$ begins to affect the distributions of magnetic surface, density and perpendicular temperature by advection

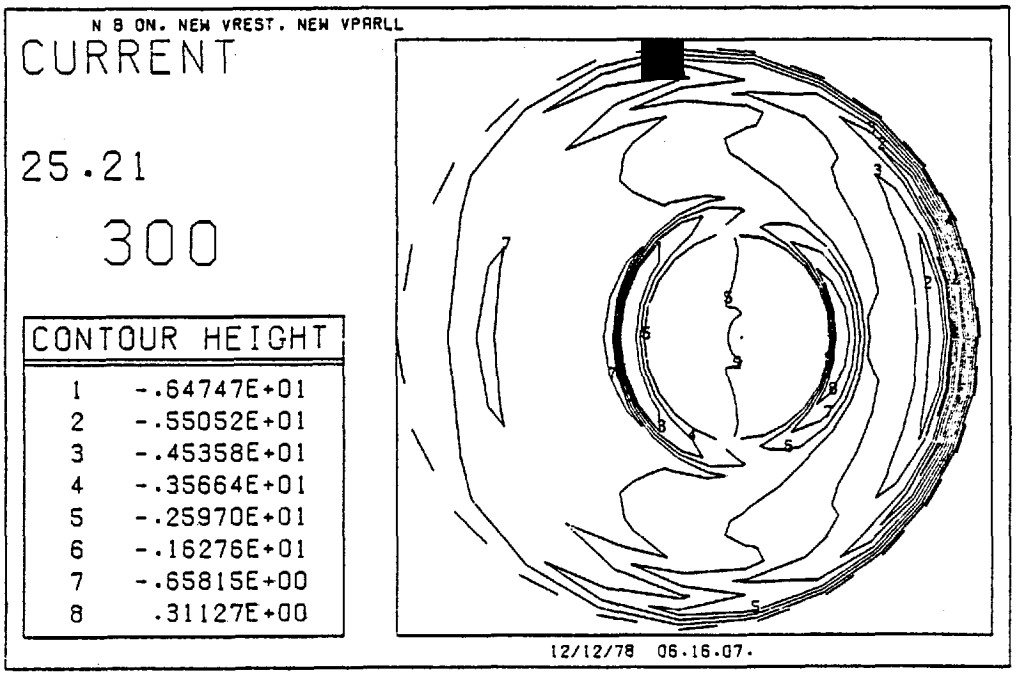

Fig. 6.15 Advection, which modifies the magnetic surface structure, also alters the current density distribution.

to the right of the magnetic axis. This motion is, therefore, not without resistance as this current distribution produces vorticity which opposes that produced by gradients of $p_{\parallel}$. Also, advection modifies $p_{\perp}$ so that $\nabla p_{\perp} \times \nabla R^2$ opposes $\nabla p_{\parallel} \times \nabla R^2$. Thus Alfven and sound waves are excited that oppose the flow produced by $p_{\parallel}$. If the source of $p_{\parallel}$ were now removed oscillation would occur about this new equilibrium. However, $p_{\parallel}$ continues to increase accompanied by the steady flow which is driving the magnetic axis towards the major axis. After 38 μs $p_{\parallel}$ has severely modified the shape of the magnetic surfaces, Fig. 6.16.

The radial profile of the safety factor, q, indicates that conditions are correct for a resistive MHD instability to occur. The q profile, Fig. 6.17, initially indicates the plasma is MHD stable, but after 38 μs the flow has modified this profile so that a local minimum

of q has now appeared.

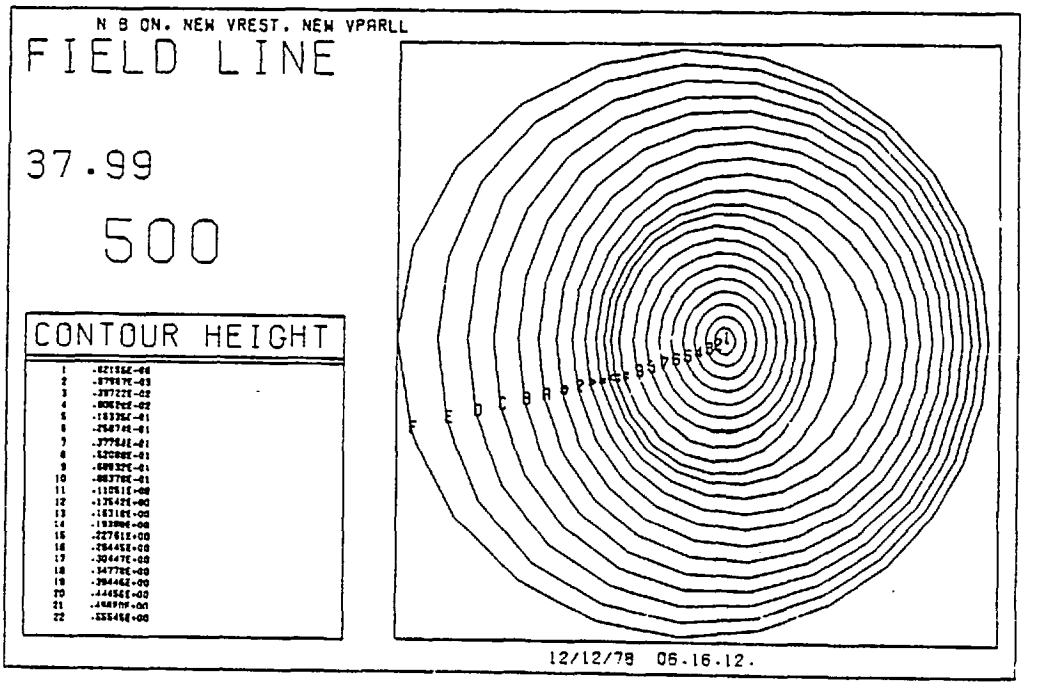

Fig. 6.16 If the parallel pressure continues to increase, the shape of the magnetic surfaces is severely modified.

As we might expect, this modification of the magnetic surfaces leads to increased transport. As in section 3 of this chapter, we integrate the mass with each surface over time and observe the variation of this integral. Table 6.2 shows the change of mass within magnetic surfaces after 38 μs of the simulation. Comparing this to Table 6.1 we see the flow produced by the source of $p_{\parallel}$ has enhanced by an order of magnitude the mass loss from the central region of the plasma. This mass has been transported to a region outside the zone where the gradient of $p_{\parallel}$ is largest. The same is also true of the perpendicular energy. The centre of the plasma is therefore losing mass at a far greater rate than that implied by classical Pfirsch-Schluter diffusion.

Finally, the loop voltage exhibits the same oscillatory behaviour seen previously, but in this run the average loop voltage, instead of remaining constant is increasing, Fig. 6.18. After about 20 μs the loop voltage becomes positive indicating that in order to keep the total

current constant, the value of the poloidal flux on the wall is being reduced.

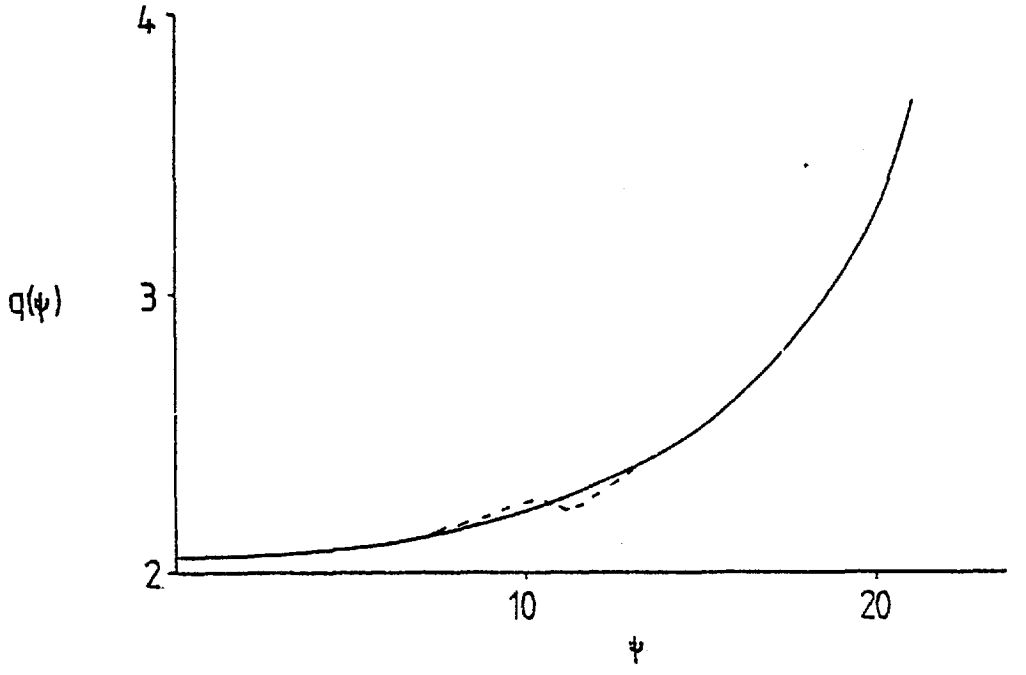

Fig. 6.17 Initial q profile (solid line) compared with the profile after 38 μs (dotted line) where a local minimum has appeared near the position of maximum parallel pressure gradient.

TABLE 6.2

Change of mass within each ψ surface for a source of $p_{\parallel}$

ψ surface	Mass change after 38 μs (kg)
4	$-1.58 \cdot 10^{-8}$
6	$-0.6 \cdot 10^{-8}$
8	$-0.1 \cdot 10^{-8}$
10	$-2.23 \cdot 10^{-8}$
12	$2.34 \cdot 10^{-8}$
14	$5.52 \cdot 10^{-8}$
16	$6.6 \cdot 10^{-8}$
18	$3.5 \cdot 10^{-8}$
20	$0.2 \cdot 10^{-8}$
22	$-1.0 \cdot 10^{-8}$

Within the plasma the energy from the source of $p_{\shortparallel}$ is going most quickly into magnetic energy, Fig. 6.19, setting up gradients of RJ_{ϕ} parallel to B_p in order to limit the flow produced by gradients of $p_{\shortparallel}$. If, once again, we consider the inductive voltage around the torus to be shorted:

$$L \frac{dI}{dt} = -I \frac{dL}{dt}$$

If U_m is the magnetic energy, then

$$\frac{dU_m}{dt} = \frac{1}{2} LI \frac{dI}{dt}$$

so the current will try to increase if $\frac{dU_m}{dt}$ is positive. In the simulation this is corrected at the edge of the plasma by setting the loop voltage so that the total current remains constant. Thus the voltage will become positive, as the magnetic energy starts to increase quickly, to reduce ψ at the wall, and therefore prevent the current from growing. Looking at Fig. 6.18 and 6.19 we see that the loop voltage goes positive at about the time that the magnetic energy starts to increase rapidly.

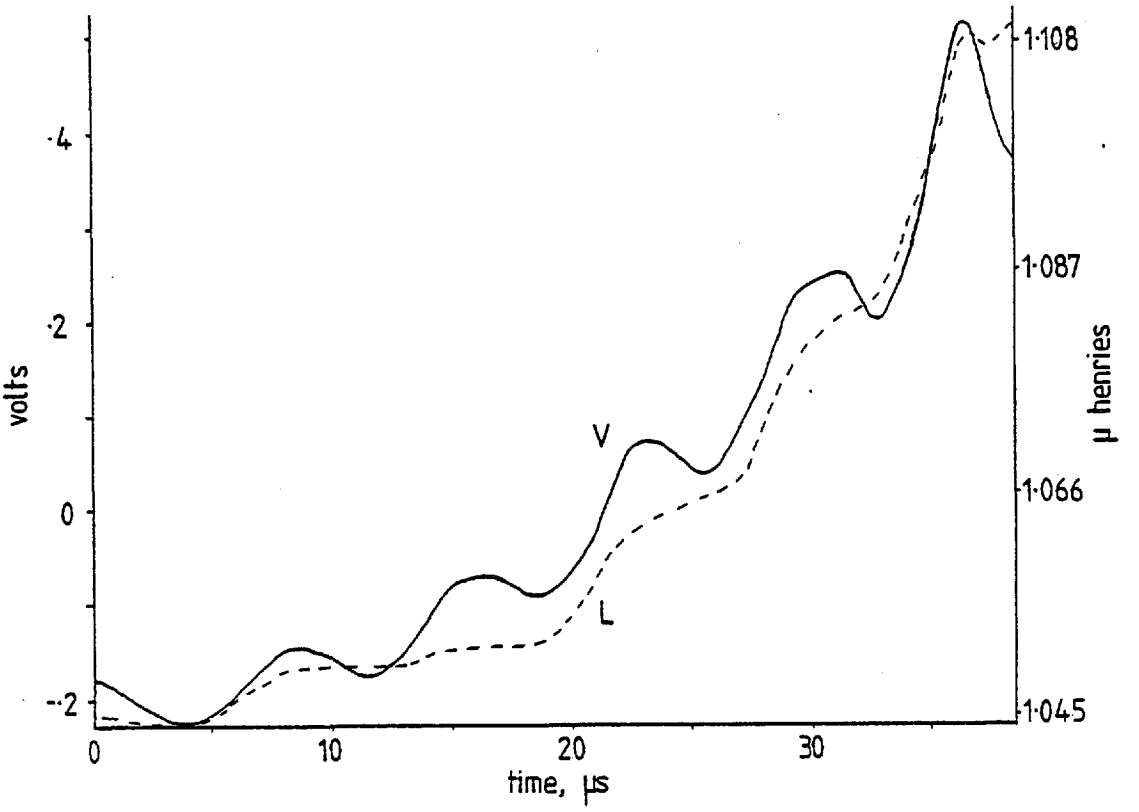

Fig. 6.18 Loop voltage and inductance against time as a source of parallel pressure is introduced.

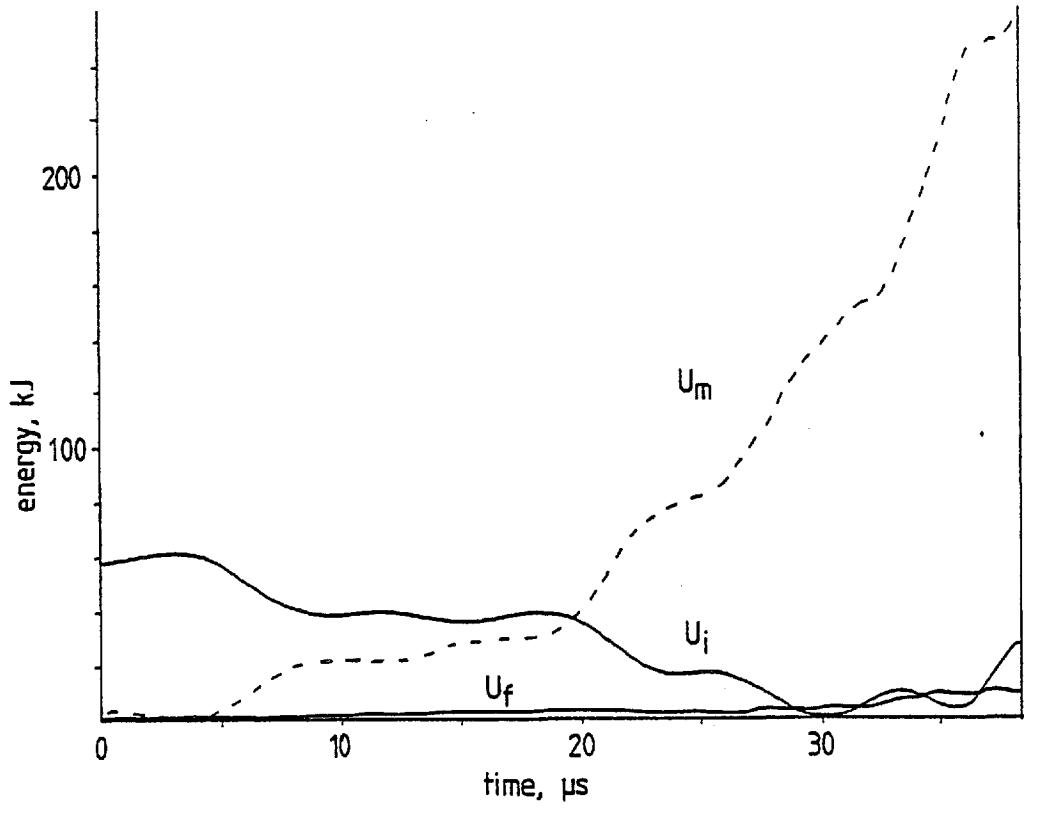

Fig. 6.19 Magnetic, internal (perpendicular) and flow energy change time history

6.6 SUMMARY

It has been shown that by choosing initial conditions close to an equilibrium, the plasma will oscillate about the equilibrium solution as magnetosonic waves propagate through the plasma. The plasma flow, being oscillatory, is larger than the steady flow required to support a stationary equilibrium state and this leads to enhanced diffusion losses, calculated to be up to ten times the classical value.

With the introduction of a neutral beam, modelled simply by a source of pressure parallel to the magnetic field, the plasma behaviour is modified by a steady flow exactly as predicted in Chapter 5. This steady flow modifies the magnetic surface structure which results in a current distribution that opposes the steady flow. The energy from $p_{\parallel}$ therefore goes into the magnetic field. In time the magnetic field becomes so distorted that a minimum of the safety factor, q, appears within the plasma indicating that disruption of the magnetic surfaces with resistive MHD instability is likely. The steady flow caused by parallel pressure gradients leads to substantially enhanced diffusion losses from the central region of the plasma.

CHAPTER 7

DISCUSSION

This thesis has presented, in essence, two important points, one physical and one computational; we discuss them in that order.

In the two regimes studied, it has been made clear that the tokamak cannot be considered as one dimensional. At early times in the discharge, it has been shown that diffusion, sound and Alfven processes are interlinked when the aspect ratio of the device is small. Preferential heating on the inner side of the torus leads to sound and Alfven waves which modify the magnetic surface structure and therefore the magnetic field diffusion. This is essentially the point made by Grad et al.[58].

At later times and higher temperatures the flow produced by a neutral beam considered as a source of parallel pressure may be described only by a two dimensional simulation. Despite the naivity of the model, an enhanced diffusion rate from the centre of the plasma is observed at least an order of magnitude greater than the classical rate.

An obvious extension to the high temperature model would be to include the effect of the electron pressure tensor on Ohms Law. While initially only the ions involved in charge exchange collisions have a high parallel pressure, these soon affect the parallel pressure of the background ions and electrons via collisions. Toroidal incompressibility could be seriously affected by large electric fields generated by the difference in perpendicular and parallel pressure.

Also it would be interesting to study the effect of various fast ion distributions upon the flow and diffusion rate. Assuming the fast ions are all at the same temperature, the spatial distribution of fast ions would give a spatial distribution of $p_{\parallel}$. Hogan and Dory[73] suggest that beam heating is peaked in the outer regions of the plasma, which would lead to a flow similar to that seen in the last chapter.

However, Rome et al.[27] find a fast ion distribution that is peaked at the magnetic axis and drops off steeply towards the plasma edge. This would produce a flow in the opposite direction to that seen in Fig. 6.7, and would result in the advection of the magnetic axis away from the major axis. Thus in both the low temperature current rise and high temperature equilibrium situations purely two dimensional phenomena can alter radically the plasma development.

Computationally, it has been shown that it is feasible to run and obtain important results from a two dimensional Lagrangian code. This, however, has not been achieved without problems and some, which are inherent in this method, remain.

Firstly, an orthogonal mesh which moves and is then reorthogonalised, must employ an interpolation procedure to redefine the dependent variables at the new mesh points. This is a source of inaccuracy. Secondly, a vector operator may not be represented as an integral quantity defined over a mesh cell, as that mesh cell must change its volume at the next timestep. This procedure would ensure that on an Eulerian mesh the method is conservative. These two problems lead us to conclude that on a two dimensional Lagrangian mesh, one cannot expect to conserve mass or energy identically.

A Lagrangian scheme was selected in order to overcome the problem of mesh interaction. This occurs when the system of equations exhibits a preferred direction (in our case around the magnetic surfaces), and is caused by the presence of the advective term. If this direction is not along a coordinate direction, drastic diffusion of the solution occurs. At the time the scheme was chosen, all algorithms for treating continuity like equations displayed this property. By choosing a Lagrangian scheme this problem was avoided by transforming to the moving frame of the fluid. However, there are available now algorithms that will solve the continuity equation on an Eulerian mesh without the problems of mesh

interaction and oscillation of the solution near a shock. The method, known as Flux Corrected Transport (FCT)[75], employs diffusion and anti-diffusion stages, first diffusing the solution across the mesh, and then reversing this apart from places where diffusion is necessary, e.g. at a shock front. It would indeed be interesting to compare our solutions with solutions from a boundary fitted Eulerian mesh using the FCT algorithm.

Boundary fitted coordinate systems are desirable and facile to implement when using a Lagrangian scheme. They may also be used with an Eulerian scheme, although an initial orthogonalisation of the mesh may be necessary. In our topology a singular point in the coordinate system must occur. At this "origin" both Lagrangian and Eulerian meshes will exhibit non-orthogonality errors unless, of course, the mesh is coincident with an orthogonal curvilinear coordinate system. Care must be taken, by considering the origin as non-orthogonal, to account for this.

Finally, we must note that the most graphic quality of a Lagrangian mesh, its power to demonstrate visually the evolution of a physical quantity, is often its most dangerous. Distortion of the surfaces representing the contours of the physical variable may lead to severe focussing of the orthogonal coordinate in some areas of the mesh. Not only does this introduce errors in the focussed region, where the mesh cells will be severely elongated or distorted, but also leave other areas of the mesh dangerously devoid of orthogonal coordinate lines and therefore lacking in resolution.

The case for a Lagrangian mesh is therefore not as strong as before the advent of FCT. It is, however, important that its feasibility has been demonstrated, and using this method results have been obtained that strongly question the one dimensional approach to the tokamak initial stages and auxillary heating.

APPENDIX A

EXPANSION OF FARADAY'S LAW

We start with Maxwells equations for the magnetic field

$$\nabla \times \underline{E} = - \frac{\partial \underline{B}}{\partial t} \quad ; \quad \nabla \times \underline{B} = \mu_o \underline{J}$$

and

$$\nabla . \underline{B} = 0$$

and a simple Ohms law

$$\eta \underline{J} = \underline{E} + \underline{v} \times \underline{B}$$

By substitution we obtain

$$\frac{d\underline{B}}{dt} = (\underline{B}.\nabla)\underline{v} - \underline{B}(\nabla.\underline{v}) - \nabla \times \eta \underline{J}$$

If R is the distance from the major axis, further rearrangement yields

$$\frac{1}{R^2} \frac{d}{dt} R\underline{B} = \frac{1}{R}(\underline{B}.\nabla)\underline{v} - R\,\underline{B}\,\nabla.\frac{\underline{v}}{R^2} - \frac{\underline{B}}{R^2}\,\underline{v}.\nabla R - \frac{1}{R}\nabla \times \left[\frac{\eta}{\mu_o} \nabla \times \underline{B}\right] \tag{A1}$$

We have seen from our ordering scheme, Chapter 2, section 1.2, that changes in the toroidal field compared to its magnitude are comparable to the total plasma beta, which is considerably less than unity.

The toroidal component of (A1) is therefore considered, and is:

$$\frac{1}{R^2 B_\phi} \frac{d}{dt} RB_\phi = \frac{1}{RB_\phi}\,\underline{B}.\nabla v_\phi - R\,\nabla.\frac{\underline{v}}{R^2} - \frac{\eta}{\mu_o}\,\frac{1}{R^2 B_\phi}\,\Delta^* RB_\phi$$

$$+ \frac{1}{RB_\phi}\,\nabla\frac{\eta}{\mu_o} . \nabla B_\phi \tag{A2}$$

Where Δ^* is the toroidal component of the curl curl operator which will be dealt with in detail in Appendix C.

The relative magnitude of the various terms in (A2) are considered

in the limit of small but finite beta. We have seen in Chapter 2 that the ratio of poloidal to toroidal magnetic field strengths and the ratio of the change in total field to total field strength are related to beta.

$$\frac{B_p}{B} \sim \beta^{\frac{1}{2}} \qquad \text{and} \qquad \frac{\delta B}{B} \sim \beta$$

We introduce a timescale T associated with changes of the total magnetic field in the fluid frame and a characteristic length L for variations of the magnetic field.

The various terms in (A2) order as follows (in exact sequence):

$$\frac{\beta}{LT} \quad , \quad \frac{\beta^{\frac{1}{2}} v_\phi}{L^2} \quad , \quad \frac{v}{L^2} \quad , \quad \frac{n}{\mu_o}\frac{\beta}{L^3} \quad , \quad \frac{n}{\mu_o}\frac{\beta}{L^3} \qquad \text{(A3)}$$

To zeroth order in $\beta^{\frac{1}{2}}$ we have the toroidal incompressibility condition, if we neglect resistive effects;

$$\nabla . \frac{\underline{v}}{R^2} = 0 \qquad \text{(A4)}$$

To first order in $\beta^{\frac{1}{2}}$, if we assume

$$v_\phi \sim O(1)\ v \qquad \text{(A5)}$$

we obtain

$$\nabla . \frac{\underline{v}}{R^2} = \frac{1}{RB_\phi}\ \underline{B} . \nabla v_\phi \qquad \text{(A6)}$$

An expression for the unknown v_ϕ may be found by considering the momentum equation, Eq. (2.14). The component along the magnetic field is:

$$\rho \frac{dv_{||}}{dt} = \rho \frac{\underline{B}}{B} \cdot \frac{dv}{dt} = \frac{-\underline{B} . \nabla p}{B} \qquad \text{(A7)}$$

Expressing the magnetic field in toroidal and poloidal components (see Appendix C):

$$\underline{B} = F\nabla\phi + \nabla\psi \times \nabla\phi = B_\phi \underline{e}_\phi + \underline{B}_p$$

we obtain

$$\rho \frac{dv_{||}}{dt} = \rho \frac{B_\phi}{B} \frac{dv_\phi}{dt} + \frac{B_p}{B} \frac{dv_p}{dt}$$

where

$$v_p = \frac{\underline{B}_p \cdot \underline{v}}{B_p}$$

(A7) may therefore be written

$$\frac{dv_\phi}{dt} = -\beta^{\frac{1}{2}} \frac{dv_p}{dt} - \frac{\underline{B} \cdot \nabla p}{\rho B} \qquad \text{(A8)}$$

It is clear from (A8) that we must consider a further ordering of the flow velocity relative to the sound speed in order to support our assumption (A5).

For the sound mach number, $M_s \gg 1$, the flow velocity is much greater than the sound speed and from (A8)

$$\Delta v_\phi \sim \beta^{\frac{1}{2}} \Delta v_p$$

and v_ϕ would disappear from an $O(\beta^{\frac{1}{2}})$ analysis. This supersonic regime would be most likely to occur in the low temperature simulations when the sound speed is relatively slow. Conversely for $M_s \ll 1$, (A8) can give us the assumption made in (A5)

$$\Delta v_\phi \sim \Delta v_p$$

if the sound speed

$$C_s^2 \sim \frac{1}{\beta^{\frac{1}{2}}}$$

In this regime v_ϕ would remain in an $O(\beta^{\frac{1}{2}})$ analysis and this would be most likely to occur in high temperature simulations where both C_s and β are larger than at low temperatures. Therefore, under certain conditions v_ϕ must be included in a first order in $\beta^{\frac{1}{2}}$ expansion of (A2).

Consider now an expansion to second order in $\beta^{\frac{1}{2}}$. To this order all the terms remaining in (A3) must be included, unless one takes account of the ordering of resistive effects. In order to write the zeroth order approximations (A4) we neglected resistive effects, by demanding

$$\frac{v}{L^2} \gg \frac{\eta}{\mu_0}\frac{\beta}{L^3}$$

Defining $\tau_f = {}^{L}/v$ and $\tau_\eta = \mu_0 L^2/\eta$ this inequality becomes

$$\tau_\eta \gg \beta\tau_f \qquad \text{(A9)}$$

Likewise, the term of the left hand side of (A2) may be neglected if

$$\frac{\beta}{LT} \ll \frac{\eta\beta}{\mu_0 L^3}$$

that is

$$T \gg \tau_\eta \qquad \text{(A10)}$$

Now T is the timescale upon which changes in the toroidal field occur in the fluid frame. This timescale which is very short is the toroidal Alfven timescale, and it is removed from the problem by considering the development of the plasma to proceed via a series of quasi-equilibria. In this sense, T may be considered long and the inequality (A10) to hold.

Therefore, to an order of $\beta^{\frac{1}{2}}$ and in the presence of finite resistivity (A2) becomes

$$\frac{\nabla.v}{R^2} = \frac{1}{RB_\phi}\,\underline{B}\,.\,\nabla v_\phi - \frac{\eta}{\mu_0}\,\frac{\Delta^* RB_\phi}{R^2 B_\phi} + \frac{\nabla\eta/\mu_0\,.\,\nabla B_\phi}{RB_\phi} \qquad \text{(A11)}$$

CORRECTIONS TO THE POLOIDAL VELOCITY

Equation (A11) is rewritten in axisymmetric cylindrical coordinates (R,ϕ,z) which after some rearrangement gives

$$\frac{\partial}{\partial R}\left(\frac{-v_R}{R} + \frac{v_\phi B_R}{RB_\phi} + \frac{\eta}{\mu_0}\frac{1}{R^2B_\phi}\frac{\partial}{\partial R}RB_\phi\right)$$

$$+ \frac{\partial}{\partial z}\left(\frac{-v_z}{R} + \frac{v_\phi B_z}{RB_\phi} + \frac{\eta}{\mu_0}\frac{1}{RB_\phi}\frac{\partial B_\phi}{\partial z}\right) = 0$$

In cylindrical notation, if a vector $\underline{C}$ is solenoidal, then

$$\frac{\partial}{\partial R}(RC_R) + \frac{\partial}{\partial z}(RC_z) = 0$$

and as seen in Chapter 2, we may fully define $\underline{C}$ in terms of Euler potentials, $\underline{C} = \nabla\zeta \times \nabla\phi$. In an axisymmetric situation this becomes

$$\underline{C} = \nabla\zeta \times \frac{e_\phi}{R}$$

therefore,

$$RC_R = -\frac{\partial\zeta}{\partial z} = \frac{-v_R}{R} + \frac{v_\phi B_R}{RB_\phi} + \frac{\eta}{\mu_0}\frac{1}{R^2B_\phi}\frac{\partial}{\partial R}RB_\phi$$

$$RC_z = \frac{\partial\zeta}{\partial R} = \frac{-v_z}{R} + \frac{v_\phi B_z}{RB_\phi} + \frac{\eta}{\mu_0}\frac{1}{RB_\phi}\frac{\partial}{\partial z}B_\phi$$

Hence we reproduce equation (2.34)

$$v_R = R\frac{\partial\zeta}{\partial z} + \frac{v_\phi B_R}{B_\phi} + \frac{\eta}{\mu_0}\frac{1}{RB_\phi}\frac{\partial}{\partial R}RB_\phi$$

$$v_z = -R\frac{\partial\zeta}{\partial R} + \frac{v_\phi B_z}{B_\phi} + \frac{\eta}{\mu_0}\frac{1}{RB_\phi}\frac{\partial}{\partial z}RB_\phi \qquad \text{(A12)}$$

The final equations (2.35) for the flow may be obtained by using Amperes Law and the momentum equations to substitute for the poloidal current terms in (A12).

APPENDIX B

DERIVATION OF THE RATE OF CHANGE OF VORTICITY

The various terms that arise when taking the curl of the momentum equation (2.14) multiplied by R^2 may be derived as follows:

$$\nabla \times (R^2\rho \frac{d\underline{v}}{dt}) = -\nabla \times (R^2\nabla p) + \nabla \times (R^2\underline{J} \times \underline{B}) \qquad (B1)$$

(i) (ii) (iii)

We take each term in turn and define:

$$P = R^2\rho$$

$$\underline{H} = \nabla \times P\underline{v}$$

(i) The term on the left hand side of (B1) is rearranged:

$$\nabla \times (R^2\rho \frac{d\underline{v}}{dt}) = \nabla \times (P \frac{d\underline{v}}{dt}) = \nabla \times (P \frac{\partial \underline{v}}{\partial t} + P\, \underline{v}.\nabla\underline{v})$$

$$= \nabla \times (\frac{\partial}{\partial t} P\underline{v} - \underline{v} \frac{\partial P}{\partial t} + P\, \underline{v}.\nabla\underline{v}) \qquad (B2)$$

Using the continuity equation with the condition of toroidal incompressibility, Eq. (2.10) gives $\frac{dP}{dt} = 0$. (B2) becomes

$$\nabla \times P \frac{d\underline{v}}{dt} = \frac{\partial}{\partial t} \nabla \times P\underline{v} + \nabla \times (\underline{v}\, \underline{v}.\nabla P + \frac{P\nabla v^2}{2} - P\underline{v} \times \nabla \times \underline{v})$$

which after some rearrangement yields:

$$= \frac{\partial}{\partial t} \nabla \times P\underline{v} + \frac{1}{2} \nabla P \times \nabla v^2 - \nabla \times (\underline{v} \times \nabla \times P\underline{v}) + \nabla \times (v^2 \nabla P)$$

Remembering that to lowest order $\nabla.\frac{\underline{v}}{R^2} = 0$ we use:

$$\frac{1}{R^2} \frac{\partial}{\partial t} R^2\underline{H} - \frac{1}{2}\nabla P \times \nabla v^2 - \nabla \times (\frac{\underline{v}}{R^2} \times R^2\nabla \times P\underline{v})$$

$$= \frac{1}{R^2} \frac{d}{dt} R^2\underline{H} - \frac{1}{2}\nabla P \times \nabla v^2 - \frac{\underline{v}}{R^2} \underline{H}.\nabla R^2 - R^2\underline{H}.\nabla\frac{\underline{v}}{R^2}$$

Now

$$\frac{d}{dt} R\underline{H} = \frac{\partial}{\partial t} R\underline{H} + \underline{v}.\nabla R\underline{H}$$

$$= \frac{d\underline{H}}{dt} + \frac{\underline{H}}{R} \underline{v}.\nabla R$$

So taking the ϕ component

$$\left(\nabla \times \left(P \frac{d\underline{v}}{dt}\right)\right)_\phi = \frac{1}{R} \frac{d}{dt} RH_\phi - \frac{1}{2}(\nabla P \times \nabla v^2)_\phi \qquad \text{(B3)}$$

because

$$H_\phi \underline{v}.\nabla R = H_\phi \frac{vR}{R}$$

which cancels with

$$-\left(R^2\underline{H}.\nabla\frac{\underline{v}}{R^2}\right)_\phi = -\left(\frac{R^2H_\phi}{R} \frac{\partial}{\partial\phi} \frac{\underline{v}}{R^2}\right)_\phi = -\frac{R^2H_\phi}{R} \frac{vR}{R^2}$$

as $\frac{\partial}{\partial\phi} \underline{e_r} = \underline{e}\phi$

and

$$\left(\frac{\underline{v}}{R^2}\right)_\phi = (\nabla\phi \times \nabla\zeta)_\phi = 0$$

(ii) The pressure term is easily derived

$$-\nabla \times R^2\nabla p = -\nabla R^2 \times \nabla p$$

taking the ϕ component

$$-(\nabla \times R^2\nabla p)_\phi = 2R(\nabla p \times \nabla R)_\phi \qquad \text{(B4)}$$

(iii) Lastly, the Lorenz force term is considered:

$$\nabla \times (R^2 \underline{J} \times \underline{B}) = R^2 \nabla \times \underline{J} \times \underline{B} + \nabla R^2 \times \underline{J} \times \underline{B}$$

$$= R^2(\underline{B}.\nabla)\underline{J} - R^2(\underline{J}.\nabla)\underline{B} + (\nabla R^2.\underline{B})\underline{J} - (\nabla R^2.\underline{J})\underline{B}$$

Consider the ϕ component

$$(\nabla \times R^2 \underline{J} \times \underline{B})_\phi = (R^2\underline{B}.\nabla\underline{J})_\phi - (R^2\underline{J}.\nabla\underline{B})_\phi$$

$$+ (\nabla R^2.\underline{B})J\phi - (\nabla R^2.\underline{J})B\phi$$

$$= R^2(\underline{B}.\nabla)J_\phi + RB_\phi(\underline{J}.\nabla R) - R^2(\underline{J}.\nabla)B_\phi - RJ_\phi(\underline{B}.\nabla R)$$

$$+ 2R(\underline{B}.\nabla R)J_\phi - 2R(\underline{J}.\nabla R)B_\phi$$

$$= R(\underline{B}.\nabla)RJ_\phi - R(\underline{J}.\nabla)RB_\phi \qquad (B5)$$

Giving:

$$(\nabla \times R^2\underline{J} \times \underline{B})_\phi = R(\underline{B}.\nabla)RJ_\phi \qquad (B6)$$

The second term on the right hand side of (B5) vanishes because RB_ϕ is an Euler potential of the current, $\underline{J}$, and as was mentioned earlier a vector field described by Euler potentials is always orthogonal to the gradients of its Euler potentials. For example, consider the current:

$$\underline{J} = \nabla \times \underline{B} \Rightarrow \nabla.\underline{J} = 0$$

$\underline{J}$ can be represented therefore:

$$\underline{J} = \nabla\alpha \times \nabla\beta$$

Assuming axisymmetry $\beta \equiv \phi$

$$\underline{J} = \nabla\alpha \times \nabla\phi = \nabla\alpha \times \frac{\underline{e}_\phi}{R}$$

$$= \nabla \times \frac{\alpha\underline{e}_\phi}{R}$$

Therefore $\underline{B} = \frac{\alpha \underline{e}_\phi}{R}$

so $\alpha = RB_\phi$

Therefore in (B5) $\underline{J}.\nabla RB_\phi = \underline{J}.\nabla\alpha = 0.$

The ϕ component of (B1) is therefore, combining the results of (i), (ii) and (iii):

$$\frac{1}{R}\frac{d}{dt} R(\nabla \times P\underline{v})_\phi - \frac{1}{2}(\nabla P \times \nabla v^2)_\phi = 2R\frac{\partial p}{\partial z} + R(\underline{B}.\nabla)RJ_\phi \qquad (B7)$$

In fact, by taking the ϕ component of the momentum equation we are, assuming the toroidal incompressibility condition, totally specifying the curl of R times the momentum equation. This is just another consequence of axisymmetry, and is demonstrated below.

From Eq. (2.10) it follows that $\underline{v}$ may be expressed by Eq. (2.11). Thus:

$$\begin{aligned}
\nabla \times P\underline{v} &= \nabla \times (PR^2\, \nabla\zeta \times \nabla\phi) \\
&= \nabla PR^2 \times (\nabla\zeta \times \nabla\phi) \\
&+ PR^2\, \nabla \times (\nabla\zeta \times \nabla\phi) \\
&= (\nabla PR^2.\nabla\phi)\nabla\zeta - (\nabla PR^2.\nabla\zeta)\nabla\phi \\
&+ PR^2\, \Delta^*\zeta\, \nabla\phi
\end{aligned}$$

Where $\Delta^*\zeta = R^2(\nabla.\frac{\nabla\zeta}{R^2})$

and is sometimes known as the Grad-Shafranov operator, which is derived more fully in Appendix C. Therefore, in axisymmetry

$$\nabla \times P\underline{v} = (PR^2\, \Delta^*\zeta - \nabla PR^2.\nabla\zeta)\nabla\phi$$

The vorticity, $\Xi = R\,\nabla \times P\underline{v}$, is thus purely toroidal and may be written

$$\underline{\Xi} = \Xi\,\underline{e}_\phi$$

We therefore arrive at the expression for the rate of change of vorticity that is used elsewhere in this work, from (B7):

$$\frac{1}{R}\frac{d\Xi}{dt} - \frac{1}{2}|\nabla P \times \nabla v^2| = 2R|\nabla p \times \nabla R| + R(\underline{B}.\nabla)RJ_\phi \qquad (B8)$$

APPENDIX C

GRAD-SHAFRANOV OPERATOR AND EQUILIBRIUM EQUATION

We define the total magnetic field as

$$\underline{B} = F\nabla\phi + \nabla\psi \times \nabla\phi \qquad (C1)$$

The first term is the toroidal field and the second the poloidal field. The toroidal field is produced by poloidal currents given by F and the poloidal field by the poloidal flux, ψ. The requirement, $\nabla.\underline{B} = 0$ demands that ∇F is perpendicular to $\nabla\phi$, i.e. in the poloidal plane. Also, F is the total poloidal current, including external currents in the coils that produce the toroidal field.

The total current density, $\underline{J}$, is given by:

$$\mu_0\underline{J} = \nabla \times \underline{B} = \nabla \times (F\nabla\phi) + \nabla \times (\nabla\psi \times \nabla\phi)$$

$$= -\nabla\phi(\nabla.\nabla\psi) - 2(\nabla\psi.\nabla)\nabla\phi + \nabla F \times \nabla\phi \qquad (C2)$$

where we have used axisymmetry to demand

$$\nabla\psi.\nabla\phi = 0$$

and subsequently the expansion

$$\nabla(\nabla\psi.\nabla\phi) = 0 = (\nabla\psi.\nabla)\nabla\phi + (\nabla\phi.\nabla)\nabla\psi \qquad (C3)$$

We note that $|\nabla\phi| = {}^{1}/_{R}$ so from (C2)

$$\nabla\phi(\nabla.\nabla\psi) + 2(\nabla\psi.\nabla)\nabla\phi = \nabla\phi\left[\nabla.\nabla\psi + 2R\nabla\psi.\nabla\left(\frac{1}{R}\right)\right]$$

$$= \nabla\phi\, R^2\left(\nabla.\frac{\nabla\psi}{R^2}\right)$$

The quantity $R^2(\nabla.\frac{\nabla\psi}{R^2})$ is sometimes termed the Grad-Shafranov operator and is usually given the symbol Δ^*. Thus

$$\Delta^*\psi = R^2(\nabla.\frac{\nabla\psi}{R^2}) \qquad (C4)$$

This term is the toroidal component of the ∇^2 operator and arises because $\nabla(\nabla\phi) \neq 0$.

Returning to (C2), the equation for the current density is

$$\mu_o\underline{J} = \dot{F}\nabla\psi \times \nabla\phi - \Delta^*\psi\,\nabla\phi \qquad (C5)$$

where $\dot{F} = \partial F/\partial\psi$.

In a steady state equilibrium situation, the momentum equation becomes

$$\nabla p = \underline{J} \times \underline{B} \qquad (C6)$$

Using the expressions (C1) and (C5) for the magnetic field and current density

$$\underline{J} \times \underline{B} = -(F\dot{F} + \Delta^*\psi)\,\frac{\nabla\phi}{\mu_o} \times (\nabla\psi \times \nabla\phi) = \nabla p$$

giving

$$\dot{p}\nabla\psi = -\frac{1}{\mu_o R^2}(F\dot{F} + \Delta^*\psi)\nabla\psi \qquad (C7)$$

as $\nabla\phi \times (\nabla\psi \times \nabla\phi) = |\nabla\phi|^2\nabla\psi$

Taking the ϕ component of (C5) and rearranging (C7) we arrive at:

$$\Delta^*\psi = -\mu_o R^2\dot{p} - F\dot{F} = -\mu_o R J_\phi \qquad (C8)$$

This is normally termed the axisymmetric equilibrium equation.

APPENDIX D

TENSOR NOTATION

The tensor notation used is that found in a number of standard works on the subject, but the notation used for covariant differentiation, whilst not the most common, is perhaps the most compact and has been taken from a treatise by Flugge[66].

As usual, repeated indices imply summation over that index:

$$a_i b^i = \sum_i a_i b^i$$

A vector may be written in terms of its contravariant or covariant components respectively:

$$\underline{a} = a^i \underline{g}_i = a_i \underline{g}^i$$

where $\underline{g}_i$ and $\underline{g}^i$ are the covariant and contravariant base vectors respectively. These have the properties:

$$\underline{g}_i \cdot \underline{g}^j = \delta_i^{\ j}$$

$$\underline{g}_i \cdot \underline{g}_j = g_{ij}$$

$$\underline{g}^i \cdot \underline{g}^j = g^{ij}$$

$$g_{ik}\, g^{jk} = \delta_i^{\ j}$$

where $\delta_i^{\ j}$ is the Kronecker delta and g_{ij} the covariant terms of the metric tensor, which has a determinant:

$$g = |g_{ij}| = 1/|g^{ij}|$$

The common derivative is denoted:

$$\underline{a}_{,i} = \frac{\partial \underline{a}}{\partial x^i}$$

and

$$a_{i,j} = \frac{\partial a_i}{\partial x^j}$$

where the length element dx^i is given by:

$$\underline{ds} = dx^i \underline{g}_i$$

The base vectors are therefore

$$\underline{g}_i = \underline{r}_{,i} = \frac{\partial \underline{r}}{\partial x^i}$$

Covariant differentiation is defined by:

$$\underline{a}_{,j} = a^{i}{}_{|j} \underline{g}_i = a_{i}{}_{|j} \underline{g}^i$$

where

$$a^{i}{}_{|j} = a^{i}{}_{,j} + a^k \Gamma_{jk}^{\ i}$$

and

$$a_{i}{}_{|j} = a_{i,j} - a_k \Gamma_{ij}^{\ k}$$

The Christoffel symbols, $\Gamma_{jk}^{\ i}$ arise from the derivatives of the base vectors.

$$\underline{g}_{i,j} = \Gamma_{ijk} \underline{g}^k = \Gamma_{ij}^{\ k} \underline{g}_k$$

Lastly, the permutation tensor is given as:

$$\varepsilon_{ijk} = \sqrt{g}\, e_{ijk}$$

or

$$\varepsilon^{ijk} = e^{ijk}/\sqrt{g}$$

where

$$e_{ijk} = e^{ijk} = +1 \qquad \text{if } i,j,k \text{ are cyclic}$$

$$= -1 \qquad \text{if } i,j,k \text{ are anticyclic}$$

$$= 0 \qquad \text{if } i,j,k \text{ are acyclic.}$$

and is known as the permutation symbol.

If the base vectors are orthogonal the metric tensor is diagonal:

$$\underline{ds}.\underline{ds} = g_{11}\, dx^{1\,2} + g_{22}\, dx^{2\,2} + g_{33}\, dx^{3\,2}$$

In the orthogonal case, we write for simplicity

$$h_i^2 = g_{ii} = 1/g^{ii}$$

$$ds^2 = (h_i\, dx^i)^2$$

$$g = h_1^2\, h_2^2\, h_3^2$$

The Christoffel symbols also take on a more regular form, given below where the summation convention, for once, does not apply:

$$\Gamma_{ij}^{k} = 0$$

$$\Gamma_{ii}^{j} = -\frac{h_i}{h_j^2}\frac{\partial h_i}{\partial x^j}$$

$$\Gamma_{ij}^{i} = \Gamma_{ji}^{i} = \frac{\partial(\log h_i)}{\partial x^j}$$

$$\Gamma_{ii}^{i} = \frac{\partial(\log h_i)}{\partial x^i}$$

Finally, in the orthogonal case, we may write a vector in terms of its components along unit vectors, $\underline{e}_i$, where

$$\underline{g}_i = h_i \underline{e}_i$$

and

$$\underline{g}^i = \underline{e}_i / h_i$$

The vector component along $\underline{e}_i$ is therefore:

$$(\underline{a})_i = a^i h_i = a_i / h_i$$

APPENDIX E

DERIVATION OF THE ENERGY FLUX EQUATION

A reduced third moment equation for a heat flux vector, $\underline{q}$, rather than the heat flux tensor $\underline{\underline{Q}}$ is obtained by contracting the general third, heat flux moment, Eq. (5.19). We note that the zero order form of the heat flux tensor, given in Eq. (5.27) implies that it is useful to define a vector with components

$$q^i = Q^{11i} + Q^{22i} + Q^{33i} \tag{E1}$$

which incidently, has non-zero component to zero order only when $i = 3$. We now split $\underline{q}$ further into a parallel and perpendicular component, defining

$$q_\perp^i = Q^{11i} = Q^{22i} \tag{E2}$$

$$q_\parallel^i = Q^{33i} \tag{E3}$$

Alternatively, $\underline{q}_\perp$ and $\underline{q}_\parallel$ may be formed using the second rank tensor $\underline{\underline{I}}_\alpha$ and the dyadic $\underline{e}_3\,\underline{e}_3$ defined in Chapter 5:

$$\underline{\underline{I}}_\alpha = \underline{\underline{I}}_2 - \underline{e}_3\,\underline{e}_3$$

where $\underline{\underline{I}}_2$ is the unit second rank tensor. Now, Eq. (E2) and (E3) are formed by:

$$\underline{q}_\perp = \frac{1}{2}\,\underline{\underline{I}}_\alpha : \underline{\underline{Q}} \tag{E4}$$

$$\underline{q}_\parallel = \underline{e}_3\,\underline{e}_3 : \underline{\underline{Q}} \tag{E5}$$

The general heat flux moment equation, Eq. (5.19), written to first order is:

$$\nabla.\underline{\underline{\underline{R}}} - \frac{1}{\rho}\{\underline{\underline{P}}\ \nabla.\underline{\underline{P}}\} - \frac{e}{m}\{\underline{\underline{\underline{Q}}} \times \underline{B}\} = \frac{\delta \underline{\underline{\underline{Q}}}}{\delta t} \tag{E6}$$

We now contract Eq. (E6) to form reduced equations for the heat flux vectors defined in Eqs. (E4) and (E5).

Taking the terms of Eq. (E6) in order we consider first:

$$(\nabla.\underline{\underline{\underline{R}}})$$

We want to substitute for zero order $\underline{\underline{\underline{R}}}$ using Eqs. (5.28) - (5.30), so it is useful now to define two second rank tensors based on the fourth rank tensor $\underline{\underline{R}}$:

$$\underline{\underline{R_\perp}} = \begin{bmatrix} 2p_\perp & 0 & 0 \\ 0 & 2p_\perp & 0 \\ 0 & 0 & p_\parallel \end{bmatrix}$$

$$\underline{\underline{R_\parallel}} = \begin{bmatrix} p_\perp & 0 & 0 \\ 0 & p_\perp & 0 \\ 0 & 0 & 3p_\parallel \end{bmatrix}$$

Now we may express the contracted form of the covariant derivative of $\underline{\underline{\underline{R}}}$ as:

$$\underline{\underline{I_\alpha}} : (\nabla.\underline{\underline{\underline{R}}}) = \nabla.\left(\frac{2p_\perp}{\rho}\ \underline{\underline{R_\perp}}\right) \tag{E7}$$

and likewise:

$$\underline{e}_3\ \underline{e}_3 : (\nabla.\underline{\underline{\underline{R}}}) = \nabla.\left(\frac{p_\parallel}{\rho}\ \underline{\underline{R_\parallel}}\right) \tag{E8}$$

The second term of Eq. (E6) is:

$$\frac{1}{\rho}\{\underline{\underline{P}}\ \nabla.\underline{\underline{P}}\}$$

Again using the reduced second rank tensors $\underline{\underline{R}}_{\perp}$ and $\underline{\underline{R}}_{\parallel}$ and remembering that the curly bracket notation means that free tensor indices are cyclicly permuted, it can be shown:

$$\frac{1}{\rho}\,\underline{\underline{I}}_{\alpha} \;:\; \{\underline{\underline{P}}\,\nabla.\underline{\underline{P}}\} \;=\; \frac{2}{\rho}\,(\underline{\underline{R}}_{\perp} - \underline{\underline{P}}).\nabla.\underline{\underline{P}} + \frac{2p_{\perp}}{\rho}\,\nabla.\underline{\underline{P}} \qquad \text{(E9)}$$

and similarly:

$$\frac{1}{\rho}\,\underline{e}_3\,\underline{e}_3 \;:\; \{\underline{\underline{P}}\,\nabla.\underline{\underline{P}}\} \;=\; \frac{1}{\rho}\,(\underline{\underline{R}}_{\parallel} - \underline{\underline{P}}).\nabla.\underline{\underline{P}} + \frac{p_{\parallel}}{\rho}\,\nabla.\underline{\underline{P}} \qquad \text{(E10)}$$

Finally, the last term on the left hand side of Eq. (E6) can easily be shown to reduce to:

$$\frac{e}{m}\,\underline{\underline{I}}_{\alpha} \;:\; \{\underline{\underline{Q}} \times \underline{B}\} \;=\; \frac{2e}{m}\,\underline{q}_{\perp} \times \underline{B} \qquad \text{(E11)}$$

and

$$\frac{e}{m}\,\underline{e}_3\,\underline{e}_3 \;:\; \{\underline{\underline{Q}} \times \underline{B}\} \;=\; \frac{2e}{m}\,q_{\parallel} \times \underline{B} \qquad \text{(E12)}$$

The reduced form of Eq. (E6) may therefore be written in two parts for the perpendicular and parallel heat flux:

$$\nabla.\left(\frac{p_{\perp}}{\rho}\,\underline{\underline{R}}_{\perp}\right) - \frac{1}{\rho}\,(\underline{\underline{R}}_{\perp} - \underline{\underline{P}}).\nabla.\underline{\underline{P}} - \frac{p_{\perp}}{\rho}\,\nabla.\underline{\underline{P}} - \frac{e}{m}\,\underline{q}_{\perp} \times \underline{B} = \frac{\delta \underline{q}_{\perp}}{\delta t} \qquad \text{(E13)}$$

$$\nabla.\left(\frac{p_{\parallel}}{\rho}\,\underline{\underline{R}}_{\parallel}\right) - \frac{1}{\rho}\,(\underline{\underline{R}}_{\parallel} - \underline{\underline{P}}).\nabla.\underline{\underline{P}} - \frac{p_{\parallel}}{\rho}\,\nabla.\underline{\underline{P}} - \frac{e}{m}\,\underline{q}_{\parallel} \times \underline{B} = \frac{\delta \underline{q}_{\parallel}}{\delta t} \qquad \text{(E14)}$$

If we now combine Eqs. (E13) and (E14), using Eq. (E1) for the total heat flux:

$$\underline{q} \;=\; 2\underline{q}_{\perp} + \underline{q}_{\parallel}$$

and defining the internal energy as:

$$\rho\varepsilon = 2p_{\perp} + p_{\parallel}$$

we obtain:

$$\nabla.\left(\frac{2p_{\perp}}{\rho}\,\underline{\underline{R}}_{\perp} + \frac{p_{\parallel}}{\rho}\,\underline{\underline{R}}_{\parallel}\right) - \frac{2}{\rho}\,\underline{\underline{P}}.\nabla.\underline{\underline{P}} - \varepsilon\nabla.\underline{\underline{P}} - \frac{e}{m}\,\underline{q} \times \underline{B} = \frac{\delta\underline{q}}{\delta t} \qquad \text{(E15)}$$

The first term in Eq. (E15) is easily rearranged, and the second and third terms are arranged to give:

$$\nabla.\frac{1}{\rho}\,(2\underline{\underline{P}}.\underline{\underline{P}} + \rho\varepsilon\,\underline{\underline{P}}) - \frac{1}{\rho}\,(2\underline{\underline{P}} + \rho\varepsilon\,\underline{\underline{I}}_2).\nabla.\underline{\underline{P}} - \frac{e}{m}\,\underline{q} \times \underline{B} = \frac{\delta\underline{q}}{\delta t} \qquad \text{(E16)}$$

Finally, by expanding the first term of Eq. (E16) and subtracting the second term we obtain

$$\nabla.\left(\frac{1}{\rho}\,(2\underline{\underline{P}} + \rho\varepsilon\,\underline{\underline{I}}_2).\underline{\underline{P}}\right) - \frac{1}{\rho}\,(2\underline{\underline{P}} + \rho\varepsilon\,\underline{\underline{I}}_2)\,\nabla.\underline{\underline{P}}$$

$$= \underline{\underline{P}} : \nabla\frac{1}{\rho}\,(2\underline{\underline{P}} + \rho\varepsilon\,\underline{\underline{I}}_2)$$

$$= \underline{\underline{P}}.\nabla\varepsilon + 2\,\underline{\underline{P}} : \nabla(\underline{\underline{P}}/\rho)$$

Thus we obtain Eq. (5.35) for the heat flux for each species when $\nu\delta\underline{q}$ is the change in heat flux resulting from inter species collisions:

$$\underline{\underline{P}}.\nabla\varepsilon + 2\,\underline{\underline{P}} : \nabla(\underline{\underline{P}}/\rho) - \frac{e}{m}\,\underline{q} \times \underline{B} = \nu\delta\underline{q} \qquad \text{(E17)}$$

REFERENCES

1. L.A. ARTSIMOVICH et al., in Plasma Physics and Controlled Nuclear Fusion Research (Proc. 2nd Int. Conf. Culham 1965) 2 IAEA (1966) 595
2. L.A. ARTSIMOVICH et al., in Plasma Physics and Controlled Nuclear Fusion Research (Proc. 3rd Int. Conf. Novosibirsk 1968) 1 IAEA (1969) 17
3. L.A. ARTSIMOVICH, Nuc. Fusion 12 (1972) 215
4. J.A. LAWSON, Proc. Phys. Soc. B70 (1957) 6
5. N.J. PEACOCK et al., Nature 224 (1969) 488
6. J. SHEFFIELD et al., in Controlled Fusion and Plasma Physics (Proc. 6th European Conf. Moscow 1973) 1 51
7. K. BOL et al., in Plasma Physics and Controlled Nuclear Fusion Research (Proc. 5th Int. Conf. Tokyo 1974) 1 IAEA (1975) 77
8. L.A. BERRY et al., in Plasma Physics and Controlled Nuclear Fusion Research (Proc. 5th Int. Conf. Tokyo 1974) 1 IAEA (1975) 113
9. H. EUBANK et al., in Plasma Physics and Controlled Nuclear Fusion Research (Proc. 7th Int. Conf. Innsbruck 1978) 1 IAEA (1979) 167
10. M.D. KRUSKAL, R.M. KULSRUD, Phys. Fluids 1 (1958) 265
11. R. CHODURA et al., in Plasma Physics and Controlled Nuclear Fusion Research (Proc. 7th Int. Conf. Innsbruck 1978) 2 IAEA (1979) 335
12. V.D. SHAFRANOV, Sov. Phys. JETP 8 (1958) 494
13. V.D. SHAFRANOV, Zh. eksp. teor Fiz 37 (1959) 1088
14. J.A. WESSON, Nuc. Fusion 18 (1978) 87
15. V.D. SHAFRANOV, Atomn. Energy 5 (1956) 38
16. V.D. SHAFRANOV, Sov. Phys. Tech. Phys. 15 (1970) 175
17. H.P. FURTH, J. KILLEEN, M.N. ROSENBLUTH, Phys. Fluids 6 (1963) 459
18. B. COPPI, J.M. GREENE, J.L. JOHNSON, Nuc. Fusion 6 (1966) 101
19. H.P. FURTH, P.H. RUTHERFORD, H. SELBERG, Phys. Fluids 16 (1973) 1054
20. R.A. DORY, Y-K.M. PENG, Nuc. Fusion 17 (1977) 21

21. H. GRAD, Phys. Fluids 10 (1967) 137

22. F.L. HINTON, J.C. WILEY, D.F. DÜCHS, H.P. FURTH, P.H. RUTHERFORD, Phys. Rev. Letts. 29 (1972) 698

23. V.A. ABRAMOV, V.V. VIKHREV, O.P. POGUTSE, in Plasma Physics and Controlled Nuclear Fusion Research (Proc. 6th Int. Conf. Berchtesgaden 1976) 2 IAEA (1977) 237

24. D.F. DÜCHS, H.P. FURTH, P.H. RUTHERFORD, Nuc. Fusion 12 (1972) 341

25. S.J. WEBB, in Plasma Physics and Controlled Nuclear Fusion Research (Proc. 6th Int. Conf. Berchtesgaden 1976) 2 IAEA (1977) 245

26. H.P. FURTH, Nuc. Fusion 15 (1975) 487

27. J.A. ROME, J.D. CALLEN, J.F. CLARKE, Nuc. Fusion 14 (1974) 141

28. J.W. CONNOR, J.G. CORDEY, Nuc. Fusion 14 (1974) 185

29. G.H. TUTTLE, D.E. POTTER, in Controlled Fusion and Plasma Physics (Proc. 6th European Conf. Moscow 1973) 1 217

30. G.H. TUTTLE, PhD thesis, London (1976)

31. D.P. STERN, Am. J. Phys. 38 (1970) 494

32. J.B. TAYLOR, in Plasma Physics and Controlled Nuclear Fusion Research (Proc. 5th Int. Conf. Tokyo 1974) 1 IAEA (1975) 161

33. I.P. SHKAROFSKY, T.W. JOHNSON, M.P. BACHYNSKI, The Particle Kinetics of Plasmas, Addison Wesley (1966)

34. L. BRAND, Vector and Tensor Analysis, Wiley (1947)

35. C. TRUESDELL, Kinematics of Vorticity, Indiana (1954)

36. D.V. ANDERSON, J. Comput. Phys. 17 (1975) 246

37. D.E. POTTER, Methods in Computational Physics 16 (1976) 43

38. D.E. POTTER, G.H. TUTTLE, J. Comput. Phys. 13 (1973) 483

39. H.P. FURTH, S. YOSHIKAWA, Phys. Fluids 13 (1970) 2593

40. M.G. HAINES, Proc. Phys. Soc. 74 (1959) 576

41. D.W. PEACEMAN, H.H. RACHFORD, Jr., J. Soc. Industrial Appl. Math., 3 (1955) 28

42. R.S. VARGA, Matrix Iterative Analysis, Prentice Hall (1962)

43. R.D. RICHTMYER, K.W. MORTON, Difference Methods for Initial Value Problems, 2nd ed., Interscience (1967)

44. D.E. POTTER, Computational Physics, Wiley (1973)

45. L. SPITZER, Physics of Fully Ionized Gases, Interscience (1956)

46. I.P. SHKAROFSKY, I.B. BERNSTEIN, B.B. ROBINSON, Phys. Fluids 6 (1963) 40

47. TFR GROUP, in Plasma Physics and Controlled Nuclear Fusion Research (Proc. 6th Int. Conf. Berchtesgaden 1976) 1 IAEA (1977) 35

48. C.W. DAVIES, Private communication

49. O. TAUSSKY, Am. Math. Mon. 56 (1949) 672

50. H.P. FURTH, M.N. ROSENBLUTH, P.H. RUTHERFORD, W. STODIEK, Phys. Fluids 13 (1970) 3020

51. B.B. KADOMTSEV, Nuc. Fusion Reactor Conference, Culham 1969, p. 210

52. A.M. ANASHIN et al., Soviet Phys. JETP 33 (1971) 1127

53. D. DIMOCK et al., in Plasma Physics and Controlled Nuclear Fusion Research (Proc. 4th Int. Conf. Maddison) 1 IAEA (1971) 451

54. D. GROVE et al., in Plasma Physics and Controlled Nuclear Fusion Research (Proc. 6th Int. Conf. Berchtesgaden 1976) 1 IAEA (1977) 21

55. A.B. BERLIZOV et al., in Plasma Physics and Controlled Nuclear Fusion Research (Proc. 6th Int. Conf. Berchtesgaden 1976) 1 IAEA (1977) 3

56. I.H. HUTCHINSON, A.H. MORTON, Nuc. Fusion 16 (1976) 447

57. S.V. MIRNOV, I.B. SEMENOV, Sov. At. Energy 30 (1971) 22

58. H. GRAD, P.N. HU, D.C. STEVENS, E. TURKEL, in Plasma Physics and Controlled Nuclear Fusion Research (Proc. 6th Int. Conf. Berchtesgaden 1976) 2 IAEA (1977) 355

59. D.L. BOWERS, B.S. LILEY, S.H. MORTON, C.E. VANCE, Plasma Phys. 13 (1971) 849

60. The JET project - Design Proposal for the Joint European Torus, Euratom Rep. EUR - 5561e (1976)

61. R. PAPOULAR, Nuc. Fusion 16 (1976) 37

62. A.I. MOROZOV, L.S. SOLOV'EV, Sov. Phys. Dokl. 4 (1960) 1031

63. A.A. GALEEV, R.Z. SAGDEEV, Sov. Phys. JETP 26 (1968) 233

64. D.F. DÜCHS, D.E. POST, P.H. RUTHERFORD, Nuc. Fusion 17 (1977) 565

65. A. MACMAHON, Phys. Fluids 8 (1965) 1840

66. W. FLÜGGE, Tensor Analysis and Continuum Mechanics, Springer Verlag (1972)

67. G.F. CHEW, M.L. GOLDBERGER, F.E. LOW, Proc. Roy. Soc. (London) A236 (1956) 112

68. A.C. RIVIERE, Nuc. Fusion 11 (1971) 363

69. J.D. CALLEN, R.A. DORY, Phys. Fluids 15 (1972) 1523

70. H. GRAD, J. HOGAN, Phys. Rev. Letts. 24 (1970) 1337

71. R.C. GRIMM, J.L. JOHNSON, J. Comput. Phys. 17 (1975) 192

72. D. PFIRSCH, A. SCHLÜTER, Report of Max Planck Institute (1962) MPI/PA(7) 62

73. J.T. HOGAN, R.A. DORY, in Controlled Fusion and Plasma Physics (Proc. 5th European Conf. Grenoble 1972) 1 (1972) 40

74. D.L. JASSBY, Nuc. Fusion 17 (1977) 373

75. J.L. BORIS, D.L. BOOK, J. Comput. Phys. 11 (1973) 38